



UNIVERSITÉ DE GENÈVE

FACULTÉ DES SCIENCES

Département de physique
nucléaire et corpusculaire

Professeur Allan G. Clark

**Recherche de leptoquarks de deuxième génération à CDF
et
développement de l'électronique pour l'ATLAS**

THÈSE

*présentée à la Faculté des sciences de l'Université de Genève pour
l'obtention du titre de Docteur ès sciences, mention physique*

par

Hisanori KAMBARA

de

Toyohashi, Japon

Thèse N° 2977

GENÈVE

Atelier d'impression de la Section de Physique

1998

Abstract

Cette thèse traitera de la recherche de leptoquarks de deuxième génération dans les données récoltées par le détecteur collisionneur à Fermilab (CDF) aux États-Unis. Les données des interactions $p\bar{p}$ à $\sqrt{s} = 1.8$ TeV concernent les années 1992 à 1995 et totalisent une luminosité de ~ 110 pb $^{-1}$. Cette analyse s'intéressera en particulier aux événements dont l'état final comprend deux muons ainsi que deux gerbes hadroniques.

Les résultats de cette analyse ne permettent pas de confirmer l'existence de leptoquarks pour une telle énergie. Cependant, une nouvelle limite quand à la section efficace de production a pu être donnée.

A l'aide des calculs théoriques les plus récents concernant la production de paires de leptoquarks [1], cette analyse permet d'exclure les leptoquarks scalaires de deuxième génération, ayant une masse plus petite que 202 GeV/ c^2 .

Le prochain collisionneur hadronique de haute énergie (LHC), actuellement en construction au CERN, permettra de rechercher des leptoquarks dans un domaine d'énergie plus élevée. Le détecteur trace constitue une pièce maîtresse de l'identification des leptons issus de la désintégration des leptoquarks. Un détecteur à micro-bandes en silicium, actuellement en cours de développement, sera utilisé dans le cadre de l'expérience ATLAS. Avec une haute luminosité et une fréquence élevée d'événements attendus au LHC, un système compact, rapide et offrant un bon rapport signal sur bruit ainsi qu'une petite dissipation de chaleur est nécessaire.

Un prototype de circuit intégré, l'ADAM, utilisé pour la lecture du détecteur de trace à micro-bandes de silicium sera décrit dans la deuxième partie de ce mémoire. Les résultats de l'étude détaillée de tests en laboratoire ainsi que de ceux effectués en faisceau test seront également présentés.

**Search for Second Generation Leptoquarks in $\sqrt{s} = 1.8$ TeV $p\bar{p}$ at CDF
and
Silicon Detector Readout Electronics Development with ATLAS**

Abstract

In this thesis, a search for second generation leptoquark is presented. It is based on the data collected at the Collider Detector at Fermilab with the Tevatron proton-antiproton collisions of $\sqrt{s} = 1.8$ TeV. A total integrated luminosity of $\sim 110 \text{ pb}^{-1}$ collected during runs in 1992-1995 is used. The search was performed on the charged dimuon plus dijet channel. No evidence for existence of leptoquark was found, and a new production cross section limit is set as a result of this analysis. Using the most recent theoretical calculation of pair leptoquark production [1], a new lower mass limit for second generation scalar leptoquark is extracted. The new limit excludes $M(LQ_2) < 202 \text{ GeV}/c^2$.

The Large Hadron Collider (LHC), a proton-proton collider with a center of mass energy (\sqrt{s}) of 14 TeV, is currently under the construction at CERN. It will be utilised to extend the searches for the leptoquarks to higher mass regions. As in CDF, tracking detectors are essential to identify charged leptons decaying from leptoquarks. A silicon strip tracking detector is being developed for the ATLAS experiment. A dense and fast readout system with a good signal to noise ratio and low power consumption are required with high luminosity and short event collision interval (25 ns) expected at the LHC. A description of a prototype front-end micro-electronic chip, the *ADAM*, for silicon strip detector readout application is presented. Results from a complete laboratory test as well as its performance on a test beam at CERN are reported.

*Submitted in partial fulfilment of the requirements for the degree of
Docteur ès sciences in physics at the University of Geneva*

Acknowledgements

I would like to express my sincere gratitude to my advisor Professor Allan Clark for the advise and encouragement he has provided through out my graduate years. Also to Dr. Xin Wu with the CDF physics analyses and Dr. Roberto Bonino concerning the ATLAS hardware work. With their patient guidances and helpful discussions, I was given my directions to come to this point today.

It has been delightful to meet such wonderful people at the CDF experiment when I visited Fermilab to work on my physics analysis. Without the suggestions and help of Dr. Kaori Maeshima, I would never have found the analysis topic which I present in this thesis. She has given me so much time and advice as I struggled to get started in the CDF experiment. For work concerning the leptoquark search, I would like to thank the members of the Exotic Physics Group of CDF. I received assistance from Manoj Pillai who provided me with the data, and from Professor Henry Frisch, Dr. Carla Grosso-Pilcher, and Dr. Michelangelo Mangano. Dr. T. Sjöstrand, the author of Pythia Monte-Carlo generator, has been so kind to give me a response every time I faced a problem. I also would like to acknowledge friends from Tsukuba University at the CDF, who have helped me with my work as well as made my stay at Fermilab very enjoyable.

While working with the ATLAS group, I must not forget to express my thanks to A. Poppleton and A. Dell'Acqua of the ATLAS Collaboration for helping me with the Monte-Carlo simulation. I would like to acknowledge those RD2 Collaboration members, especially Francis Anghinolfi at CERN, who have contributed their work and effort to the development of the ADAM chip. I received enormous help from Annie Leger and Daniel La Marra at University of Geneva while I was testing the ADAM chip.

It really is my parents back home who have taught me the value of education and the merit of exploration. Numerous of letters from my mother and my sister while I stayed so far from home have given me the encouragement that I needed. I am eternally grateful to them for always being behind me and for having made it possible to come this far. And my love and gratitude for you who always stayed besides me to give me a reason to go on. To you all, I dedicate this thesis.

神原久徳

平成九年拾貳月

Curriculum Vitae

L'auteur naquit à ville d'Okazaki, préfecture d'Aichi, au Japon, le 17 février 1969. Après avoir terminé sa scolarité secondaire au Japon, il obtint une licence ès sciences en physique et astrophysique à l'Université de Californie à Berkeley aux Etats-Unis en 1991. Il travailla ensuite un été en tant qu'étudiant auprès de l'Organisation Européenne pour la Recherche Nucléaire (CERN) à Genève, en Suisse. Il y travailla dans le domaine de l'électronique de lecture de détecteurs silicium à bandes et les faisceaux tests relatifs au détecteur de traces interne de l'expérience ATLAS. Ce travail fut effectué dans le groupe du Professeur Allan Clark, de l'Université de Genève, où l'auteur obtint une équivalence de Diplôme de Physicien en mars 1993. Il continua ensuite le programme d'études du troisième cycle, sous la direction du Professeur Allan Clark. Il effectua un travail d'analyse de hardware, qui constitue une partie de cette thèse. Il rejoignit ensuite l'expérience CDF (*Collider Detector at Fermilab*) à accélérateur du Tevatron en 1995 et y effectua l'analyse de physique sur laquelle est basée cette thèse.

The author was born in Okazaki-city, Aichi prefecture, Japan on February 17, 1969. After completing the secondary education in Japan, he graduated with Bachelor of Art degrees in physics and astrophysics from the University of California at Berkeley, U.S.A., in 1991. He then worked as a summer student at European Organisation for Nuclear Research (CERN) in Genève, Swizerland, for one summer. The work involved the micro electronic readout system of silicon strip detectors and, the associated test beam analysis for the ATLAS Inner Tracking detector. He worked in the group of Professor Allan Clark with the University of Genève, where the author completed the equivalence of the diplôme work in March 1993. He continued on with his graduate student study program under the supervision of Professor Allan Clark. He completed a hardware analysis project as a part of this thesis. He then joined the Collider Detector at Fermilab (CDF) experiment at the Tevatron accelerator at Fermilab in 1995. The physics analysis of this thesis is based on the data collected at the CDF experiment.

“Why climb mountains ?”

“Because they are there.”

–George Mallory

*for my parents back home
for my sisters
and for you especially
who always gave me the courage*

Contents

Abstract	i
Acknowledgements	iii
Curriculum Vitae	v
Table of Contents	vii
1 Résumé	1
1.1 Introduction générale	1
1.2 La description de la physique	2
1.3 Recherche de leptoquarks de deuxième génération à CDF	2
1.3.1 Les leptoquarks dans les collisions hadroniques	3
1.3.2 L'analyse de données	4
1.3.3 Le bruit de fond et l'erreur systématique	8
1.3.4 Les résultats	9
1.4 L'expérience ATLAS au LHC	11
2 General Introduction	12
3 Leptons, Quarks, and Leptoquarks	15
3.1 Quarks, leptons, and gauge bosons	16
3.1.1 Historical progress	16

3.1.2	Fermions	16
3.1.3	Gauge bosons	18
3.1.4	The Standard Model	19
3.1.5	Symmetry and unifications	21
3.1.6	Standard Model Inadequacies	23
3.2	The Leptoquark theory	25
3.2.1	SU(5) GUT unified model	25
3.2.2	Pati-Salam colour symmetrical model	28
3.2.3	Technicolour model	28
3.2.4	Other models	29
3.3	Leptoquark Production at $p\bar{p}$ Collider	29
3.3.1	Production diagrams	30
3.3.2	The Leading Order production cross section	32
3.3.3	Higher order corrections	34
3.3.4	NLO v.s. LO	37
3.3.5	Numerical calculations	38
3.4	Leptoquark decay	39
3.5	Existing leptoquark search limits	41
3.5.1	Non-hadron collider searches	41
3.5.2	Previous LQ_2 search at Tevatron	41
3.5.3	Summary of existing leptoquark mass limits	42
4	The CDF Experimental Apparatus	44
4.1	The Tevatron collider	44
4.2	The CDF detector	47
4.2.1	CDF coordinate system	49
4.2.2	CDF sub-detectors	50
4.3	Tracking at CDF	52

4.3.1	The Solenoid	53
4.3.2	The SVX	53
4.3.3	The VTX	54
4.3.4	The CTC	55
4.4	The Calorimetry	57
4.4.1	The Central and Plug calorimeter: Electromagnetic	59
4.4.2	The Central and Plug calorimeter: Hadronic	61
4.4.3	Forward calorimeter	62
4.5	The muon chamber	62
4.5.1	The CMU	64
4.5.2	The CMP	67
4.5.3	The CMX	67
4.6	Trigger system	68
4.6.1	Level-1 trigger	69
4.6.2	Level-2 trigger	72
4.6.3	Level-3 trigger	74
4.7	Data Collection	74
5	A Second Generation Leptoquark Search at CDF	76
5.1	Introduction	76
5.2	Data Samples and Pre-Selection Criteria	77
5.2.1	Run IA data pre-selection	77
5.2.2	Run IB data pre-selection	78
5.3	Event selection criteria	79
5.3.1	Muon kinematics study	79
5.3.2	Other muon distributions	80
5.3.3	Muon selection	81
5.3.4	Event topology cut	87

5.3.5	Event cut statistics	89
5.4	Cosmic rays and reconstructed mass deviation	93
5.4.1	Cosmic ray muons	93
5.4.2	Reconstructed mass deviation	97
5.4.3	Candidate event distributions and comparison with Monte Carlo	101
5.4.4	Comments on the Previous Analysis	101
5.5	Signal Detection Efficiency	103
5.5.1	Monte Carlo samples	103
5.5.2	Method and Calculated Efficiencies	104
5.5.3	Total event detection efficiency, ε_{tot}	116
5.6	Background	118
5.6.1	Drell-Yan	118
5.6.2	Heavy flavour decay	120
5.6.3	W^+W^-	121
5.6.4	$Z \rightarrow \tau^+\tau^-$	121
5.6.5	Fake muons	122
5.6.6	Total expected background	122
5.6.7	Expected background with mass constraint	122
5.6.8	Systematic Uncertainties	123
5.6.9	Difference of event selection for quoted numbers	125
5.7	Upper Limit and Calculation Method	127
5.7.1	Cross section calculation with background	127
5.7.2	Upper limit	129
5.8	Conclusion on the leptoquark search	130
6	The Large Hadron Collider and ATLAS experiment	134
6.1	The LHC and its physics potential	135
6.1.1	Leptoquark searches at LHC	136

6.2	The ATLAS experiment	141
6.2.1	The ATLAS detector overview	142
6.2.2	Calorimetry	143
6.2.3	Muon spectrometer and magnet	143
6.2.4	The Inner Detector	144
6.3	The Semiconductor Tracking detectors (SCT)	148
6.3.1	The Barrel Silicon Tracker	149
7	The ADAM Chip	152
7.1	Introduction	152
7.2	The ADAM Chip	153
7.2.1	The Architecture of ADAM	153
7.3	ADAM chip components	154
7.3.1	NICON front-end pre-amplifier	155
7.3.2	DHARP	156
7.3.3	CRIAD Analogue to Digital Converter	157
7.3.4	APC-3 Logic and Pipeline Address	160
7.3.5	ADAM Chip Specifications	162
7.4	The ADAM Test Setup	162
7.4.1	The ADAM Test board	162
7.4.2	ADAM Test board Sequence	165
7.4.3	The Piggy Back	167
7.4.4	DAQ Systems	168
7.5	Measurement Results of ADAM chip	168
7.5.1	CRIAD non-linearity and measurements	168
7.5.2	The Baseline–Time Column Dependent Pedestal	171
7.5.3	Pedestal with NICON amplifier	171
7.5.4	Pedestal and Noise with Baseline Subtraction	173

7.5.5	Linearity	175
7.5.6	Gain Correspondence	176
7.5.7	Load Capacitor and Noise Increase	176
7.5.8	Multi-Trigger readout during the digitisation and readout process	178
7.5.9	<i>REIN</i> delay	181
7.5.10	Double Pulse Resolution	182
7.5.11	Power Consumption	183
7.6	Summary of Performance Measurements	183
7.7	The ADAM in the Test Beam	184
7.7.1	The H8 Test Beam	184
7.7.2	Results	184
7.8	Conclusion for ADAM Chip	187
8	Conclusion	188
	Appendix	190
A	Spontaneous symmetry breaking	190
B	Muon trigger at CDF	193
C	SUSY and Compositeness search at ATLAS	195
C.1	Search for SUSY particles	195
C.2	Search for Compositeness	198
	References	200

Chapter 1

Résumé

1.1 Introduction générale

Le travail de recherche dans le domaine de la physique des particules comporte plusieurs aspects. Il s'agit d'abord de comprendre les lois physiques de la nature. Ceci motive dans un deuxième temps la construction de détecteurs qui nous permettront de tester un modèle théorique, ou de rechercher de nouveaux phénomènes. L'analyse des données expérimentales à l'aide d'outils informatiques est un autre domaine du travail de recherche. Nous retrouverons plusieurs de ces aspects dans cette thèse puisqu'elle comprend le développement d'un détecteur ainsi qu'une analyse de résultats expérimentaux.

Ce travail de thèse s'organise de la manière suivante : dans un premier temps au Chapitre 3, nous introduirons le modèle standard, ainsi que ses extensions. Nous pourrions vérifier la validité de ce modèle à l'aide des observations expérimentales. Une de ces observations consiste à trouver des leptoquarks dans le cadre de l'expérience CDF, qui utilise les faisceaux du Tevatron de Fermilab aux États-Unis. Une description de l'accélérateur et du détecteur CDF est donné au Chapitre 4. La deuxième partie de cette thèse contiendra l'analyse des données récoltées jusqu'en 1995 qui sont présentées au Chapitre 5. Finalement, la dernière partie décrira le développement de l'électronique permettant la reconstruction des traces dans le détecteur interne de l'expérience ATLAS au LHC, étant donné que ce dernier est important pour la recherche des leptoquarks. La description de l'expérience ATLAS est donnée au Chapitre 6 et sera suivie par une description du développement du détecteur au Chapitre 7.

1.2 La description de la physique

Les nombreux modèles théoriques qui tendent à expliquer les phénomènes de la physique dans cette thèse ont tous un point commun : décrire les forces qui expliquent les interactions des particules. Le modèle standard (MS) [2], le modèle physique le plus unanimement reconnu aujourd’hui dans la communauté de la physique des hautes énergies qui est basé sur le groupe de jauge $SU(3)_C \otimes SU(2)_L \otimes U(1)_Y$. Il nous fournit de manière remarquable l’une des descriptions les plus satisfaisantes de la phénoménologie moderne de la physique des particules. Le but ultime est de comprendre le mode d’interaction entre les particules et de trouver l’existence d’une théorie englobant toutes les particules observables ainsi que toutes les forces connues.

A la fin du siècle dernier, Maxwell réussit à lier la force électrique et la force magnétique en une théorie unique connue sous le nom de “*force électromagnétique*”. Dans les années 1960, S. Glashow, A. Salam, et S. Weinberg [3, 4, 5] établirent la théorie de la force “*électro-faible*”, unifiant ainsi la force électromagnétique et la force faible. L’étape suivante vers une théorie unifiée consisterait à unifier la force nucléaire (force forte) et la force électro-faible. Cette unification impliquerait une nouvelle particule de jauge, un médiateur de l’interaction entre familles de quarks et de leptons. Une telle particule, introduite au tant qu’extension du MS, est généralement appelée *leptoquark*.

1.3 Recherche de leptoquarks de deuxième génération à CDF

Cette partie est consacrée à l’analyse physique, à savoir la recherche de leptoquarks de deuxième génération (LQ_2) à CDF. Les leptoquarks sont appelés particules “*exotiques*”, puisque leur existence prédite par certains modèles théoriques n’a pas encore été vérifiée. Ainsi, l’on peut s’attendre à une particule relativement massive, si bien que les énergies actuellement disponibles ne permettent pas leur observation. L’emploi d’accélérateurs plus performants permet d’explorer des domaines d’énergie inconnus et offre la possibilité de découvrir de nouvelles particules.

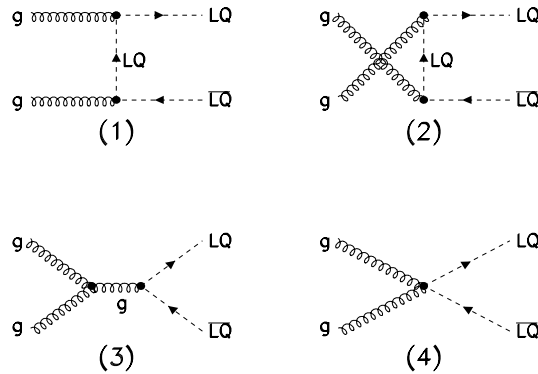


Figure 1.1: Les diagrammes de Feynman qui décrivent les processus partoniques $gg \rightarrow LQ_2 \overline{LQ}_2$.

1.3.1 Les leptoquarks dans les collisions hadroniques

Dans le collisionneur hadronique au Tevatron [6], les leptoquarks sont produits en solitaire ou par paire. Pour les productions en solitaire, la constante de couplage de Yukawa λ pour les leptoquarks n'est pas connue et par conséquent la section efficace est dépendente du modèle choisi. Par contre, lors des productions par paires, les leptoquarks sont directement créés par des collisions de partons interagissant selon la QCD, de même que pour les productions des quarks lourds. La force de couplage ne dépend dans cas que des nombres quantiques des leptoquarks et il est possible de déterminer la section efficace. Dans la recherche directe des leptoquarks (Chapitre 5), la théorie d'ordre plus élevée (Calcul du *Next-to-Leading Order* [1]) est comparée avec les résultats expérimentaux, afin d'extraire la limite inférieure de la masse des leptoquarks.

La section efficace pour les productions par paires est dépendente du spin et du facteur de couleur des leptoquarks. Dans le cas des leptoquarks scalaires, la section efficace peut être calculer précisément, car il n'y a pas de paramètres libres ni d'hypothèses. Ces productions sont réalisées par la fusion de deux gluons ou par l'annihilation de quark-antiquark.

$$\begin{aligned}
 q + \bar{q} &\rightarrow LQ + \overline{LQ} \\
 g + g &\rightarrow LQ + \overline{LQ}
 \end{aligned}
 \tag{1.1}$$

Les Figures 1.1 montrent les diagrammes de Feynman pour la fusion de deux gluons. Ces

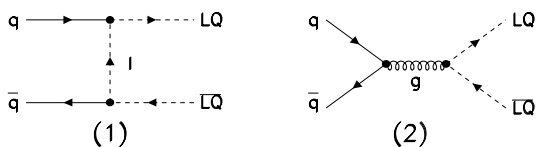


Figure 1.2: Les diagrammes de Feynman qui décrivent les processus $q\bar{q} \rightarrow LQ_2\overline{LQ_2}$.

processus sont identiques aux productions des squarks, $gg \rightarrow \widetilde{q}\overline{\widetilde{q}}$. Ces deux processus donnent la même section efficace [7].

Les diagrammes de Feynman qui décrivent les interactions $q\bar{q} \rightarrow LQ_2\overline{LQ_2}$ sont montrés sur les Figures 1.2. Les calculs détaillés de la section efficace ainsi que les résultats numériques sont décrit au Chapitre 3.3.

Les leptoquarks se désintègrent dans la deuxième génération de leptons et de quarks selon la formule $LQ_2 \rightarrow \mu^\pm, \nu_\mu + q_2$. La valeur β caractérise le rapport de désintégration entre lepton chargé (μ^\pm) et non-charge (ν_μ). Les canaux de désintégration possibles sont

$$\begin{aligned} LQ_2 &\rightarrow q_2\mu^\pm, & \text{Br} &= \beta \\ LQ_2 &\rightarrow q_2\nu_\mu, & \text{Br} &= 1 - \beta \end{aligned} \quad (1.2)$$

Dans cette analyse, nous nous sommes concentrés sur les leptoquarks qui peuvent se désintégrer en un quark et un lepton chargé avec $\beta = 1.0$. Cette recherche est donc basée sur les événements contenant deux muons et ≥ 2 gerbes ($LQ_2\overline{LQ_2} \rightarrow \mu^+\mu^-jj + X$).

Une recherche précédente, utilisant les données de CDF de 19 pb^{-1} (Run IA) [8], a exclu les leptoquarks de masse inférieure à $131 \text{ GeV}/c^2$ pour $\beta = 1.0$ et $96 \text{ GeV}/c^2$ pour $\beta = 0.5$. D'autres résultats ont été publiés par une autre expérience de Fermilab, DØ [9]. Les autres générations (premier et troisième) de leptoquarks, observées à Fermilab ainsi que dans d'autres laboratoires, seront décrites à la Section 3.5.

1.3.2 L'analyse de données

Le Détecteur à Collisionneur de Fermilab (CDF) utilise le faisceau du Tevatron, collisionneur proton-antiproton dont l'énergie dans le centre de masse ($\sqrt{s} = 1.8 \text{ TeV}$) est la plus élevée

au monde actuellement. L'analyse concernant la recherche de leptoquarks présentée dans cette thèse est basée sur les données récoltées durant les années 1992 à 1995 (Run IA et IB), correspondant à une luminosité intégrée de $\sim 110 \text{ pb}^{-1}$. L'accélérateur du Tevatron et du détecteur CDF sont brièvement décrits au Chapitre 4.

La sélection des muons

Les événements qui nous intéressent doivent répondre à plusieurs critères de sélection.

Premièrement, on ne garde que les événements contenant deux muons. Nous avons utilisé la technique de Monte Carlo pour étudier en détail les propriétés du signal pour une masse du LQ_2 comprise entre 100 et 240 GeV/c^2 . Nous avons utilisé le générateur PYTHIA avec la fonction de distribution partonique, CTEQ4M [10], pour générer les leptoquarks de deuxième génération. Le QFL [11] est une simulation rapide et fiable du détecteur CDF. Les valeurs de coupure pour la sélection des candidats LQ_2 ont été choisies selon la technique de Monte Carlo. Ces valeurs ont été optimisées de façon à éliminer le bruit de fond tout en gardant une détection du signal efficace. Nous avons également utilisé la méthode de Monte Carlo pour évaluer les erreurs systématiques.

Deuxièmement, il faut que le premier muon ait une impulsion transversale p_T plus grande que 30 GeV/c et que le deuxième muon ait une impulsion transversale plus grande que 20 GeV/c . Ces impulsions transversales sont mesurées par une Chambre à Trace Centrale (CTC). Un des muons doit avoir une trace dans le CTC qui corresponde à la région "fiduciale" du détecteur à chambre de muons central (CMU ou CMU/CMP). Le muon satisfaisant ce critère est défini comme un muon "tight". L'autre muon peut être un muon "loose" qui contiendra aussi le muon "tight". Le muon "loose" est un muon ayant une trace dans le CTC qui ne doit pas forcément tomber dans la région "fiduciale" du détecteur à chambre de muons. Cette trace doit cependant traverser au moins 75 % du CTC dans la direction radiale. Cette dernière condition garantit la qualité de trace du muon, donc ses caractères cinématiques.

Troisièmement, on exige d'autres critères de façon d'augmenter la qualité des muons. L'un d'eux est l'isolation du muon, c'est-à-dire que la somme de l'énergie autour du muon, définie dans l'espace $\eta-\phi$ de 0.4, ou $\Delta R = \sqrt{(\Delta\eta)^2 + (\Delta\phi)^2} \leq 0.4$, doit être inférieure à 2.0 GeV . Un autre est que les vertex correspondent à des vertex détectés par le détecteur VTX ($< 5\text{cm}$).

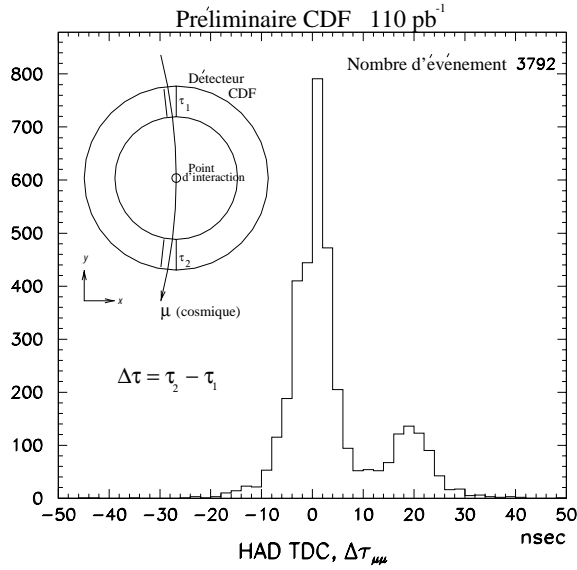


Figure 1.3: $\Delta\tau$ de dimuon, mesuré par TDC du calorimètre hadronique pour les événements avec plus que deux muons de haute impulsion p_T . Run IA+B.

La sélection topologique

Dans cet échantillon d'événements ayant une grande énergie transversale, on exige que le nombre de gerbes soit plus grand ou égal à deux avec une énergie transversal plus grande que 30 GeV pour la première gerbe et plus grande que 15 GeV pour la deuxième gerbe. Les énergies de ces gerbes, mesurées par des calorimètres, sont définies par un algorithme "cone" avec $\Delta R \leq 0.7$ dans l'espace $\eta - \phi$. Les deux gerbes doivent satisfaire à la condition $|\eta| < 2.4$, i.e. dans la région centrale du détecteur. Cependant, des corrections sont à apporter à l'énergie, afin de déterminer la masse invariante de la gerbe + muon ($M_{\mu j}$). En effet, il faut tenir compte des erreurs dues à l'énergie contenue en dehors du cone d'une part, à l'énergie provenant d'autres interactions d'autre part ("underlying events"), et tenir compte des erreurs dues à la géométrie du détecteur. Les résonances des autres particules telles que Z^0 , J/ψ et Υ sont rejetées en éliminant les événements ayant une masse invariante de dimuon $M_{\mu\mu} < 11 \text{ GeV}/c^2$ et $76 < M_{\mu\mu} < 106 \text{ GeV}/c^2$. Onze événements ont survécu à toutes ces coupures.

Les rayons cosmiques peuvent simuler des événements de dimuons de haute impulsion transversale. Cependant, de tels muons, avec leur vitesse avoisinant celle de la lumière, pren-

Type de critères	Nombre d'événements restant	
	Run IA	Run IB
Nombre total d'échantillons	5444	25490
1 ^{er} muon sélectionné	1188	5656
2 ^{eme} muon sélectionné	716	3437
2 gerbes	104	833
Energie transversale des gerbes	7	57
Masse invariante $M_{\mu\mu}$	1	10
Rayons cosmiques	1	10

Table 1.1: Statistiques des événements sélectionnés.

ment un temps fini pour traverser le détecteur. Le détecteur CDF a un diamètre de ~ 6 m au niveau des calorimètres. Ces rayons laissent une trace en entrant par le sommet du détecteur et en sortant par le bas de celui-ci. Le calorimètre enregistre le temps de détection des particules (informations de TDC). Les particules qui proviennent des collisions du faisceau dans le centre du détecteur doivent être enregistrées approximativement au même moment par le calorimètre. En revanche, les muons provenant des rayons cosmiques atteignent le calorimètre inférieur environ ~ 20 ns plus tard. La Figure 1.3 illustre $\Delta\tau$ de dimuon. On utilise également l'information de l'angle d'ouverture ($\Delta\phi$) du système de dimuon pour détecter les événements provenant de ces rayons cosmiques¹. On applique les coupures $\Delta\tau < 13$ ns et $\Delta\phi < 3.0$. Aucun des 11 événements sélectionnés n'ont été identifiés comme étant des rayons cosmiques.

Le nombre des événements retenus après chaque coupure est présenté dans la Table 1.1. Les 11 événements ayant survécus à la sélection sont montrés sur la Figure 1.4 dans la Section 1.3.4 dans le plan de masse invariante des gerbes-muons ($M_{\mu j}^1$ v.s. $M_{\mu j}^2$). Avec deux muons et deux gerbes, il existe deux possibilités d'appariement de gerbe-muon. Pour déterminer la masse des leptoquarks nous avons choisi la combinaison ayant la plus petite différence de masse invariante, puisque les deux leptoquarks issus d'un événement doivent avoir la même masse.

Dans le cas de la désintégration d'une paire de leptoquarks, les masses de deux gerbes-muons reconstruites doivent être inférieures à la résolution σ_r déterminée par Monte Carlo.

¹Les muons des rayons cosmiques sont dos-à-dos ("back-to-back"), i.e. $\Delta\phi \approx \pi$

Mathématiquement,

$$\Delta|M_{\mu j}^1 - M_{\mu j}^2| < 3\sigma_r \quad (1.3)$$

Ces limites égales à $3\sigma_r$ pour des masses de $M_{LQ} = 100$ à $240 \text{ GeV}/c^2$ sont représentées graphiquement sur la Figure 1.4.

En raison des caractéristiques du détecteur et des fausses identifications de gerbes, la déviation de la résolution de la masse est asymétrique, ce qui conduit à une forme ovale telle qu'on peut le voir sur la Figure 1.4. Ce “*mass balancing*” réduit le bruit de fond substantiellement, puisque dans les événements contenus dans ce bruit de fond, les masses invariantes des gerbe-muons reconstruites ne sont pas corrélées.

1.3.3 Le bruit de fond et l’erreur systématique

Le bruit de fond pour les leptoquarks de deuxième génération provient des événements avec deux muons ayant une grande impulsion transversale et qui coïncident avec plus de deux gerbes de haute énergie. Les sources possibles sont soit des processus de Drell-Yan d’ordre plus élevés, des désintégrations de quarks lourds ($\bar{b}b$ ou $\bar{t}t$ dans les canaux dimuons), WW , $Z^0 \rightarrow \tau^+\tau^-$, soit encore des événements avec deux “*fake*” muons associés avec deux gerbes. Les “*fake*” muons sont des muons provenant des gerbes qui déclenchent le trigger ou provenant des gerbes hadroniques de haute énergie transversale atteignant la chambre à muons. Le bruit de fond principal résulte du processus de Drell-Yan ($Z^0/\gamma \rightarrow \mu^+\mu^-$ et plus de deux gerbes). Ces gerbes proviennent des radiations dans l’état initial ou final. Les autres bruits de fond, p.ex., $\bar{b}b$ ou $Z^0 \rightarrow \tau^+\tau^-$ sont négligeables. Nous avons utilisé, pour estimer ce bruit de fond, la technique de Monte Carlo et également les données de CDF. Cette estimation donne un bruit de fond de 14 ± 1.8 pour une luminosité intégrée de 109 pb^{-1} , avant d’appliquer le critère de “*mass balancing*”.

Quand on applique l’algorithme de “*mass balancing*”, la contribution du bruit de fond diminue substantiellement, p.ex. 0.1 événements pour $LQ_2 = 200 \text{ GeV}/c^2$. Dans nos résultats finaux, nous n’avons pas effectué, par prudence, la soustraction du bruit de fond pour calculer la limite de la section efficace de la production de leptoquarks.

Le nombre, N , d'événements attendus est donné par la formule

$$N = \mathcal{L} \cdot \beta^2 \cdot \sigma(M_{LQ_2}) \cdot \varepsilon_{totale} \quad (1.4)$$

où \mathcal{L} est la luminosité intégrée des donnés, β le rapport de désintégration entre le lepton chargé et non-chargé, $\sigma(M_{LQ_2})$ la section efficace pour une masse donnée et où ε_{total} est l'efficacité totale pour une paire de leptoquarks observée.

On décompose l'efficacité totale de la façon suivante.

$$\varepsilon_{total} = \varepsilon_{\mu\text{-geom}P_T} \cdot \varepsilon_{\mu ID} \cdot \varepsilon_{trig} \cdot \varepsilon_{2gerbes} \cdot \varepsilon_{mass.inv.} \cdot \varepsilon_{M(LQ_2)} \quad (1.5)$$

Chaque composante de ε_{total} est évaluée en fonction de la masse des leptoquarks en utilisant la méthode de Monte Carlo et les donnés. L'efficacité totale est défini de façon à correspondre à 9% pour $M(LQ_2) = 100 \text{ GeV}/c^2$ et à 22% pour $M(LQ_2) = 240 \text{ GeV}/c^2$. Cette efficacité, donnée dans la Table 1.2, augmente de façon monotone avec la masse des leptoquarks.

Les erreurs systématiques sont estimées par le Monte Carlo. La source principale des erreurs est due à la compréhension limitée des radiations de gluons dans les états initiaux et finaux. Nous avons calculé la limite de la section efficace expérimentale avec 19% pour $M(LQ_2) = 100 \text{ GeV}/c^2$ et à 10% pour $M(LQ_2) = 240 \text{ GeV}/c^2$ d'erreur systématique. Ceci est décrit dans la Table 1.2.

1.3.4 Les résultats

Nous avons calculé les limites pour $\sigma(p\bar{p} \rightarrow LQ_2 \overline{LQ_2}) \cdot \beta^2$ pour un niveau de confiance de 95%. La section efficace de la production de leptoquarks est donnée par la formule

$$\sigma(M_{LQ_2}) \cdot \beta^2 = \frac{N}{\mathcal{L} \cdot \varepsilon_{totale}} \quad (1.6)$$

où N est le nombre d'événements observés. Les résultats expérimentaux sont montrés dans la Figure 1.4. La masse limite des leptoquarks dépend uniquement du modèle théorique choisi. Nous avons choisi le modèle théorique le plus récent, "Next-to-Leading Order Calculation" [1], et nous en avons déduit la masse limite de $M(LQ_2) > 202 \text{ GeV}/c^2$ ($\beta = 1.0$) pour les

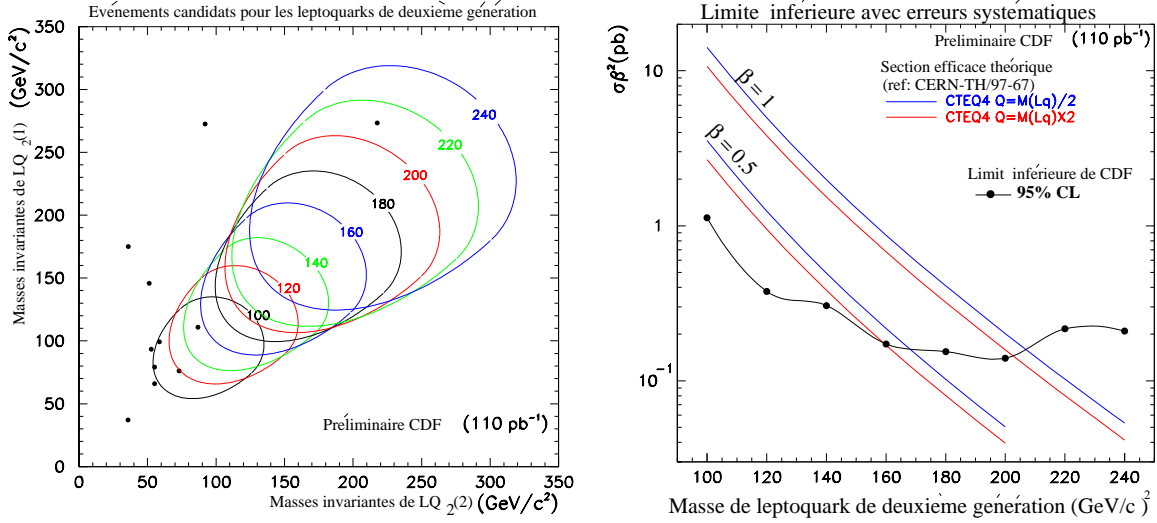


Figure 1.4: (Gauche) Distribution des masses invariantes des gerbe-muons pour les candidats de LQ_2 , avec les délimitations de “mass balancing”. (Droite) Limites pour $\sigma(p\bar{p} \rightarrow LQ_2 \overline{LQ_2}) \cdot \beta^2$ pour un niveau de confiance de 95% en fonction de la masse des leptoquarks avec une erreur systématique et statistique. La soustraction du bruit de fond n’est pas effectué.

$MassedeLQ_2$ (GeV/c^2)	120	160	200	240
Efficacité totale	0.13	0.17	0.20	0.22
Erreurs systématiques	0.15	0.14	0.11	0.10
Bruit de fond attendu	3.77	1.14	0.28	0.09
Nombre de événement observé	1	0	0	1
σ (à 95 % <i>C.L.</i>) en pb	0.34	0.16	0.13	0.19

Table 1.2: Résultat expérimentale pour masses de LQ_2 différents pour 109 pb $^{-1}$ de donnés CDF.

leptoquarks scalaires de deuxième génération.

La non-observation de LQ_2 nous a permis de fixer une nouvelle limite inférieure à sa masse. Ce résultat a été présenté dans plusieurs conférences [12, 13] et un proceeding (une publication suivant la présentation de la conférence) a été publié [14].

1.4 L'expérience ATLAS au LHC

Si la théorie suppose l'existence des leptoquarks, cette existence n'est pas confirmée expérimentalement, car la masse des leptoquarks est trop élevée pour être observée avec l'énergie du Tevatron. La prochaine génération d'expériences hadroniques avec des énergies toujours plus élevées sera possible au Large Collisionneur Hadronique (LHC), actuellement en cours de construction au CERN, avec des faisceaux de proton-proton qui atteindront une énergie dans le centre de masse (\sqrt{s}) de 14 TeV, alors que l'énergie du Tevatron s'élève à 1.8 TeV. Le LHC rendra donc possible l'étude d'un domaine d'énergie inexploré expérimentalement. L'existence de leptoquarks de masse jusqu'à 1 TeV pourra y être testée.

Le développement d'une expérience au LHC avec luminosité et énergie élevées demande l'emploi de détecteurs adaptés. L'un des outils de détection les plus efficaces aujourd'hui dans le domaine des particules à haute énergie est celui qui utilise les matériaux semi-conducteurs, en raison de leur capacité à repérer le passage de particules chargées, de leur rapidité à acquérir des données et de leur précision de leur mesure dans l'espace. Les détecteurs de traces jouent un rôle essentiel pour identifier les leptons chargés, issus de la désintégration des leptoquarks, les jets de hadrons et les vertex secondaires des particules à longue durée de vie.

La dernière partie de cette thèse décrira le développement du détecteur ATLAS et du collisionneur LHC, à Genève en Suisse. ATLAS est l'une des deux expériences de haute énergie du LHC, qui doit être opérationnelle en 2005. Une description des appareils de l'expérience, de leurs spécificités et des possibilités d'études qu'offrira ATLAS dans le domaine de la physique est donnée au Chapitre 6. Cette partie sera suivie par les résultats du développement de la puce "ADAM", l'électronique destinée à la lecture des données que produira le détecteur interne au silicium.

Chapter 2

General Introduction

The research work of Elementary Particle Physics is based on our current understanding of the laws of physical nature and theoretical predictions. It guides us to design experiments and to develop detector technologies. Following the construction of an experiment, we analyse the data collected from collider detectors to perform experimental measurements. This allows us to verify the theoretical predictions and to search for new phenomena.

This thesis reports both a physics analysis and a detector development. For the physics analysis, it presents a search for leptoquarks with the Tevatron $p\bar{p}$ collider at Fermilab, carried out at the Collider Detector at Fermilab (CDF) experiment using the data collected up to 1995. For the detector development, a work on the Inner Tracking Detector of the ATLAS experiment at Large Hadron Collider (LHC) project at CERN is presented. A brief summary of this thesis follows.

First of all, I introduce today's most widely accepted model, called the Standard Model (SM), and its possible extensions that we can explore with our experimental apparatus. There are numerous theoretical models which attempt to explain the phenomena of Elementary Particle Physics. All of them essentially contain the same ultimate idea– to explain fundamental particles and forces acting between them. Fundamental particles refer to the smallest building units, and the forces hold these particles together and are responsible for their interactions. The Standard Model, based on an $SU(3)_C \otimes SU(2)_L \otimes U(1)_Y$ gauge group, is one of the most remarkably successful descriptions of the Elementary Particle Physics theory. This theory will be introduced briefly in Chapter 3. Much literature [2] is available for full details.

According to the Standard Model, there are two types of fundamental particles; fermions which carry spin of $\frac{1}{2}$ and gauge bosons with spin of 1. The massive elementary particles which make up the universe are fermions¹, while interactions between fermions are carried out by gauge bosons. The fermions are divided into two families, called leptons and quarks. Our aim is to understand the interactions between those elementary particles, and to find a single unified theory which embodies the observable particles and the forces in the universe. At the end of the last century, Maxwell succeeded to unify the electric and magnetic forces into a single theory called electromagnetism, which was later developed into quantum electrodynamics (QED). By S. Glashow, S. Weinberg, and A. Salam [3, 4, 5] in the early 1960's combined the theory of electromagnetism with the theory of weak forces to form a single theory of electroweak forces. A possibility for further unification is to combine the strong nuclear force and the electroweak force. This predicts new gauge particles which will mediate interactions between lepton and quark families. The particles to mediate such interaction are predicted in many extensions of the Standard Model, and they are generally called *leptoquarks*.

Leptoquarks are classified as exotic particles since their existence is predicted in certain theoretical models yet they have not as yet been observed experimentally. The mass of leptoquarks is assumed to be very heavy since we have not seen evidence of their existence within the energy scale of existing accelerators. Past experiments have placed lower mass limits on the leptoquarks. With modern high energy particle accelerators, our ability to search for heavy particles is extending to much higher regions. In the next part of this thesis, I will present a search for exotic particles, particularly in the second generation leptoquarks (LQ_2). Second generation leptoquarks are assumed to decay into a second generation charged lepton and a quark ($LQ_2 \rightarrow \mu^\pm + q_2$). The analysis was made using data from the Collider Detector at Fermilab (CDF) [6], near Chicago. The CDF detector is installed at the Tevatron accelerator that collides protons and anti-protons ($p\bar{p}$) at a center of mass energy of 1.8 TeV. It is currently the highest existing man made collision energy in the world. The leptoquark search reported in this thesis is based on 109 pb^{-1} integrated luminosity collected during the years 1992-93 and 1994-95 (Run IA and IB). The lower mass limits from previous searches, including other generations of leptoquarks, are shown in Section 3.5. Following a brief description of the

¹Neutrinos, ν , with spin of $\frac{1}{2}$ are known to exist yet the existence of the mass of this particle is still under question.

Tevatron accelerator and the CDF detector in Chapter 4, the analysis method and the results will be presented in Chapter 5. No evidence for second generation leptoquark production was observed, and a new lower mass limit was set. This result has been presented in several conferences [12, 13] and a proceedings has been published [14]. A publication for the Physics Review Letters is in preparation.

If leptoquarks exist their mass is higher than what is accessible using existing data from the Tevatron collider. Thus we need to turn our attention to experiments with higher colliding energy. The next generation of high energy experiments will be operated with the Large Hadron Collider (LHC), which is currently under the construction at CERN, near Geneva, Switzerland. The LHC will collide proton-proton (pp) beams at the center of mass energy of 14 TeV. With large improvements in both detector technologies and beam energy, the LHC experiments will offer a wide possibility to probe the unexplored energy regions both within and beyond the Standard Model. For example, we will be able to detect leptoquarks with mass up to $1 \text{ TeV}/c^2$ at the LHC.

The LHC's high energy and high luminosity hadron beams require the development of appropriate detection apparatus. One of the most useful high energy particle detection tools existing today makes use of semiconducting materials for charged particle detection. Semiconductor detectors have fast data processing speed and spatial precision measurement ability. Tracking detectors are essential to identify charged leptons decaying from leptoquarks, as well as to identify the jets and displaced vertices from long-lived particles.

The last part of this thesis explains the detector development for the Inner Tracking Silicon Detector of the ATLAS experiment. The ATLAS experiment is one of two LHC high luminosity experiments, expected to start operating in year 2005. An outline of the experimental apparatus designs and physics potentials are presented in Chapter 6, followed by development results of a fully integrated prototype readout electronic chip for a Silicon Inner Tracking Detector, the ADAM, in Chapter 7.

Chapter 3

Leptons, Quarks, and Leptoquarks

The ultimate goal of Particle Physics studies is to identify the fundamental and structureless units of matter, and the forces that act between them. It is to define a single unified theory in the simplest form which describes the fundamental laws of physics that govern all observable phenomenologies.

One of the first attempts to find a solution to this question was made some 25 centuries ago by Greek philosopher Anaximenes of Miletus¹. He proposed four elements, air, water, earth, and fire, to be constitutes of all matters of nature. Since then, many attempts and efforts have been made to extend Anaximenes' theory and to find the nature of forces that govern the physical phenomena of the universe in which we live. We very briefly describe the history of the progression towards today's the most widely accepted Particle Physics model called the Standard Model (SM) and other unification theories in this Chapter. Further unification theories are then discussed, in particular those concerning lepton and quark interactions. This is the motivation for the analysis presented in Chapter 5, which searches for mediators between leptons and quarks.

¹(570-500 B.C.) Pupil of Anaximander. It is maintained that the Milesian cosmology was based on the primitive and popular theory of 'the four elements'. The "*fifth element*" was introduced by Greek philosopher Plato (Athens, 430-350 B.C.). In his trilogy *Timaeus* he speaks of his theory of four basic elements, and hints for a fifth: *ether*.

3.1 Quarks, leptons, and gauge bosons

3.1.1 Historical progress

The theory of the unification of forces began with Newton in the seventeenth century after his first observation of the earth's gravitational attraction. He explained that the force governing celestial and terrestrial mechanics was nothing different from what acts on an apple to make it fall from the tree. It was the first quantitative progression towards the definition of force and a subsequent unification. His work describes the gravitational force, one of the four fundamental forces understood today.

Progress was later made with Maxwell's remarkable unification of the electric and magnetic forces into a single theory, called "*electromagnetism*", in nineteenth century. This is the framework of $U(1)$ gauge invariance which describes the second of the four forces. It was only in the twentieth century that the two other forces were introduced, the *weak* and the *strong* forces. Today numerous modern theories exist which describe unification of these four forces, however none are yet supported with any experimental evidence.

While physicists studied the *forces* between matter, the interest was also in the discoveries of *elements* of matter. We can say that the elementary physics was born in 1897 with J. J. Thompson's observation of the electron. It was the first discovery of an "*elementary particle*". The modern era of the particle physics started at the turn of the century.

3.1.2 Fermions

Attention was then turned to the discovery of the fundamental particles. A major progress took place with the discovery of the meson family (π 's) predicted by Yukawa in the 1940's. This was followed by Rochester and Bulter's K^0 observation [15] in the late 1940's². By the year 1960 the number of known baryon and meson particles exceeded a hundred, and the theoretical interest was to find an underlying system to classify them. In 1953, Gell-Mann [16] and Nishijima [17] developed a way to classify known particles by assigning "*strangeness*" numbers. Strangeness (like electric charge, lepton number, or baryon number) is conserved

²Rochester and Bulter's K^0 discovery was carried out in the cloud chamber with cosmic ray through the decay $K^0 \rightarrow \pi^+ + \pi^-$. Subsequent Kaon studies lead to the introduction of strangeness.

in the strong interactions, but this quantity is *not* conserved in the weak interactions. This introduction of a new quantum number eventually lead to the arrangement of the particle families.

A theoretical arrangement of baryon and meson families structure was proposed by Gell-Mann and Ne’eman independently [18] in 1961. This theory is called the *Eightfold Way*. The idea was to arrange baryon and meson families into geometrical patterns, according to their charge, strangeness, and other quantum numbers. This arrangement has not only made a table for known elementary particles, but it has also predicted new particle discoveries such as Ω^- [19] by filling empty slots in its configuration. Gell-Mann was able to predict the characteristics of the Ω^- particle such as its mass, life time³, and production mechanism. It was the first experimentally verified prediction made in the $SU(3)$ group. The success of $SU(3)$ group theory eventually led to the quark model which is part of the Standard Model.

The Eightfold Way, with its successful predictions supported by corresponding experimental evidence, seemed to complete the table of elementary particles for a while. But a question remained: why do hadrons arrange themselves into such patterns? In 1964, Gell-Mann [20] and Zweig [21] independently proposed an idea that hadrons are made up from more fundamental constituents, called “*quarks*”. This theory initially contained three flavours of quarks, *up*, *down*, and *strange*. It rationalised hadron spectroscopy and it eventually grew to the idea of colour charges [22, 23]. It assigned three colour charges to quarks, which implied that hadrons that are the bound states of quarks can only appear in a colour neutral way. Baryons are composed of three quarks with three different colour charges which yields a neutral colour state, while mesons, made up with a quark and an antiquark, contain a colour charge and corresponding anti-colour charge. This new quantum number postulated in the first instance to avoid the apparent paradox that the quark model seemed to require spin-1/2 which should satisfy Fermi-statistics however it appeared to follow the bosonic statistics. Evidence was proved by experimental measurements of the total cross section for the annihilation of e^-e^+

³His production was based on the equal spacing on of the mass on his Octet table, using the formula:

$$M_{\Delta} - M_{\Sigma^*} = M_{\Sigma^*} - M_{\Xi^*} = M_{\Xi^*} - M_{\Omega^*}$$

collider. The results are expressed in terms of the cross section ratio

$$R \equiv \frac{e^-e^+ \rightarrow \text{Hadrons}}{e^-e^+ \rightarrow \mu^-\mu^+}. \quad (3.1)$$

The data from SLAC and PETRA [24] was used. It showed that the ratio of the total cross section of lepton pair production and quark pair production is proportional to the sum of charges squared of all the leptons and quarks that can be energetically pair-produced.

3.1.3 Gauge bosons

Along with new particle discoveries, progress has been made on the understanding of nuclear binding forces (*weak* and *strong*) and intermediators.

In the 1960's S. Glashow, together with S. Weinberg and A. Salam [3, 4, 5], proposed a new theory unifying the electromagnetic and weak nuclear forces, so called *electroweak* force based on the $SU(2) \otimes U(1)$ gauge group. It explains the combined force with the exchange of spin-1 gauge bosons. There are one massless boson (γ) which carries long range electromagnetic force and three massive bosons, W^\pm which carry the short range weak force and Z^0 for both the electromagnetic and the weak force.

The gauge bosons W^\pm transmit charged current in weak interactions. They transmute one member of a fermion doublet⁴ into another, in which one unit of charge is exchanged. One of the fundamental leptonic vertices is $\ell^- \rightarrow W^- + \nu_\ell$, where a negatively charged lepton is converted into the associated neutrino with emission of a W^- (or absorption of W^+). In the hadronic channel, it results in generation mixing, *i.e.*, W -coupling allows the charge-changing transitions to another generations. It occurs with an emission of a real or virtual W boson which materialises as lighter quarks or leptons.

The Z^0 boson transmits a neutral current weak interactions. In the late 1950's, Bludman [25] proposed the existence of neutral weak interactions mediated by an uncharged partner of W 's. Glashow [3] published on the unification of weak and electromagnetic interactions in the early 60's, in which he required the existence of a third boson in a triplet vector boson configuration. His theory includes the existence of a neutral weak process, yet the question

⁴Here, fermion doublet refers to $\begin{pmatrix} e \\ \nu_e \end{pmatrix}$ for leptons and $\begin{pmatrix} u \\ d \end{pmatrix}$ for quarks, for example.

Force	boson	symbol	charge*	spin	mass (GeV)	range (strength [†])
Strong	gluon	g	0	1	0	$10^{-15}m$ (10)
Weak	W-boson	W^\pm	± 1	1	81	$10^{-12}m$ (10^{-2})
	Z-boson	Z^0	0	1	92	
Electromagnetic	photon	γ	0	1	0	∞ (10^{-13})
Gravitational	gravitron	G	0	2	0	∞ (10^{-42})

Table 3.1: Fundamental forces and gauge bosons. *Charge is give in unit of proton charge. [†]The strength of force is in approximation, since the dependence of distance is ignored here.

why the mass of the mediators is heavy was not explained. Higgs [26] overcame this problem by “spontaneous symmetry breaking”, and introduced a notion of *Higg’s fields*. In 1967, Weinberg and Salam [4, 5] formulated Glashow’s model of a “spontaneously broken gauge theory”⁵ which explains the origin of the mass term for massive vector mediators with an existence of spin-0 Higgs boson particle. In 1971, ’t Hooft [27] succeeded in proving the renormalisation of this model. One of the best known examples is the neutrino scattering by quark or charged leptons, measurements of which played a vital part in establishing the electroweak theory.

These predictions were confirmed experimentally in the early 1980’s at the CERN $\bar{p}p$ Collider by the UA1 and UA2 experiments. They showed experimental confirmation for the existence of W^\pm [28, 29] and Z^0 [30, 31] bosons. These results confirmed a crucial aspect of the Standard Model, by experimentally observing the long awaited intermediate vector bosons.

3.1.4 The Standard Model

In recent years physicists have developed a theory called the Standard Model that attempts to describe all matter and forces in the universe, with the exception of gravity. The elegance lies in its ability to explain hundreds of particles and complex interactions in terms of a few fundamental particles and interactions. The SM is based on a gauge field theory with local gauge invariance $SU(3)_C \otimes SU(2)_L \otimes U(1)_Y$, and it describes their interactions via three forces out of four known fundamental forces in nature, listed in Table 3.1.

The strong force is transmitted by massless spin-1 gluons (denoted by $g_i, i = 1 \dots 8$), while the weak force is transmitted by massive spin-1 triplet gauge bosons (W^\pm and Z), closely

⁵See Appendix A for more on the broken symmetry theory

Lepton	symbol	charge	spin	mass	Mean life time
Electron	e^\pm	± 1	$1/2$	0.51 MeV	$> 4.3 \times 10^{23}$ years
Electron Neutrino	ν_e	0	$1/2$	< 10 eV	> 300 s/eV [†]
Muon	μ^\pm	± 1	$1/2$	106 MeV	2.2×10^{-6} seconds
Muon Neutrino	ν_μ	0	$1/2$	< 0.17 MeV	∞
Tau	τ^\pm	± 1	$1/2$	1.78 GeV	2.9×10^{-13} seconds
Tau Neutrino	ν_τ	0	$1/2$	< 24 MeV	∞

Table 3.2: Leptons in SM. [†]Life time for ν_e is given in units of τ/m_{ν_e} .

Quark	symbol	charge	spin	mass
Up	u	$+2/3$	$1/2$	2 to 8 MeV
Down	d	$-1/3$	$1/2$	5 to 15 MeV
Charm	c	$+2/3$	$1/2$	1.0 to 1.6 GeV
Strange	s	$-1/3$	$1/2$	0.1 to 0.3 GeV
Top	t	$+2/3$	$1/2$	179 ± 8 GeV
Bottom	b	$-1/3$	$1/2$	4.1 to 4.5 GeV

Table 3.3: Quarks in SM.

analogous to the photon (γ) in electromagnetism. The quantum treatment of gravity is still an open question⁶ and it is not included in this model. These forces are all described by gauge theories and the mediator particles are called gauge bosons.

Matter constituents are categorised into two kinds: leptons and quarks. They each have three doublets of particles and the members of each of the doublets bear very closely related properties. They are called fermions and follow spin $1/2$ Fermi-Dirac statistics. Leptons are particles that may be observed in free confinement and they do not interact with strong forces. Quarks, which carry three colour charges, exist only in doublet or triplet colour neutral configurations and interact with the strong force through the electroweak force. In this theory, all naturally occurring particles are colourless. The first doublet of quarks consists of one *up* and one *down* quark which are the primary constituent of protons and neutrons. The corresponding generation of lepton family is the electron and electron-neutrino. The general properties of lepton and quark families are given in Table 3.2 and 3.3.

⁶However the Einstein field equations indicate that it is transmitted by massless spin-2 gravitons.

The known quarks are grouped into three *generations* with two flavours in each generation, yielding a total of six flavours. Leptons are categorised into three generations, with a charged lepton and neutrino-lepton in each generation. Each of the leptons and the quarks has an associated anti-particle, with identical mass and spin but opposite electric (for leptons and quarks) and colour (for quarks only) charge. Charged leptons (i.e., ℓ^-) have their anti-particles (ℓ^+), while anti-neutrinos are symbolled as $\bar{\nu}$. The anti-quarks are denoted \bar{q} , with their anti-colour charge. For gauge bosons anti-particles also exists; W^- and W^+ are anti-particles to each other, and neutral bosons Z^0 , γ , and gluons are identical to their anti-particles.

The characteristics of these fundamental particles can be understood with the aid of symmetry understandings of the gauge theory which allow us to group known particles.

3.1.5 Symmetry and unifications

The use of symmetries to understand particle interactions started with Einstein's theory of gravity. He identified the invariance group of space and time in his theory of general relativity. Identifying and understanding the existing symmetries allowed a classification and simplification of physical interactions.

In the SM, the gauge symmetries refer to transformations among massless quarks and leptons of definite chirality. They come in six *flavours* of three *generations* which are indistinguishable copies of each other as far as the weak interaction is concerned. Each quark flavour comes in three *colours*, while leptons have no colour.

The internal symmetries of the elementary particles, in terms of gauge theory, are expressed as follows:

$U(1)$ **Hypercharge:** $U(1)$ symmetry associates with simultaneous phase changes of each particle, a quantum number called *weak hypercharge*. Interactions are explained by the quantised electrodynamic theory. The coupling strength of this group is expressed by α , a dimensionless measure of the interaction strength.

$SU(2)$ **Weak isospin:** The generators for the lowest-dimension nontrivial representation of the

rotation group are expressed as

$$\mathbf{J}_i = \frac{1}{2}\sigma_i \quad \text{with} \quad i = 1, 2, 3 \quad (3.2)$$

where σ_i are the Pauli matrices with non-zero trace. The eigenvectors for σ_3 are the two column vectors,

$$\begin{pmatrix} 1 \\ 0 \end{pmatrix}, \quad \begin{pmatrix} 0 \\ 1 \end{pmatrix} \quad (3.3)$$

which represent the spin-1/2 particles, spin up and down respectively. Each generation family forms a doublet of the *weak isospin group*, and the $SU(2)$ symmetry is responsible for the weak interactions. The isospin in the $SU(2)$ group arises for nucleon having an internal degree of freedom with two allowed states, first proposed by Heisenberg [35]. In the nuclear interaction, the proton and neutron are indistinguishable. The fundamental presentation of $SU(2)$ symmetry yields $\binom{n}{p}$ states in isospin (\mathbf{I}_3) doublets. Isospin is conserved in all strong interactions.

$SU(3)$ **Colour:** The strong interaction is carried by colour forces with strength determined by the colour index. The fundamental representation of $SU(3)$ is a triplet. The three quarks of each flavour therefore form a triplet representation of the *colour group*, expressed with an $SU(3)$ symmetry which forms a set of unitary 3×3 matrices with $\det U = 1$. The colour charges are a direct presentation of this $SU(3)$ symmetry group. They are denoted by λ_i , with $i = 1 \dots 8$, the so called Gell-Mann λ -matrices, analogous to the $SU(2)$ group of σ_i for the Pauli spin matrices. The simultaneous eigenvectors are

$$R = \begin{pmatrix} 1 \\ 0 \\ 0 \end{pmatrix}, \quad G = \begin{pmatrix} 0 \\ 1 \\ 0 \end{pmatrix}, \quad B = \begin{pmatrix} 0 \\ 0 \\ 1 \end{pmatrix} \quad (3.4)$$

which corresponds to the three colour states nominally called *red*, *green*, and *blue*. Interactions of this group are explained by the theory of quantum chromodynamics (QCD). The overall coupling strength is characterised by α_s , the strong coupling constant.

The gauge invariance of the Dirac field of vector interactions involves a unitary 1×1 matrix U which transforms a vector field $\psi^l \rightarrow U\psi$, where $U^\dagger U = 1$. The group of all such matrices is $U(1)$, and the group is called $U(1)$ *gauge invariance*. This is the framework which describes the

electromagnetic field. The electroweak gauge theory is based on the $SU(2) \times U(1)$ symmetry group, which is later extended to $SU(3)$ symmetry group with quantum chromodynamics, using an additional degree of freedom called published *colour* charge. It describes the strength of strong interaction. The SM generates all the known fundamental interactions with the exception of gravity using the gauge invariance of $SU(3) \times SU(2) \times U(1)$.

Thus the known elementary particles in the SM (including anti-particles) add up to 12 leptons, 36 quarks, and 12 mediators, filling the “*periodic table*”. With additional Higgs particles, there are a minimum of 61 elementary particles that we need to count in with the SM. Although many believe in the SM, some search for simpler models using more fundamental units of building blocks or maybe with higher symmetry to explain matter, as was done in Mendeleev’s periodic table⁷. Some of the inadequacies of the SM that lead us to believe that there may be simpler models which lie beyond the SM, perhaps with higher unifications, are listed in the following Section.

3.1.6 Standard Model Inadequacies

In the lepton and quark model described in section 3.1.4 there are three generations, yet why mother nature repeats herself three times, not more nor less, has not been fully understood. In the every-day world we observe only first generation particles (electrons, e-neutrinos, and up/down quarks). Why does the natural world need the two other generations? Quarks have three colour charges and this quantity of *three* is not fully explained. Leptons and quarks, both in a family of fermions, have such remarkable symmetries, though no theory explains the essential reason. The recent discovery [32] of the top quark at the Tevatron $p\bar{p}$ collider has filled the last number in the SM mass table⁸. But physicists were unable to accurately predict top’s mass without experimental evidence because the SM lacks a mathematical model for finding a pattern for particle masses⁹. The mass spectrum of three generations of fermions

⁷The well-known Mendeleev’s table was indeed once believed to be a table of “*elementary particles*” yet we now know that its chemical elements are built up of the more fundamental electrons and nuclei.

⁸The neutrino mass, $m(\nu_\tau)$ is however still under determined.

⁹However, the mass of the top quark is restricted by a variety of measurements [33]. Due to radiative corrections which depend on the top quark circulating as a virtual particle inside the loop in the Feynman diagram, a number of experimentally accessible processes depend on the top quark mass. There are about a dozen such measurements [34] which have been made so far, including the width of the Z , $b\bar{b}$ mixing (which historically gave the first hints that the top quark was very massive), and certain aspects of muon decay.

remain a question in the SM.

The electroweak symmetry has a structural problem which is associated with Higg's sector. The most noticeable feature of electroweak symmetry, $SU(2) \otimes U(1)$ gauge invariance, is broken. With a spontaneous symmetry breaking of this theory, the Higgs boson with spin of 0 is introduced to give a mass term to fermion families which are massless in symmetry-conserved $SU(2) \otimes U(1)$ gauge invariant group.

The SM provides the mechanism to calculate the quantity of CP violation using the Kobayashi-Matsukawa matrix. The non-zero diagonal elements of this matrix is associated with the amount of CP violation phenomenologies. Yet the SM and associated theories gives no explanations to fill these non-zero diagonal elements, nevertheless this quantity has been experimentally measured.

There is more incompleteness to the SM. The universe seems to break baryon symmetry. Our world is made up of matter rather than anti-matter. According to our experiments, there should be equal amounts of matter and antimatter in the universe, but we observe the universe to be mostly made of matter. If the big-bang has provoked to create equal number of matters and anti-matters, it implies a breaking symmetry of baryon numbers in the process of evolution, which is not explained in the SM interaction theories.

Those are strong reasons that some believe in further explanations to combine and simplify those unknown values in terms of fewer parameters. Today, many unification theories have been proposed to combine the known properties of fundamental forces and matter. Historical unifications have lead us to believe in higher symmetries which can describe the existing physical laws with a single unified theory as in the electroweak unification. We understand today that all massive objects in our universe are made of matter which is comprised of leptons and quarks. Their remarkable similarities suggest the possibility of an unique categorisation, leading to searches for higher symmetry to combine the strong force with the electroweak force. This will give rise to a theory with new gauge bosons that interacts between lepton and quark families. In many unification theories, such intermediators are generally referred as *leptoquarks*.

These results collectively limit the top mass to roughly $140 \pm 30 \text{ GeV}/c^2$.

3.2 The Leptoquark theory

Leptons and quarks have, in many aspects, enormous similarities; for example their appearance as three generations and their conspiracy to cancel anomalies. Such evidence suggests that leptons and quarks may be related as part of some higher symmetries which may or may not be accessible at the energy scale of existing accelerators. Ignoring the specific prediction of mass and coupling constants, we can predict a particle which mediates between the quark and lepton families.

Leptoquarks appear in many theoretical extensions to the SM. Leptoquarks are colour-triplet bosons which carry both baryon and lepton quantum numbers and which couple to both quarks and leptons. Leptoquarks, in searches with a mass accessible via direct production in current accelerators, are usually assumed to couple to quarks and leptons of the same generation [37] in order to avoid large flavour-changing neutral current (FCNC) processes. Leptoquarks are therefore usually categorised in three generations, coupling uniquely within the corresponding generation of leptons and quarks. They may also have various other quantum numbers such as charge Q and weak isospin that are model dependent.

Descriptions of those theories which predict such leptoquarks follow.

3.2.1 $SU(5)$ GUT unified model

This model postulates that the SM with $SU(3) \otimes SU(2) \otimes U(1)$ may be described by a $SU(5)$ group of global gauge transformations. Georgi and Glashow [38] proposed in 1980 that the electroweak and strong nuclear force can be combined by using a grand unified group, based on 5×5 traceless Hermitian matrices, in which strong, weak, and electromagnetic couplings will merge into a single value at very high energy scale.

The $SU(2) \times U(1)$ unification gauge group of electroweak theory prediction is in a very good agreement with experimental data. The coupling strength parameters are characterised by “running coupling constants” which depends on the q or the momentum transfer of the interaction. They well are determined in the accessible energy scales. The coupling strength of the $U(1)$ Abelian group is g' and the $SU(2)$ group is g for the non-Abelian field. A related quantity, the weak mixing (Weinberg) angle θ_W ($\tan \theta_W \equiv \frac{g'}{g}$), is known in this model

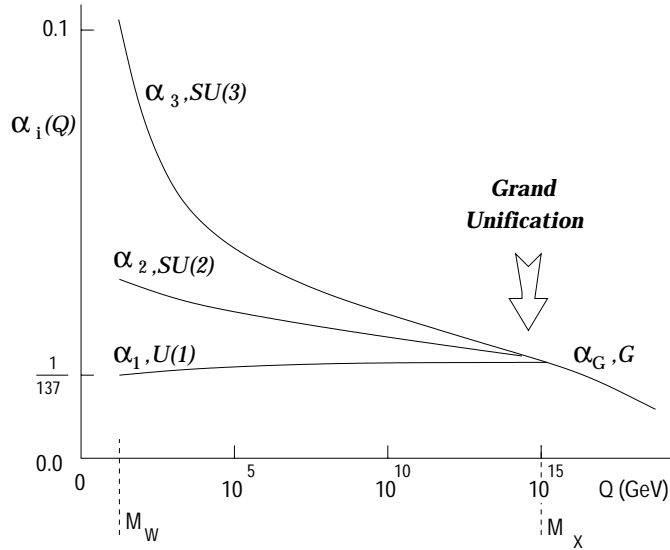


Figure 3.1: Evolution of the coupling constants with energy according to GUT model [36]. $i = 1, 2, 3$ denotes subgroup $SU(3)$, $SU(2)$, $U(1)$ respectively.

from experimental measurement¹⁰. Furthermore the non-Abelian $SU(3)$ colour field has an associated coupling g_s (where $\alpha_s = g_s^2/4\pi$).

The idea of the unification is to introduce a higher set of transformations G which can relate g , g' , and g_s . We seek a larger global group which contains the colour gauge group $SU(3)$ describing the strong interactions, as well as the electroweak $SU(2) \times U(1)$ gauge transformations. Such a group combines the strong coupling constant α_s with g and g' . The Grand Unification Theories (GUT) postulate that the SM symmetry subgroups are part of a single group \mathcal{G} , given by

$$\mathcal{G} \supset SU(3) \times SU(2) \times U(1) \quad (3.6)$$

which describes all the interactions with a single coupling g_G to which all couplings are related.

Figure 3.1 shows a quantitative evolution of the coupling constants for this approach. At very large energy scale of $q = M_X \approx 10^{15}$ GeV, or the distances of $\sim 10^{-29}$ cm, the three couplings merge into a single grand unified coupling g_G , but this energy scale is far beyond

¹⁰We can derive the relation

$$M_W = M_Z \cos \theta_W \quad (3.5)$$

from W^\pm and Z^0 propagators and vertices. The experiments at CERN in 1983 [28, 29, 30, 31] have measured the mass of W and Z , and result yielded $\theta_W \sim 28.7^\circ$ with $M_W = 81.8$ GeV/ c^2 and $M_Z = 92.6$ GeV/ c^2 .

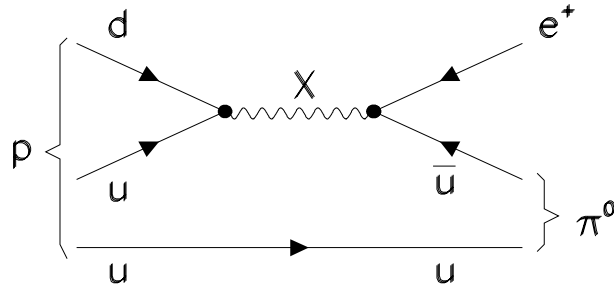


Figure 3.2: One of the Feynman diagrams describing the proton decay $p \rightarrow e^+ \pi^0$. The $SU(5)$ grand unified theory predict this process with intermediate boson labelled “X”, which has leptoquark and diquark couplings.

the available energy scale today.

This theory searches for two additional new groups of bosons. It describes the colour triplet states of quarks and doublet flavour of leptons in a single unified $SU(5)$ symmetry. It therefore predicts the exchange of gauge bosons between quarks and leptons. In addition to two known massive bosons, Z^0 and W^\pm in $SU(2) \times U(1)$ group, the new groups of bosons in the GUT are denoted as X and Y , with electric charges $-\frac{1}{3}$ and $-\frac{4}{3}$ respectively. They appear in 3 different colour eigenstates.

The gauge boson relevant to the $SU(5)$ unified theory must be very heavy because they are associated with a spontaneous symmetry breakdown at a very short distance. Predictions indicate that their mass is about $\hbar c/L$, or $\sim 10^{15}$ times the mass of proton. Such a scale is not directly reachable, however it may be possible to observe the effect from their virtual boson exchanges. There is a model which predicts a proton decay to a lepton and pion ($p \rightarrow e^+ \pi^0$) with a gauge boson exchange. The gauge boson mediates between the quark and the lepton and it carries a quantum number of leptoquark. Figure 3.2 shows one of the diagrams describing the proton decay, mediated by the X boson which carry leptoquark-like couplings¹¹.

¹¹Recent experiments (IMB, Kamiokande, and Fréjus) has set a lower limit on the mode dependent proton meanlife time to be $> 9 \times 10^{32}$ years for $\tau(p \rightarrow e^+ \pi^0)$ [39].

3.2.2 Pati-Salam colour symmetrical model

For very heavy leptoquarks, well above the TeV energy scale, flavour changing neutral current (FCNC) constraints can allow couplings to quarks and leptons in different generations, with mediators which carry the characteristics of leptoquarks. This is the case, for example, for the so-called Pati-Salam leptoquarks [40]. They appear as gauge vector bosons in a grand-unified extension of the SM based on an enlarged colour group $SU(4)_c$, with $SO(10)$ unified gauge theories. It treats the strong, weak, and electromagnetic interactions of leptons and hadrons as a renormalisable group with the fundamental symmetry structure based on

$$SU(4)_L \otimes SU(4)_R \otimes SU(4)'. \quad (3.7)$$

In this model, quarks have four *colours* in which it takes the lepton number as the fourth colour. However, Pati-Salam leptoquarks can be searched *indirectly* through decays such as $B_s^0 \rightarrow e\mu$ and $B_d^0 \rightarrow e\mu$ [41]. The analysis coming from CDF presented in Chapter 5 concentrates on *direct* leptoquark searches. An indirect search for leptoquarks compatible with this model has been made by other CDF collaboration members [42].

3.2.3 Technicolour model

In this theory [43], the Higgs mechanism of spontaneous symmetry breaking of the $SU(2)_L \times U(1)$ electroweak model is eliminated. In the Higgs model the masses for W^\pm and Z^0 are given by introducing the elementary Higgs scalar boson with spin 0, while the Technicolour model replaces it by composite states of elementary particles. The composite scalars are meson bound states of a *new* strong interaction between new fermions, expressed with a gauge group:

$$\mathcal{G}_{TC} \times SU(3)_C \times SU(2)_L \times U(1) \quad (3.8)$$

where \mathcal{G}_{TC} is the gauge group of the Technicolour interaction. The properties of the leptoquarks are described within the scalar bound states of technicolour theory.

3.2.4 Other models

There are a number of other models which contain bosons with leptoquark characteristics. They include:

- Composite models: A quark and lepton substructure [44, 45, 46] predicts a leptoquark-like model beyond the electroweak scale ($\Lambda_{Fermi} \sim 300$ GeV). Quarks and leptons emerge in this model as bound states of fundamental fields, yet they are singlets with respect to the strong electroweak gauge force.
- Supersymmetry (SUSY): Supersymmetry models predict supersymmetric partners for known particles (called *sparticles*), by introducing a spin 1/2 Majorana generator. In the Minimal Supersymmetric Model (MSSM), R -parity can be violated. This theory leads to the existence of a heavy supersymmetric flavour partner \tilde{t} , which can be produced via $eq \rightarrow \tilde{t} \rightarrow eq$. This is a leptoquark-like interaction.

These models, together with possibilities of the associated future searches, are described in more detail in Appendix C.

Superstring[47], Horizontal symmetry[48] and the Strong coupling SM [49] theories also predict the existence of leptoquark mediators.

3.3 Leptoquark Production at $p\bar{p}$ Collider

In hadronic collisions at the Tevatron, leptoquarks can be either singly or pairly produced. In the single production, the Yukawa coupling λ of the leptoquark is unknown therefore the production cross section is model dependent. However in the pair production, it proceeds through QCD interactions, as in heavy quark pair productions. The coupling strength therefore only depends on the leptoquark quantum numbers, and it can be determined.

In the direct leptoquark search presented in the Chapter 5, we use the Next-to-Leading Order production calculations shown in this Section to extract an experimental limit for pair produced scalar leptoquarks.

3.3.1 Production diagrams

The effective leptoquark Lagrangian takes a form with the most general dimensionless $SU(3) \times SU(2) \times U(1)$ invariant couplings, satisfying baryon and lepton number conservation [50]. Leptoquarks are then assumed to be produced as a particle and anti-particle pair in the $p\bar{p}$ collisions. We also assume that leptoquarks couple only to lepton-quark pairs.

The pair production cross section depends on the spin and colour factor of the leptoquarks, though the gluons couplings. In the case of scalar leptoquarks, the cross section can be calculated completely since there are no free parameters or assumptions. However for vector leptoquarks the coupling strength depends on the model. The gluon coupling is fixed by the gauge invariance, however in the composite model (see Appendix C) in which leptons and quarks are composite of more fundamental units, the vector leptoquarks can acquire unknown *anomalous* couplings to the gluon vertices. A possible coupling for this model is the so-called *anomalous chromomagnetic moment*, denoted as κ .

The production of scalar leptoquarks at the hadron collisions is possible via gluon-gluon fusion and quark-antiquark annihilation.

$$\begin{aligned} q + \bar{q} &\rightarrow LQ + \overline{LQ} \\ g + g &\rightarrow LQ + \overline{LQ} \end{aligned} \tag{3.9}$$

Figure 3.3 shows the corresponding Feynman diagrams for gluon-gluon fusion. These processes are identical to those for squark production, $gg \rightarrow \tilde{q}\tilde{q}$, hence the two processes yield the same production cross section [7]. The diagrams responsible for the reaction $q\bar{q} \rightarrow LQ_2\overline{LQ}_2$ are shown on Figure 3.4.

In the analysis presented in Chapter 5, a search was made for scalar leptoquarks carrying a charge of $Q = +\frac{2}{3}$ and $Q = -\frac{1}{3}$ and coupling directly to the second generation lepton and quark pair.

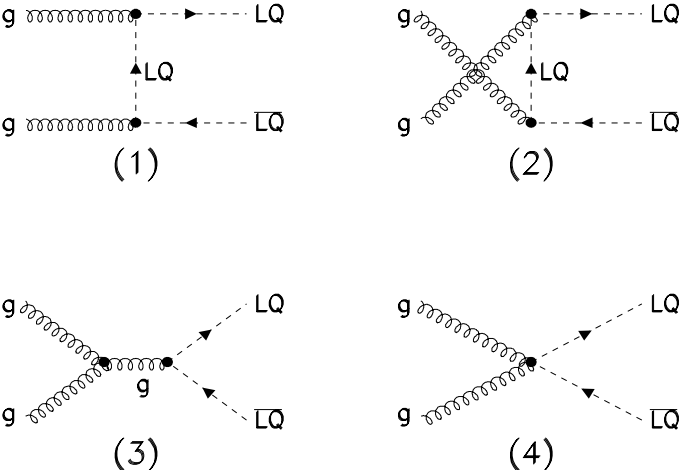


Figure 3.3: Feynman diagrams responsible for the parton level process $gg \rightarrow LQ_2 \overline{LQ}_2$.

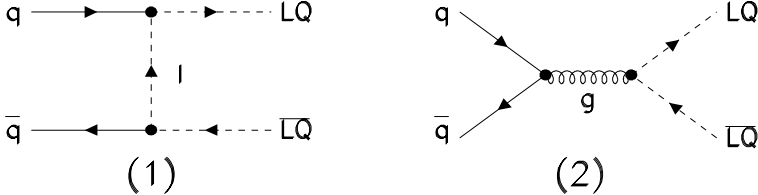


Figure 3.4: Feynman diagrams responsible for the process $q\bar{q} \rightarrow LQ_2 \overline{LQ}_2$.

3.3.2 The Leading Order production cross section

With point-like leptoquarks with mass well below TeV/c^2 scale, gluon-leptoquark interactions are determined by the non-abelian scalar QCD $SU(3)_C$ gauge symmetry. Therefore the predicted production of scalar leptoquarks is parameter free and leptoquark bosonic couplings can be determined completely. The effective Lagrangian describing the interaction of the scalar leptoquarks is given by [51]

$$\mathcal{L}_{scalar}^g = \sum_{scalar} \left[\left(D_{ij}^\mu LQ^j \right)^\dagger \left(D_\mu^{ik} LQ_k \right) - M_{LQ}^2 LQ^{i\dagger} LQ_i \right] \quad (3.10)$$

where M_{LQ} denotes the leptoquark mass and D_{ij}^μ is the covariant derivative, given by

$$D_{ij}^\mu = \partial_\mu \delta^{ij} - ig_s t_a^{ij} \mathcal{A}_\mu^a \quad (3.11)$$

in which g_s is the strong coupling constant, t_a denotes the generators of $SU(3)_C$, and the term \mathcal{A}_μ is the local transformation field, which includes a non-Abelian tensor term¹². The differential pair production cross section for gg and $q\bar{q}$ scattering is given by

$$\frac{d\hat{\sigma}_{LQL\bar{Q}}^{q\bar{q}}}{d \cos \theta} = \frac{\pi \alpha_s^2}{18 \hat{s}} \beta^3 \sin^2 \theta \quad (3.14)$$

$$\begin{aligned} \frac{d\hat{\sigma}_{LQL\bar{Q}}^{gg}}{d \cos \theta} &= \frac{\pi \alpha_s^2}{6 \hat{s}} \beta \left[\frac{1}{32} (25 + 9\beta^2 \cos^2 \theta - 18\beta^2) \right. \\ &\quad \left. - \frac{1}{16} \frac{(25 - 34\beta^2 + 9\beta^4)}{1 - \beta^2 \cos^2 \theta} + \frac{(1 - \beta^2)^2}{(1 - \beta^2 \cos^2 \theta)^2} \right] \end{aligned} \quad (3.15)$$

where θ is the leptoquark scattering angle in the parton-parton center of mass frame, $\beta =$

¹²This can be derived analogous to QED Lagrangian development. However in QCD, the antisymmetric tensor is expressed by

$$\mathcal{F}_{\mu\nu} = F_{\mu\nu}^a T^a,$$

which can be developed to

$$\mathcal{F}_{\mu\nu} = \partial_\mu \mathcal{A}_\nu - \partial_\nu \mathcal{A}_\mu - ig [\mathcal{A}_\mu, \mathcal{A}_\nu] \quad (3.12)$$

$$= \frac{1}{-g^2} [D_\mu, D_\nu] \quad (3.13)$$

See ref. [52], for more detailed explanations.

$\sqrt{1 - 4M_{LQ}^2/\hat{s}}$, and α_s is the strong coupling constant. The integral pair production cross section for leptoquark pairs are given by integrating equations 3.15, which can be written as [1]:

$$\hat{\sigma}_{LO} (q\bar{q} \rightarrow LQ\bar{L}\bar{Q})_S = \frac{\alpha_s^2 \pi}{27\hat{s}} 2\beta^3 \quad (3.16)$$

$$\begin{aligned} \hat{\sigma}_{LO} (gg \rightarrow LQ\bar{L}\bar{Q})_S &= \frac{\alpha_s^2 \pi}{96\hat{s}} [\beta(41 - 31\beta^2) \\ &+ (18\beta^2 - \beta^4 - 17) \log \frac{1 + \beta}{1 - \beta}] \end{aligned} \quad (3.17)$$

where $\sqrt{\hat{s}}$ is the invariant energy of the subprocess. All quark flavours have been assumed to be massless. Since the interesting region of colliding parton-parton energy is of the order of a few hundred GeV, with leptoquark mass well above quark masses (besides from top quark, which is very unlikely to be in the interacting partons in $p\bar{p}$ colliding environment), then they are negligible in leptoquark cross section calculations. The quantity $\sqrt{\hat{s}}$ is the amount of energy carried by the interacting partons in colliding protons or anti-protons, and here we need to further investigate the parton densities.

For the vector leptoquarks, additional anomalous couplings (κ_V) to gluons must be taken into account. However, if we consider that vector leptoquarks are completely fundamental objects, couplings to vector leptoquark pair and gluon(s) can be evaluated because it is fixed by extended gauge invariance. Yet these couplings violate unitary in the production cross section, and they vanish in any theory in which vector leptoquarks appear as fundamental gauge bosons of any extended gauge group.

Analogous to the scalar leptoquarks as in Equation 3.16 and 3.17 the partonic cross sections for vector leptoquarks are given by [53],

$$\hat{\sigma}_{LO} (q\bar{q} \rightarrow LQ\bar{L}\bar{Q})_V = \frac{\alpha_s^2 \pi}{27\hat{s}} \frac{\beta^3}{1 - \beta^2} \left[23 - 3\beta^2 + \frac{4}{1 - \beta^2} \right] \quad (3.18)$$

$$\begin{aligned} \hat{\sigma}_{LO} (gg \rightarrow LQ\bar{L}\bar{Q})_V &= \frac{\alpha_s^2 \pi}{24\hat{s}} \frac{1}{1 - \beta^2} \left[\beta \left(\frac{523}{4} - 90\beta^2 + \frac{93}{4}\beta^4 \right) \right. \\ &\left. - \frac{3}{4} (65 - 83\beta^2 - 19\beta^4 - \beta^6) \log \frac{1 + \beta}{1 - \beta} \right] \end{aligned} \quad (3.19)$$

Here the cross section is given with vanishing anomalous couplings $\kappa_v, \lambda_v = 0$ [54].

We consider only scalar leptoquark production in the analysis presented in this thesis.

3.3.3 Higher order corrections

To calculate the production cross section for Next-to-Leading Order, we need to include QCD radiative corrections to the equation (3.16) shown above for scalar leptoquark production¹³. We start with the momentum assignment to the lowest order gluon-gluon fusion process ($gg \rightarrow LQ\overline{LQ}$), by denoting:

$$g(k_1) + g(k_2) \rightarrow Q(p_1) + Q(p_2) \quad (3.20)$$

where k_i and p_i are the momentum carried by incoming gluon and outgoing leptoquarks.

We choose the kinematic variables

$$\begin{aligned} s &= 2k_1 \cdot k_2, \\ t_1 &= t - m^2 = (k_1 - p_1)^2 - m^2, \\ u_1 &\equiv u - m^2 = (k_1 - p_2)^2 - m^2 \end{aligned} \quad (3.21)$$

The list of possible corrections can be listed as:

- ▷ **Compton process:** to calculate the cross section to order α_s^3 , inelastic Compton processes have to be added. The Feynman diagrams to such processes are shown in Figure 3.5.
- ▷ **Virtual Corrections:** to the order of α_s corrections, virtual corrections include self-energy diagrams or loop diagrams, and vertex corrections for quarks, gluons, and leptoquarks, shown as in Figure 3.6. This can be evaluated thorough SM scalar QCD rules and initial/final state interactions.
- ▷ **Gluon radiations:** bremsstrahlung gluons emitted from all coloured lines and from scalar vertices should be included into the corrections. Some diagrams for this process

¹³Detail of this section is worked out in ref. [1].

are shown in Figure 3.7.

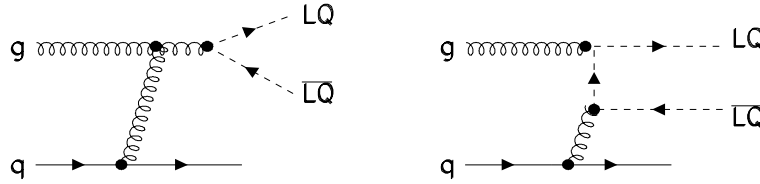


Figure 3.5: Feynman diagrams showing for the gluon quark subprocesses for leptoquark pair production.

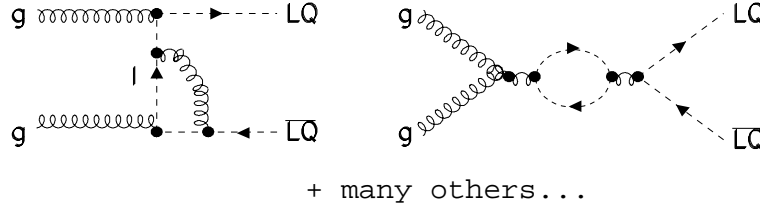


Figure 3.6: Some Feynman diagrams representing for order- g^2 virtual loop processes in pair leptoquark production.

The correction to the differential cross section in equation (3.15) requires the calculation of the Feynman diagrams where the virtually emitted gluons or other bosons make a “loop” and are re-absorbed, as shown in Figure 3.6. The ultraviolet (UV), infrared (IR), and the collinear or mass (M) singularities are taken into account by using n -dimensional regularisations [55].

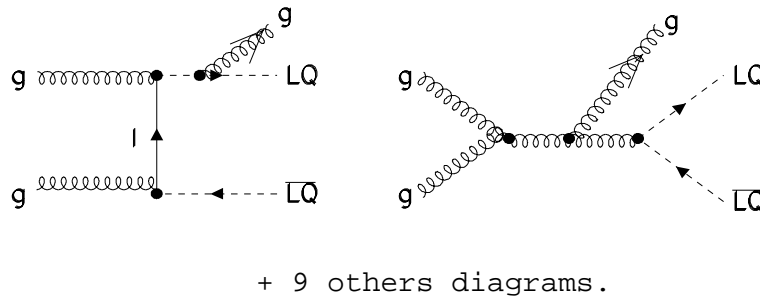


Figure 3.7: Some Feynman diagrams for order- g^3 contributions with gluon bremsstrahlung reactions.

The gluon bremsstrahlung cross section is given by adding a gluon in the final state in the process shown in Equation 3.20. It is written as:

$$g(k_1) + g(k_2) \rightarrow Q(p_1) + Q(p_2) + g(k_3) \quad (3.22)$$

where $g(k_3)$ term specifies the radiated gluon.

There are a total of 11 diagrams contributing to this kind of process¹⁴. Some diagrams responsible for such processes are shown in Figure 3.7. Gluon radiations can occur on all coloured lines and also from scalar vertices. An extra term (k_3 for an outgoing radiating gluon) in Equation 3.21 is added, and the computation is made by adopting the phase space slicing method [55].

Those QCD radiative corrections and amplitude calculations are evaluated in Feynman's gauge, using the method of isolating singularities by means of dimensional regularisation followed by renormalisation. It is carried out by using $\overline{\text{MS}}$ scheme¹⁵, with an introduction of cut-off Δ . The total parton perturbative cross section is then expressed in terms of renormalisation and factorisation scaling terms and scaling functions:

$$\hat{\sigma}_{ij}(s, M_{LQ}^2) = \frac{\alpha_s^2 \mu^2}{M_{LQ}^2} \left[f_{ij}^{(0)}(\eta) + 4\pi\alpha_s \mu^2 \left\{ f_{ij}^{(1)}(\eta, r_t) + \bar{f}_{ij}^{(1)}(\eta) \ln \left(\frac{\mu^2}{M_{LQ}^2} \right) \right\} \right] \quad (3.23)$$

where μ is the renormalisation scale and the factorisation scale variable, in which we used $\mu_R = \mu_F = \mu$ for simplicity. The index i and j goes for g , q , and \bar{q} , over all possible parton interactions. The scaling functions f depends on r_t , the ratio of top quark mass to leptoquark mass, $r_t = m_{top}/M_{LQ}$, and the η , given by

$$\eta = \frac{\hat{s}}{4M_{LQ}^2} - 1 \quad (3.24)$$

where $\sqrt{\hat{s}}$ is the parton invariant energy.

¹⁴There are 5 possible gluon radiation from the left diagram in Figure 3.7 and 6 (one coming from the vertex) possibilities from the right diagram.

¹⁵ $\overline{\text{MS}}$ is "Non-minimal subtraction scheme", by Buras and Bardeen. In order to compute the contribution from diverging *virtual* loop diagrams, one needs to calculate an infinite number of their amplitudes in the Feynman diagrams. To avoid the divergence with vacuum polarisation, the $\overline{\text{MS}}$ scheme calculation avoids to have natural logarithmic term in the renormalisation, unlike "Minimum subtraction scheme". See ref. [52] page 87-88.

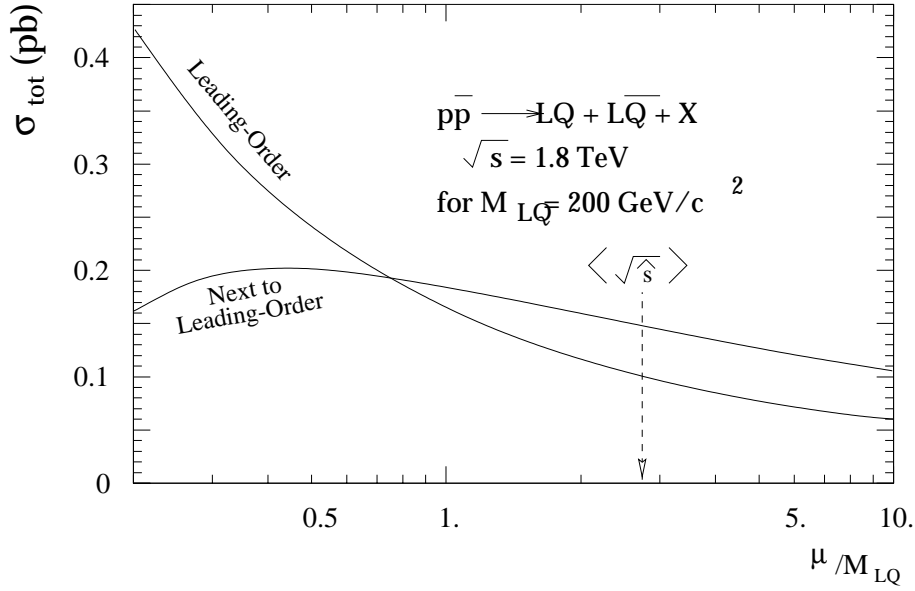


Figure 3.8: Renormalisation/factorisation scale dependence of the total cross section for LO and NLO calculation. (ref.[1])

The Next-to-Leading Order total cross section for the pair produced scalar leptoquarks can then be expressed by folding gluon-gluon and quark-antiquark initial states in $p\bar{p}$ collisions:

$$\sigma [p\bar{p} \rightarrow LQ + \bar{L}\bar{Q} + X] = \sum_{i,j=g,q,\bar{q}} \int d\tau \frac{d\mathcal{L}^{ij}}{d\tau} \hat{\sigma}(\hat{s} = \tau s) \quad (3.25)$$

However for the large leptoquark masses $M_{LQ} > 100 \text{ GeV}/c^2$, the initial state and parton momenta are dominated by the quark-antiquark state.

3.3.4 NLO v.s. LO

By including a Next-to-Leading Order (NLO) calculation instead of a Leading Order (LO) calculation, one can verify the accuracy by comparing the dependence on the renormalisation/factorisation scale variable μ_R . The difference of $\sigma(\mu = 2M_{LQ})$ and $\sigma(\mu = M_{LQ}/2)$ for LO calculations is $\sim 100\%$ at the interesting mass region of $M_{LQ} \sim 200 \text{ GeV}/c^2$, while with the NLO calculation, this dependence is strongly reduced to $\sim 30\%$.

Figure 3.8 shows the dependence of the renormalisation/factorisation scale dependence for

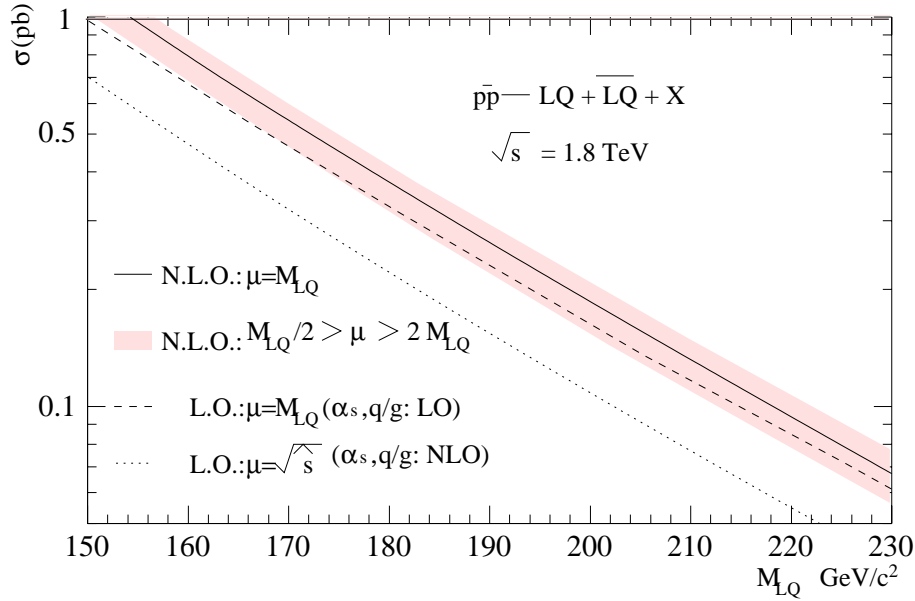


Figure 3.9: Total cross section in pb for the production of leptoquark pairs at Tevatron as a function of the leptoquark mass. The Next-to-Leading Order calculation is compared with other Leading Order calculations. (ref.[1])

LO and NLO calculations as a function of μ/M_{LQ} , in the region of the interest to this search.

3.3.5 Numerical calculations

The numerical results using the Next-to-Leading Order QCD corrections for the pair produced leptoquark cross section at the Tevatron collider is shown in Figure 3.9. The parton densities are taken from the CTEQ4M structure functions [56].

The theoretical uncertainty at NLO, due to the choice of the renormalisation and/or factorisation parameter μ , is demonstrated by taking two extreme choices of $\mu = 2M_{LQ}$ and $\mu = M_{LQ}/2$, which is expressed in the shaded band of Figure 3.9.

Table 3.4 shows the numerically calculated result for total production cross section for pair produced scalar leptoquarks in Tevatron collider, via gluon-gluon fusion, quark-antiquark annihilation, and gluon-quark interaction calculation¹⁶, comparing Leading Order and Next-to-Leading Order calculations are shown. The CTEQ4M parton densities is taken at the

¹⁶The negative sign of $\tilde{\sigma}_{gq}$ is a mere artifact of subtracting collinear initial-state singularities via mass factorisation.

M_{LQ} GeV/ c^2	$\sigma_{q\bar{q}}$		σ_{gg}		$\tilde{\sigma}_{gq}$	σ_{tot} (pb)		K $= \sigma_{NLO}/\sigma_{LO}$
	L.O.	N.L.O.	L.O.	N.L.O.	N.L.O.	L.O.	N.L.O.	
150	0.741	0.722	0.244	0.490	-0.028	0.985	1.184	1.20
175	0.318	0.311	0.071	0.146	-0.010	0.389	0.447	1.15
200	0.142	0.141	0.022	0.047	-0.004	0.164	0.184	1.12
250	0.030	0.030	0.003	0.006	-0.001	0.033	0.035	1.08

Table 3.4: Pairly produced Leptoquark cross section numerical calculation result for the Tevatron $p\bar{p}$ collider, give in units of pb. (ref.[1])

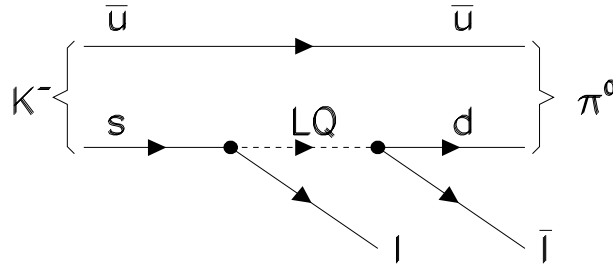


Figure 3.10: One example of the flavour changing neutral current decay process, $K^- \rightarrow \pi^- \ell \bar{\ell}$, induced by leptoquark mediators which couple to more than one generation of quarks.

central value at $\mu = M_{LQ}$.

This theoretical cross section is used to evaluate the lower leptoquark mass limit in the experimental results given in Chapter 5.

3.4 Leptoquark decay

It is possible that the leptoquarks give rise to the flavour changing neutral currents (FCNC) since the $SU(2)_L$ eigenstates of the quarks and leptons are not the mass eigenstates [7]. However the evidence of the flavour mixing induced FCNC involves many unknown parameters and are assumed to be suppressed. Examples of inter-generation decays are $K_L^0 \rightarrow e\mu$, $D^0 \rightarrow \pi^0 e\mu$, or $B^0 \rightarrow \mu\tau$, and one such process induced by leptoquarks is shown in Figure 3.10.

Experimental limits for these inter-generation decays show that the decay rate of such processes is very small [57]. Hence we focus on the leptoquarks decaying to the same generation of lepton and quark.

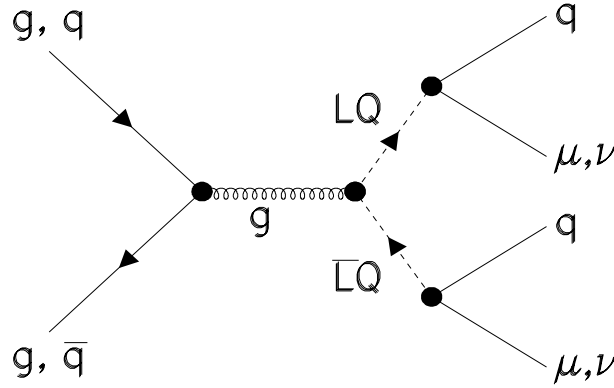

 Figure 3.11: The Feynman diagrams for LQ_2 decay.

Figure 3.11 shows the possible decay for the second generation leptoquark. Since the leptoquarks are produced in pairs, its decay products will have two leptons and two quarks. The branching ratio β defines the possible leptoquark decay channels. In the second generation, we assume the following two decay modes:

$$\begin{aligned}
 LQ_2 &\rightarrow q_2 \mu^\pm, & \text{Br} &= \beta \\
 LQ_2 &\rightarrow q_2 \nu_\mu, & \text{Br} &= 1 - \beta
 \end{aligned} \tag{3.26}$$

The value of β ranges from 0 to 1.0, although in the absence of a right-handed ν_μ we expect $\beta > 0.5$. With this parameter, we expect three types of signature for leptoquark pair productions.

$$\begin{aligned}
 (i) & \quad \nu\bar{\nu} + 2 \text{ jets} & (\beta = 0) \\
 (ii) & \quad \ell\nu + 2 \text{ jets} & (\beta = 0.5) \\
 (iii) & \quad \ell^+\ell^- + 2 \text{ jets} & (\beta = 1)
 \end{aligned} \tag{3.27}$$

In the neutrino decay channel (i), we estimate that events will have a large background from a number of processes, and a determination of the invariant mass with two missing transverse

momenta will be difficult. Events of type (ii) will have two jets, a charged lepton, and missing transverse energy signature. The SM background signatures include $p\bar{p} \rightarrow WZ, ZZ, Z + \text{gluon radiations}$. We can construct the transverse mass with signature including missing transverse momentum. The signature type (iii) with dijet plus two charged particle may be the most promising.

3.5 Existing leptoquark search limits

There have been several direct searches for leptoquarks, in e^-e^+ , $e^\pm p$, and $p\bar{p}$ colliders.

3.5.1 Non-hadron collider searches

The current mass limit for the leptoquarks has been performed by various experiments¹⁷; at LEP (L3 collaboration) with e^+e^- collisions at $\sqrt{s} = 90$ GeV, the search excludes $M(LQ_2) < 44.5$ GeV/ c^2 ($C.L. = 95\%$) independent of the branching ratio β for the pair produced second generation leptoquarks. For the singly produced second generation leptoquark, the DELPHI collaboration has set a limit from the analysis of Z decays. The limit for a leptoquark coupling of electromagnetic strength, assuming $\beta(lq) = \frac{2}{3}$, is 77 GeV/ c^2 . From the HERA ep collider, a first generation leptoquark mass limit has been set at 275 GeV/ c^2 , however, this limit is sensitive to the model used for the leptoquark decay coupling.

3.5.2 Previous LQ_2 search at Tevatron

At the $p\bar{p}$ collider at Fermilab ($\sqrt{s} = 1.8$ TeV), previous searches for pair produced second generation leptoquarks have been made both by the DØ and the CDF experiments. The previous published second generation leptoquark search at CDF[8] excluded $M(LQ_2) < 131$ GeV/ c^2 for $\beta = 1$ and $M(LQ_2) < 96$ GeV/ c^2 for $\beta = 0.5$ at 95% $C.L.$, using an integrated luminosity of 19.3 pb⁻¹ from Run IA.

The most recent result at CDF[59] has searched using a total integrated luminosity of 66.7 pb⁻¹ from Run IA and IB. A total of 4 candidate events were observed for LQ_2 candidates

¹⁷Searches includes by the CDF[8] and DØ[9] collaboration with Tevatron $p\bar{p}$ collider at Fermilab, Aleph, Delphi, L3 and OPAL collaborations with LEP e^+e^- collider at CERN, and H1 and ZEUS with HERA ep collider[58].

Experiment	Signature	95% CL mass limit (β)
CDF [60]	$eejj$	113 GeV/ c^2 (1.0)
		80 GeV/ c^2 (0.5)
D \emptyset [61]	$eejj, e\nu jj$	130 GeV/ c^2 (1.0)
		116 GeV/ c^2 (0.5)
HERA (H1) [62]	ej	275 GeV/ c^2 [†] (1.0)
CDF [8]	$\mu\mu jj$	131 GeV/ c^2 (1.0)
		96 GeV/ c^2 (0.5)
D \emptyset [9]	$\mu\mu jj, \mu\nu jj$	119 GeV/ c^2 (1.0)
		97 GeV/ c^2 (0.5)
CDF [63]	$\tau\tau jj$	99 GeV/ c^2 [‡]

Table 3.5: Published mass limit for three generations of leptoquarks.

with an estimated background of 4.8 ± 1.3 . This search excluded $M(LQ_2) < 180$ GeV/ c^2 for $\beta = 1$ and $M(LQ_2) < 141$ GeV/ c^2 for $\beta = 0.5$ at 95%*C.L.*. However, this limit .

3.5.3 Summary of existing leptoquark mass limits

Direct searches for leptoquarks in all three generations (electron, muon, and tau channels) have been performed at the hadron colliders.

Table 3.5 lists previously published results on the leptoquark mass¹⁸. The mass limit depends on the theoretical cross section models. In particular, CDF and D \emptyset has used Leading Order (LO) theory while the most recent results use the Next-to-Leading Order (NLO) calculations. Table 3.6 summarise the recent results coming from Tevatron hadron collider.

¹⁸(For Table 3.5), [†] This limit is sensitive to leptoquark decay coupling. Shown result is with $\lambda = \alpha_{EM}$. [‡] Not relevant of β since $M_{top} > M_{LQ3}$.

Experiment	Signature	95% CL mass limit (β)
CDF [65]	$eejj$	210 GeV/ c^2 (1.0)
DØ [64]	$eejj, e\nu jj$	175 GeV/ c^2 (1.0) 147 GeV/ c^2 (0.5)
CDF [14]	$\mu\mu jj$	195 GeV/ c^2 (1.0)
DØ [64]	$\mu\mu jj, \mu\nu jj$	167 GeV/ c^2 (1.0)
CDF [64]	$\tau\tau jj$	110 GeV/ c^2
DØ [64]	$b\bar{b}\nu_\tau\nu_\tau$	80 GeV/ c^2

Table 3.6: Non-published recent results for leptoquark mass limits at hadron colliders.

Chapter 4

The CDF Experimental Apparatus

The Tevatron $\bar{p}p$ Collider at Fermilab is currently the world's highest energy particle accelerator. The Collider Detector at Fermilab (CDF) was the first general-purpose detector built to exploit physics at the Tevatron.

The design purpose of the Collider Detector at Fermilab is to identify and measure the energy and momentum of particles produced in $p\bar{p}$ collisions. It was first commissioned in 1987 and collected data corresponding to an integrated luminosity of 4.3 pb^{-1} in the 1988-1989 Collider Run. Since then the CDF detector has undergone several upgrades, some of which are crucial to this analysis. The upgrades include the addition of a Silicon Micro-Strip Vertex detector (SVX), an extension of the muon coverage and several enhancements in the Data Acquisition system. The second sets of run took a place from 1992-93 (Run IA, with an integrated luminosity, $\int \mathcal{L} dt = 19 \text{ pb}^{-1}$) and 1994-95 (Run IB, $\int \mathcal{L} dt = 90 \text{ pb}^{-1}$). These data samples are used for the second generation leptoquark search in Chapter 5. This chapter briefly describes the Tevatron and an overview of both the Collider and the CDF detector.

4.1 The Tevatron collider

The Tevatron collider at Fermilab is a superconducting synchrotron designed to accelerate protons and antiprotons for high energy physics experiments, located at Batavia (Illinois, U.S.A.). The Tevatron is 6.3 km in circumference, utilising superconducting magnets and radio-frequency fields to accelerate charged particles. The accelerator is capable of accelerating

proton and antiproton beams up to 900 GeV, therefore yielding a colliding center of mass energy (\sqrt{s}) of 1.8 TeV. It started the operation in 1987. Its luminosity was typically at $\sim 10^{31} \text{cm}^{-2} \text{s}^{-1}$ during the latest run, and the CDF experiment has collected a total integrated luminosity of $\sim 110 \text{pb}^{-1}$ during the Run I period ending in December 1995. The Tevatron accelerator consists of several stages and in each stage protons and antiprotons are accelerated to reach the final energy of 900 GeV in the Tevatron main ring. The source of protons is taken from hydrogen gas in the pre-accelerating stage. The schematic presentation of the Tevatron is as shown in Figure 4.1, and the acceleration stages consist of:

1. Pre-accelerator (Cockroft-Walton). \Rightarrow 750 keV.
2. Linear accelerator. (*length=150 m*) \Rightarrow 400 MeV.
3. Booster. (*circumference=475 m*) \Rightarrow 8.0 GeV.
4. Accumulator.
5. Proton and antiproton injectors.
6. Main ring (*circumference=6.3 km*) \Rightarrow 150 GeV.
7. Tevatron ring (*circumference=6.3 km*) \Rightarrow 900 GeV.

The proton and antiproton beams undergo the following acceleration steps: the protons used in the collisions originate from Hydrogen gas molecules which are first ionised and the resulting negative ions are accelerated to 750 keV in the Cockroft-Walton electrostatic generator. The Hydrogen ions are then accelerated to 400 MeV in a 150 meter long linear accelerator (LINAC). The ions emerge from the LINAC through a carbon foil that strips their outer electrons to leave a pure proton beam. The booster ring, a synchrotron accelerator, is 470 meters in circumference, where the protons produced from the LINAC are accelerated to 8 GeV. In the booster, proton bunches are collected and injected into the Main Ring. The Main Ring, also a synchrotron accelerator, consists of a 6.3 km string of alternating dipole (bending) and quadrupole (focusing) magnets. The Main Ring also contains RF cavities that boost the protons to 150 GeV. The Main Ring then injects these protons into the Tevatron or to fixed target experimental stations. Protons from the Main Ring are also used for antiproton production.

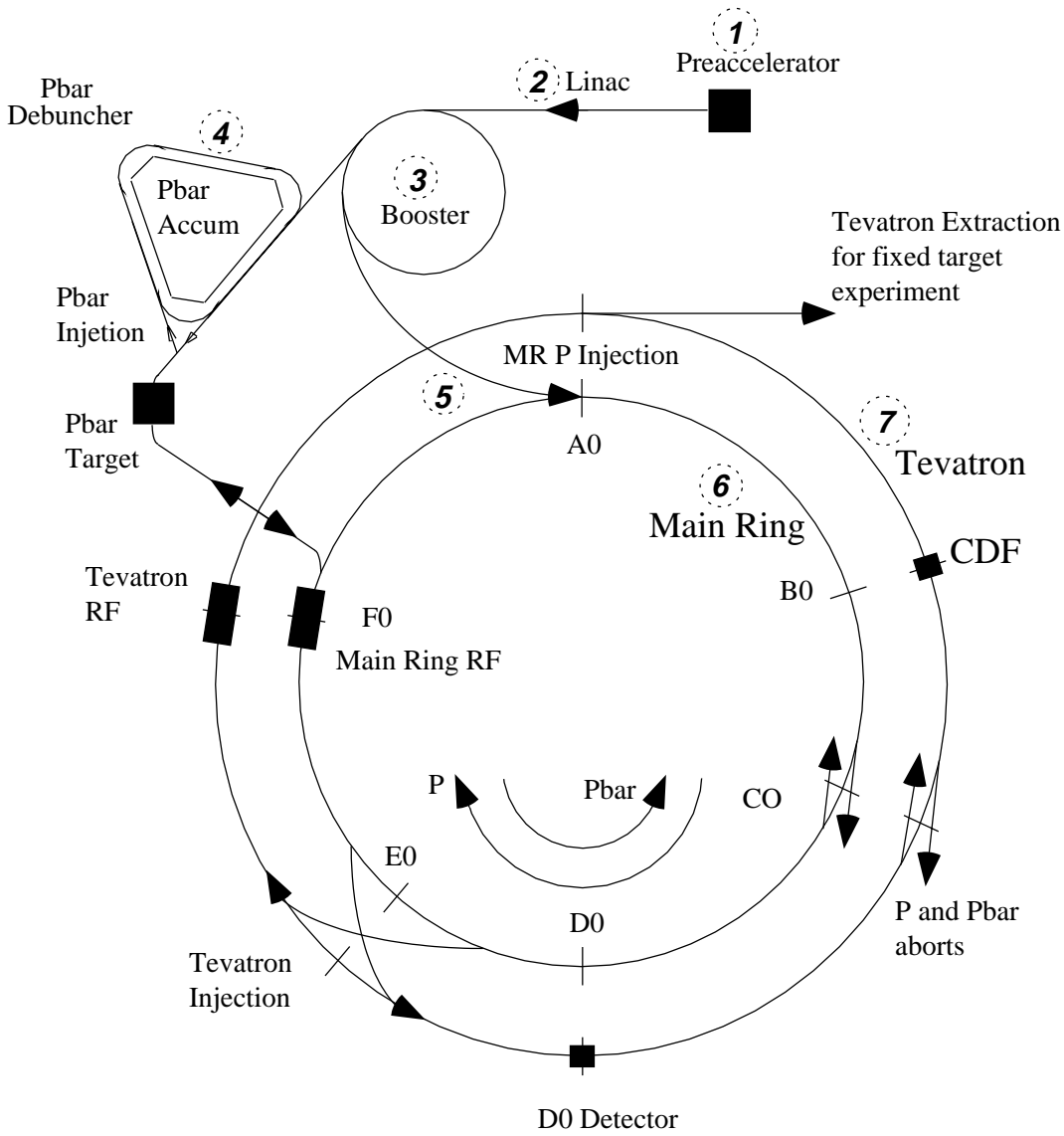


Figure 4.1: The Tevatron collider at Fermilab.

The proton beam from the Main Ring is focused on a tungsten target which produces antiprotons as a result. The typical production rate of the antiproton is in order of $4 \times 10^{10} \bar{p}/hr$. Antiprotons are collected and stored in the Accumulator Ring, where stochastic cooling is used to reduce their spatial and momentum dispersion. After enough antiprotons have been accumulated, they are re-injected first into the Main Ring to be accelerated to 150 GeV as for the protons, then injected into the Tevatron ring to be accelerated to the final energy of 900 GeV travelling in counter direction from the proton beam. The Tevatron is a ring of superconducting magnets that lies directly beneath the Main Ring. In the Tevatron protons and antiprotons are accelerated to 900 GeV and then made to collide at two interaction regions, $B\bar{\theta}$ and $D\bar{\theta}$, at which are housed Fermilab's two general purpose Collider detectors, CDF and $D\bar{\theta}$ respectively.

At the $B\bar{\theta}$ interaction region, the beam is roughly Gaussian in cross-section with a radius defined by $\sigma \sim 40 \mu m$. It is focused by quadrupole magnets which have the field strength of ~ 5.7 Tesla. The longitudinal profile of the beam is approximately Gaussian with a length of 30 to 35 *cm*. The machine has 6 bunches each of protons and antiprotons. The interaction interval is approximately 3.5 μs . Specifications of the Tevatron are given in Table 6.1 of Chapter 6, and are compared with the specifications of the CERN Large Hadron Collider ¹.

4.2 The CDF detector

The Collider Detector at Fermilab (CDF) is designed to identify and measure the properties of particles emerging from the Tevatron collisions, and the detector consists of many sub-detectors to obtain maximum detection efficiency and a substantial geometric coverage for relevant physics processes. The detector is required to have precise tracking for the detection and reconstruction of the charged particles from $\bar{p}p$ interactions. A very fine granularity for the calorimeters is required to measure the position and energy of electromagnetic and hadronic showers. Further more, good muon identification is needed for many analyses. The perspective view of CDF detector is shown in Figure 4.2. The detector is symmetrical in forward-backward direction about the interaction point located in the center of the apparatus. The detailed

¹For CERN Large Hadron Collider, please refer to Chapter 6.

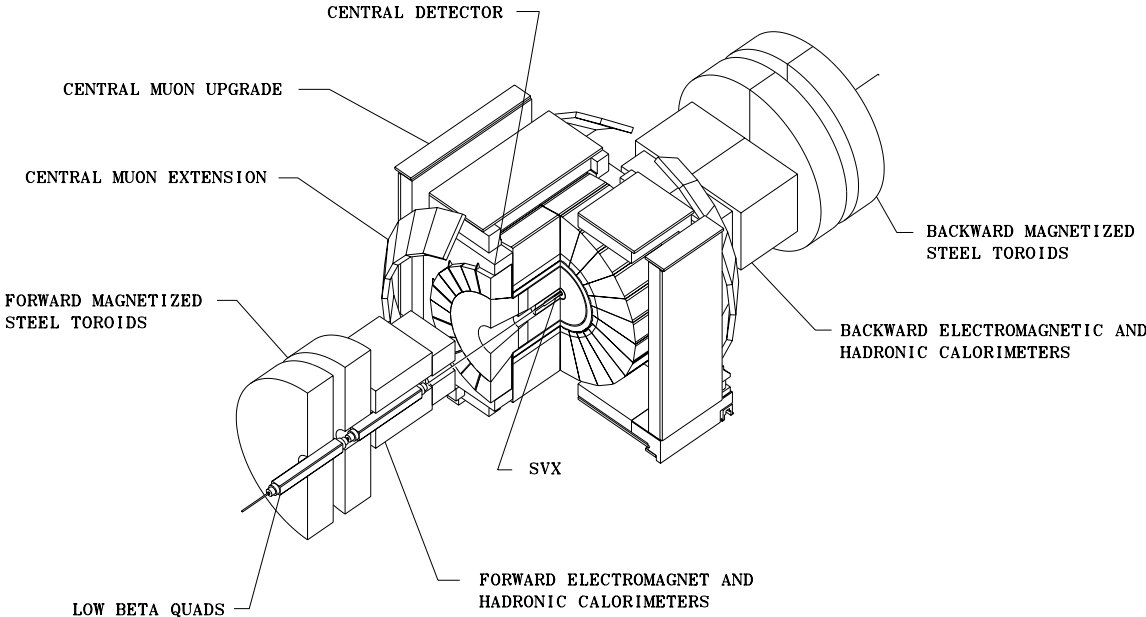


Figure 4.2: Perspective view of the CDF detector. Components with their names are shown.

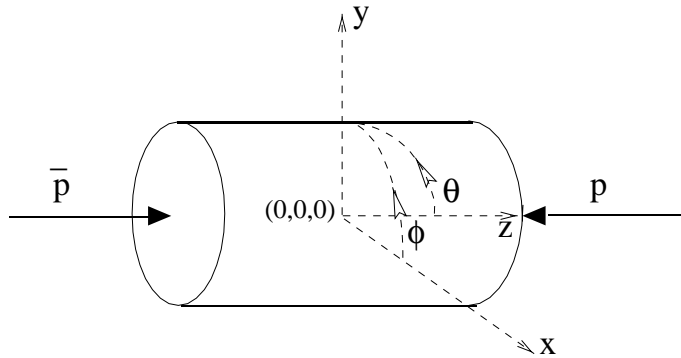


Figure 4.3: The CDF coordinate system.

description of the CDF detector can be found in Reference [66], and here a brief overview of the experiment relating to the leptoquark search analysis is given.

4.2.1 CDF coordinate system

CDF employs a right-handed coordinate system, in order to characterise the detected particles. Figure 4.3 shows the overall CDF coordinate frame, in both the Cartesian and cylindrical systems:

- Cartesian coordinate system:

z -axis: it lies parallel to the beam axis, positive to the the proton direction.

y -axis: it points upwards from the plane of the Tevatron.

x -axis: points radially outwards as shown in Figure 4.3.

- Polar coordinate system:

ϕ : Azimuthal angle about z -axis, 0 at x -axis, and it increases clockwise.

θ : Polar angle relative to z -axis, 0 at y -axis.

r : Radial distance from the z -axis.

- Interaction point is at $(0,0,0)$ for both coordinate systems.

It is useful to work in terms of the geometric parameter “*rapidity*”, defined by

$$y = \frac{1}{2} \ln \left(\frac{E + P_Z}{E - P_Z} \right) \quad (4.1)$$

and the closely related pseudorapidity,

$$\eta = -\ln \left(\tan \frac{\theta}{2} \right) = \frac{1}{2} \ln \left(\frac{P + P_Z}{P - P_Z} \right) \quad (4.2)$$

Both η and y describe the direction of particles in the detector and the longitudinal boost of the parton collision frame. Compared to parton collision energies at the Tevatron, the parton masses are taken to be zero and in this limit η and y are equivalent. Through out the analysis, we define the *transverse momentum* or *transverse energy*, denoted by p_T and E_T , respectively, by:

$$p_T = |\mathbf{p}| \times \sin \theta \quad (4.3)$$

$$E_T = E \times \sin \theta \quad (4.4)$$

These variables describe the particle kinematics in $x - y$ plane.

It is useful to refer a radial distance of ΔR , and it is used to define the $\phi - \eta$ geometrical space throughout the analysis. The definition of ΔR is

$$\Delta R = \sqrt{\phi^2 + \eta^2} \quad (4.5)$$

where ϕ is the azimuthal angle about z -axis in the polar coordinate and η is the rapidity. This quantity is used for defining the size of cone to calculate the jet energy, for example.

4.2.2 CDF sub-detectors

The quadrant cross section view of the CDF detector is shown in Figure 4.4. The detector is forward-backward symmetric about the interaction point which is at the lower-left edge on the beam line in Figure 4.4. The central part of the detector extends to $|\eta| \simeq 1.1$. Radially from the most inner layer, the detector consists of the Silicon Vertex detector (SVX) just after

The CDF Detector

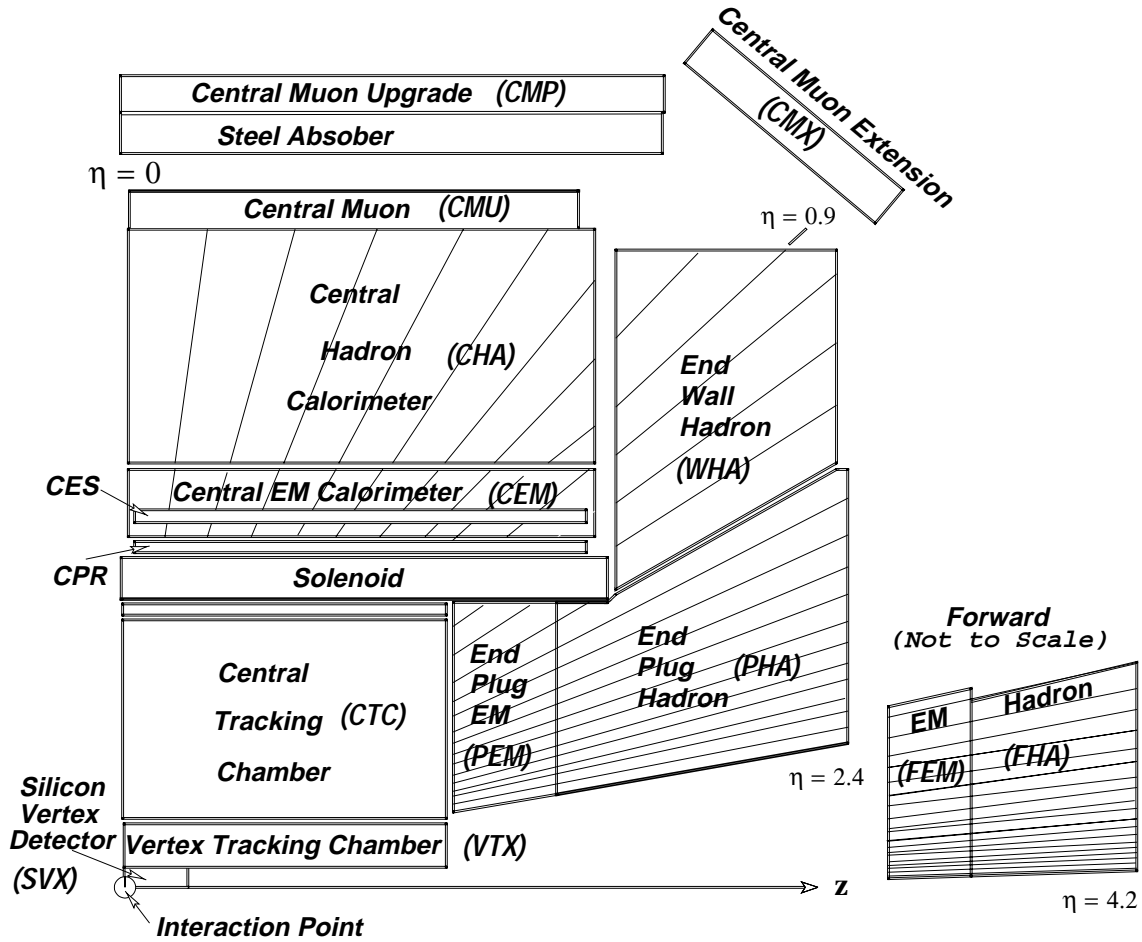


Figure 4.4: Schematic drawing of one quadrant of the CDF central detector. The projective tower geometry of the calorimeters is indicated. Note that the forward calorimeters are actually located further upstream and downstream than shown here. CES stands for Central Electromagnetic Shower-maximum detector and CPR for Central Pre-Radiator.

Tracking System	Polar Angle Coverage	Radial Coverage(<i>cm</i>)	Length (<i>cm</i>)	Layers	Spatial Resolution(μm)
SVX	$ \eta < 1.2$	$3.0 < r < 7.9$	30	4	15
SVXP	$ \eta < 1.2$	$2.9 < r < 7.9$	30	4	13
VTX	$ \eta < 3.25$	$7 < r < 21$	143.5	24	200-500
CTC	$ \eta < 1.5$	$30.9 < r < 132$	160.7	60,24	200

Table 4.1: Tracking Subsystem Properties

the beam pipe, the Vertex Time projection chamber (VTX), the Central Tracking Chamber (CTC). These detectors are surrounded by the superconducting solenoid magnet, permitting a precise measure of the location of the interaction point, and momentum measurements of charged particles. In general, the SVX is used to measure displaced vertices, and the VTX is to reconstruct the z coordinates of the vertices of interactions. The CTC together with the SVX provides tracking information for charged particles and measures the momentum of charged particles.

The outer layers consist of the electromagnetic and hadronic calorimeters and muon chambers. The muon chambers consist of the Central (CMU), the Plug (CMP) and the intermediate (CMX) chambers. In addition in the plug region ($1.2 < |\eta| < 2.4$) electromagnetic and hadronic calorimeters are further placed. Both the electromagnetic and hadronic calorimeters measure the energy of incoming particles, and are used to measure the energy of electrons and jets emerging from the interactions. The informations coming from these calorimeters are used for jet identification. The forward/backward region extends to $|\eta| = 4.2$ with calorimeters and muon toroidal spectrometers are mounted about 6 m far from the interaction point.

4.3 Tracking at CDF

The CDF charged particle tracking system is located inside the 4.8 meter long superconducting solenoid of radius 1.5 meter, in the polar angular range between $\sim 8^\circ$ and $\sim 172^\circ$. Three dimensional track reconstruction is possible from 40° to 140° . The physical properties of all of the tracking subsystems are listed in Table 4.1.

4.3.1 The Solenoid

The solenoid produces a 1.412 Tesla magnetic field. The tracking system achieves excellent resolution due to this high magnetic field which is monitored by an NMR probe with an accuracy of one part in ten thousand. The solenoid is made from a NbTi/Cu superconducting material, with 4.8 meter in length and 1.5 in radius just outside of the CTC. The magnetic field flux is returned through a steel yoke. The yoke also functions as a support the calorimeters located radially outside the solenoid. The magnetic field and its fluctuations are monitored and mapped precisely and recorded for offline corrections, for computing the momentum of the charged particles with curvatures determined from the track.

4.3.2 The SVX

The Silicon Vertex detector [67, 68] was installed for the Run IA, and it has been upgraded for higher luminosity for Run IB. It is located at the most inner part of the detector system, just outside of the beam pipe. Its purpose is to provide precise tracking in the $r - \phi$ plane in order to measure the transverse impact parameters of the primary and secondary interaction points. Particles emerging from the collision with life time in order of 10^{-12} seconds will travel some $100 \mu m$ before decaying to secondary particles, and one can identify such decay vertices with a precise measurement of reconstructed tracks, using the SVX informations.

The SVX consists of two wedges, 3 layers of silicon in inner wedge, and 1 layer in outer wedge, as shown in Figure 4.5. A total of four layers of silicon micro strips are installed. Layer 0 is at 3.0 cm in radius, up to 7.9 cm at layer 3, and the total length is 51 cm . Each layer consists of 12 wedges, covering 30° in ϕ and 25.5 cm in z . Two layers are laid along the beam line, symmetrically placed about $z = 0$. A wedge consists of a ladder with 3 microstrip detector panels each, 8.5 cm in length, placed parallel to the beam line. The $r - \phi$ readout pitches vary from layer to layer, and they are from $55 \mu m$ to $60 \mu m$. The total number of readout channels of the SVX is 46080. At both ends of the cylinder, a beryllium support structure which contains readout electronics modules and cooling pipes is placed. The SVX is operated at a nominal temperature of $20^\circ C$.

Tracking with the SVX uses hit information from CTC, when a CTC track matches with at least two hits in SVX and those hits are not associated with any other tracks. The spatial

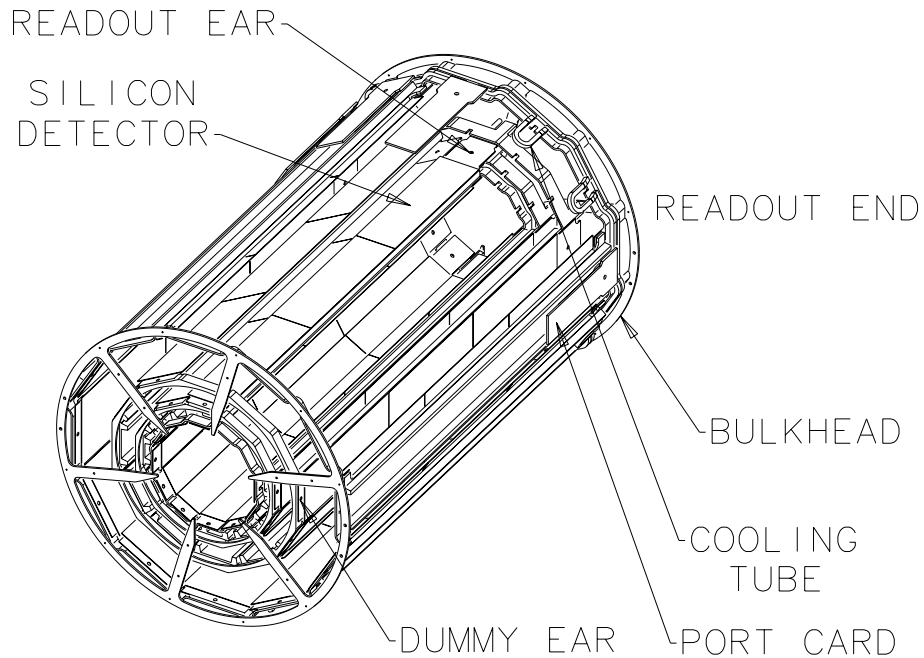


Figure 4.5: An isometric view of the SVX detector. $r = 7.9 \text{ cm}$, $l = \pm 25.5 \text{ cm}$.

resolution of the detector, coming from the offline analysis, is of order $\sim 10\mu\text{m}$. The SVX is also surrounded in the solenoid magnetic field which enables a momentum measurement of charged particles.

The SVX is used for identifying secondary vertices from heavy meson decay, for example B mesons, and the technique is popularly called *b-tagging*. It is used, for example, to identify the b-quarks in top quark analyses. In the analysis presented in this thesis, we do not use information from the SVX.

4.3.3 The VTX

The Vertex Time Projection Chamber (VTX) [69] for the Run IA and Run IB is an upgrade of a similar chamber (VTPC) used during the 1988 - 1989 runs. The upgrade was required because of the increased luminosity in Run IA and Run IB. The SVX was introduced at the same time, and it was necessary to make a space for the installation between VTX and the beam pipe. The chamber consists of two barrels, divided into two segments (*east* and *west*),

and it covers $|\eta| < 3.25$ of pseudorapidity and extends 22 cm in r direction. Two segments are symmetric about the interaction point ($z = 0$) and each segment consists of two barrels. The drift area in the detector is filled with Argon-Ethane gas. It is optimised to provide a good pattern recognition in the $r - z$ plane. By measuring the drift times of electrons hitting sense wires, a primary particle track can be reconstructed. The azimuth of a track is obtained from charge induced on the cathode pads. The VTX provides 3-D track reconstruction for its full geometrical coverage.

The main purpose of the VTX detector is to determine the precise information of the event vertex in the z direction, with a resolution of $1 \sim 2\text{ mm}$ depending on track multiplicity in the event. The identified vertices are then matched with tracks found in the event to find the interaction vertex. In the analysis presented in this thesis, the muons decaying from the leptoquarks are assumed to emerge from an unique vertex, since the decay width of the leptoquark is assumed to be very small. The two CTC tracks identified as muon candidates should match with the same VTX vertex within 5 cm in order to pass the dimuon identification criteria.

4.3.4 The CTC

The Central Tracking Chamber (CTC) [70] is a wire drift chamber of length 3.2 meters along the beam direction. In the radial direction the most inner layer has radius at $r = 30.9\text{ cm}$, and at the most outer layer $r = 130.2\text{ cm}$.

The chamber consists of 84 layers of sense wires grouped into 9 superlayers: 5 axial superlayers parallel to the beam line which enable track reconstruction in $r - \phi$ plane, and 4 stereo superlayers, interleaving axial superlayers, which are inclined at $\pm 3^\circ$ to provide stereo track reconstruction, that is in the $r - z$ plane. Figure 4.6 shows the end-plate of the CTC showing the wire slots. 5 axial superlayers contain 12 sense wire layers each, and 4 of the stereo superlayers contain 6 sense wire layers each. All superlayers are divided into cells such that the maximum drift distance is less than 40 mm , or corresponding to 800 ns of drift time.

The excellent momentum resolution achieved by the CTC is largely due to the large magnetic field and the large tracking volume. The drift time of the collected charge to the axial wires gives the $r - \phi$ position of the hits, determined by Time Digital Converter (TDC) with

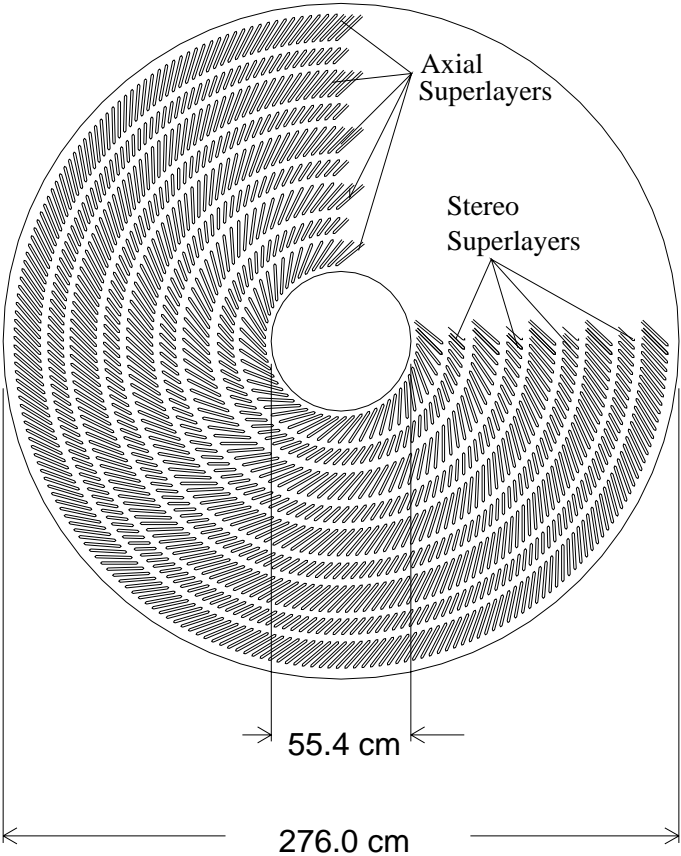


Figure 4.6: The CTC end-plate showing the wire slots.

the resolution of ~ 100 ns or order of a few millimetres of spatial dimension. Informations from stereo wires are also used to determine the z position of the hits. The resolution in the z direction is approximately 4 mm.

The measurement of charged particle momenta uses the CTC tracking information. It is computed by determining the curvature of the fitted track. The resolution of p_T for the CTC tracking is measured to be

$$\Delta p_T/p_T = 0.010 \times p_T$$

where p_T is given in a unit of GeV/ c .

The tracking information is used to identify electrons by matching tracks to energy deposited in the electromagnetic calorimeters and to identify muons by matching tracks to hits in the muon chambers. An absence of tracks matched to electromagnetic clusters in the calorimeter is also used to identify photons. The CTC, together with SVX information, is also used to identify secondary vertices due to decay of long-lived particles. In the leptoquark search analysis, muons are identified both from the muon chamber information and CTC tracking information, and the momentum is measured by the CTC track curvatures. The muon tracks in the CTC are then matched with hits from the muon chambers located farther back in the CDF detector system.

4.4 The Calorimetry

The main purpose of the calorimeters is to measure the energy and geometrical position of electrons and hadronic jets. The CDF has both electromagnetic and hadronic calorimeters installed. It is essential for leptoquark analysis where we need to detect both lepton and hadron energies for the reconstruction of the parent particles. It also measures the missing traverse energy in the event.

The missing traverse energy, often denoted by \cancel{E}_T , indicates the amount of energy in the transverse plane carried by undetectable particles such as neutrinos. In $\bar{p}p$ collisions, the total initial traverse energy is zero. The conservation of the momentum implies that total traverse energy in the final state should also be zero. However, when neutrinos are produced in the

System	η range	Energy Resolution ($\frac{\%}{\sqrt{E}}$ + constant term)	Position Resolution	Thickness
CEM	$ \eta < 1.1$	$13.5\% \oplus 2.0\%$	$0.2 \text{ cm} \times 0.2 \text{ cm}$	$18X_0$
PEM	$1.1 < \eta < 2.4$	$28\% \oplus 2\%$	$0.2 \text{ cm} \times 0.2 \text{ cm}$	$18-21X_0$
FEM	$2.2 < \eta < 4.2$	$25\% \oplus 2\%$	$0.1 \text{ cm} \times 0.4 \text{ cm}$	$25X_0$
CHA	$ \eta < 1.1$	$75\% \oplus 3\%$	$0.2 \text{ cm} \times 0.2 \text{ cm}$	$4.5 \Lambda_{abs}$
PHA	$1.1 < \eta < 2.4$	$90\% \oplus 4\%$	$0.2 \text{ cm} \times 0.2 \text{ cm}$	$5.7 \Lambda_{abs}$
FHA	$2.2 < \eta < 4.2$	$130\% \oplus 4\%$	$0.2 \text{ cm} \times 0.2 \text{ cm}$	$7.7 \Lambda_{abs}$

Table 4.2: Calorimetry at CDF. \oplus indicates quadrature sum. X_0 and Λ_{abs} are the radiation and absorption lengths respectively.

interaction and they carry a fraction of total energy in the event away and it will not leave any signals in the detector. Thus the vector sum of the transverse energy, measured by the calorimeters, will not be zero.

In the CDF, \cancel{E}_T is measured by computing the negative vector sum of the all deposited transverse energy in the calorimeters, or

$$\cancel{E}_T = - \sum_{\phi=0}^{2\pi} E_{T(\phi)} \quad (4.6)$$

The coverage extends $2^\circ \sim 178^\circ$ in θ and full 2π coverage in ϕ . The CDF calorimeters are symmetric in ϕ , and are divided into three segments (central, plug, and forward) divided along the η . The Table 4.2 briefly summarises the properties of the CDF calorimeter system.

Each segments are organised with an electromagnetic calorimeter followed by a hadronic calorimeter. Figure 4.7 shows the CDF calorimeter segments shown in $\eta - \phi$ plane.

The Central calorimeter consists of two parts: The Central Electromagnetic (CEM) [71] and Central Hadronic (CHA) [72] calorimeters. The CEM placed inside of the CHA covering full ϕ and η range up to ± 1.1 . For higher pseudorapidity in the central region, Plug Electromagnetic (PEM) [73] and Plug Hadronic (PHA) [74] calorimeter are placed, covering $1.1 < |\eta| < 2.4$.

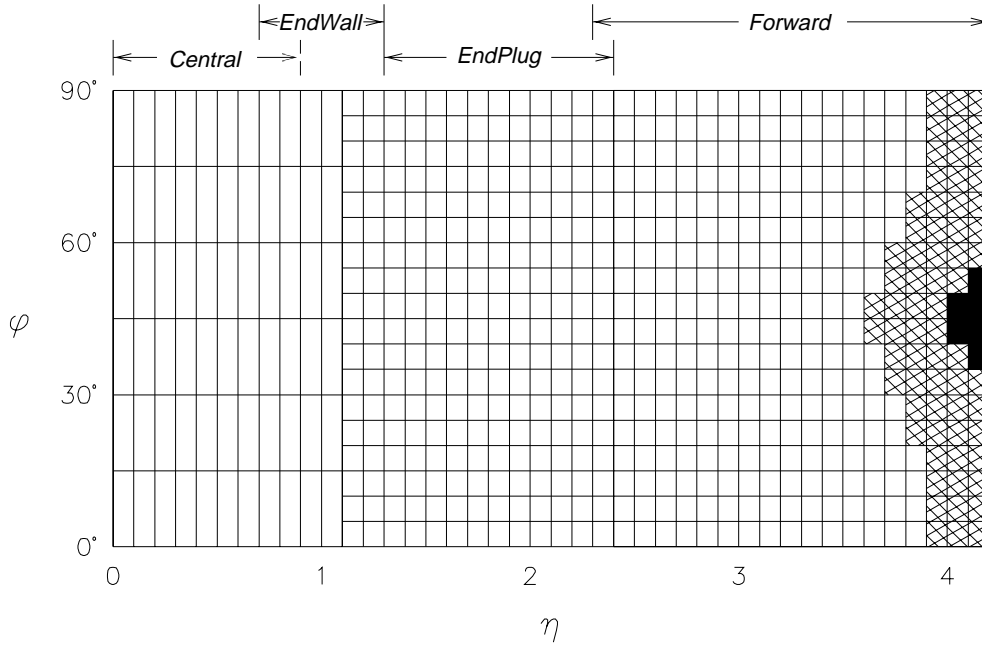


Figure 4.7: The CDF calorimeter segments shown in $\eta - \phi$ plane.

4.4.1 The Central and Plug calorimeter: Electromagnetic

The CEM uses scintillator as the active media and photo-tube for its readout. The electromagnetic calorimeter uses lead absorber interspersed with polystyrene scintillator. The CEM consists 31 units of 0.5 cm thick layer of scintillator interspersed with 30 sheets of 0.32 cm thick lead absorber. The energy resolution is $13.5\%/\sqrt{E} \oplus 2.0\%$. It is segmented into two halves in z -plane, divided symmetrically at $\eta = 0$. Each half is further segmented into 24 wedges, each covering 15° in ϕ and pseudorapidity range of $0 < |\eta| < 1.1$. Each wedge is divided into 10 towers along the z -axis. Figure 4.8 shows a perspective view of a central calorimeter wedge, with tower numbers marked from 0 to 9.

The geometrical coverage of the CEM active area is wellknown in using the CES chamber information. The chamber has cracks for installation and construction reasons. The total acceptance loss due to explicit fiducial requirements is 18.7%.

The Central Electromagnetic Shower counter (CES) is a proportional chamber. A perspective view of the CES is shown in Figure 4.9. The CES is made up with strips perpendicular to the beam line and wires along the beam axis. It measures the shower position with z and

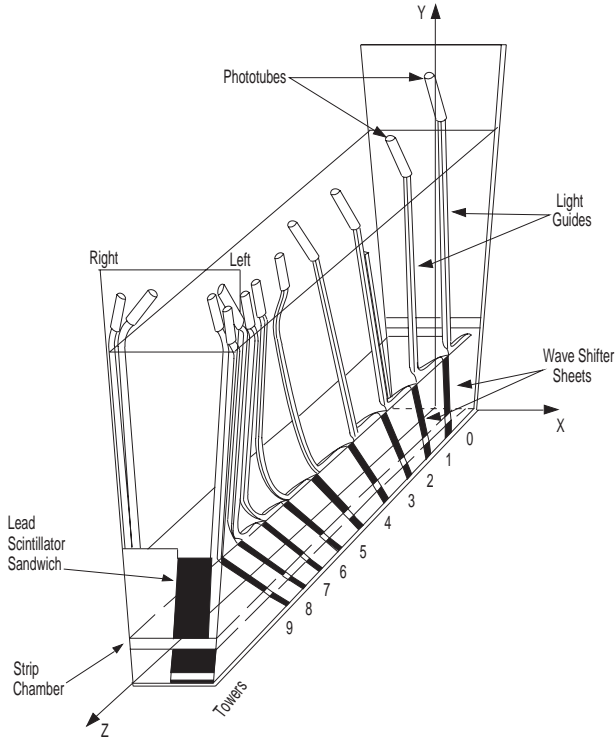


Figure 4.8: Perspective view of a Central calorimeter wedge.

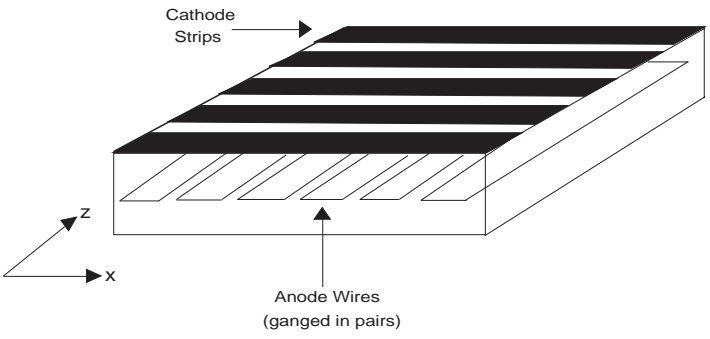


Figure 4.9: Perspective view of a CES chamber.

$r - \phi$ resolution of $2 \text{ mm} \times 2 \text{ mm}$. The shower centroid measured in the CES is then matched with tracks from the CTC to select electron candidates. This is the one of the most crucial technique to electron identification at the CDF detector.

4.4.2 The Central and Plug calorimeter: Hadronic

The Central Hadronic Calorimeter (CHA) lays after CEM, covering $|\eta|$ up to 0.9. It is mounted around the solenoid consisting of steel plates and acrylic scintillator. Because of being placed in outer radius, the CHA covers the pseudorapidity range $|\eta| < 0.9$, with the end-wall hadron calorimeter (WHA) extending this coverage out to $|\eta| < 1.3$. The CHA consists of 32 layers of 1 cm thick scintillator interleaved with layers of 2.5 cm thick steel. The WHA is made up of 15 layers of 5 cm thick steel followed by 1 cm thick scintillator. It presents 4.5 absorption lengths of material and has an energy resolution of $75\%/\sqrt{E} \oplus 3\%$.

The CDF collaboration has studied jet energy systematic errors. The uncertainty on absolute jet energy scale due to the hadronic and electromagnetic detector effect is given by the so called *Behrens curve* [75]. The absolute E_T scale for jet clustering is based primarily on the real data. Using single charged tracks in minimum bias data and charged pions and electrons in test beam, the detector response to charged particles can be directly measured by examining the energy to momentum (E/P) distribution. Comparing with the Monte Carlo simulation, we measure the uncertainty in the calorimeter response. Convolving the uncertainty into the jet response results in the *Behrens curve*. The jet uncertainty is measured to be 2% for top quark mass analysis at CDF.

In the plug region, gas proportional chambers are used with cathode pads as its readout system. The PEM uses lead absorber and conductive plastic proportional tube arrays, and its performance is characterised by its energy resolution of $28\%/\sqrt{E} \oplus 2.0\%$. Geometrical position resolution is obtained from its strip size ($2 \text{ mm} \times 2 \text{ mm}$). The PHA consists of steel plates and conductive plastic proportional tube arrays. It has an energy resolution of $130\%/\sqrt{E} \oplus 4\%$.

When heavy particles are produced from the interaction, the secondary decay particles tend to have small rapidity. To detect such interactions the central part of the detector plays

important role. In the leptoquark analysis the interesting leptoquark mass regions are well over $100 \text{ GeV}/c^2$ (see Section 5.3.1 for its kinematics). Consequently leptoquarks are produced in the central region, and decay mainly into the central part of the detector. Therefore we use the jet information from the central and plug calorimeters. We do not use data from forward/backward calorimeters for jet identification because of their poor resolutions and high noise to signal ratio.

4.4.3 Forward calorimeter

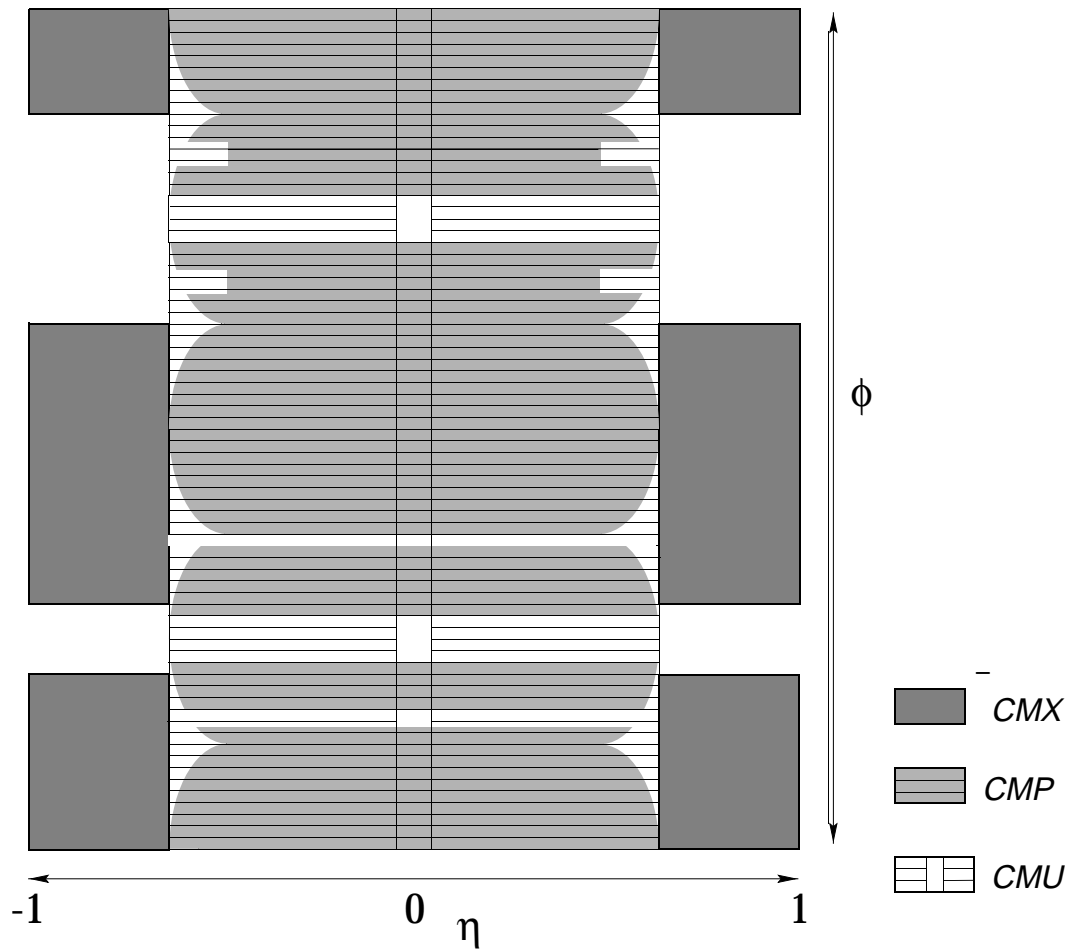
The forward calorimeters consist of electromagnetic shower counter (FEM) and hadron calorimeter (FHA). Each of the forward calorimeters are composed of proportional chambers and steel plates. It is situated 6.5 m from the interaction point, and it is designed to cover a pseudorapidity region of $2.2 \leq |\eta| \leq 4.2$ and full azimuthal angle coverage. The FEM consists of 30 layers of proportional chamber with cathode pad readout. The FHA is also made of proportional chamber with iron plate intervals.

The information of forward calorimeter is used for missing traverse momentum measurement.

4.5 The muon chamber

Because of the long muon life time and high penetration, the detector is located at the outer most layers of the detector. In the CDF detector configuration, muon chambers are placed outside of the hadronic calorimeters, after a steel absorber to eliminate any electromagnetic and hadronic showers. Muon chambers in the CDF detector are classified into three parts: the central Muon chamber (CMU), the Central Muon upgrade (CMP), and the Central Muon extension (CMX). The geometrical coverage on $\eta - \phi$ plane of each detector is shown in Figure 4.10.

In the second generation leptoquark analysis, good muon identification is a key requirement to find possible candidate events. It is important to understand the functionality of the muon chambers and the fiducial regions in order to match the muon tracks coming from inner tracking detector to the informations coming from the muon chambers. This ensures quality

Figure 4.10: CDF $\eta - \phi$ map for central muon chambers.

muon selections.

There is also Forward Muon Chamber (FMC) which covers high η regions, however it is not used in this analysis. The kinematics of muons decaying from leptoquarks have been studied using Monte-Carlo generators (see Chapter 5.3). It shows the large distribution of muons in central regions.

4.5.1 The CMU

The Central Muon Chamber (CMU) [76] covers regions of $56^\circ < \theta < 124^\circ$ ($|\eta| < 0.63$) and about 85 % of the ϕ coverage. The CMU is located behind the central hadron calorimeter 3.47 m from the beam axis. The CMU has 48 segments of 12.6° in ϕ direction called *wedges*, which corresponds to CHA wedges with 1.2° of gap. This gap comes from fitting the CMU wedge to the corresponding wedge of CHA, since the CMU is located at greater radial distance in r . Due to the thickness of the calorimeters (the absorption length $X_0 = 4.9$) and steel absorber placed before the muon chamber, only muons above $p_T \sim 1.4$ GeV/ c reach the muon chambers. The layout of the CMU system is shown in Figure 4.11.

The chambers operate in the limited streamer mode with argon/ethane bubbled through ethanol. The geometrical resolution of the CMU is ~ 250 μm in the drift direction and 1.2 mm along the sense wire.

Each muon chamber is divided into three modules, which consists of four layers of four rectangular drift cells with dimension of 63.5 mm wide \times 26.8 mm high \times 2261 mm long, parallel to the beam axis. There is a sense wire at the center of each cell, as shown in Figure 4.12.

Particles traversing the muon chamber radially pass through all four cells. The sense wires in the outer two cells are offset by 2 mm with respect to the two inner wires in order to resolve the left-right ambiguity for track azimuthal measurement. Sense wires in alternate cells of the same layer are connected at the end of the chamber ($\phi=90^\circ$) and are read out separately at the other end.

To resolve the transverse projection of a track which arrives to the muon chamber after passing through the solenoid magnetic field, we define α as the angle between the trajectory in a muon chamber on a reference plane containing the beam axis. It is related to the traverse

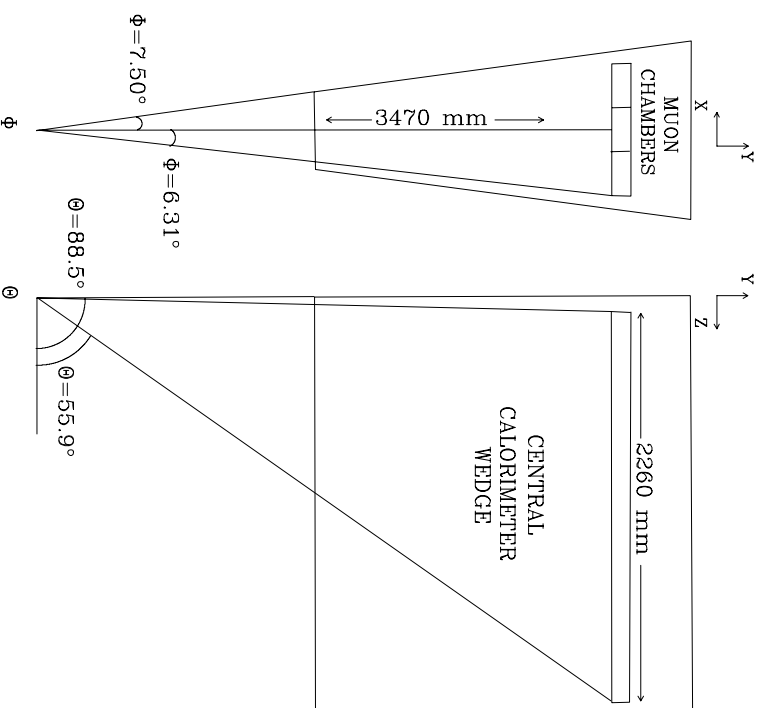


Figure 4.11: Layout of the GMU system.

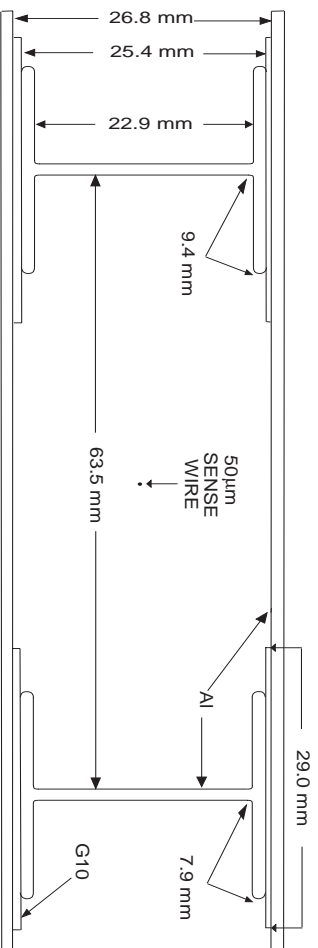


Figure 4.12: A cell of the central muon chamber.

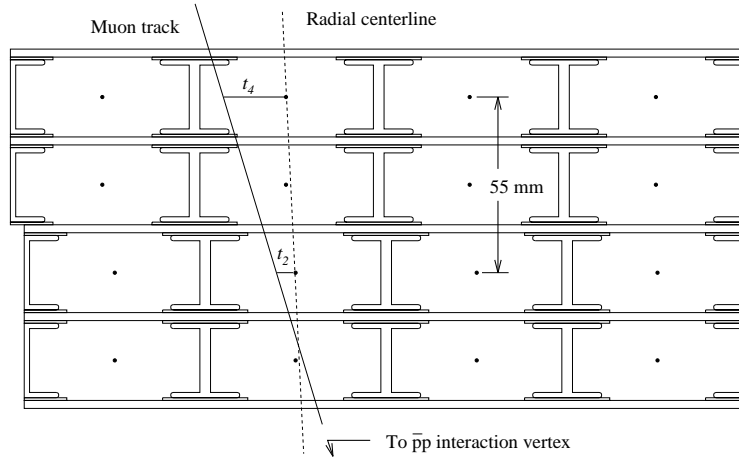


Figure 4.13: Cross section of CMU module showing the position of the sense wires and drift time.

momentum of the track (p_T). There are two different methods to compute this value.

One way is to use the relation between the curvature of the muon tracks in the solenoid field and the transverse momentum, in which the angle α is given by following formula:

$$\sin(\alpha) = \frac{qBL^2}{2Dp_T} \quad (4.7)$$

where q is the charge of the particle, B is the magnitude of the magnetic field, L is the distance of the chamber from the beam line, D is the curvature of the track, and p_T is transverse momentum coming from CTC tracking information.

Another method is to determine the angle α by measuring the difference of arrival times of charge, or drift time electrons produced by the muon traversing the media to the four sense wires within a muon tower. Two of the sense wires are offset by known amount to resolve the parity ambiguity. It is therefore determined which side of the sense wires (in ϕ) is hit first. Figure 4.13 shows a track traversing a muon tower.

The relation between α and drift time Δt is given by

$$\Delta t = H\alpha/\nu \quad (4.8)$$

where H is the separation of the sense wire layers and ν is the drift velocity of the ionization

electrons.

As a result a muon tower provides two independent measurements of α . The muon p_T information from α is used by the trigger system, but not in the offline analysis because the CTC information provides a better p_T measurement.

4.5.2 The CMP

The Central muon upgrade chamber (CMP) [78] was installed at the upgrade on 1992, to minimise the “punch through”² background which is caused by high p_T hadrons. The CMP coverage is approximately the same as the CMU in η , and the distance from the beam axis is further, at ~ 535 cm. The CMP chambers consist of a four sided boxes around the CDF detector, namely north wall and south wall chambers and top yoke and bottom yoke chambers. On two sides of the detector are steel walls. The CMP provides additional muon detection coverage behind 0.6 m of additional steel behind the CMU. Consequently the minimum muon energy required to reach CMP is $p_T > 2.5$ GeV/c.

4.5.3 The CMX

The Central muon extension chamber (CMX) [79] is another muon chamber installed in upgrade in 1992 to extend the muon detection coverage. The CMX consists of four free standing arches and extends muon coverage from 0.6 to 1.0 in pseudorapidity and has 80% coverage in ϕ . Figure 4.14 shows the layout of the drift tubes in a 15° wedge of the CMX chamber.

The CMX chambers are mounted on four free-standing arches adjacent to the central detector. There are eight layers of drift chambers grouped into four radially aligned pairs. Adjacent layers are offset by a half of cell. High p_T muons, in case of heavy particle such as leptoquark decay, typically traverse between four and six drift chambers.

²Most hadrons shower in the calorimeter, but some travel to the CMU chamber without showering or shower late. The *punch through* is when energetic hadronic jets (π, K) goes through the shielding to reach muon chambers can fake a muon. See Section 5.6.5.

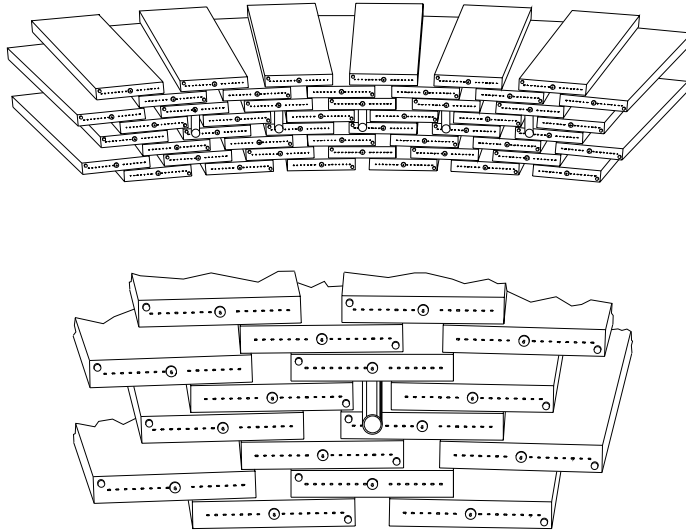


Figure 4.14: The layout of the drift tubes of the CMX. The figure shows the section of 15° . The tubes are mounted on four free standing arcs which span 240° in ϕ and cover the pseudorapidity region of 0.6 to 1.0.

4.6 Trigger system

In normal operational conditions, the Tevatron $p\bar{p}$ luminosities of Run IA and IB were respectively $\sim 0.54 \times 10^{31} \text{ cm}^2/\text{s}$ to $\sim 1.6 \times 10^{31} \text{ cm}^2/\text{s}$, with a bunch crossing rate of $3.5\mu\text{s}$. The effective $p\bar{p}$ inelastic cross section is roughly $\sim 50 \text{ mb}$ at $\sqrt{s} = 1.8 \text{ TeV}$. This corresponds to an event rate of order 10^5 per second. The purpose of the CDF trigger system is to reduce this large event rate by making decisions of filtering to keep only interesting events, given the limited capacity of the data writing speed onto magnetic tape, typically a few Hz .

The first collision indication consists of scintillator planes at both ends of the interaction region. Any hard collision will be accompanied by fragments travelling along the beam pipe. These scintillator planes detect the fragments of the colliding protons and anti-protons. This is often referred as a minimum bias trigger or Level-0 trigger. A small fraction of these events were written to tape and used to study acceptances.

The CDF trigger system is defined as Level-1 [80], Level-2 [81], and Level-3 [82], and they are defined as follows:

- Level-1:

- Beam-to-beam counter must indicate a collision.
- Require minimum energy to be deposited in the calorimeter.
- Level-2:
 - Calorimeter clusters are identified (EM and/or HAD).
 - CTC tracks are recognised (reconstructed) by Central Fast Tracker (CFT) [83].
 - Matching is made reconstructed tracks from CFT, with energy deposited in the calorimeters.
 - Matching with reconstructed tracks from CFT, with energy deposited in the muon chambers.
 - The missing transverse momentum calculation is made.
- Level-3:
 - Final and complete event selection with online system.

The Level-1 trigger should be processed within the $3.5 \mu\text{sec}$ of bunch crossing time in order to accept the next event. In this level, there is no deadtime of the trigger decision making. The Level-2 trigger, more complicated and sophisticated than the first level trigger, takes order of $\sim 30 \mu\text{sec}$ to be processed. The Level-1 trigger output rate, or Level-2 input rate, is ~ 100 times smaller than the Level-1 trigger input rate; therefore Level-2 deadtime accumulation is small.

The events passing the Level-2 trigger are then sent to Level-3 for a complete online event reconstruction. The events processed in a computer farm and the events passing through the selection criteria are recorded onto magnetic tapes. The Level-3 trigger speed is in order of a few Hz . Some of these events satisfying specific requirements are called “express stream events” and flagged for immediate offline analysis. Figure 4.15 shows the CDF muon trigger path.

4.6.1 Level-1 trigger

The Level-1 trigger is based on the analogue signal from the calorimeter, and this serves as the primary trigger for electron, photons, and hadronic jets. Signals from the calorimeter towers

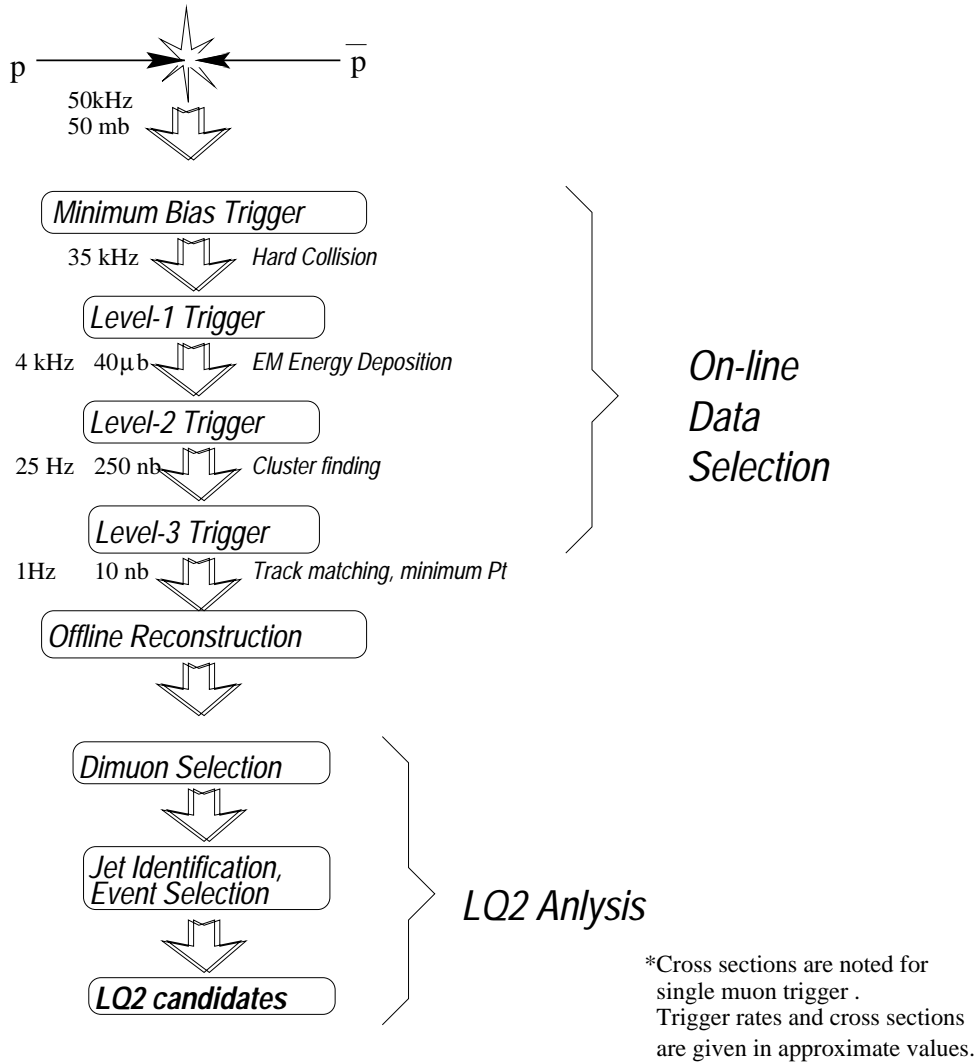


Figure 4.15: Trigger and event selection path for second generation leptoquark analysis. The event rate is given for a typical luminosity $\mathcal{L} \sim 0.8 \times 10^{30} \text{ cm}^{-2} \text{ s}^{-1}$.

are added to the size of $(\Delta\phi = 15^\circ) \times (\Delta\eta = 0.2)$ about the highest energy cell. These clusters are then corrected for variations in gain and offset. Then these data are then multiplied by $\sin\theta$, where θ is the polar angle. This defines a cluster tower. The trigger decision is made when any of the single towers has the value over the threshold. The thresholds are set individually for the different regions of the calorimeter. The lowest threshold is used in the CEM in which the threshold was set at 6 to 8 GeV . The highest thresholds are used in the forward EM calorimeters and in the plug and forward HAD calorimeters. In these regions the thresholds were often set out to 50 GeV .

A second calorimeter trigger has a lower threshold of $\sim 4 GeV$ in all regions except for the PHA and FHA. However this trigger operates in only one crossing out of every 40, hence the contribution of events coming from this trigger is much lower in comparison to the main calorimeter trigger.

The muon trigger plays an important role in the second generation leptoquark analysis presented in the next Chapter. The Level-1 muon triggers require hits in the sense wires of the muon chambers. It can be separated into two types: single muon and dimuon triggers. These triggers require either one or two stubs in the muon chambers above a momentum threshold, with a lower threshold used in the dimuon triggers.

The muon flight path is straight into the muon chambers with the absence of the solenoid magnetic field. The trajectory through the muon chambers forms an angle with respect to the radial path, as indicated in Figure 4.13. The size of this angle is a function of the deflection that the muon has experienced inside of the solenoid magnetic field. This is proportional to the p_T of the muon. This angle is measured by the Level-1 trigger, by making fast analogue measurement of t_2 and t_4 (refer to Figure 4.13), and determine the quantity $\Delta t = t_4 - t_2$. For the CMU the momentum threshold for the single muon trigger is 6 GeV/c and 3.3 GeV/c for dimuons. In the regions of the CMU that are covered by the CMP, a corresponding coincidence of hits in the CMP is required as confirmation of the hits in the CMU. Triggers for the CMX use a higher momentum threshold of 10 GeV/c for single muons which is in-time with signals from the CSX scintillators and associated hadron TDC's. This particular CMX trigger was introduced in the Run IB data taking period. The CMX muon trigger is not used in Run IA.

The cross section at Level-1 for the calorimeter trigger is $\sigma \sim 20 \mu b$ and for the single

muon CMU-CMP trigger is $\sigma \sim 40 \mu\text{b}$, while the total Level-1 cross section is $\sigma \sim 100 \mu\text{b}$. This corresponds to a Level-1 accept rate of $\sim 1\text{-}2 \text{ kHz}$, a reduction of over 2 orders of magnitude from the input rate.

4.6.2 Level-2 trigger

The events sent from Level-1 to Level-2 undergo fast reconstruction of the tracks using the CDF Fast Tracker (CFT), which will be matched with clusters from the EM calorimeter and/or muon chamber in $r - \phi$ space, as well as other minimum energy deposit requirements.

The most important additional information used at Level-2 comes from tracking. The CFT uses the $r - \phi$ information from the axial superlayers of the CTC to make a fast measurement of the traverse momentum of charged particle tracks. The CFT computes two passes looking for hits in a superlayer. It first searches for hits near to a wire, called prompt hits. The second search looks for hits that have drifted a greater distance, called delayed hits. A track typically has one prompt hit and two delayed hits on each of the axial layers. This yields a total of 15 hits for a given track.

The pattern of hits is compared with lookup tables for pattern recognition. The prompt hit on the outermost superlayer is used to start the lookup, and also defines the exit ϕ of the track. Tracks are binned in eight p_T ranges and by charge, with a resolution of $\delta p_T/p_T^2 \sim 3.5\%$. The nominal p_T threshold of a given bin is defined by the 90% efficiency point for that bin. For Run IA the p_T bins were at 3.0, 3.7, 4.8, 6.0, 9.2, 13.0, 16.7, and 25.0 GeV/ c . For Run Ib, the values were 2.2, 2.7, 3.4, 4.7, 7.5, 12.0, 18.0, and 27.0 GeV/ c , allowing triggering on tracks with lower p_T .

The Level-2 single muon trigger asks for a CFT track above a p_T threshold which matches to a muon stub. For each wire in the outermost superlayer of the CTC and for each p_T bin, the trigger logic makes an extrapolation of a straight line of the track to the muon chambers. Some tolerance is allowed to account for multiple scattering, resulting in a window of $\Delta\phi = 5^\circ - 10^\circ$. For each CFT track above the p_T threshold, the list of muon towers with stubs is compared to the list of expected hits to find a match. For Run IA (IB) the p_T threshold for the lowest p_T CMU trigger was 6.0 GeV/ c (7.5 GeV/ c).

In the Level-2 trigger decision, the trigger logic builds calorimeter clusters instead of using

the informations from single calorimeter towers. There are two different thresholds. The higher threshold is referred to as the *seed* threshold and the lower threshold is referred to as the *shoulder* threshold. Clustering begins with towers above the seed threshold. After finding the seed tower, the four nearest neighbours in η - ϕ space are examined to determine if they satisfy the shoulder threshold. If a tower above the shoulder threshold is found, it is added to the cluster and its neighbours are also examined for the shoulder threshold. This process stops when no tower in the neighbours has deposited energy above the shoulder threshold. Once a cluster is found, it is added to a list, along with associated event informations such as E_T , $E_T \sin\phi$, $E_T \cos\phi$, η , and ϕ . Several passes exist for cluster finding method at Level-2, which includes the jet cluster finding and two passes of electron/photon cluster finding. In electron/photon cluster finding only the information from the EM calorimeters is used to build the clusters. Detection of lower E_T clusters with the second pass using lower seed/shoulder thresholds is done after two passes of cluster finding has been performed.

Electrons are found by matching CFT tracks to the clusters, taking the ϕ informations of the cluster. This is almost identical to the matching for muons tracks and the stub hits, except the 15° calorimeter wedge is used in place of the 5° CMU tower. The E_T threshold used for the single electron trigger was 6.0 GeV in Run IA and 8.0 GeV in Run IB, while the corresponding track p_T thresholds were identical to those in the single muon triggers.

In Run IB an additional requirement was placed on the 8 GeV single electron trigger. The shower position information from the CES was used by matching CFT tracks to a group of four adjacent CES wires (corresponding to $\sim 2^\circ$ in ϕ) whose summed energy was above the given threshold. The electron triggers required an additional criterion that the tracks matching to an electron cluster must also match to a CES cluster.

At CDF, the cross section for the single electron trigger was $\sigma \sim 300 \text{ nb}$, while the cross section for the single CMU-CMP muon trigger was $\sigma \sim 250 \text{ nb}$. Due to high background rates at higher luminosity, these triggers were both assigned variable pre-scales. A fraction of events passing the trigger was written out at high luminosity with the pre-scales. For the electron trigger, the trigger was pre-scaled by as much as a factor of 4, while the (low p_T) muon trigger was pre-scaled by as much as a factor of 8. Higher p_T electron and muon triggers (i.e., used in the leptoquark analysis) are not typically pre-scaled, since the cross section for these types

of triggers are much lower than low p_T triggers.

4.6.3 Level-3 trigger

The Level-3 trigger makes the final decision whether to reject the event or write onto the magnetic tape for later off-line analysis. It is also used to split the data into several output streams based on the reconstructed object type in the events. Here, “object” refer to particles. As there are many Level-3 triggers, the discussion is restricted to the triggers relevant to the analysis presented in this thesis.

The inclusive muon trigger requires $p_T > 8.0 \text{ GeV}/c$ and applies χ^2 matching cuts between the track and the hits in the CMU chambers. The primary inclusive electron trigger requires $E_T > 7.5 \text{ GeV}$ and $p_T > 6.0 \text{ GeV}/c$. Tracks are required to match within 3 cm in x and 10 cm in z . Further selection cuts are made using offline quantities, such as the ratio of hadronic to electromagnetic energy (HAD/EM), and χ^2 cuts for the matching of the tracks to position information from the strip and wire chambers. These cuts are described in further detail in the following chapter. The cross section for each of these triggers at Level-3 is $\sim 10 \text{ nb}$, corresponding to a rate of less than 1 Hz .

4.7 Data Collection

The CDF data was written in 3 types of *streams*: Express line, the Stream 1, and the Stream 2. The Express line are the data which were kept on the disk temporarily for immediate off-line data analysis. These data include a very small fraction of events. The Stream data were written on the tape. The Stream 1 data include all events while the Stream 2 data contain only a fraction of the data. The Stream 1 data was split into classified data sets according to the types of the triggers.

Figure 4.16 shows a chart of the integrated luminosity for the Run I period. The leptoquark analysis presented in this thesis uses both the Run IA and IB data samples, with $\bar{p}p$ center of mass beam energy at 1.8 TeV . We do not use the Run IC data in the analysis presented in this thesis. The data loss (the difference between shaded area and the solid area) is due to the delay between the beam delivery and detector start-up, or technical error on the data

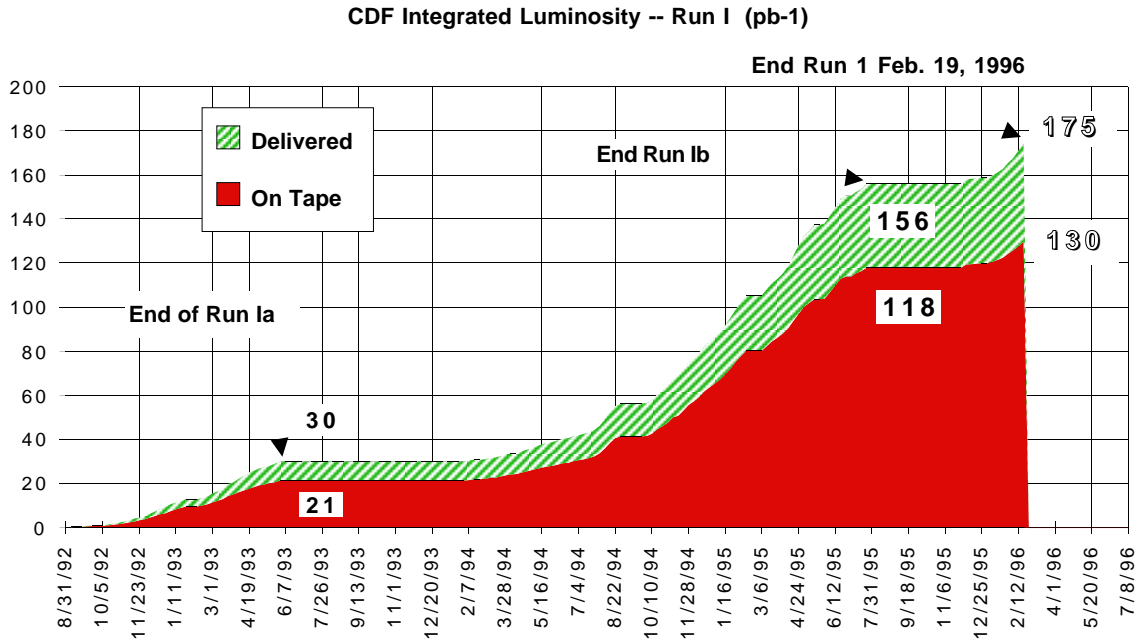


Figure 4.16: CDF Run I integrated luminosity chart. The Run I is divided into 3 subdivisions: IA ($\sim 6/7/93$) and IB ($\sim 7/31/95$) at $\sqrt{s} = 1.8$ TeV, and IC (\sim end of 95) at $\sqrt{s} = 630$ GeV.

processing. At off-line, we then select the “good” runs for data analysis³. Out of 118 pb^{-1} of data written on the tape, we use a total integrated luminosity of 109 pb^{-1} for the second generation leptoquark analysis.

³At CDF, the *bad* runs refer to the runs which had did not have all the detector elements were not functioning correctly.

Chapter 5

A Second Generation Leptoquark Search at CDF

5.1 Introduction

In this Chapter, a search for pair produced second generation leptoquarks, LQ_2 , decaying into dimuon and dijet, based on the data samples collected at Collider Detector at Fermilab during the 1992-93 and 1994-95 Tevatron runs is presented. A search was made for high traverse momentum (p_T) dimuon events to identify possible candidates. Using the most recent Next-to-Leading Order calculation for the leptoquark pair production cross section [1], the lower mass limit for second generation leptoquarks is set ¹.

In this search, we use the 109 pb⁻¹ integrated luminosity from Run IA+B data samples at CDF. We will first explain the data samples used, then two muon event selection method in Section 5.2. In Section 5.3 we define the event selection cuts to identify possible candidate events and distributions for those events are also shown. In Section 5.4 final event selections, the cosmic ray veto and LQ_2 mass constraints cut are explained. In Section 5.5, we explain the signal detection efficiencies and show the numerical results. Section 5.6 will list the possible backgrounds and their calculation method. The signal systematic uncertainty is also reported in this section. In Section 5.7 we describe the experimental cross section calculation method

¹This is documented as a CDF internal note [84].

and present a preliminary limit for second generation leptoquark.

5.2 Data Samples and Pre-Selection Criteria

We first define loose criteria to select dilepton events from the entire event samples to reduce the amount of the data samples². This is called the *pre-selection* of the data sample, which will be followed by more strict event selection (see Section 5.3). In this Section, we describe the *pre-selection* of the event sample.

We first ask for events with at least two muons (for Run IA pre-selection) or two leptons (for Run IB pre-selection). Muons are detected by looking at the Central Tracking Chamber (CTC) tracks (ref. Section 4.3.4), and we use the traverse momentum p_T measured by the CTC for a minimum momentum criteria.

For muon fiducial criteria, we also use muon chamber (CMU, CMP, and CMX. See Section 4.5) information to match the CTC tracks. To match CTC tracks with muon chamber stubs, the extrapolated CTC track is transformed to muon chamber local wedge coordinates. The CTC track in the muon chambers is described by two straight lines. The difference between the fit parameters (slope and intercept in each of the two planes) for the CTC track and the muon chamber stub gives the quality of the match. These quantities define the fiducial quantities $\Delta x(CMU)$, $\Delta x(CMP)$, and $\Delta x(CMX)$ for Central Muon Chamber (CMU), Plug Muon Chamber (CMP), and Muon Extension Chamber (CMX) respectively.

5.2.1 Run IA data pre-selection

The Run IA dimuon data sample³ corresponds to an integrated luminosity of 18.82 ± 0.68 pb⁻¹ [87]. At this stage, loose muon selection criteria are applied to select two muons, namely 1st and 2nd leg muons. The 1st muon has higher p_T by definition and also the selection criteria for the 1st muon is tighter.

The selected muon data must pass the following criteria.

²These dilepton events have been selected within the CDF collaboration [85, 86] for Run IA+B.

³The data sample is made within the CDF electroweak group. It occupies 10 exabyte cassettes, or about 30 GigaBytes.

- 1st leg muon
 - $p_T > 18$ GeV/ c , measured by the CTC.
 - Energy deposited in the Electromagnetic (EM) Calorimeter < 2 GeV; consistent with a minimum ionising particle measured by Central Electromagnetic Calorimeter (CEM).
 - Energy deposited in the Hadronic (HAD) Calorimeter < 6 GeV; measured by the Central Hadronic Calorimeter (CHA).
 - Fiducial cut. The extrapolated track from the CTC is required to fall within the CMU or both the CMU and and the CMP fiducial region, depending on whether there is a hit in the CMU or both the CMU and CMP. It can be defined as;
 - * CMU ($\Delta x(CMU) \leq 2.5$ cm),
 - * CMP ($\Delta x(CMP) \leq 10.0$ cm), or
 - * CMX ($\Delta x(CMX) \leq 8.0$ cm).
- 2nd leg muon with $p_T > 15$ GeV/ c .

This sample consists of 5444 events.

5.2.2 Run IB data pre-selection

We use the full Run IB dilepton samples corresponding to an integrated luminosity of 88.57 ± 7.09 pb⁻¹ ⁴. The data selection was initially made for dilepton events. We apply following pre-selection cuts to select inclusive dimuon samples:

- A central muon with $p_T > 18$ GeV/ c , measured by CTC.
- EM Energy < 2 GeV.
- HAD Energy < 6 GeV.

⁴This data sample was originally made within the CDF collaboration [86] as high p_T dilepton samples. The total integrated luminosity for Run IB is 90.22 pb⁻¹ and a total of 88.57 ± 7.09 pb⁻¹ [87] corresponds to runs for which the muon chambers were functioning. These events are kept on disk [88] and are accessible to CDF members.

- Fiducial cut. The CTC track of the muon must match with
 - CMU ($\Delta x(CMU) \leq 4.0 \text{ cm}$),
 - CMP ($\Delta x(CMP) \leq 8.0 \text{ cm}$), or
 - CMX ($\Delta x(CMX) \leq 8.0 \text{ cm}$).
- E(Isolation) < 2 GeV. E(Isolation) is defined as $E_T(\text{cone } 0.4) - E_T(\text{muon tower})$ measured by calorimeter. This requires the muon to be well isolated from other jets and electromagnetic showers.

This sample contains $\sim 25K$ events⁵.

There are small differences on the pre-selection setting between Run IA and IB because they were processed using different type of filtering procedure, for example, in the muon stab matchings. However the final event selection criteria for the analysis are tighter than the pre-selection filtering therefore it does not effect on the final event candidate for high p_T dimuon events.

5.3 Event selection criteria

From the pre-selected dilepton event sample, we first look for events with two muons which pass the *muon quality* cuts (muon ID). After we select events with two “good” muons, we will then apply additional criteria for the final event selection of LQ_2 candidate events. In this Section, the muon kinematics from both data and leptoquark Monte Carlo simulation are shown. From this, we decide the values for various cuts to select good muons. Then we describe the muon selection method, followed by other event topology criteria.

5.3.1 Muon kinematics study

We study both the data samples and Monte Carlo to decide the cut values for muon and jet selections. PYTHIA [10] is a general physics simulation package (we used v5.7) together

⁵The total number of events is counted after removing the duplicated events at the filtering.

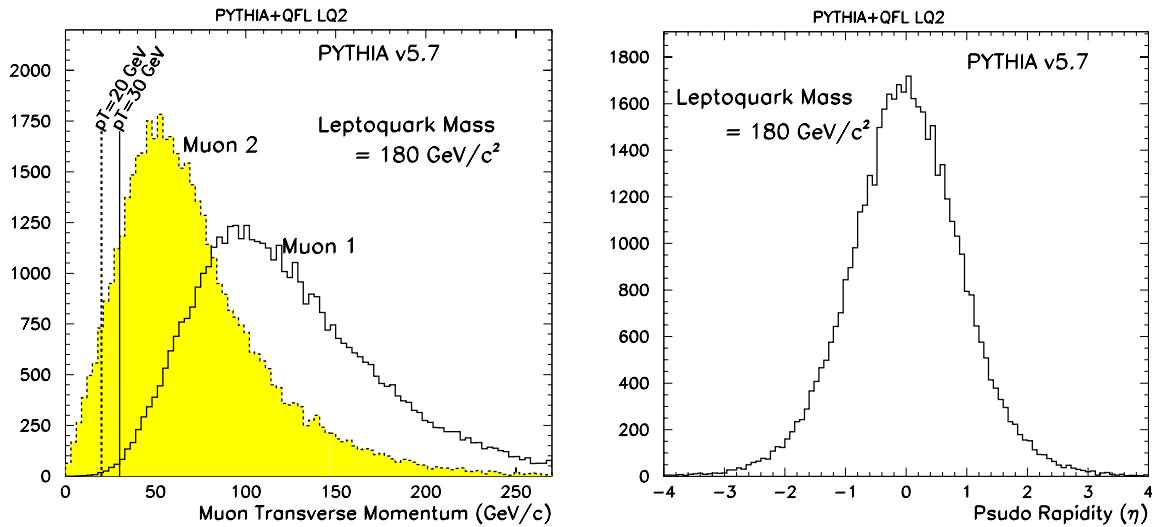


Figure 5.1: LQ_2 muon kinematic distribution. Traverse momentum (left) and rapidity (right). For the muon rapidity, only one of the LQ_2 is plotted per event since two distributions are identical. The MC sample is from LQ_2 mass at $180 \text{ GeV}/c^2$. Plotted data is after reconstruction. No cuts are applied. PYTHIA+QFL (CTEQ4).

with the QFL [11] fast CDF detector simulation program. Throughout this analysis, we used PYTHIA+QFL Monte Carlo simulation unless noted otherwise.

Figure 5.1 shows the muon p_T and the rapidity distribution of muons decaying from generated leptoquarks for a leptoquark mass at $180 \text{ GeV}/c^2$. This mass value was chosen to be consistent with the previous and currently on-going analysis (see Section 3.5.3). However, we have generated the leptoquark mass in the range $100 \text{ GeV}/c^2$ to $240 \text{ GeV}/c^2$ to study its kinematics. We decided on the muon kinematic cuts optimising to the mass region between $180 \text{ GeV}/c^2$ to $220 \text{ GeV}/c^2$.

The `tight` and `loose` cut values described in Section 5.3.3 have been defined by studying those distributions.

5.3.2 Other muon distributions

We impose other muon quality criteria such as

- ▷ Limit on the energy deposit in the calorimeter for being consistent with a minimum ionising particle,

- ▷ The muon track, as measured by the CTC is extrapolated to the position of the muon chamber. The closest stub position that matches the track should be within a certain distance perpendicular to the radial direction.
- ▷ Two muon vertices to be within certain distance to make sure that they are associated with the same interaction point. We compare the muon tracks from the CTC with the event vertex information from the VTX.
- ▷ The Z vertex of the interaction should be within the fiducial volume of the detector.
- ▷ High p_T muons should be well isolated. We define a cone of $\Delta R = 0.4$ in $\eta - \phi$ space ($\Delta R = \sqrt{\phi^2 + \eta^2}$). The Isolation is defined by

$$Isolation = E_t(0.4) - E_t \quad (5.1)$$

where $E_t(0.4)$ is the energy from the calorimeter clusters within the cone and E_t is the transverse energy in the muon tower.

Figures 5.2 to 5.8 show the distributions described above, both from the data sample and from the Monte Carlo. The data sample contains both Run IA and IB events, after the pre-selection (see Section 5.2 for pre-selection cut values) has been applied. The leptoquark Monte Carlo samples are generated for a leptoquark mass at $180 \text{ GeV}/c^2$. In these Figures both the first muon hitting Central Muon Chamber (defined as CMUO muon.) by transverse momentum and all CMUO muons are plotted. Note that some plots are in a logarithm scale while others are in a linear scale. The applied criteria values are also marked with dashed lines.

5.3.3 Muon selection

For selecting two muon tracks, we define the following two muon selection definitions :

1st leg muon: A muon track from the CTC that matches with a stub in the fiducial region of the central muon detector (CMU or CMU/CMP), and passing **tight** muon cuts described below.

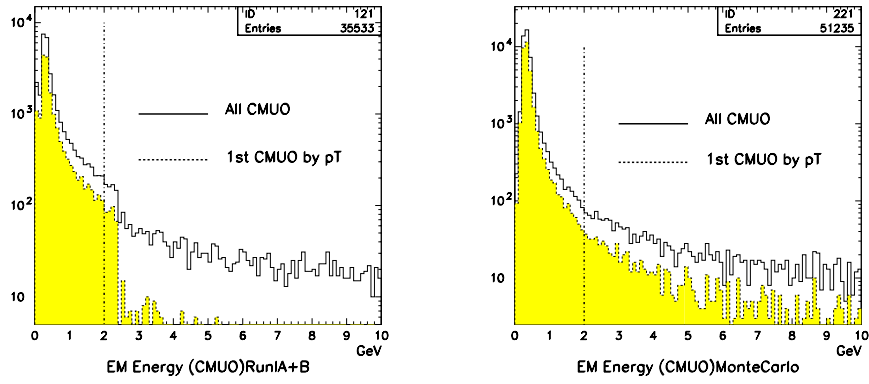


Figure 5.2: Energy deposited in the Electromagnetic Calorimeter from CMUO muon tracks.

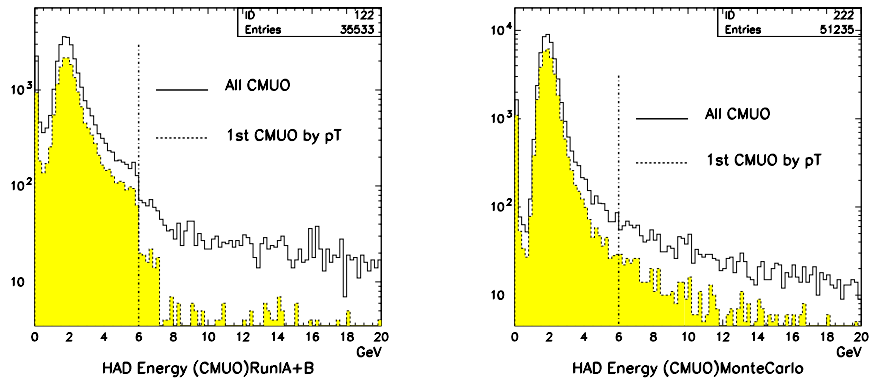


Figure 5.3: Energy deposited in the Hadronic Calorimeter from CMUO muon tracks.

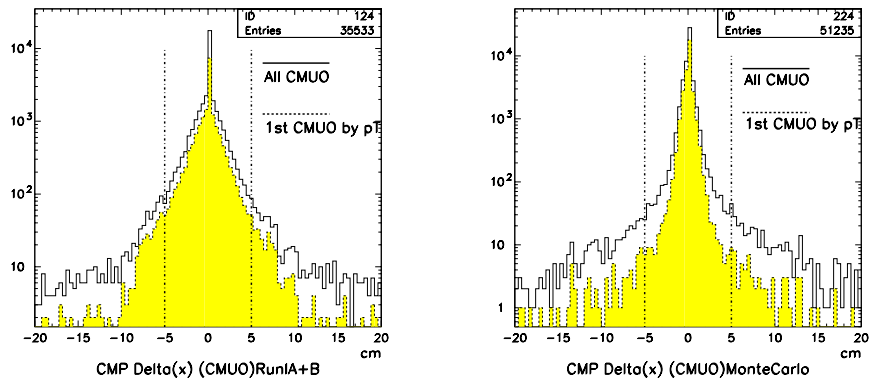


Figure 5.4: Distribution for $\Delta x(CMP)$ of CMUO.

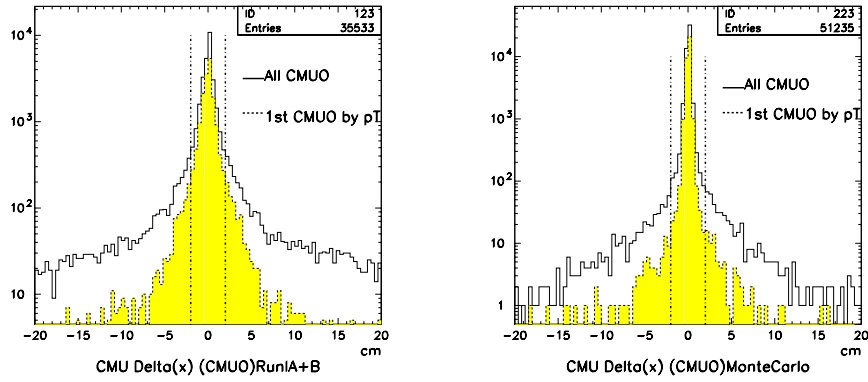


Figure 5.5: Distribution for $\Delta x(CMU)$ of CMUO.

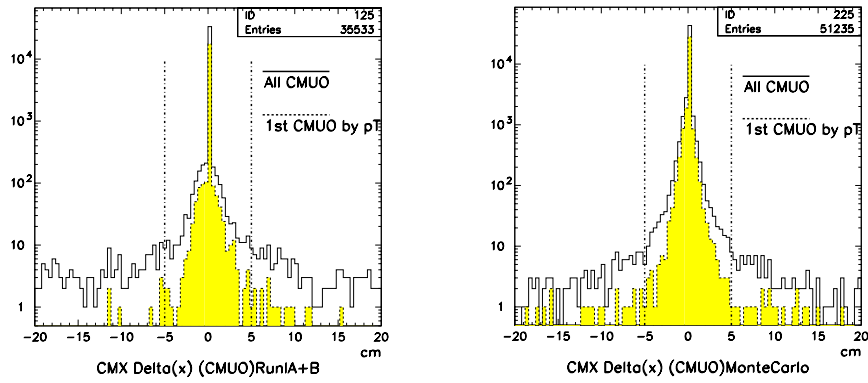


Figure 5.6: Distribution for $\Delta x(CMX)$ of CMUO.

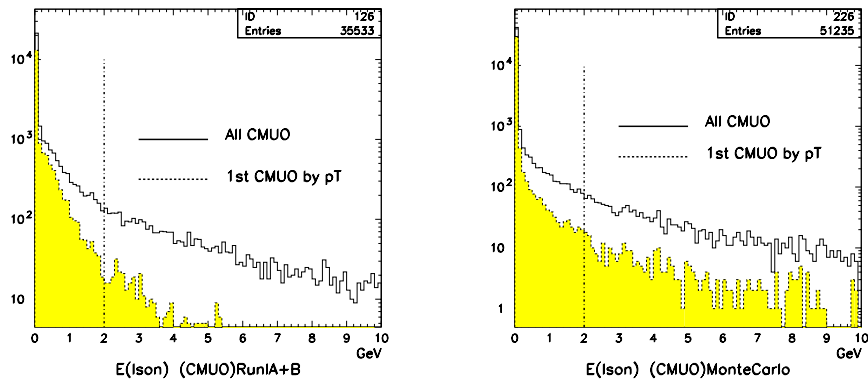


Figure 5.7: Distribution for muon isolation, defined by $E_{Iso} = E_t(0.4) - E_t$ (Equation 5.1).

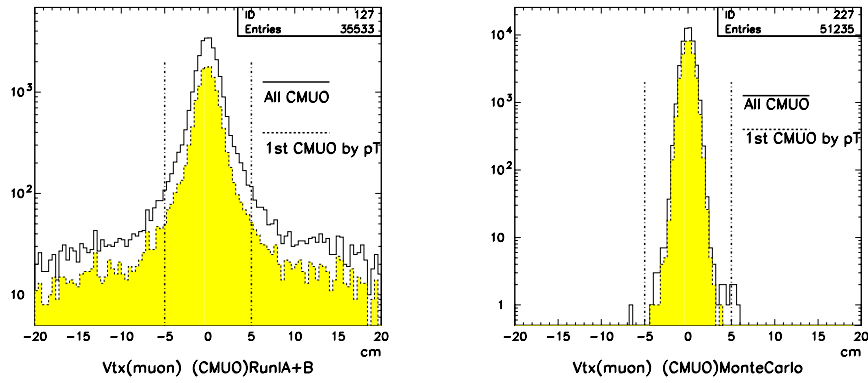


Figure 5.8: Distribution for difference of the muon track vertex and the event vertex found by VTX.

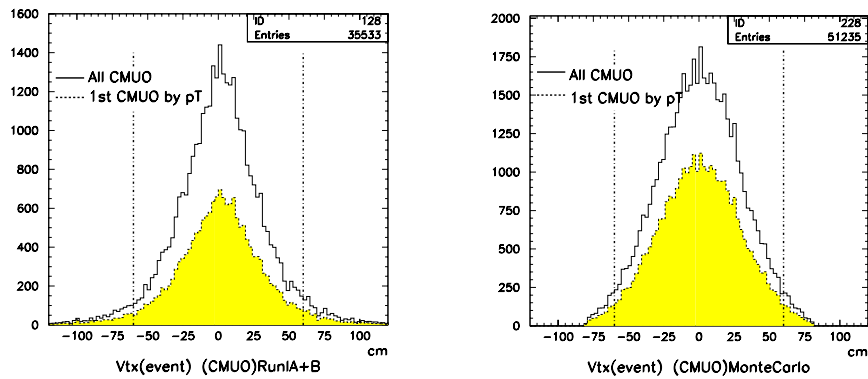


Figure 5.9: Event vertex distribution.

2nd leg muon: A muon track from the CTC which does not necessary matches with a stub in the central muon chambers, passing the `loose` muon cuts.

Tight muon selection

The 1st muon selection is required to pass `tight` selection criteria. The muon kinematic criteria values are optimised from Monte Carlo studies (see Section 5.3.1 for the muon kinematic distributions). It is required to be a CMUO type muon (hitting the CMU or CMU/CMP muon chambers) and is required to satisfy the following criteria:

- ▷ $p_T > 20$ GeV/ c . Use beam constrained value. If beam constraint fails, use non beam constrained p_T .
- ▷ E_{EM} (Energy deposited in electromagnetic calorimeter) < 2 GeV.
- ▷ E_{HAD} (Energy deposited in hadronic calorimeter) < 6 GeV.
- ▷ The track from CTC must match with the CMU stub perpendicular to the radial direction, $|\Delta x(CMU)| < 2$ cm.
- ▷ The track from CTC must match with the CMP stub if there is CMP confirmation. $|\Delta x(CMP)| < 5$ cm.
- ▷ Muon Z vertex cut. Require the matching between the track Z and the closest vertex given from VTX (ref. 4.3.3) information. $\min|\Delta(Z_\mu - Z_{VTX})| < 5.0$ cm.
- ▷ Event vertex cut. The closest Z vertex to the muon Z vertex from VTX must be within 60 cm from the center of the detector: $|Z_{VTX(min)}| < 60.0$ cm.
- ▷ Fiducial cut: The track from the CTC must fall into the good fiducial region of CMU (if no CMP confirmation) or either CMU or CMP (if there is CMP confirmation).
- ▷ Isolation cut: The E_T sum of all towers measured by the calorimeter within the 0.4 cone in $\eta - \phi$ space of the muon track must be less than 2 GeV.

The muon passing these `tight` cuts with the highest p_T is taken to be 1st leg muon.

Loose muon selection

The 2nd leg muon can be a loose muon (which also contains tight muons), which then can be either a CMUO or CMIO type of muon. A CMIO muon is associated with a muon track detected by the CTC but with no matching with Muon Chambers. Since the CMIO does not require a hit on the muon chamber stub, we do not require a fiducial selection for the loose muon.

- ▷ $p_T > 20 \text{ GeV}/c$.
- ▷ $E_{EM} < 2 \text{ GeV}$.
- ▷ $E_{HAD} < 6 \text{ GeV}$.
- ▷ Muon Z vertex cut. $\min|\Delta(Z_\mu - Z_{VTVZ})| < 5.0 \text{ cm}$.
- ▷ Event Z vertex cut. $|Z_{VTVZ}| < 60.0 \text{ cm}$.
- ▷ For a CMIO type muon, the CTC exit radius must be less than 103.6 cm . Since CMIO muons have no matching stub in any muon chamber we require the track to traverse a minimum radial distance in the CTC to have a quality track.

A muon passing the above cut with the highest p_T , excluding the 1st leg muon, is defined as a 2nd leg muon. Events with one tight CMUO and one loose CMUO is defined as CMUO-CMUO events, whereas events with one tight CMUO and one CMIO are defined as CMUO-CMIO events.

The table 5.1 summaries the muon selection criteria and the differences of pre-selection and selection requirements. From this Table, one can see that the final muon selection criteria are tighter than both pre-selections. The final muon selection also imposes additional criteria.

We then apply a muon p_T cut, $\max(p_T(\mu_1), p_T(\mu_2)) > 30 \text{ GeV}/c$, that is one of the selected muons must have $p_T > 30 \text{ GeV}/c$. This cut is applied to reject any possible low mass backgrounds such as $Z \rightarrow \tau^+\tau^-$ or $\bar{b}b$ while keeping a good efficiency for a signal since the LQ_2 mass limit was set above $180 \text{ GeV}/c^2$ from the previous analysis at CDF [8].

Type of Criteria	Pre-Selection		Final Selection
	Run IA	Run IB	
$p_T(\mu_1)$	$> 18\text{GeV}/c$	$> 18\text{GeV}/c$	$> 30\text{GeV}/c$
$p_T(\mu_2)$	$> 15\text{GeV}/c$	$> 15\text{GeV}/c$	$> 20\text{GeV}/c$
$E_{HAD}(\mu_1)$	$< 6\text{ GeV}$	$< 6\text{ GeV}$	$< 6\text{ GeV}$
$E_{EM}(\mu_1)$	$< 2\text{ GeV}$	$< 2\text{ GeV}$	$< 2\text{ GeV}$
$ \Delta x(CMU)_{\mu_1} $	$< 2.5\text{ cm}$	$< 4.0\text{ cm}$	$< 2.0\text{ cm}$
$ \Delta x(CMP)_{\mu_1} $	$< 10.0\text{ cm}$	$< 8.0\text{ cm}$	$< 5.0\text{ cm}$
$E_{iso}(\mu_1)$		$< 2\text{ GeV}/c$	$< 2\text{ GeV}/c$
tight muon fiducial cut for μ_1	no	no	yes
$E_{HAD}(\mu_2)$			$< 6\text{ GeV}$
$E_{EM}(\mu_2)$			$< 2\text{ GeV}$
$\min \Delta(Z_{\mu_1} - Z_{VTVZ(i)}) $			$< 5\text{ cm}$
$ Z_{VTVZ}(\mu_1) $			$< 60\text{ cm}$
CTC exit radius for CMIO			$< 103.6\text{ cm}$

Table 5.1: Muon pre-selection and selection criteria.

5.3.4 Event topology cut

Figure 5.10 shows the dimuon invariant mass distribution from the data, after muon cuts are applied. These events are dominated with $Z^0 \rightarrow \mu^+\mu^-$ events.

After two muons are selected, we then apply event selections in order to eliminate any possible background while rejecting the minimum number of possible event candidates.

Duplicated events and bad run removal Any duplicated events and runs on the bad run list are removed⁶.

2 jet cut LQ_2 particles decaying in dimuon + dijet channels should have well defined high p_T muons and high E_T jets. By requiring two jets in a dimuon event, we can reduce backgrounds such as $Z \rightarrow \mu\mu$. We require 2 jets, with $E_T(\text{jet } 1) > 30\text{ GeV}$ and $E_T(\text{jet } 2) > 15\text{ GeV}$, respectively. Both jets are required to satisfy $|\eta| < 2.4$. These cuts are applied on the raw jet E_T ⁷ and a cone of 0.7 in $\eta - \phi$ space.

Invariant mass cut The major background for this analysis comes from Drell-Yan processes in which the Z^0 decays into the dimuon channel with ≥ 2 jets resulting from gluon

⁶This is due to tape reading errors occurring during the event pre-selection.

⁷The raw jet energy refers to the energy deposited in the calorimeters without any offline corrections according to geometrical responses of the apparatus.

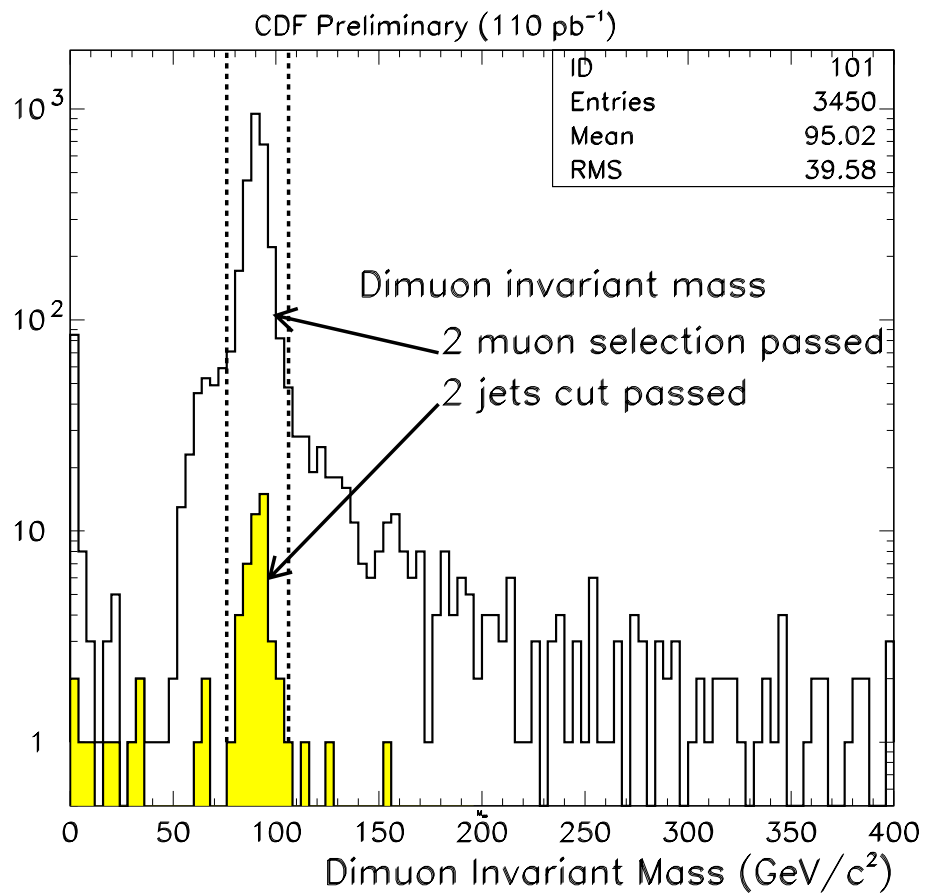


Figure 5.10: Dimuon invariant mass from Run IA+B. Solid line is the dimuon invariant mass distribution with events passing the muon selection cuts. Shaded line indicates the events that passed 2 jet requirement.

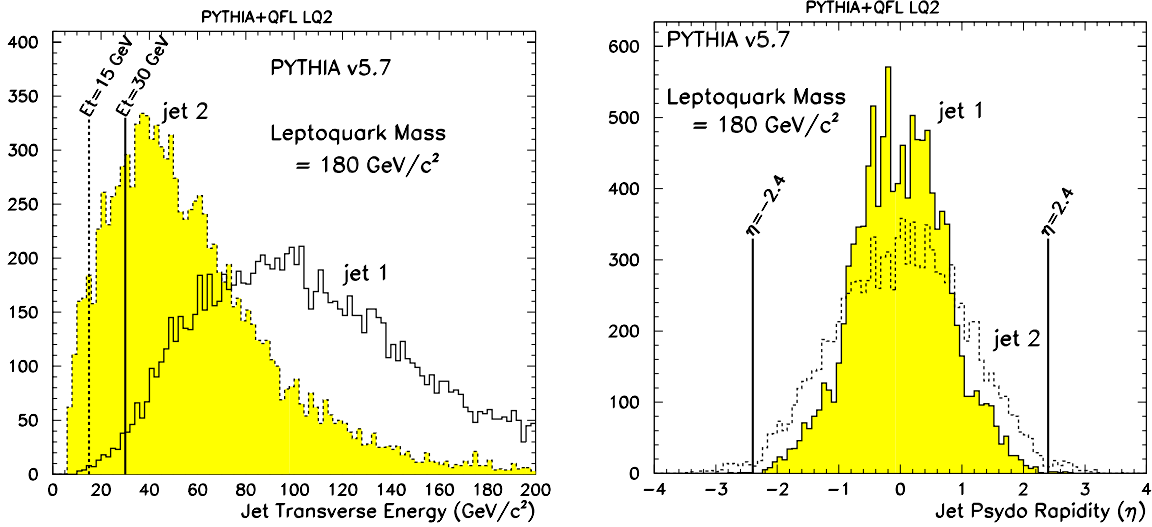


Figure 5.11: Kinematic distribution of jets emerging from the LQ_2 decay. Mass of LQ_2 is at $180 \text{ GeV}/c^2$. Events shown here have passed the muon quality cuts. PYTHIA+QFL.

radiation. We reject events in the Z^0 invariant mass region, $76 < M_{\mu\mu} < 106 \text{ GeV}/c^2$. We also remove events with $M_{\mu\mu} < 11 \text{ GeV}/c^2$ to remove resonances from heavy flavour meson decays such as J/ψ or Υ .

Figure 5.11 shows the p_T and pseudorapidity distributions of the leptoquark jets using the Monte Carlo generator with the CTEQ4 structure function, for the events which passing the muon cuts.

5.3.5 Event cut statistics

Table 5.2 and Table 5.3 show the muon selection statistics for CMUO-CMUO and CMUO-CMIO types of events.

Table 5.4 shows the number of events passing the final event selections. A total of 11 events survive the selection criteria and remain as possible candidates satisfying the event topology criteria of the second generation leptoquarks.

There are two possible combinations of the LQ_2 invariant mass reconstruction from 2 muons and 2 jets in the final states. We take the combination of the two LQ_2 masses in which the difference of 2 reconstructed LQ_2 invariant mass is smaller, since the LQ_2 pair is assumed

Type of cut	# of events passed	
Total number of events	5444	
Total number of CMUO ≥ 1	3964	
$p_{T\mu_1} > 20 \text{ GeV}/c$	2951	
$E(\text{HAD})_{\mu_1} < 6 \text{ GeV}$	2685	
$E(\text{EM})_{\mu_1} < 2 \text{ GeV}$	2663	
$ \Delta x(\text{CMU})_{\mu_1} < 2 \text{ cm}$	2468	
$ \Delta x(\text{CMP})_{\mu_1} < 5 \text{ cm}$	2381	
$\min \Delta(Z_{\mu_1} - Z_{\text{VTVZ}(i)}) < 5 \text{ cm}$	1941	
$ Z_{\text{VTVZ}(\mu_1)} < 60 \text{ cm}$	1842	
tight muon fiducial cut for μ_1	1809	
$E_{\text{iso}(\mu_1)} < 2 \text{ GeV}/c$	1188	
	CMUO-CMUO	CMUO-CMIO
$N(\text{CMUO}) \geq 2$	723	
$N(\text{CMIO}) \geq 1$		453
$p_{T\mu_2} > 20 \text{ GeV}/c$	628	422
$E(\text{HAD})_{\mu_2} < 6 \text{ GeV}$	606	365
$E(\text{EM})_{\mu_2} < 2 \text{ GeV}$	584	345
$\min \Delta(Z_{\mu_2} - Z_{\text{VTVZ}(i)}) < 5 \text{ cm}$	522	317
$ Z_{\text{VTVZ}(\mu_2)} < 60 \text{ cm}$	522	317
CTC exit radius $< 103.6 \text{ cm}$ (CMIO only)		194

Table 5.2: Run IA Muon cut statistics.

Type of cut	# of events passed	
Total number of events	25490	
Total number of CMUO ≥ 1	18684	
$p_{T\mu_1} > 20 \text{ GeV}/c$	15280	
$E(\text{HAD})_{\mu_1} < 6 \text{ GeV}$	14820	
$E(\text{EM})_{\mu_1} < 2 \text{ GeV}$	14410	
$ \Delta x(\text{CMU})_{\mu_1} < 2 \text{ cm}$	13533	
$ \Delta x(\text{CMP})_{\mu_1} < 5 \text{ cm}$	13324	
$\min \Delta(Z_{\mu_1} - Z_{\text{VTVZ}(i)}) < 5 \text{ cm}$	9250	
$ Z_{\text{VTVZ}(\mu_1)} < 60 \text{ cm}$	8661	
tight muon fiducial cut for μ_1	8513	
$E_{\text{iso}(\mu_1)} < 2 \text{ GeV}/c$	5656	
	CMUO-CMUO	CMUO-CMIO
$N(\text{CMUO}) \geq 2$	3552	
$N(\text{CMIO}) \geq 1$		1968
$p_{T\mu_2} > 20 \text{ GeV}/c$	3049	1844
$E(\text{HAD})_{\mu_2} < 6 \text{ GeV}$	2909	1573
$E(\text{EM})_{\mu_2} < 2 \text{ GeV}$	2790	1436
$\min \Delta(Z_{\mu_2} - Z_{\text{VTVZ}(i)}) < 5 \text{ cm}$	2529	1307
$ Z_{\text{VTVZ}(\mu_2)} < 60 \text{ cm}$	2526	1302
CTC exit radius $< 103.6 \text{ cm}$ (CMIO only)		911

Table 5.3: Run IB Muon cut.

Type of cut	Run 1A	Run IB
Total number of events after muon cut	716	3437
Duplicated events removal	716	3374
Bad runs	601	3208
p_T of one of $\mu > 30$ GeV/ c	559	2960
2 jet cuts	104	833
$E_T(\text{jet 1}) > 30$ GeV	21	141
$E_T(\text{jet 2}) > 15$ GeV	7	57
Invariant Mass cut	1	10

Table 5.4: Event cut statistics.

Run #	Evt #	$M_{\mu\mu}$	M_{LQ1}	M_{LQ2}	μ_{1PT}	μ_{2PT}	j1 E_T	j1 η	j2 E_T	j2 η
46492	200434	18.9	93.4	52.8	34.2	24.8	49.3	1.6	22.3	-0.3
60998	535375	114.8	175.1	35.9	146.1	21.6	103.5	-0.8	34.5	-2.0
63078	25391	61.0	79.1	55.2	38.7	24.1	50.0	-0.3	32.3	0.9
63719	31054	153.8	273.4	217.7	96.3	49.5	54.5	-2.4	44.6	1.7
63883	187651	66.0	76.2	73.1	33.1	30.4	40.9	-0.3	42.0	-1.0
65471	47719	34.9	110.9	86.8	22.3	30.9	200.8	-0.1	89.2	0.1
68444	163722	127.9	272.5	92.0	30.9	139.1	101.3	0.1	40.4	1.7
68685	596595	30.3	145.8	51.2	36.1	57.8	68.7	-1.6	22.3	1.7
69760	26273	66.8	37.0	35.8	46.8	23.8	42.9	-0.7	27.6	0.0
70000	27755	23.5	65.9	55.2	40.2	22.4	38.8	-0.7	18.1	0.3
71022	466439	35.3	99.2	58.7	32.1	27.2	38.8	1.9	23.5	-1.4

Table 5.5: LQ_2 candidates from Run IA and IB.

to have equal mass.

Figure 5.12 shows the invariant mass distribution of dimuon events with high E_T jets which pass the event selections and Table 5.5 presents the kinematic information for each of the 11 events.

CDF event display from candidate events

Figure 5.13 shows the CDF event display from one of the high mass LQ_2 event candidates. The event shown is Run 63719 Event number 31054, from Run IB. Two muon tracks are found in the CTC display as straight tracks, and two jets are clearly identified in the calorimeter towers.

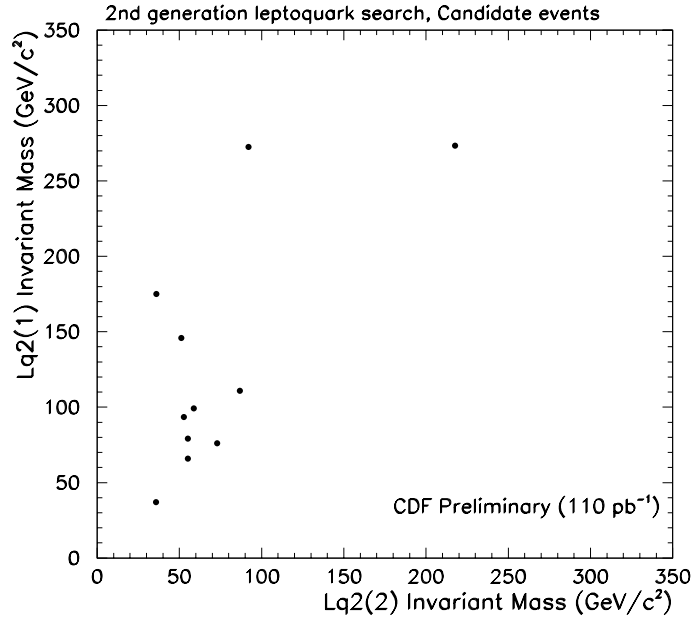


Figure 5.12: Mass distribution of the LQ_2 candidate events. $LQ_2(1)$ v.s. $LQ_2(2)$. $M_{LQ}(1) > M_{LQ}(2)$.

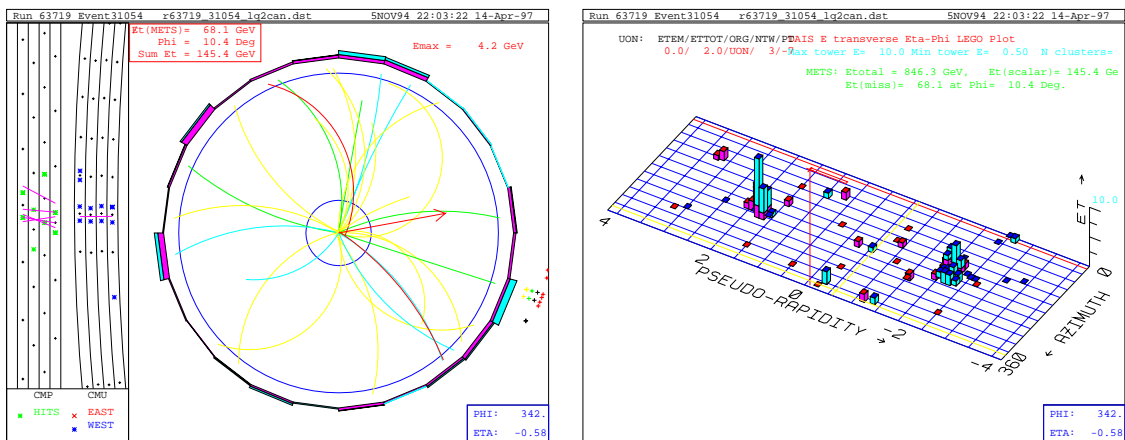


Figure 5.13: CDF event display from the LQ_2 event candidate. Run 63719 Event 31054. CMUO-CMIO event. Two muon tracks are found in the CTC display (left). The calorimeter tower shows two high energy jets (right).

5.4 Cosmic rays and reconstructed mass deviation

In this section, we show the final event selection criteria used in the analysis: cosmic ray rejection and the use of a leptoquark pair mass constraint. High energy muons originating from cosmic rays can fake dimuon events. Any possible events characterised to be cosmic rays should be removed. As a result, we did not find any cosmic candidate events in our final event samples.

We then define the final event selection which is required for the mass balancing of pair produced leptoquarks to select the final event candidates in intervals of nominal mass.

5.4.1 Cosmic ray muons

Cosmic rays are streams of high energy particles originated from the outer space, or those interacting with upper atmosphere of the earth and creating secondary particles with high momenta. Muons have high penetrating characteristics, and can travel down to the detector apparatus. When such high energy muons hit the detector they can fake a dimuon event. Any event with 2 jets in coincidence with such cosmic ray event will give a background to the LQ_2 signal. However removal of the high p_T cosmic muons are possible by studying their characteristics, as described below:

$\Delta\phi$: Cosmic rays emerging from the upper atmosphere should enter the detector from the top and exit to the bottom of the detector⁸. Since the momentum of such muons should be large, it traverses the detector with little effect from the solenoid magnetic field. This will yield the $\Delta\phi$ to be approximately π , that is a *back-to-back* dimuon candidate.

$\Delta\tau$: Particles from $\bar{p}p$ collisions will exit from the detector at apparently the same time regardless of the geometrical direction. However, a cosmic ray muon takes some interval of time to traverse the detector, $\Delta\tau$, which is approximately 20 ns⁹. The muons are detected with the central muon detector (CMU) as well as matching the tracks from the CTC. We use TDC information from the hadronic calorimeter tower transversed by the

⁸In CDF coordinates, in coming cosmic muon should be near $\phi = \pi/2$ and outgoing is at $\phi = 3\pi/2$

⁹We estimate $\Delta\tau \sim 2R/c$ where R is the radius of the CDF detector and c is the speed of light, for relativistic particles. Since we consider only for the high p_T muons ($> 20\text{GeV}/c$), the error is less than 10^{-3} .

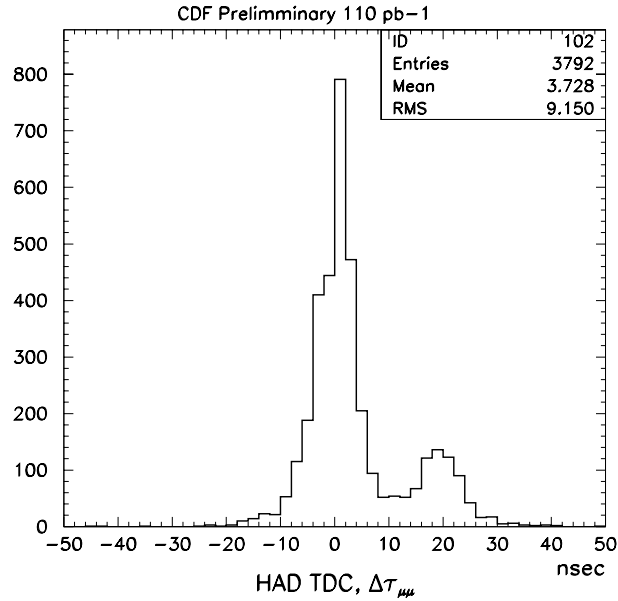


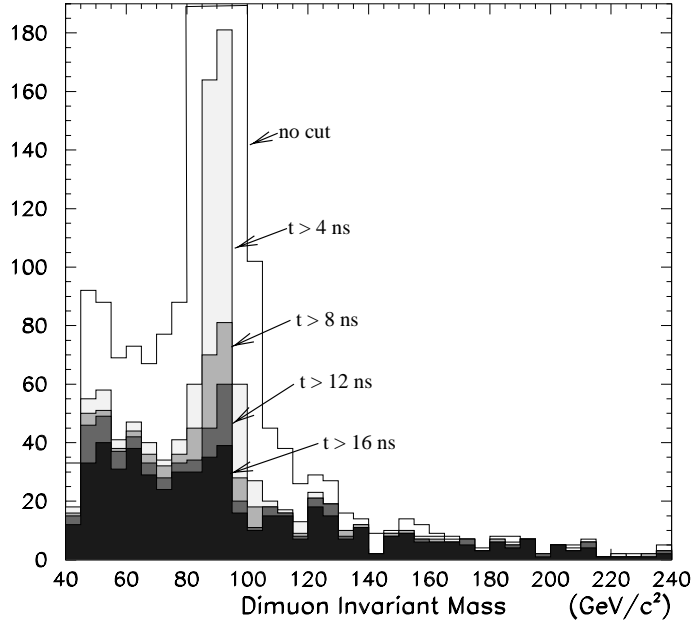
Figure 5.14: Difference of Hadron TDC, $\Delta\tau$ for events with more than two high p_T muons, after muon selection cut. The muon close to the top of the detector is the muon 1 by definition. Run IA+B dimuon samples.

two muons to evaluate $\Delta\tau$. The interaction of the $p\bar{p}$ collision occurs in the middle of the detector, hence $\Delta\tau$ should be zero within the resolution of the TDC.

Vertex: Cosmic ray events have no correlation with spatial or timing of the vertex with the *real* events from $p\bar{p}$ collision. We can study the impact parameter (δ_0) of such events to eliminate the cosmic rays.

To study cosmic ray events, we take the data sample from the dimuon events, after applying dimuon selection criteria. We consider both CMUO-CMUO and CMUO-CMIO dimuon events. The majority of events are from Z^0 decays and significant cosmic background is also present.

Figure 5.14 shows the difference of the TDC for the hadron calorimeter, from the two muons. By definition, the first muon is closer to the *top* of the detector, or $|\phi_\mu - \pi/2|$ is smaller. There are two groups of distribution. The smaller (right) group is possible dimuon events from cosmic rays, where the time elapse between top and bottom hadronic calorimeters is peaked at 20 *ns*. From this figure, we consider a cut at $\Delta\tau > 13$ ns to reject cosmic ray

Figure 5.15: $\Delta\tau_{TDC}$ cut on dimuon events.

events.

However when we study the cosmic muon rejection efficiency we found out that although this cut is efficient, it also removes the “real” muons coming from interactions. We took Z^0 events from dimuon samples, and studied the effect of $\Delta\tau_{TDC}$ cut. If this cut is efficient, it should not eliminate the few Z^0 events appearing in the Z^0 dimuon mass window between 76 to 106 GeV/c^2 . We have varied the cut value of $\Delta\tau_{TDC}$ up to 16 ns, and have plotted the events selected as cosmic ray candidate. Figure 5.15 shows the corresponding plot.

One can see that cutting at 4 ns rejects a large amount of Z^0 . The 12 ns plot indicates that this cut still cuts Z^0 events, and it continues up to 16 ns. From this Figure we conclude that cosmic ray rejection using TDR timing information is not efficient, since an extreme cut value of $\Delta(t) > 16$ ns still rejects Z^0 events.

However we have further investigated on the combined cosmic veto with $\Delta(t)$ and $\Delta(\phi)$ cut. We applied the combination of $\Delta(t)_{TDC} > 13$ ns and $\Delta(\phi)$, or the 3 dimensional opening angle of the dimuon system to be larger than 3.0.

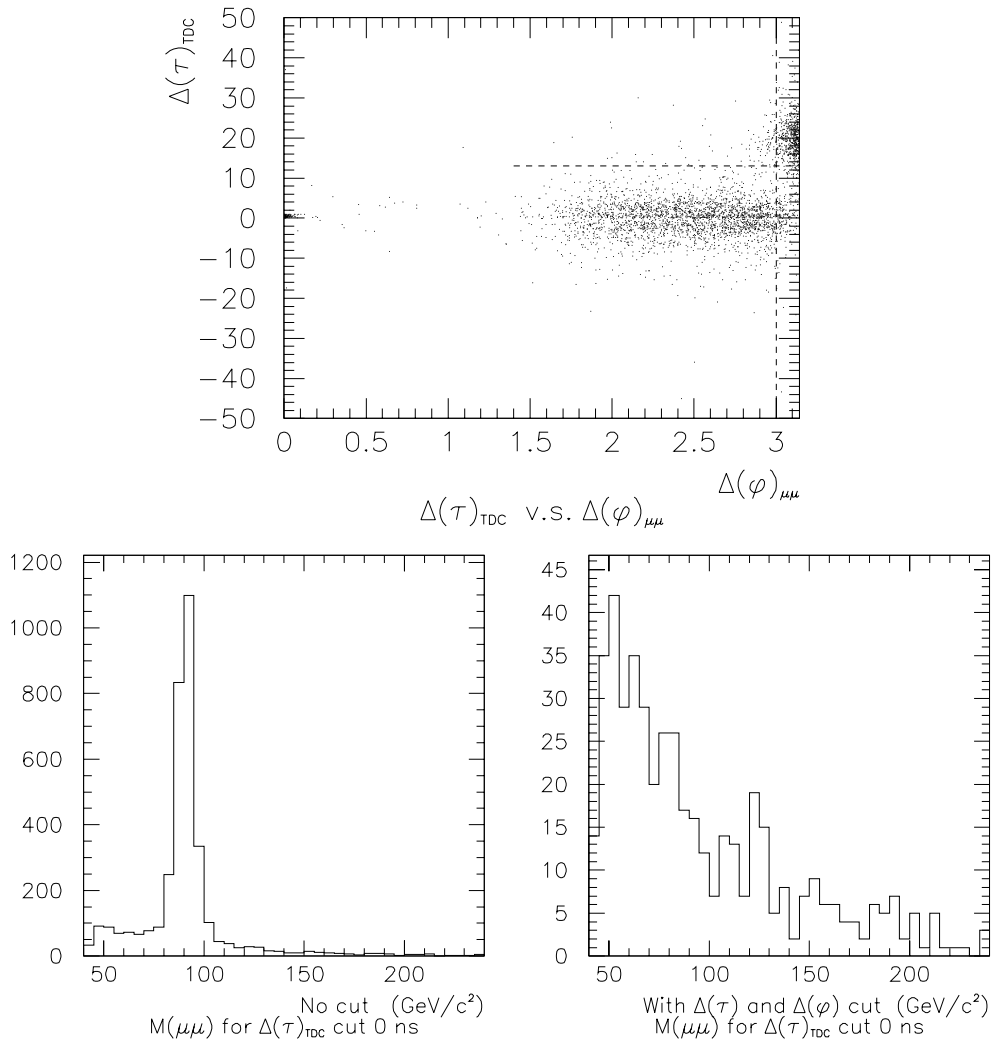


Figure 5.16: Cosmic veto with $\Delta(t)$ and $\Delta(\phi)$ cut. The upper plot indicates the distribution on the $\Delta(t)$ and $\Delta(\phi)$ map. The lower left plot shows the dimuon invariant mass with no cosmic ray veto, while the lower right plot shows the dimuon invariant mass of the events removed with combined $\Delta(t)$ and $\Delta(\phi)$ cut. Data from inclusive high p_T dimuon are used.

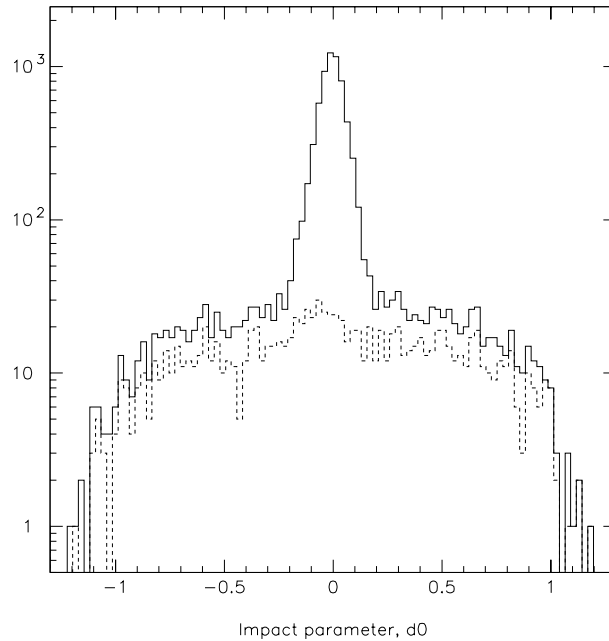


Figure 5.17: Cosmic ray veto effect on the impact parameter. Solid line indicates before the cosmic ray veto with $\Delta(t)$ and $\Delta(\phi)$, while dotted line indicates the events removed by cosmic veto.

Figure 5.16 shows the cut region on the $\Delta(t) - \Delta(\phi)$ map and the result with the cut. One can see that this cut does not remove any Z^0 signals. We can also see the effect of this cut by examining a similar plot for the impact parameter. Figure 5.17 shows the result of this cosmic ray veto on the impact parameter. It indicates the efficient result.

When we apply a two jets requirement on our data sample (111 events remaining), there are no events being vetoed by the cosmic cut. We conclude that this cut is fully efficient to reject cosmic rays.

5.4.2 Reconstructed mass deviation

The final criteria to enhance a possible LQ_2 signal is to apply a mass constraint on the selected event samples. In order to calculate the deviation of the reconstructed leptoquark mass from its true value, we use LQ_2 Monte Carlo samples. The LQ_2 mass distributions are plotted on the Figure 5.18 (left). The right plot shows the expected mass distribution when we partially use the reconstructed 4-momentum. The mass is asymmetric as shown and most of the deviation is due to the reconstruction resolution of the jets. The muon mass reconstruction resolution

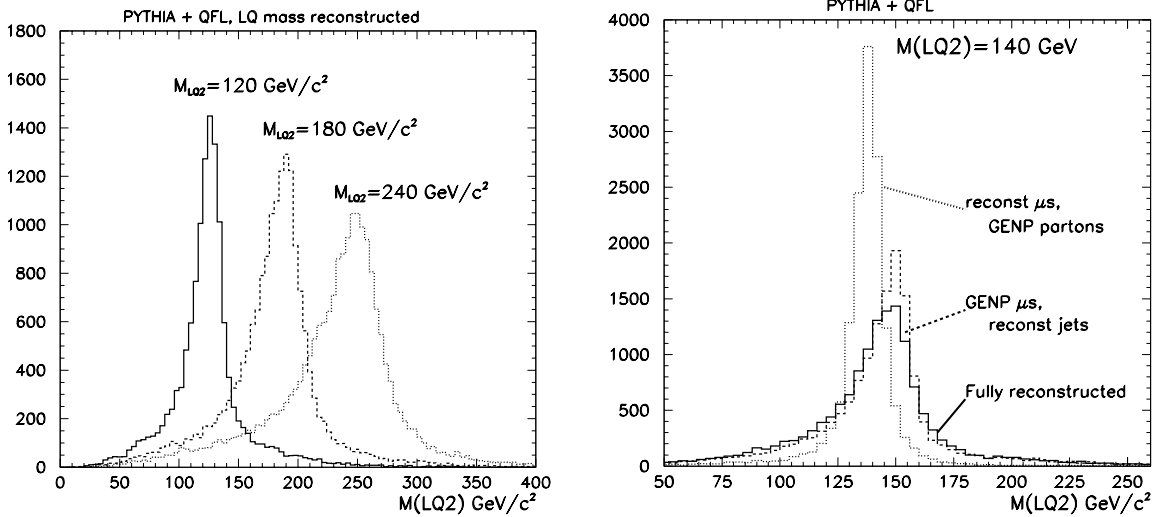


Figure 5.18: (left) LQ_2 reconstructed mass distribution from Monte Carlo samples. Each mass point contain $\sim 30K$ events. The 3σ width is calculated from this distribution. (right) Reconstructed LQ_2 mass distribution for $M(LQ_2)=140\text{GeV}/c^2$. The 3 superimposed plots are the mass spectrums for fully reconstructed, reconstructed jets (muons from GENP bank), and reconstructed muons (jets from GENP parton bank). PYTHIA + QFL.

decreases with increasing p_T .

The LQ_2 mass distributions is fitted to two half Gaussians, to compute the effective deviation for the positive and negative side from the most probable (peak) value for the reconstructed LQ_2 mass. The events must pass all the LQ_2 candidate selection criteria. We also plot the difference of the reconstructed leptoquark pair mass and fit with Gaussian.

Figure 5.19 on top shows the reconstructed mass distribution with the 2 half Gaussian fit and the bottom plot is the distribution of the mass difference of the reconstructed leptoquarks. Deviations from the LQ_2 mass distributions (σ_{high} and σ_{low}) and the mass difference of reconstructed events are quoted in Table 5.6.

We then require $3 \times \sigma_{high}$ for the maximum higher mass deviation value of the LQ_2 mass, and $3 \times \sigma_{low}$ for the maximum lower deviation. The maximum deviation of the difference of the LQ_2 mass pair is $3 \times \sigma_{\Delta}$. The graphical presentation of this configuration is shown on the Figure 5.20.

Figure 5.21 shows the reconstructed LQ_2 mass, plotted as M_2 against M_1 . Note that M_1 is defined to be the reconstructed leptoquark which has the higher invariant mass. The contour

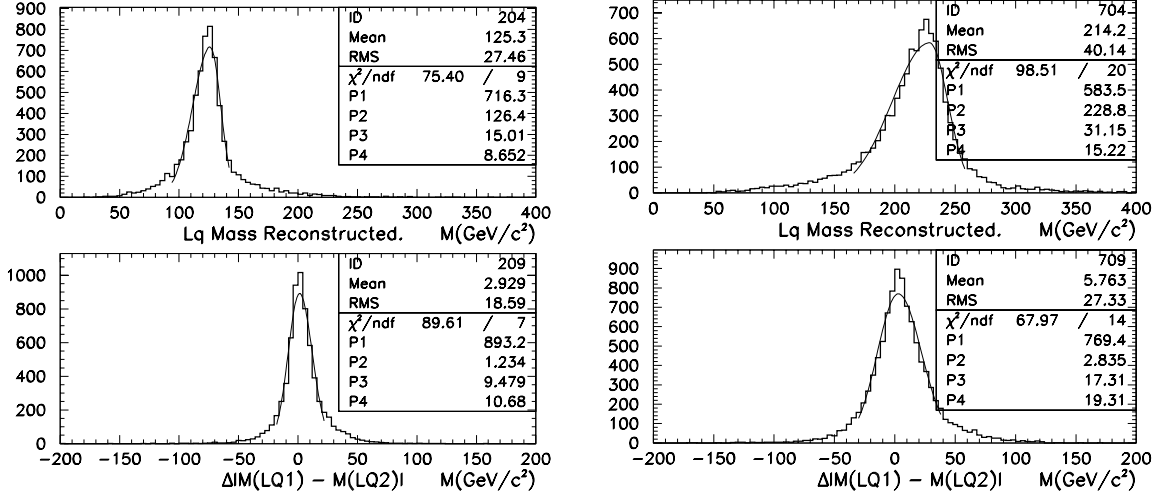


Figure 5.19: LQ_2 reconstructed mass distributions with 2 half Gaussian fit (top), and the distributions of the difference of the two reconstructed LQ_2 mass, $|\Delta(M_1 - M_2)|/2$ (bottom). Shown LQ_2 mass generated are at 120 (left) and 220 (right) GeV/c^2 . PYTHIA+QFL.

LQ_2 mass	σ_{low}	σ_{high}	σ_{Δ}
100	17.9	11.2	12.13
120	21.2	12.2	14.28
140	25.6	12.3	15.57
160	28.5	15.2	17.81
180	32.4	16.8	19.83
200	37.5	18.8	23.19
220	44.1	21.5	25.93
240	46.5	24.1	28.39

Table 5.6: LQ_2 mass and difference of mass deviation for the LQ_2 distribution. Units are all in GeV/c^2 .

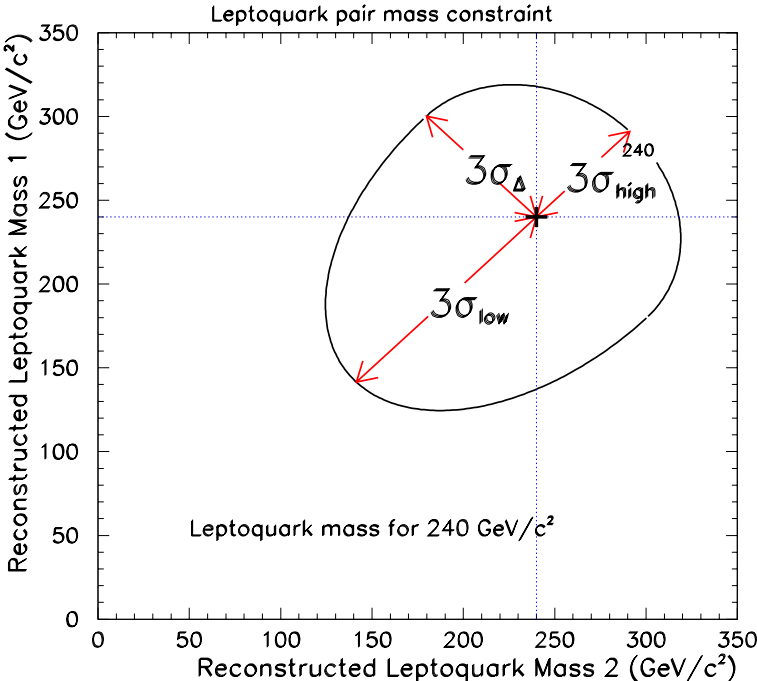


Figure 5.20: The LQ_2 pair mass constraint on the $M_{LQ_2}(2)$ v.s. $M_{LQ_2}(1)$ mapping. Drawn configuration is for $M(LQ_2) = 240 \text{ GeV}/c^2$.

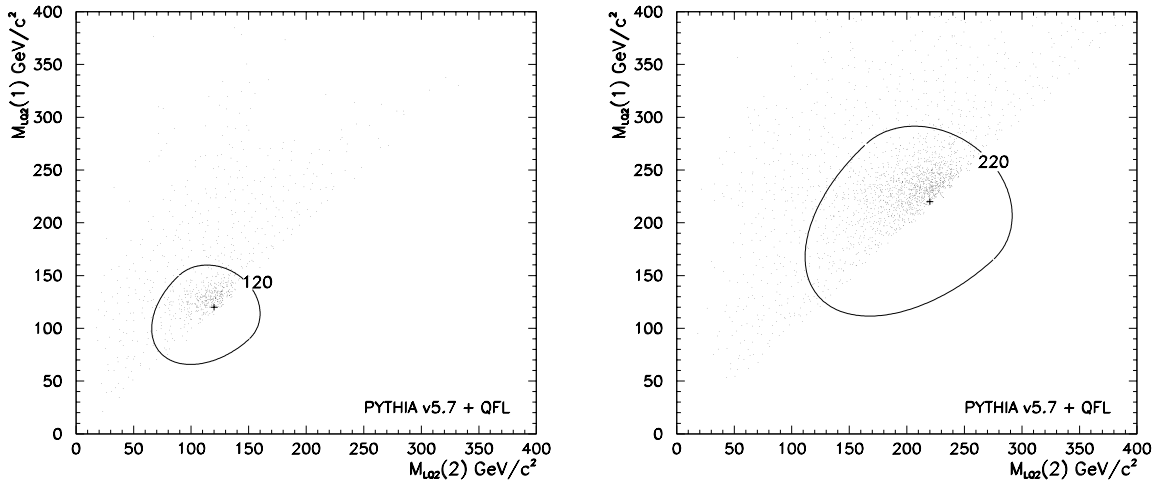


Figure 5.21: The reconstructed LQ_2 invariant mass, $M(1)$ plotted against $M(2)$. By definition, $M(1)$ is the one with higher invariant mass. The drawn contour is 3σ distribution. Given data from leptoquark mass at 120 and 220 GeV/c^2 .

drawn is the corresponding deviations as computed above.

5.4.3 Candidate event distributions and comparison with Monte Carlo

Figure 5.22 shows the reconstructed mass distribution for the candidate events, after possible cosmic ray events removal. The contour indicates the mass deviation from the Monte Carlo samples for 8 LQ_2 mass points, from 100 to 240 GeV/c^2 .

We select the events falling within the contour to be the final candidates for the given LQ_2 mass to compute the mass limit.

5.4.4 Comments on the Previous Analysis

From the previous analysis [59], 4 LQ_2 candidates were noted. We have studied those events, and here found that two of the events pass the event selection criteria. Table 5.7 summarises the 4 events of the previous analysis.

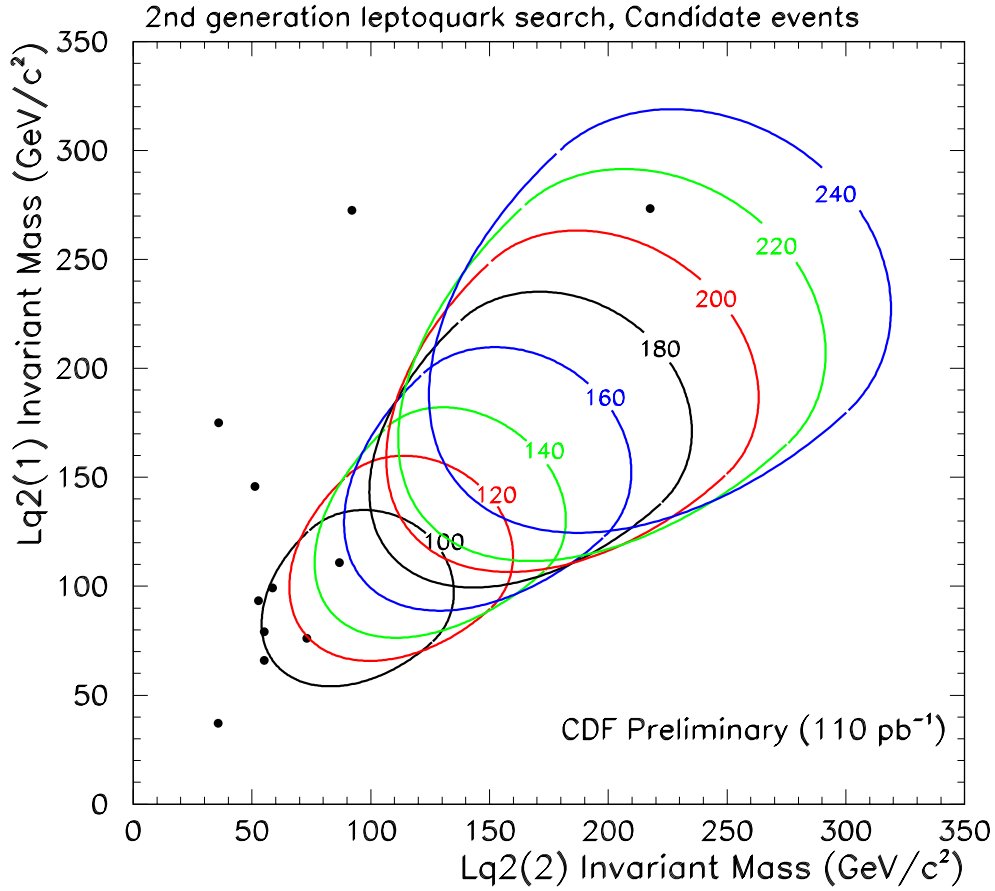


Figure 5.22: Mass distribution of the LQ_2 candidate events, plotted with the mass constraint regions. $LQ_2(1)$ v.s. $LQ_2(2)$.

Run #	Event #	Comments
46492	200434	passed.
47007	250998	Bad run cut failed. E_T cut on jet: $E_{T_{jet2}} = 13.8$ GeV.
63650	394129	Failed 1 st muon isolation cut $E_{iso} = 14.6$ GeV.
63719	31054	passed.

Table 5.7: LQ_2 candidate from previous analysis.

#	Run no.	Evt no.	$M_{\mu\mu}$	M_{LQ_1}	M_{LQ_2}	μ_{1PT}	μ_{2PT}	j1 E_T	j1 η	j2 E_T	j2 η
1	46492	200434	18.9	51.1	92.8	34.2	24.8	38.0	1.59	15.2	-.27
2	47007	250998	58.1	69.0	68.6	31.1	25.8	43.1	.46	13.8	1.25
3	63650	394129	74.5	58.8	79.4	21.7	68.6	32.2	1.74	16.9	.35
4	63719	31054	153.8	222.7	278.4	96.3	49.5	42.0	-2.18	37.3	1.79

Table 5.8: LQ_2 candidate from previous analysis. The events #2 and #3 failed the event selection criteria in this analysis.

5.5 Signal Detection Efficiency

In order to calculate the expected number of events, the signal detection efficiency needs to be evaluated for a range of LQ_2 masses. We use both data and Monte Carlo samples to derive the total signal efficiency, ε_{total} .

5.5.1 Monte Carlo samples

We use the Monte Carlo generator using the CTEQ4 structure function [10] to study the signal detection efficiency for LQ_2 selection. We suppose that the leptoquarks decay into the fermions of same generation so that the flavours of the leptoquark are defined by the quark and lepton flavours in the decay mode. In the Monte Carlo generator, we have forced the decay mode to be $LQ_i \rightarrow q\ell$, where q denotes a quark and ℓ denotes a lepton.

The $LQ_2 \rightarrow q\ell$ vertex contains an undetermined Yukawa coupling strength, λ [89], which affects both the width of the leptoquark and the production cross section. For the calculation of the cross section with the Monte Carlo generator we use the k factor calculated in [7] for the $p\bar{p}$ collider in the LQ_i pair production channel, where k is a factor to scale the leptoquark coupling g to the electromagnetic coupling e . The k factor is set to $\lambda^2/(4\pi\alpha_{em})$. We assume LQ_2 decays to μ and quark (s or c , and the spin is assumed to be zero, i.e., its decay is isotropical for scalar leptoquarks).

We generated $\sim 30K$ events for 8 LQ_2 mass points, from 100 GeV/ c^2 to 240 GeV/ c^2 with 20 GeV/ c^2 interval to calculate signal detection efficiencies.

5.5.2 Method and Calculated Efficiencies

The number of expected events, N , is given by

$$N = \mathcal{L} \cdot \beta^2 \cdot \sigma(M_{Lq_2}) \cdot \varepsilon_{total} \quad (5.2)$$

where \mathcal{L} is the total integrated luminosity of the sample, β is the decay branching ratio to the charged lepton + quark channel, $\sigma(M_{Lq_2})$ is the cross section for given mass, and ε_{total} is the total efficiency for observing the leptoquark pair.

We decompose the total efficiency into the following parts:

$$\varepsilon_{total} = \varepsilon_{geom,pT} \cdot \varepsilon_{\mu ionization} \cdot \varepsilon_{trig} \cdot \varepsilon_{ID} \cdot \varepsilon_{2jets} \cdot \varepsilon_{Event} \cdot \varepsilon_{M(Lq)} \quad (5.3)$$

Each component of ε_{total} must be evaluated.

Geometrical and p_T Efficiency, $\varepsilon_{geom,pT}$

We use the LQ_2 Monte Carlo samples to determine the acceptance for the geometrical and p_T requirement for the muons. We apply fiducial and transverse momentum cuts of $p_T > 20\text{GeV}/c$ on all the muons found after the QFL detector simulations. These muons are matched with the Monte Carlo generator at the generation level¹⁰, with a requirement of $\Delta R < 0.4$, where ΔR is the radial distance between two points in the detector in $\eta - \phi$ space ($\Delta R = \sqrt{\phi^2 + \eta^2}$).

This requires that the set of events we take to calculate the geometrical and p_T efficiency must have only *real* muons from the direct LQ_i decay. Events with fake muons or secondary decay muons in the Monte Carlo sample are rejected at this stage and will not effect the $p_T + geom.$ efficiency calculation.

The reason for taking only *real* muons is that in the muon ID efficiency described in the next subsection is calculated from the Z^0 candidates. The muons from the Z^0 decays in the data are all *real* muons, after requiring Z^0 event selection criteria. We then take the product of those two efficiencies, $\varepsilon_{geom,pT}$ and ε_{ID} , to calculate the total dimuon event detection efficiency. Hence we must calculate $\varepsilon_{geom,pT}$ from *real* muons, asking the GENP matching.

¹⁰At the CDF Monte-Carlo generator, the generation level particle bank is called GENP bank.

Mass(LQ_2)	$\varepsilon_{pt-geom}$	$\varepsilon_{pt-geom}^{CMUO-CMUO}$	(%)	$\varepsilon_{pt-geom}^{CMUO-CMIO}$	(%)
100	0.338	0.237	(70.1%)	0.101	(29.9%)
120	0.388	0.275	(70.9%)	0.113	(29.1%)
140	0.419	0.292	(69.7%)	0.127	(30.3%)
160	0.449	0.318	(70.8%)	0.131	(29.2%)
180	0.460	0.330	(71.7%)	0.130	(28.3%)
200	0.475	0.340	(71.6%)	0.136	(28.6%)
220	0.477	0.341	(71.5%)	0.137	(28.7%)
240	0.488	0.352	(72.1%)	0.136	(27.9%)

Table 5.9: Muon p_T +Geometry cut efficiencies.

Table 5.9 shows the calculated efficiencies for $\varepsilon_{geom,pT}$. The total $\varepsilon_{geom,pT}$ can be decomposed into two types of events, CMUO-CMUO and CMUO-CMIO, and they are also noted.

Muon ID efficiency, ε_{ID}

We derive this efficiency from the loose dimuon data samples, or the event samples after the pre-selection has been applied (See 5.2). Bad runs and duplicated events are removed before studying the muon ID efficiency.

We require a **tight** muon cut as defined in section 5.3.3 to a CMU or CMU/CMP muon, and the highest p_T passing the cut is selected as the 1st leg. The highest p_T of all other CMUO muons with $p_T > 20$ GeV/ c forming a Z^0 candidate (opposite charge, $76 < M_{\mu\mu} < 106$ GeV/ c^2) with the 1st leg is chosen as the 2nd leg.

If no second leg CMUO muon is found, the highest p_T CMIO muon with $p_T > 20$ GeV/ c and CTC exit radius > 103.6 cm forming a Z^0 candidate with the 1st leg is chosen as the 2nd leg.

Since in the tight cut there is a fiducial cut which correlates with the matching cuts, we separate the Z^0 events to two categories:

F: Fiducial-fiducial, or both muons fall in the fiducial category.

N: Fiducial-non fiducial, or one muon is in the fiducial region and the other in a non-fiducial area.

The total number of Z^0 events therefore is $F + N$. We are interested in finding the muon ID efficiency, and they are categorised as:

ε_t : Efficiency for **tight** muons. Since the **tight** cut requires a fiducial cut, the event is in the fiducial-fiducial (F) category.

ε_t^F : Efficiency for **loose** muons in the fiducial-fiducial (F) event category.

ε_t^N : Efficiency for **loose** muons in the fiducial-non fiducial (N) event category.

We define efficiency relations for the number of events with one leg passing the **tight** cut in two different fiducial categories, avoiding double counting:

$$F_t = 2\varepsilon_t \cdot F - \varepsilon_t^2 \cdot F \quad (5.4)$$

$$N_t = \varepsilon_t \cdot N \quad (5.5)$$

where F_t is the number of fiducial-fiducial events with one leg passing the **tight** cut, and N_t is the number of fiducial-non fiducial events with one leg passing the **tight** cut (the second leg criteria not yet applied). For events with the first leg passing the **tight** cut and the second leg passing the **loose** cut, the corresponding relations are:

$$F_{tl} = 2\varepsilon_t \varepsilon_t^F \cdot F - \varepsilon_t^2 \cdot F \quad (5.6)$$

$$N_{tl} = \varepsilon_t \varepsilon_t^N \cdot N \quad (5.7)$$

where F_{tl} is the number of fiducial-fiducial events with the first leg passing the **tight** cut and second leg passing **loose** cut, and N_{tl} is the same number for fiducial-non fiducial events. We also can define the same relation for events which pass **tight** cut for both legs.

$$F_{tt} = \varepsilon_t^2 \cdot F \quad (5.8)$$

$$N_{tt} = 0 \quad (5.9)$$

where F_{tt} and N_{tt} are the number of events with both legs passing the `tight` cut in fiducial-fiducial and fiducial-non fiducial categories, respectively.

Now we calculate the efficiencies by eliminating the unknown variables F and N in the above equations. Taking Equations 5.4 and 5.8, we obtain:

$$\varepsilon_t = \frac{2F_{tt}}{F_t + F_{tt}} \quad (5.10)$$

For the `loose` leg in the fiducial-fiducial category, we combine Equation 5.4 and 5.6, and substituting the result from Equation 5.10. It gives;

$$\varepsilon_l^F = \frac{F_{tl} + F_{tt}}{F_t + F_{tt}} \quad (5.11)$$

For fiducial-non fiducial type of events, we do not have to worry about overlapping, and

$$\varepsilon_l^N = \frac{N_{tl}}{N} \quad (5.12)$$

A total of 461 (Run IA) and 2462 (Run IB) Z^0 events are selected, where 160 (IA) and 829 (IB) are *ff* (fiducial-fiducial region) and 301 (IA) and 1635 (IB) are *fn* (fiducial-non fiducial). 116 (IA) and 533 (IB) events Z^0 have both legs passed the `tight` cut. Table 5.10 shows the efficiencies for the `tight` cut muon ID efficiencies and Table 5.11 shows the efficiencies for the `loose` cut muon ID efficiencies.

We require two muons, hence the Muon ID efficiencies should be calculated using the above result. They are separated into two categories, CMUO-CMUO and CMUO-CMIO and they are evaluated using the following formulae to avoid double counting:

$$\varepsilon_{\text{CMUO-CMUO}}^{id} = \varepsilon_t(2\varepsilon_l^{ff} - \varepsilon_t) \quad (5.13)$$

$$\varepsilon_{\text{CMUO-CMIO}}^{id} = \varepsilon_t\varepsilon_l^{fn} \quad (5.14)$$

Type of cut	Run IA		Run IB	
	N_{pass}/N_{tot}	$\varepsilon(\%)$	N_{pass}/N_{tot}	$\varepsilon(\%)$
$E(\text{EM})_{\mu 1} < 2 \text{ GeV}$	268/276	97.1 ± 1.0	1311/1362	96.2 ± 0.5
$E(\text{HAD})_{\mu 1} < 6 \text{ GeV}$	274/276	99.3 ± 0.5	1331/1362	97.7 ± 0.4
$ \delta x(\text{CMU})_{\mu 1} < 2 \text{ cm}$	262/276	94.9 ± 1.0	1270/1362	93.2 ± 0.7
$ \delta x(\text{CMP})_{\mu 1} < 5 \text{ cm}$	196/196	$100^{+0.0}_{-0.5}$	949/956	99.3 ± 0.3
$\min \Delta(Z_{\mu 1} - Z_{\text{VTVZ}(i)}) < 5 \text{ cm}$	271/276	98.2 ± 0.8	1336/1362	98.1 ± 0.4
$ Z_{\text{VTVZ}(\mu 1)} < 60 \text{ cm}$	276/276	$100^{+0.0}_{-0.1}$	1362/1362	$100^{+0.0}_{-0.1}$
$E_{iso(\mu 1)} < 2 \text{ GeV}/c$	257/276	93.1 ± 1.5	1223/1362	89.8 ± 0.8
ε_t	232/276	84.0 ± 2.2	1066/1362	78.3 ± 1.1
ε_l^{ff}	261/276	94.5 ± 1.4	1263/1362	92.7 ± 0.7

Table 5.10: **tight** leg muon ID efficiencies.

Type of cut	Run IA		Run IB	
	N_{pass}/N_{tot}	$\varepsilon(\%)$	N_{pass}/N_{tot}	$\varepsilon(\%)$
$\text{CEM} < 2 \text{ Gev}$	288/301	95.7 ± 1.2	1532/1635	93.7 ± 0.6
$\text{CHA} < 6 \text{ Gev}$	289/301	96.0 ± 1.1	1574/1635	96.3 ± 0.5
$\text{Delta Z} < 5 \text{ cm}$	293/301	97.3 ± 0.9	1617/1635	98.9 ± 0.2
$Z_v < 60 \text{ cm}$	301/301	$100^{+0.0}_{-0.3}$	1630/1635	99.7 ± 0.1
ε_l^{fn}	271/301	90.0 ± 1.7	1476/1635	90.3 ± 0.7

Table 5.11: **loose** leg muon ID efficiencies. The correlation with **tight** leg has been accounted by avoiding double counting.

ε_{muonID}	Run IA	Run IB
CMUO-CMUO	0.882	0.839
CMUO-CMIO	0.882	0.839

Table 5.12: Muon ID efficiencies for event type and Run IA and IB, evaluated from data.

using appropriate efficiencies for Run IA and IB. With the above formulae and results from Table 5.10 and 5.11, we extract the muon ID efficiencies for Run IA and IB, for the two types of muon events given in Table 5.12.

Tracking

The above muon ID efficiencies includes the detector tracking efficiencies. We take the tracking efficiency studied by other CDF analyses [90]. The efficiency for offline track reconstruction algorithm to reconstruct a track is estimated by examining good W events, passing high E_t and missing E_t requirements. Events with no three-dimensional track pointing at the cluster were counted as tracking failures. In Run IA, the tracking efficiency was found to be $99.7 \pm 0.2\%$. In Run IB, we use high- p_T electron candidates which passed the Level-3 trigger¹¹ to measure the Level-3 tracking efficiency. The plateau efficiency is measured to be $99.46 \pm 0.04\%$. A small decrease of the efficiency was expected between Run IA and IB for degradation of the CTC performance for the later runs. We found the tracking efficiencies to be nearly fully efficient for high- p_T tracks, hence we do not take this factor into account.

Muon ID efficiencies from Run IA and IB mainly differs because of the isolation cut on the `tight` muons due to the increase of luminosity for Run IB, which yields lower isolation efficiency for muons. We use Monte Carlo events to determine the fraction of CMUO-CMUO and CMUO-CMIO events after it passes through Muon p_T and geometrical constraint, and determine the combined muon ID efficiencies.

Table 5.13 shows the Run IA and IB combined total muon ID efficiencies.

¹¹The trigger for Level-3 here is `ELEA_CEM_25GEV_W_NOTRK`.

Mass(LQ_2)	CMUO-CMUO	CMUO-CMIO	Total (ε_{id})
100	0.593	0.214	0.808
120	0.600	0.209	0.809
140	0.590	0.217	0.807
160	0.600	0.209	0.809
180	0.608	0.202	0.810
200	0.606	0.205	0.811
220	0.605	0.206	0.811
240	0.611	0.200	0.810

Table 5.13: Total Muon ID efficiency, normalised to Run IA and IB luminosity and fraction of muon type determined with Monte Carlo.

Trigger type	Run 1A efficiency
CMUP	0.870 ± 0.070
CMNP	0.774 ± 0.058

Table 5.14: Combined trigger efficiencies for Run IA.

Trigger efficiency, ε_{trig} , combined with ε_{ID}

The trigger efficiency calculation is taken from the data in Run IA, while in Run IB, we use the trigger simulation.

Run IA

The trigger efficiency calculation for Run IA follows the scheme of the Drell-Yan dimuon analysis [87]. We define CMUP muon to be a muon track hitting the CMU *and* CMP and CMNP muon to be a muon track hitting the CMU but it does *not* have a hit in CMP. Two high p_T central muon triggers are used, the CMNP and the CMUP, or

- CMU_CMP_CFT_0_2[*]
- CMUNP_CFT_9_2_4DEG

The combined L1 and L2 trigger efficiencies for these two triggers (T_P , T_N) has been calculated in CDF 3510 using Z^0 events, as given in Table 5.14. The L3 efficiency is mostly included in the muon identification discussed above.

Since we only require the `tight` muon to be fiducial CMNP or CMUP muons, to calculate the combined muon ID and trigger efficiency, we have to separate events into the following 5 categories:

- ▷ CMUP-CMUP: both muons are in fiducial area of CMUP
- ▷ CMNP-CMUP: one muon in fiducial area of CMNP, the other in fiducial area of CMUP
- ▷ CMNP-CMNP: both muons are in fiducial area of CMNP
- ▷ CMUP-non-fiducial: one muon in fiducial area of CMUP, the other in non-fiducial area.
- ▷ CMNP-non-fiducial: one muon in fiducial area of CMNP, the other in non-fiducial area.

Thus the id efficiencies of these 5 categories of events are calculated according to the following formulae:

1. $\varepsilon_1^{id} = \varepsilon_t(2\varepsilon_l^{ff} - \varepsilon_t)$
2. $\varepsilon_2^{id} = \varepsilon_1^{id}$
3. $\varepsilon_3^{id} = \varepsilon_1^{id}$
4. $\varepsilon_4^{id} = \varepsilon_t\varepsilon_l^{fn}$
5. $\varepsilon_5^{id} = \varepsilon_4^{id}$

Then the trigger efficiencies are:

1. $\varepsilon_1^{tr} = T_P(2 - T_P)$
2. $\varepsilon_2^{tr} = T_P - T_P T_N / ps + T_N / ps$
3. $\varepsilon_3^{tr} = T_N(2 - T_N) / ps$
4. $\varepsilon_4^{tr} = T_N$
5. $\varepsilon_5^{tr} = T_N / ps$

Event type	ε_i^{id}	ε_i^{tr}	combined
1 (1A)	0.882	0.983	0.867
2 (1A)	0.882	0.971	0.856
3 (1A)	0.882	0.949	0.837
4 (1A)	0.756	0.870	0.658
5 (1A)	0.756	0.774	0.658

Table 5.15: Combined trigger efficiencies.

Thus the combined efficiency for the i^{th} category is just $\varepsilon_i^{ID}\varepsilon_i^{trig}$. Table 5.15 shows the results.

The combined efficiency of all events is then

$$\varepsilon_{id}\varepsilon_{tr} = F_i\varepsilon_i^{id}\varepsilon_i^{tr} \quad (5.15)$$

where F_i is the fraction of events in each category. The Run IA combined muon ID plus trigger efficiencies are computed to be 71.0 % ($M_{LQ} = 100 \text{ GeV}/c^2$) to 71.3 % ($M_{LQ} = 240 \text{ GeV}/c^2$) according to above method for Run IA efficiency. There is little mass dependency. Table 5.18 shows the numerical results.

Run IB

For Run IB, the CDF muon trigger simulation routine¹² is used to estimate the muon trigger efficiency for this analysis. Details are documented in the reference [91].

A total of 16 triggers used in the top muon trigger analysis in Run IB, including 13 muon triggers. The Monte Carlo events are fed into the muon trigger simulations and according to the muon type (CMU, CMP, or CMX), the trigger criteria is checked. The trigger simulation includes both the trigger efficiencies and the pre-scale factors. The efficiencies for the level 1 and level 2 muon triggers are measured from data [92], and are included in the trigger simulation routine. The trigger requirement for 3 types of muons are listed in Table 5.16. See Appendix B for detailed explanations for meaning of symbolised trigger names.

We use Monte Carlo to generate leptoquark events for mass intervals of between 100

¹²The code is found in the \$TOP_FND/sim_mutrigger.cdf in the CDF offline package. It is first developed for top quark analysis. Available to the CDF collaboration members.

Bit number	Type of Trigger	Type of muon		
		CMU	CMP	CMX
3	MET_35_TW0*	✓	✓	✓
4	MET_35_TEX*	✓	✓	✓
5	CMNP_CFT_12_5DEG_V*	✓		
6	CMUP_CFT_12_5DEG_V*	✓		
7	CMNP_JET*	✓		
8	CMUP_JET*	✓		
9	CMU_CMP_JET*	✓		
10	CMNP_CFT_12_5DEG_M*	✓		
11	CMUP_CFT_12_5DEG_M*	✓		
12	CMX_CFT_12_5DEG_V*			✓
13	CMX_JET*			✓
14	CMX_CFT_12_5DEG_M*			✓
15	CMX_CFT_12_5DEG_E*			✓

Table 5.16: List of triggers and criteria for different type of muons. See Appendix B for detailed explanations for meaning of symbolised trigger names.

Mass(LQ_2)	ε_{ID}	ε_{trig}	$\varepsilon_{ID+trig}$
100	0.808	0.827	0.668
120	0.809	0.846	0.684
140	0.807	0.865	0.698
160	0.809	0.864	0.699
180	0.810	0.876	0.710
200	0.811	0.882	0.715
220	0.811	0.884	0.717
240	0.810	0.887	0.718

Table 5.17: Efficiency for Muon ID, Trigger, and combined Muon ID + trigger for Run IB.

GeV/ c^2 and 240 GeV/ c^2 . These events are input to the muon trigger simulation, and we evaluate the muon trigger efficiency for a given leptoquark mass. The muon trigger efficiencies are summarised in Table 5.17.

Run IA+B combined

We then combine the Run IA and IB muon ID and trigger efficiency by calculating the weighting average according to the relative luminosity (of 18.8 pb $^{-1}$ for Run IA and 88.6 pb $^{-1}$ for Run IB). Table 5.18 shows the calculated results.

Mass(LQ_2)	Muon ID + trigger efficiency		
	Run IA	Run IB	Combined
100	0.710	0.668	0.675
120	0.709	0.684	0.688
140	0.712	0.698	0.700
160	0.713	0.699	0.701
180	0.711	0.710	0.710
200	0.713	0.715	0.715
220	0.711	0.717	0.716
240	0.714	0.718	0.717

Table 5.18: Efficiency for combined Muon ID + trigger for Run IA+B.

Mass(LQ_2)	$\langle P_T^\mu \rangle \text{GeV}/c$	ϵ_{ion}
100	74.5	0.980
120	87.8	0.972
140	100.8	0.963
160	113.0	0.955
180	126.4	0.945
200	131.7	0.937
220	148.9	0.928
240	158.3	0.920

Table 5.19: Efficiency of the combined EM and HAD muon ID minimum ionising efficiency (determined from a GEANT simulation) and average p_T of muon for given LQ_2 mass (PYTHIA).

Muon ID minimum ionising efficiency, ϵ_{ion}

In our muon selection, we require both muons be minimum ionising as a result of the cut used in [85]. However, the muon ionization during traversing the detector material depends on the p_T of the muons and therefore the efficiency of the ionization is p_T dependent. We use samples generated by GEANT Monte Carlo simulation package and is also computed using muons coming from Z^0 decay. In the data, the average p_T of muons are approximately 45 GeV/ c . The average p_T of muons decaying from leptoquarks are function of its mass. We add a correction factor ϵ_{ion} , derived from the Monte-Carlo simulation, depends on the muon p_T and hence on the leptoquark mass.

We obtain an increase of approximately 11 GeV/ c in average muon momentum and this results in a lost of 0.38% in the efficiency. Thus we use the formula

Mass(LQ_2)	ε_{events}	$\varepsilon_{events}^{CMUO-CMUO}$	$\varepsilon_{events}^{CMUO-CMIO}$
100	0.754	0.537	0.217
120	0.787	0.562	0.225
140	0.832	0.583	0.249
160	0.856	0.606	0.249
180	0.880	0.635	0.245
200	0.894	0.640	0.254
220	0.909	0.650	0.258
240	0.920	0.665	0.255

Table 5.20: Event selection efficiencies.

$$1.0 - (\langle P_T^\mu \rangle - 50) \times 0.0038 \quad (5.16)$$

to calculate the relative correction factor for the minimum ionising cut efficiency. The result is given in Table 5.19.

The 2 jet efficiency, ε_{2jets}

We require for $E_{Tjet1} > 30$ GeV and $E_{Tjet2} > 15$ GeV for Monte Carlo generated LQ_2 events, using the raw energy, as in the event topology cut we applied on the data samples. Both jets are required to be within $|\eta| < 2.4$. The efficiency ε_{2jets} is calculated using events passing the muon geom+ p_T selection and the muon ID cut. The 2 jet efficiency is listed in the Table 5.21.

Event cut efficiency, ε_{Event}

We require the reconstructed dimuon mass to be outside the Z^0 region ($76 < M_{\mu\mu} < 106$ GeV/ c^2) and above resonances from heavy flavour decays ($M_{\mu\mu} > 10$ GeV/ c^2). This efficiency is calculated from Monte Carlo samples, after the event passes all other filters. ε_{Event} is calculated with events passing the muon geom+ p_T , muon ID, and 2 jets cuts. Table 5.20 shows the evaluated event selection efficiency, as a function of the LQ_2 mass.

Leptoquark pair mass constraint efficiency, ε_{mass}

We choose the final LQ_2 candidates by applying the mass contour as explained in Section 5.4.2. We take LQ_2 Monte Carlo events and compute the ratio of number of events passing

LQ_2 mass	$\varepsilon_{\mu\mu^l, geom}$	$\varepsilon_{\mu ID+trig}$	ε_{ion}	ε_{2jets}	ε_{events}	ε_{mass}	ε_{total}
100	0.338	0.675	0.980	0.694	0.767	0.767	0.090
120	0.388	0.688	0.972	0.747	0.807	0.812	0.126
140	0.424	0.700	0.963	0.785	0.835	0.812	0.152
160	0.442	0.701	0.955	0.809	0.856	0.815	0.167
180	0.462	0.710	0.945	0.833	0.877	0.818	0.185
200	0.474	0.715	0.937	0.857	0.900	0.833	0.204
220	0.482	0.716	0.928	0.866	0.908	0.841	0.212
240	0.490	0.717	0.920	0.880	0.919	0.833	0.218

Table 5.21: Total event detection efficiencies. Calculated from Run IA + B dimuon data and PYTHIA+QFL MC samples.

the mass constraint to the number of events passing all cuts except the mass constraint cut. The numerical value is quoted in Table 5.21.

5.5.3 Total event detection efficiency, ε_{tot}

Table 5.21 shows the run IA, run IB and total combined efficiency as function of LQ_2 mass. Figure 5.23 shows the graphical presentation of the event detection efficiencies. All efficiencies, except the total efficiency, are calculated successive order. The total efficiency is the multiple sum of all efficiencies.

From the total efficiency, ε_{total} , we calculate the expected number of events from the data samples of 109 pb^{-1} .

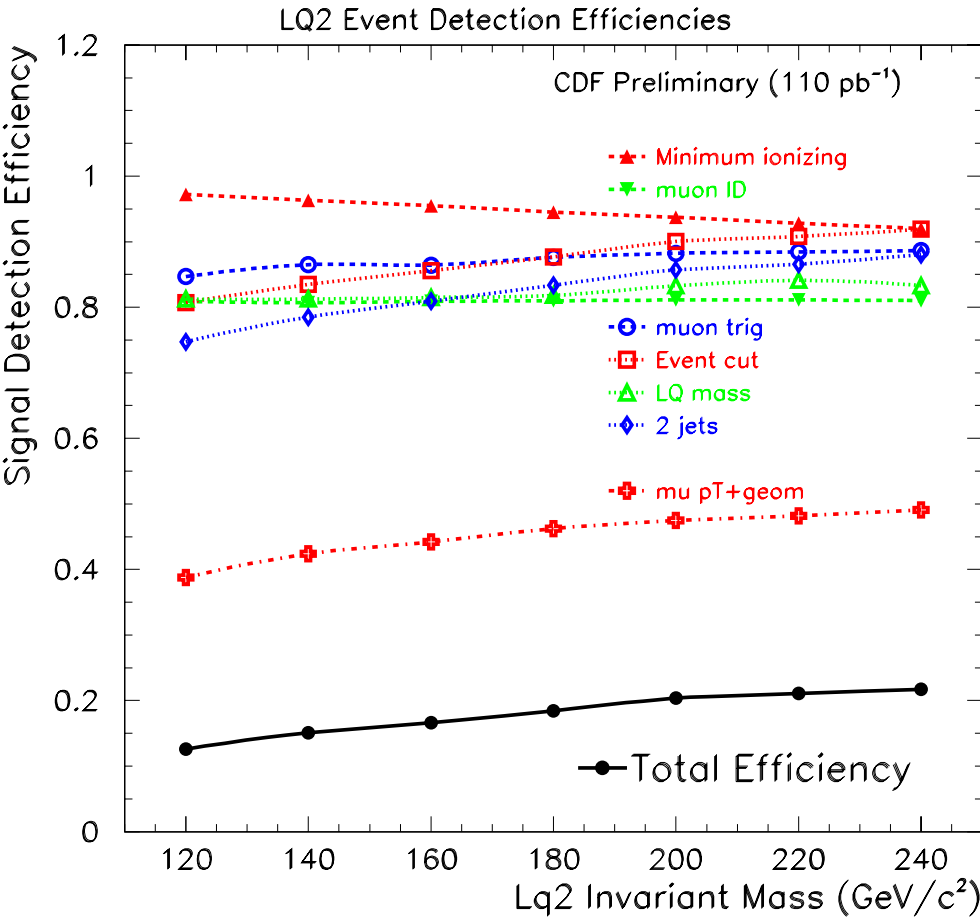


Figure 5.23: Total event detection efficiencies.

5.6 Background

The background for the LQ_2 search results from events which have a high p_T dimuon and two associated high E_T jets. The possible sources of this background are higher order Drell-Yan processes, heavy flavour decay (from $b\bar{b}$ or $t\bar{t}$ in dilepton channel), WW , $Z \rightarrow \tau^+\tau^-$, and fake dimuon events with 2 associated jets.

5.6.1 Drell-Yan

The higher order Drell-Yan (DY) processes give the major contribution to the background for the LQ_2 search where we select the high p_T dimuon plus dijet final state.

Monte Carlo Generator

We used the Monte Carlo generator with the CTEQ4 structure function was set to generate Drell-Yan event samples. The PYTHIA process is set to $q\bar{q}(qg) \rightarrow Z^0/\gamma^* + X$, in which Z^0/γ^* decaying into dimuon channels¹³. The generated dimuon mass spectrum is shown in Figure 5.24.

We have generated a total of $> 50K$ Drell-Yan + jets events, in 3 different $M_{\mu\mu}$ mass region around Z^0 mass (10 – 76, 76 – 106, 106 – 900 GeV/ c^2), to evaluate the DY background.

We have also generate DY events with no recoiling jets ($q\bar{q}(qg) \rightarrow Z^0/\gamma^*$) to calculate the relative muon detection efficiencies for dimuon DY events, also in 3 dimuon mass regions¹⁴.

DY calculation method

The method we use to approximate the Drell-Yan background is similar to the previous LQ_2 analysis, evaluated by calculating the relative event detection with given cross sections and luminosity from the Monte Carlo generator.

We use the $Z^0 \rightarrow \mu^+\mu^-$ distribution from the data to predict the background coming from the continuum outside the Z^0 mass window. This assumes that the jet activities (i.e., E_T and

¹³In PYTHIA v5.7, this process is obtained by setting the MSEL=13 or ISUB=15, 30. The decay of Z^0 is forced to $\mu^+\mu^-$. The $M_{\mu\mu}$ resonance range is set by CKIN(41) - (44). We generated the mass between 10 - 900 GeV/ c^2 .

¹⁴PYTHIA v5.7. ISUB=1. Z^0 decay forced to $\mu^+\mu^-$. The $M_{\mu\mu}$. resonance range is set by CKIN(41) - (44).

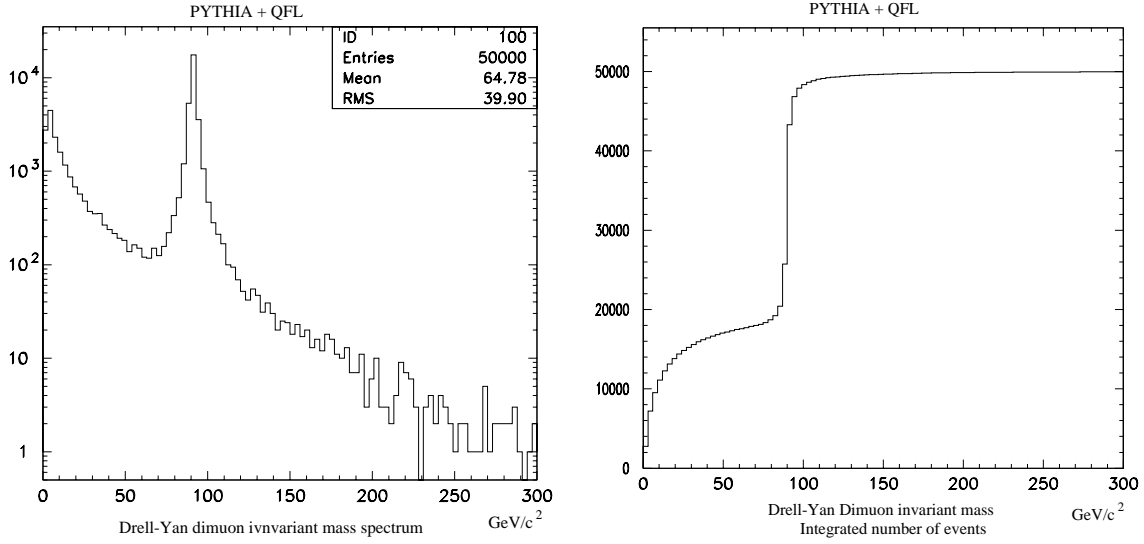


Figure 5.24: Drell-Yan dimuon invariant mass spectrum (left) and integrated histogram (right). 50k events generated. PYTHIA generator output. Production of $Z^0/\gamma^* + \text{jets}$.

kinematic distributions) are similar in these two regions, and that the ratio of events within and outside the Z^0 mass window are the same before and after the two jets requirement. Nevertheless there are differences in the p_T distribution of the dimuon system in these mass windows, therefore we need to correct the bias in the jet cut efficiencies introduced by this method. The correction factor is evaluated by the Monte Carlo.

The DY background contribution in our final data sample A^{DY} is calculated by the following formula.

$$A_{dy}^{data} = A_{Z^0}^{data} \frac{B_{lo}^{data} \cdot f_{lo} + B_{hi}^{data} \cdot f_{hi}}{B_{Z^0}^{data}} \quad (5.17)$$

where $A_{Z^0}^{data}$ is the number of events found in the Z^0 window from the data *after* all cuts, $B_{Z^0}^{data}$ is the same number but *before* the two jets cut (after the muon ID cuts). B_{hi}^{data} and B_{lo}^{data} are the number of events observed above and below the Z^0 region, respectively, *before* the two jets cut. $f_{lo,hi}$ are the corresponding correction factors derived from Monte Carlo which account for the difference in jet activity within and outside the Z^0 region.

We have generated DY + jets events in the following three mass windows: The *Low* mass region from Z^0 window ($10 - 76 \text{ GeV}/c^2$), the Z^0 ($76 - 106 \text{ GeV}/c^2$), and the *High* mass then

$M_{\mu\mu}$	$A/10k$	$B/10k$	A/B	f
$10 < M_{\mu\mu} < 76 \text{ GeV}/c^2$ (low)	340	1140	0.298	0.979
$76 < M_{\mu\mu} < 106 \text{ GeV}/c^2$ (Z^0)	758	2492	0.304	1.0
$106 < M_{\mu\mu} \text{ GeV}/c^2$ (high)	848	2668	0.318	1.046

Table 5.22: Efficiencies for passing the event (2 jet) cut of Drell-Yan study for the different dimuon invariant mass region. $N_{\mu cuts}$ indicates the number of events passing the muon cuts and w is the relative weight to the Z^0 events. 10k events are generated for each category. PYTHIA + QFL.

Z^0 ($76 - 106 \text{ GeV}/c^2$). We then analyse these events as done in the data, and calculate the fraction of events passing the two jets cut. We calculate the fraction f 's, normalised to Z^0 window, by decomposing the dimuon mass region using the formula below:

$$f_{lo,hi} = \frac{A_{lo,hi}^{mc} B_{Z^0}^{mc}}{A_{Z^0}^{mc} B_{lo,hi}^{mc}} \quad (5.18)$$

where B_{lo}^{mc} , B_{hi}^{mc} , and $B_{Z^0}^{mc}$ are the normalised number of events passing the dimuon requirement (before the 2 jet cut) *below*, *above*, and within the Z^0 dimuon invariant mass window. A denotes the same number after the 2 jet cut.

DY background estimation

Table 5.22 shows the calculated statistics for the DY Monte Carlo generation and the predicted background.

We observed $A_{Z^0} = 47$, $B_{lo} = 226$ and $B_{hi} = 454$, $B_{Z^0} = 2708$ in Run IA+B data, and from the formula (5.18) and Table 5.22, we obtain the expected number of events from the DY background, A^{DY} , to be 12.08 ± 1.8 .

5.6.2 Heavy flavour decay

Top quark production: $t\bar{t}$

We use the $t\bar{t}$ Monte Carlo samples generated by ‘‘Top Group’’¹⁵. The Herwig generator (version 5.6, $M(t\bar{t}) = 175 \text{ GeV}/c^2$), has been used. The TOPFND filter passed 47.5% of events

¹⁵for more information, see http://www-cdf.fnal.gov/internal/physics/top/monte_carlo.html

on raw $t\bar{t}$ events which requires at least one high p_T isolated lepton. We passed these events on our filter to compute the expected $t\bar{t}$ back ground.

We take the top pair production cross section to be $4.75_{-0.68}^{+0.63}$ pb [93]. We apply the LQ_2 event selection criteria filter on 2852 events of the MC samples, and find 395 events passing the cuts. The equivalent cross section of this sample is 28.5 fb^{-1} . We then multiply this figure with the additional muon identification factor of 0.95^2 and trigger efficiency of 95.5% [94]. Normalising to our data of 107.4 pb^{-1} , we find the expected $t\bar{t}$ total background to be $1.28_{-0.18}^{+0.17}$.

Bottom quark production: $b\bar{b}$

A previous analysis [59] has made a study of the expected $b\bar{b}$ background using the Monte Carlo samples. This was quoted in top background search analysis [95]. Using 67.5 pb^{-1} of $b\bar{b}$ samples with high p_T leptons, no event passed the LQ_2 event selection criteria. This result is applicable to our analysis. Normalising to 107.4 pb^{-1} , the expected background is $0.0_{-0.0}^{+1.59}$.

5.6.3 W^+W^-

We generated 10k W^+W^- events using the Monte Carlo generator, with both W 's decaying to the $\mu + \nu_\mu$ channel. This is equivalent to an integrated luminosity of 114.8 fb^{-1} , given the cross section $\sigma_{(WW \rightarrow \mu\nu\mu\nu)}$ is calculated to be 0.087 pb using the Monte Carlo generator. The total WW production cross section is 9.53 pb [96].

We then applied the event filter and 67 events passed the event selections. Normalising to the cross section of WW process, the expected number of WW events surviving the cuts, using 107.4 pb^{-1} of data, is calculated to be 0.06 ± 0.01 .

5.6.4 $Z \rightarrow \tau^+\tau^-$

The background study from $Z \rightarrow \tau^+\tau^-$ has been made with Monte Carlo data generated [97] using the ISAJET generator. We found 2 events pass the event selection criteria from total integrated luminosity of 804 pb^{-1} , which is approximately 7.5 times larger than the total integrated luminosity from the data. Hence our estimation is 0.27 ± 0.19 for the $Z \rightarrow \tau^+\tau^-$ background contribution.

Type	Expected
Drell-Yan	12.08 ± 1.8
$t\bar{t}$	$1.28^{+0.17}_{-0.18}$
$b\bar{b}$	$0.0^{+1.59}_{-0.0}$
WW	0.06 ± 0.01
$Z \rightarrow \tau^+ \tau^-$	0.27 ± 0.19
Fake muon	0.28 ± 0.22
total background	13.97 ± 1.84

Table 5.23: Expected background for LQ_2 signal detection.

5.6.5 Fake muons

Fake muons are the muons coming from jets or pion decay which pass the trigger requirement. The punch through, when pions and kaons from energetic hadronic jets penetrate the shielding to reach the muon chambers, can also fake a muon. The probabilities of punch through using Monte Carlo simulations, depending on the threshold of 3 to 9 GeV/c. It is calculated to be 0.1 to 1 % [98] from π and K s.

We normalise the expected fake muon events from the Run IA result [59] to Run IA+B integrated luminosity and obtain 0.28 ± 0.22 events.

5.6.6 Total expected background

Table 5.23 shows the expected background for the second generation leptoquark search.

The background expected in our analysis is 13.97 ± 1.84 , while 11 events passing the cuts from our data sample.

5.6.7 Expected background with mass constraint

The expected number of background events, evaluated in the previous section are obtained before applying LQ_2 pair mass constraint. To evaluate the expected background contribution for the given LQ_2 mass, it is necessary to compute the leptoquark pair mass constraint efficiency, $\varepsilon_{M(Lq)}$ for each of the background signals.

Table 5.24 shows the efficiencies with a mass constraint selection for each of the background signals. We multiply this number with number of expected background events to calculate

LQ_2 mass	Mass constraint efficiencies, ε_{mass}					Total
	DY	$t\bar{t}$	$b\bar{b}$	WW	$Z \rightarrow \tau^+ \tau^-$	
100	0.39	0.44	0.0	0.37	1.0	5.58
120	0.26	0.37	0.0	0.26	0.5	3.77
140	0.15	0.21	0.0	0.11	0.0	2.09
160	0.087	0.070	0.0	0.04	0.0	1.14
180	0.048	0.029	0.0	0.00	0.0	0.617
200	0.022	0.011	0.0	0.00	0.0	0.279
220	0.0072	0.0058	0.0	0.00	0.0	0.094
240	0.0072	0.0032	0.0	0.00	0.0	0.091

Table 5.24: Background efficiencies for mass constraint and total number of expected background for LQ_2 mass.

the final contribution of background in order to evaluate the limit for LQ_2 mass.

5.6.8 Systematic Uncertainties

Possible sources of systematic uncertainty for the detection of leptoquarks have been studied. We need to include both the statistical and systematic uncertainly estimates into the upper limit LQ_2 mass calculation.

The major contributions to the the systematic uncertainty are:

Gluon Radiation : To study the effect from the gluon radiation we have generated LQ_2 events without initial and final gluon radiation¹⁶. The total event detection efficiency is calculated and half of the difference with respect to the default setting is taken to be the systematic uncertainty for the gluon radiation. The uncertainty increases as the LQ_2 mass increases. The two jet cut has a much higher systematic uncertainty for the lower mass as expected, but when we apply the mass constraint cut, ε_{mass} is close to 1.0 for all masses with no gluon radiation since the amount of the extra jets which encounter for misidentifying the jet for reconstructing the LQ_2 invariant mass is small.

Q^2 scale : The jet E_T spectrum and muon p_T spectrum depends largely on the Q^2 scale. This systematic uncertainty is calculated using a similar method to that for the gluon radiation. We generated LQ_2 events with default Q_0^2 , $Q^2 = Q_0^2 \times \frac{1}{4}$, and $Q^2 = Q_0^2 \times 4$,

¹⁶The initial and final gluon radiation is turned on/off by setting MSTP(61) MSTP(71) with PYTHIA.

where Q_0^2 is the default PYTHIA scale¹⁷, and calculated the total signal detection efficiencies. The variation of the Q^2 scale effects on the cross section of the LQ_2 production, and is taken into account to calculate the signal detection efficiencies. We took the half of the average difference of total signal detection efficiency, ε_{total} , to be the systematic uncertainty.

Jet energy scale : We have adjusted the energy by $\pm 10\%$ for the LQ_2 events generated by Monte Carlo, and calculated the 2 jet cut efficiencies. The systematic uncertainty for the jet energy scale is the average difference of the 2 jet cut efficiency with the default (unadjusted jet energy) efficiency, or $\left((\varepsilon_{2jet}^{+10\%} - \varepsilon_{2jet}^{def}) + (\varepsilon_{2jet}^{-10\%} - \varepsilon_{2jet}^{def}) \right) / 2$.

Detector simulation : We use the quoted detector simulation uncertainty from ref. [59], which takes half of the difference between the result from CDFSIM and from QFL detector simulators.

Structure function : The muon detection efficiency depends on the p_T spectrum, and the p_T spectrum is sensitive to the choice of the structure function. However we did not find the structure function has a large effect on the signal detection efficiency. We used the quoted systematic uncertainties from the structure function [59].

Monte Carlo statistics : This uncertainty is the statistical error on the total number of the events generated for each LQ_2 mass point times the total signal detection efficiency for the given mass. The error is slightly higher for the lower mass since ε_{total} for smaller mass is lower.

Luminosity : The uncertainty of the integrated luminosity for Run IA and B has been evaluated at the CDF [87]. The run IA with $\mathcal{L} = 18.82 \pm 0.68 \text{ pb}^{-1}$ and IB with $\mathcal{L} = 88.57 \pm 7.09 \text{ pb}^{-1}$, the fractional uncertainty is 0.072.

For the detector simulation and structure function systematic error, we have taken the analysis result from the last analysis (See next Section (5.6.9) for the difference of the efficiency calculation between this analysis and the previous analysis).

¹⁷The Q^2 scale is adjusted with MSTP (32) and PARP (34).

LQ_2 mass (GeV/c^2)	100	120	140	160	180	200	220	240
gluon radiation.	0.133	0.106	0.084	0.100	0.067	0.057	0.063	0.038
Jet scale	0.037	0.025	0.017	0.012	0.010	0.008	0.006	0.005
MC stat Sys.	0.022	0.019	0.017	0.016	0.016	0.015	0.015	0.015
Q^2 scale	0.092	0.038	0.005	0.015	0.012	0.003	0.010	0.005
Detector simulation	0.060	0.060	0.060	0.060	0.060	0.060	0.060	0.060
Structure function	0.009	0.012	0.014	0.006	0.007	0.013	0.006	0.015
Luminosity calculation	0.072	0.072	0.072	0.072	0.072	0.072	0.072	0.072
Total uncertainty	0.192	0.150	0.129	0.139	0.118	0.112	0.115	0.104

Table 5.25: Systematic uncertainty for LQ_2 detection by components. The total uncertainty is the quadrature sum of all uncertainties.

5.6.9 Difference of event selection for quoted numbers

Since the previous analysis had eventually identical muon selection cuts to calculate the event selection efficiencies and systematic errors, we have taken some previously calculated efficiencies and error values in this analysis. We list the common and difference criteria of the muon selection below.

▷ The common criteria are:

- $p_T > 20 \text{ GeV}/c$
- $EM < 2 \text{ GeV}$
- $HAD < 6 \text{ GeV}$
- $EM+HAD > 0.1 \text{ GeV}$
- Z vertex match $< 5 \text{ cm}$
- $\Delta x(\text{CMU}) < 2 \text{ cm}$ for 1^{st} leg and 2^{nd} leg if CMUO
- $\Delta x(\text{CMP}) < 5 \text{ cm}$ for 1^{st} leg and 2^{nd} leg if CMUO
- Fiducial cut for 1^{st} leg

▷ The requirements applied only in the previous analysis are:

- CTC hits on > 3 axial SL, > 2 axial SL, and > 6 total SL
- Impact parameter $\delta 0 < 3 \text{ mm}$

- Muon isolation cut ($I < 5$ GeV)
 - Track quality
- ▷ The requirements applied only in this analysis are:
- CTC minimum exit radius requirement for CMIO (103.6 *cm*)
 - Muon isolation cut ($I < 2$ GeV)
 - Z vertex from VTX < 60 *cm*

The difference on the event selection criteria is small. By taking some values from the previous analysis, it has little or no effect on the final cross section calculation.

5.7 Upper Limit and Calculation Method

In this section we summarise the upper limit calculation method and apply the calculation to the experimental data, to provide a limit on the second generation leptoquarks.

5.7.1 Cross section calculation with background

Leptoquark production is described by following formula:

$$\sigma(M_{LQ_2}) \cdot \beta^2 = \frac{N}{\mathcal{L} \cdot \varepsilon_{total}} \quad (5.19)$$

where $\sigma(M_{LQ_2})$ is the production cross section of the leptoquark at given mass M_{LQ_2} , β is the branching ratio for $LQ_2 \rightarrow \mu + q$, N is the number of observed events with background subtracted, \mathcal{L} is the total integrated luminosity of the data analysed, and ε_{total} is the total efficiency for detecting LQ_2 events.

We apply the LQ_2 mass constraint to the leptoquark mass distribution, shown in Figure 5.22. If we suppose that the reconstructed invariant mass of the background events are spread evenly, the mass constraint will eliminate most of the background events since the two reconstructed leptoquark invariant mass candidates of the backgrounds are not correlated. See Table 5.24. The limits of number of events is given by using Poisson's formula assuming no background.

$$1 - CL = e^{-N_0} \sum_{n=0}^{n_0} \frac{N_0^n}{n!} \quad (5.20)$$

where n_0 is the observed number of events in each LQ_2 mass contour, and N_0 is the upper limit for the number of events with CL that we are interested in to compute.

When backgrounds are present, we need to modify equation (5.20) to take it into account. Suppose n_b is the expected total background and N_b is the upper limit of background contribution, then the renormalised Poisson's probability for background is:

$$P(n_b; N_b) = \frac{e^{-N_b} \frac{N_b^{n_b}}{n_b!}}{e^{-N_b} \sum_{n=0}^{n_b} \frac{N_b^n}{n!}} \quad (5.21)$$

While the probability without background is still given by equation (5.20). Then the probability for observing a total number of events $n = N_b + N_0$ is

$$P_{tot}(n; N_b, N_0) = \sum_{n=0}^{n_0} P(n_b; N_b) P(n - n_b; N_0) \quad (5.22)$$

and

$$\sum_{n=0}^{\infty} P_{tot} = 1.0. \quad (5.23)$$

Then the upper limit N for desired $C.L.$ is given by the background subtracted equation :

$$1 - CL = \frac{e^{-(N_b+N)} \sum_{n=0}^{n_0} \frac{(N_b + N)^n}{n!}}{e^{-N_b} \sum_{n=0}^{n_0} \frac{N_b^n}{n!}} \quad (5.24)$$

When systematic uncertainties are present, the calculation requires Gaussian smearing with equation (5.24). With background present the number of expected signal and background are computed assuming Gaussian smearing, and summed. The upper limit is calculated by solving for N in the equation :

$$1 - CL = \frac{\int_0^{\infty} dx G(x; N_b, \sigma_b) \int_0^{\infty} dy G(y; N, \sigma) e^{-(x+y)} \sum_{n=0}^{n_0} \frac{(x+y)^n}{n!}}{\int_0^{\infty} dx G(x; N_b, \sigma_b) e^{-x} \sum_{n=0}^{n_0} \frac{x^n}{n!}} \quad (5.25)$$

where we introduced σ for the systematic uncertainty for the expected signal, and σ_b is for the expected background. The Gaussian smearing function is defined as :

$$G(x; \mu, \sigma) = A(\mu, \sigma) e^{-\frac{(x-\mu)^2}{2\sigma^2}} \quad (5.26)$$

where $A(\mu, \sigma)$ is a normalisation factor for Gaussian distribution,

LQ_2 mass (GeV/ c^2)	100	120	140	160	180	200	220	240
Signal detection efficiency, ε_{total}	0.090	0.126	0.152	0.167	0.185	0.204	0.212	0.218
Expected Bkgnd (w/ Mass Const.)	5.58	3.77	2.09	1.14	0.617	0.279	0.094	0.091
Systematic Error	0.192	0.150	0.129	0.139	0.118	0.112	0.115	0.104
N of Events observed	4	1	1	0	0	0	1	1
Expected Signal ($= \sigma_{LQ_2} \cdot \mathcal{L} \cdot \varepsilon_{total}$)	94.5	42.6	20.7	10.4	5.4	2.9	1.5	0.8

Table 5.26: Experimental results for second generation leptoquark search. Number of events observed are with mass constraint.

LQ_2 mass (GeV/ c^2)	100	120	140	160	180	200	220	240
Upper limit without background subtraction (statistic error only)								
$N_{CL=95\%}(poisson)$	9.15	4.74	4.74	3.00	3.00	3.00	4.74	4.74
Cross section upper limit (pb)	0.95	0.35	0.29	0.17	0.15	0.14	0.21	0.20
Upper limit with background subtraction (statistic error only)								
$N_{CL=95\%}(poisson)$	5.22	3.55	3.80	3.00	3.00	3.00	4.65	4.66
Cross section upper limit (pb)	0.54	0.26	0.23	0.17	0.15	0.14	0.21	0.20
Upper limit with systematic uncertainty (no background)								
$N_{CL=95\%}(poisson + gaussian)$	10.9	5.11	4.99	3.10	3.06	3.06	4.92	4.89
Cross section upper limit (pb)	1.13	0.38	0.31	0.17	0.16	0.14	0.22	0.21

Table 5.27: Cross sections of LQ_2 and upper limit, $\mathcal{L} = 107.4 \text{ pb}^{-1}$. The experimental cross section is calculated for branching ratio $\beta = 1.0$.

$$A(\mu, \sigma) \int_0^\infty dx G(x; \mu, \sigma) = 1 \quad (5.27)$$

We have applied the LQ_2 mass constraint cut in our event selection, in which the background contributions into the candidate events are small. In this particular case which there is no background contribution, we can simplify the equation(5.25) to make a conservative assumption calculation, given by :

$$1 - CL = \int_0^\infty dy G(y; N, \sigma) e^{-y} \sum_{n=0}^{n_0} \frac{y^n}{n!} \quad (5.28)$$

5.7.2 Upper limit

Tables 5.26 and 5.27 summarise our search for the 2^{nd} generation leptoquark search. The theoretical cross section can be calculated by the Monte Carlo generator (the default is CTEQ-4M structure function), which was used to calculate the systematic uncertainties in this analysis.

However the theoretical cross section for the LQ_2 production is model dependent. In the analysis, we use the NLO calculation for scalar pairly produced leptoquark production from a recent publications [1] relevant to $p\bar{p}$ collisions at Tevatron. The uncertainty of theoretical calculation is included by taking two extreme Q^2 scale ($Q^2 \times 4$ and $Q^2 \div 4$), and numerical values are listed in Table 5.28. This is used to extract the lower mass limit for second generation leptoquark production.

LQ_2 mass (GeV/c^2)	100	120	140	160	180	200	220	240
$\sigma_{LQ} : \text{CTEQ4M } (Q^2 \div 4)$	14.2	4.98	1.98	0.87	0.41	0.20	0.10	0.05
$\sigma_{LQ} : \text{CTEQ4M } (Q^2 \times 4)$	10.7	3.81	1.54	0.68	0.32	0.16	0.80	0.04

Table 5.28: Theoretical cross section with NLO calculation [1]. Quoted numbers are in pb.

The calculated cross section with $C.L. = 95\%$ is given by:

$$\sigma_{Lq2}(95\%C.L.) \cdot \beta^2 = \frac{N(95\%C.L.)}{\mathcal{L} \cdot \varepsilon_{total}} \quad (5.29)$$

The Figure 5.25 shows the $95\%C.L.$ upper limits on σ_{Lq2} as a function of the leptoquark mass, together with the theoretical cross section. Results are shown with and without background subtraction, with statistical error only. From this we extract a mass limit for the scalar second $195 \text{ GeV}/c^2$ ($\beta = 1.0$) with or without background subtraction.

When we include the systematic uncertainty, we make an assumption that the background contributions in the mass constraints of the LQ_2 mass regions are small. This is a conservative assumption since any additional background contribution will shift the mass limit higher. The Figure 5.26 shows the $95\%C.L.$ cross section upper limits for the LQ_2 mass with systematic uncertainties. From this, we extract lower mass limit for the second generation scalar leptoquarks, which excludes $202 \text{ GeV}/c^2$ for $\beta = 1.0$.

5.8 Conclusion on the leptoquark search

In a search for second generation scalar leptoquarks in dimuon plus dijet channel using the full Run IA+B data of integrated luminosity of 109 pb^{-1} collected at CDF, we have found 11 events as possible LQ_2 candidates with a total expected background of 14.0 events. We used

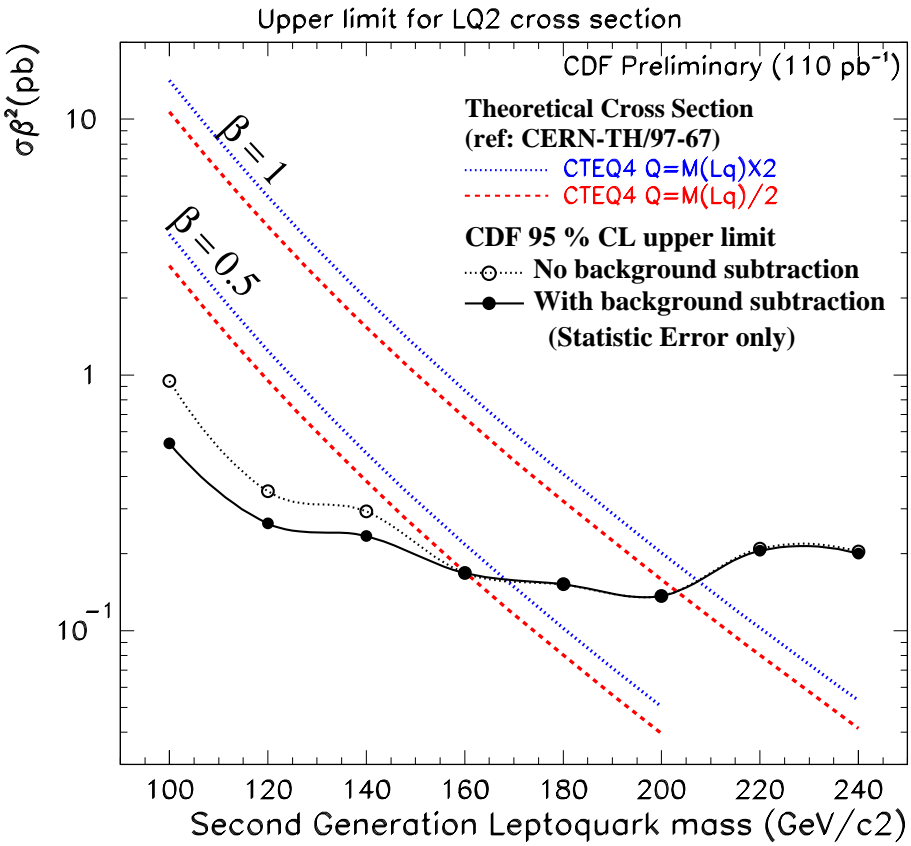


Figure 5.25: 95% C.L. upper limits on σ_{Lq2} function of the leptoquark mass. Statistical error only.

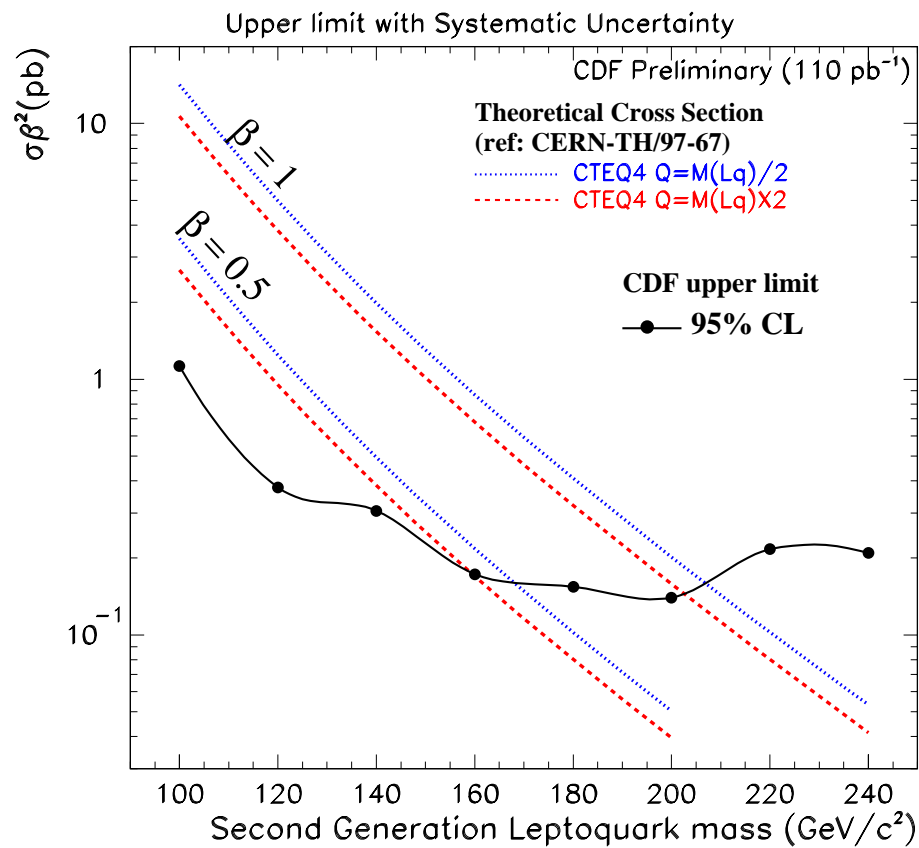


Figure 5.26: 95%*C.L.* upper limits on σ_{Lq2} function of the leptoquark mass. Calculated with statistical and systematic uncertainty. No background subtracted.

mainly the PYTHIA Monte Carlo program with CTEQ4M structure function to evaluate LQ_2 detection study, and have calculated the lower limit on the production cross sections σ_{LQ_2} , function of the leptoquark mass. We compared our result with the most recent theoretical Next-to-Leading Order calculation for the production cross section [1] of pairly produced leptoquarks at Tevatron collider, and set a 95% C.L. lower limit on second generation leptoquark mass. The new mass limit exclude $< 202 \text{ GeV}/c^2$ for $\beta = 1.0$. A publication of this analysis result is now in preparation ¹⁸.

As a result of this analysis, we found that the leptoquarks, bosons mediating between the lepton and quark family predicted in many theoretical models, do not exist within the mass range reachable with the current high energy Collider. This particular analysis has excluded the existence of second generation leptoquarks up to $\sim 200 \text{ GeV}/c^2$ (95% C.L.) with the Tevatron Collider. The CDF is now under its upgrade, and a new Tevatron run will start in the year 1999. More data will be collected with higher luminosity Tevatron operation, and it will improve the lower mass limit of the leptoquark searches.

Beyond that, interest shall turn towards the next generation of the high energy Collider, the LHC, which is currently under construction. A physics study of the ATLAS experiment shows that leptoquarks with mass range up to $1 \text{ TeV}/c^2$ will be possible to be observed within the first year of the LHC operation. Currently intense research and development for the various components of the apparatus are in progress within the ATLAS collaboration to optimise the design and operational procedures of the detector. Chapter 6 will describe the LHC accelerator and the ATLAS experiment with their physics possibilities. Chapter 7 will describe a work towards the ATLAS detectors, in the context of the future leptoquark search program.

¹⁸Collaboration approval for a Physics Review Letter article is in progress.

Chapter 6

The Large Hadron Collider and ATLAS experiment

The Large Hadron Collider (LHC) is a proton-proton accelerator which is planned to be operated from the year 2005, and it will be the highest energy accelerator ever constructed. It will be installed in the existing Large Electron Positron (LEP) tunnel at CERN. While currently the highest energy accelerator, the Tevatron (see Chapter 4), has a center of mass collision energy (\sqrt{s}) of 1.8 TeV, the LHC is planned to reach at the $\sqrt{s} = 14$ TeV with a luminosity of $\mathcal{L} = 10^{34} \text{cm}^{-2} \text{s}^{-1}$. A full study of the Standard Model will be possible including the observation of possible Higgs particles in the mass range $100 < m_h < 800 \text{ GeV}/c^2$. It will also be possible to probe beyond the Standard Model, extending the leptoquark search to higher mass regions. Two high luminosity experiments, namely ATLAS¹ and CMS will be built. In this Chapter some aspects of LHC and the ATLAS detector, as well as related physics study possibilities, are presented. A study on the leptoquark searches at ATLAS has shown the discovery potentials and its limit. Chapter 7 then describes one of the detector development projects, focusing on the silicon tracking front-end electronics development.

Parameter type	LHC	Tevatron
Circumference	26.6 km	6.3 km
Proton Beam Energy	7.0 TeV	900 GeV
Luminosity	$10^{34} cm^{-2} s^{-1}$	$10^{31} cm^{-2} s^{-1}$
Crossing Time	25 ns	3500 ns
Collision frequency	40 MHz	300 kHz
Collisions	proton-proton	proton-antiproton
Dipole Magnet	8.4 Tesla	5.7 Tesla
Number of bunches	2835	6
Experiment	ATLAS, CMS ALICE, LHC-B [†]	CDF, DØ

Table 6.1: Proposed specification of the LHC, compared with Tevatron. [†] For low luminosity experiments.

6.1 The LHC and its physics potential

Table 6.1 summarises some important specifications of the LHC, compared with the existing Tevatron collider. Experiments planned at the high luminosity collision points at LHC are ATLAS [102, 103] and CMS [104]. There are two experiments planned for low luminosity collision points, and they are LHC-B [105] and ALICE [106]. The schematic layout of the LHC is shown in Figure 6.1 with the approximate location of these experiments.

Today, the Standard Model (SM) has explored the mass scale up to $175 \text{ GeV}/c^2$ with the discovery of the top quark [32] by the CDF collaboration at Fermilab in 1995, completing the observation of six known quark flavours. This discovery gave a rise to a narrower mass constraint for the yet undiscovered Higgs boson which is predicted in the SM. Detailed top quark studies will be made at Tevatron Run II, and later at the LHC, with $t\bar{t}$ production rate over 10k per day with the initial low luminosity ($\mathcal{L} = 10^{33} cm^{-2} s^{-1}$) operation. B-physics studies have wide possibilities at the LHC, including the search for and precise quantitative measurement of CP-violations and B-mixing.

A number of theories exists today which indicate that new physics could (*must*) appear with a mass scale below $\sim 1 \text{ TeV}/c^2$, within and beyond the SM. Within the SM, Higgs boson search is one of the main topics at LHC. An exotic particle studies such as the leptoquark search at Fermilab (see Chapter 5) have explored the energy scale up to several hundred GeV

¹“ATLAS” stands for **A** **T**roidal **L**HC **A**pparatus, being constructed by ~ 1700 collaborators in 144 institutes around the world.

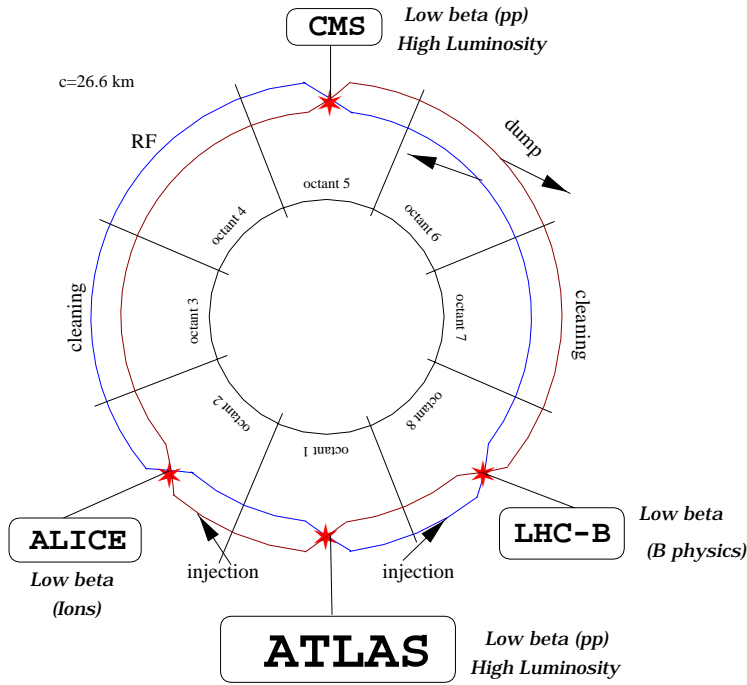


Figure 6.1: The geometrical layout of the LHC at CERN.

with the Tevatron accelerator ($\sqrt{s} = 1.8$ TeV). No solid evidence for such particles has been found up to today, and we now wait for the data from LHC to perform further searches. With the beam energy of $\sqrt{s} = 14$ TeV and very high luminosity at LHC, one can expect to perform a search in the leptoquarks for the mass regions up to TeV range. Other searches such as Super-symmetric particle (SUSY), Compositeness of leptons and quarks, and many other search topics are aimed to be studied at the LHC experiments. In the following Section, the search possibilities for leptoquark production at LHC with subsequent detection at ATLAS, is discussed.

6.1.1 Leptoquark searches at LHC

With Tevatron runs up to the end of 1995, lower mass limits for leptoquarks set by the CDF collaboration are: $M(LQ_1) > 210$ GeV/ c^2 , $M(LQ_2) > 202$ GeV/ c^2 , and $M(LQ_3) > 99$ GeV/ c^2 for three generations of the scalar leptoquark searches, decaying to charged leptons

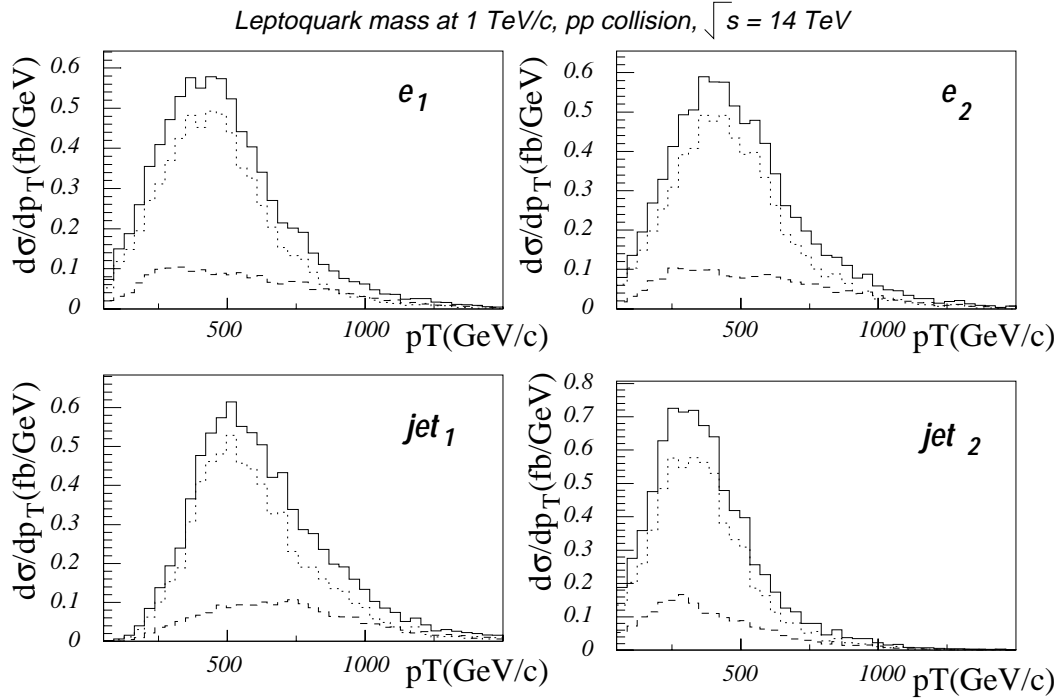


Figure 6.2: p_T distribution of decay product from pair produced first generation leptoquark of $M_{LQ} = 1$ TeV/ c^2 . The dashed (dotted) line is for $q\bar{q}$ (gg) fusion contribution. The solid line is for the total distribution.

and corresponding quark generations². At the LHC, observation of leptoquarks with mass up to ~ 1 TeV will be possible.

The kinematic distributions from pair produced leptoquark (the first generation, *i.e.*, decaying to electron channel) is shown in Figure 6.2 [110]. The leptoquark mass is set at 1 TeV/ c^2 . The production from quark-antiquark annihilation and gluon-gluon fusion contributions are indicated with dashed and dotted lines, respectively. The PYTHIA Monte Carlo is used with CTEQ2L parton distribution function [111]. The transverse momentum distributions of two leptons and two jets are shown. A cut of $p_T > 50$ GeV/ c has been applied on the leptons.

The major backgrounds coming from the SM to this search are; (1) $Z^*/\gamma^* + jets$ (Drell-Yan, QCD events), (2) $t\bar{t}$, (3) ZZ and WZ production (Electroweak processes). Calculations

²The result for 2nd generation search is from the result presented in this thesis. The 1st and 3rd generation searches are from the published results.

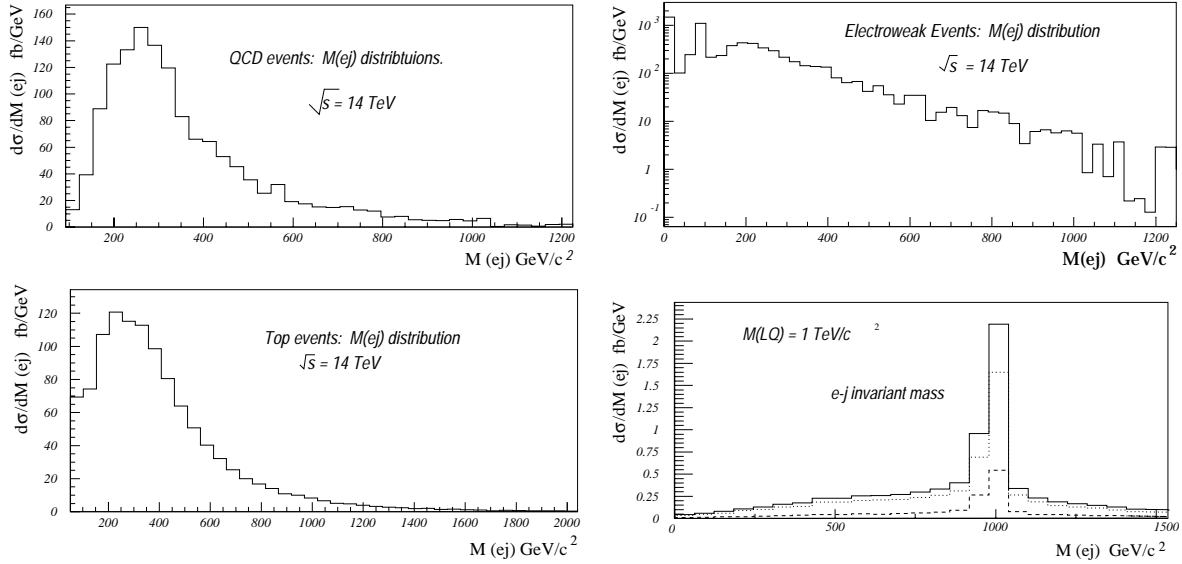


Figure 6.3: $M(ej)$ distribution from $1 \text{ TeV}/c^2$ for pairly produced scalar leptoquarks and 3 types of possible backgrounds. The dashed (dotted) line is for $q\bar{q}$ (gg) fusion contribution. The solid line is for the total distribution.

[112] show that the contribution from the process (3) is negligible compared to the other two. In the 3 cases, the background to leptoquark pair production can be suppressed by cutting two jets with $E_T > 200 \text{ GeV}$ and $|\eta| < 2.5$.

In speaking of the leptoquark searches at the ATLAS experiment, the mass resolution depends largely on the calorimeter jet energy resolution. From simulation studies at ATLAS, a jet energy uncertainty of 27 GeV is expected for a leptoquark mass of $1 \text{ TeV}/c^2$. This uncertainty will increase to 38 GeV for $M_{LQ} = 1.5 \text{ TeV}/c^2$.

Figure 6.3 shows the reconstructed invariant mass distributions for lepton-jet combinations for quoted of backgrounds compared with that of the leptoquarks of mass at $1 \text{ TeV}/c^2$. The leptoquark invariant mass distribution has tails on both lower and higher mass regions due to the misidentification of jets. Energetic jets from gluon radiation can be misidentified as jets decaying from the leptoquarks, which can give a wrong mass combinations.

Figure 6.4 shows a Monte-Carlo study of the $e - jet$ invariant mass reconstruction for $M_{LQ} = 1 \text{ TeV}/c^2$, after applying the above criteria with an integrated luminosity of 10^5 pb^{-1}

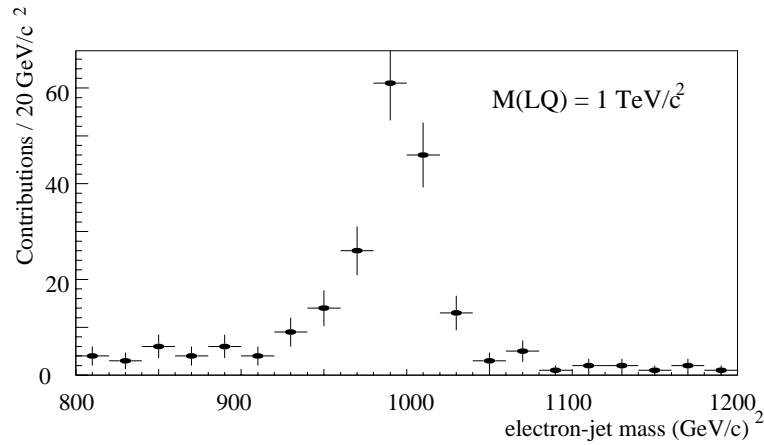


Figure 6.4: $e - jet$ invariant mass distribution with first generation leptoquark pair production at $M_{LQ} = 1 \text{ TeV}/c^2$ for $\int dt\mathcal{L} = 10^5 \text{ pb}^{-1}$ at LHC.

at the ATLAS experiment. A total of 131 events survived the cuts in this Monte Carlo study with the ATLAS acceptance and detector efficiency, also simulated and computed by a Monte Carlo simulation³. The signal can be easily be observed if the leptoquark exists at mass less than $1 \text{ TeV}/c^2$ with an integrated luminosity of 10^4 pb^{-1} , equivalent to one year of integrated luminosity with initial low luminosity running at LHC.

The cross sections for scalar leptoquark production at $p\bar{p}$ and pp colliders have been calculated [109], and they show the approximate limit of the leptoquark discovery possibilities as a function of the leptoquark mass. The numerical values of the cross section are calculated by determining the different resulting parton-parton luminosity.

Figure 6.5 shows the pair production cross sections for scalar leptoquarks at the Tevatron and the LHC for a mass values grater than $100 \text{ MeV}/c^2$. The different respective contributions to the cross section by quark-antiquark and gluon-gluon scattering are due to the behaviour of the different parton luminosities. However the quark contribution is the largest contribution at the Tevatron in this mass range, while at the LHC the dominant contribution is due to gluon-gluon fusion. Quark contributions also become important when M_{LQ} becomes large at the LHC. The signal limit in the Figures are computed by estimating the number of signals at $> 95\%$ Confidence Level, including associated backgrounds. They are estimated to be

³For more detail, see ref. [103].

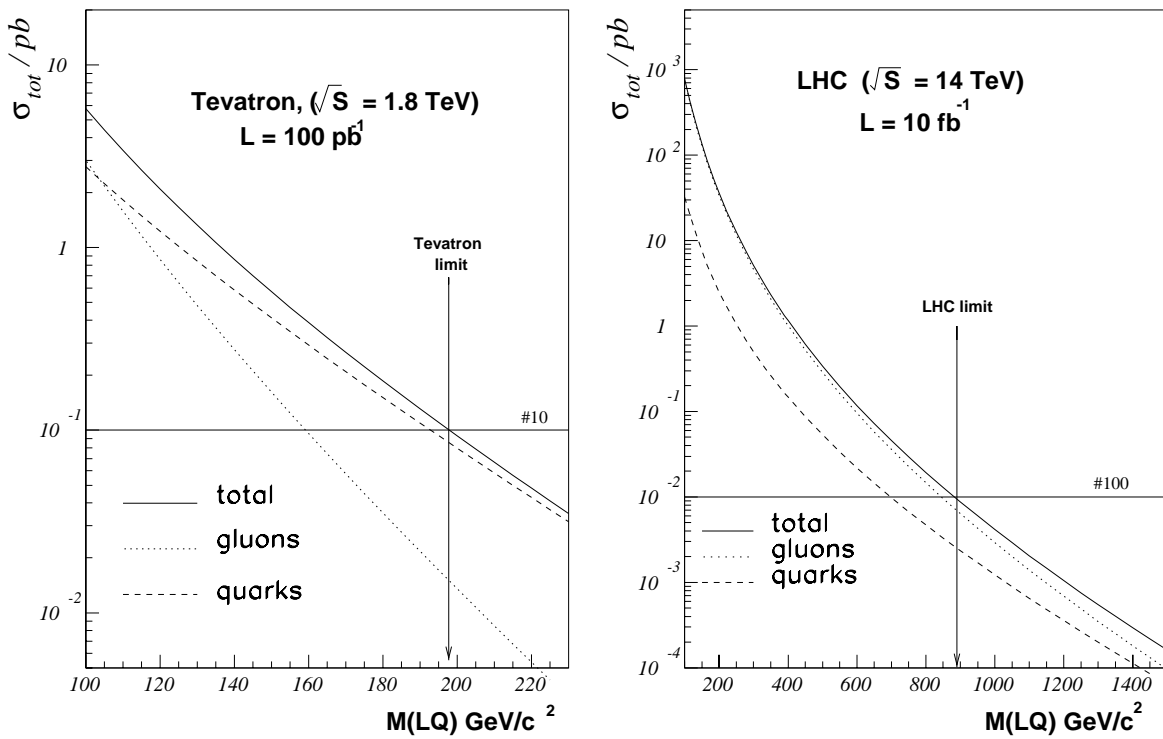


Figure 6.5: Integrated cross sections for scalar leptoquark pair production for Tevatron (Run 1992-1995) (left) and LHC (1 year low luminosity run) (right). Estimated number of signals at > 95% C.L., including associated backgrounds are 10 events for Tevatron and 100 events for LHC.

10 events for Tevatron, and 100 events for LHC. From this calculation, we can expect the discovery of leptoquarks for masses up to $\sim 1 \text{ TeV}/c^2$.

Searches for the Supersymmetric particles (SUSY) and Compositeness of leptons and quarks also represent the indirect searches for the leptoquark-like particles. See Appendix C for these experimental search limits at the ATLAS.

6.2 The ATLAS experiment

This general purpose detector (length 42 m , diameter 22 m , and weight 7000 tons) is aimed to have sensitivity to a variety of final-state signatures. Many of the phenomena being studied at the LHC require high luminosity and the primary goal of the detector is to have a fast operational rate and to provide as many signatures associated with identified high p_T electron, gamma, muon, jet and/or missing transverse energy signals. It is also important to have a good measurement of the vertex to identify the displaced vertices from heavy particle decays as well as distinguish the different event vertices in the high collision rate operation. The basic design considerations and goals for the ATLAS detector are listed below.

- ▷ **Tracking:** Finding precise vertex identification is important for differentiating tracks from different events at the same bunch crossing. Multiple events occurring from a same bunch crossing are expected at LHC collisions. At the ATLAS collision point, we expect ~ 23 interactions per bunch crossing during the operation at a luminosity of $10^{34} \text{ cm}^{-2} \text{ s}^{-1}$. An efficient and precise tracking system is required to differentiate these interactions. This role is particularly important for heavy flavour tagging from their displaced secondary vertices.
- ▷ **Calorimetry:** Electron and photon identification and jet energy measurement, as well as missing transverse momentum measurements require a good electromagnetic calorimetry.
- ▷ **Muon system:** Precise muon momentum measurement at both high and low luminosities, and low p_t trigger capability at low luminosity for b -physics studies.
- ▷ **Coverage:** A large coverage of pseudorapidity for efficient event reconstruction..

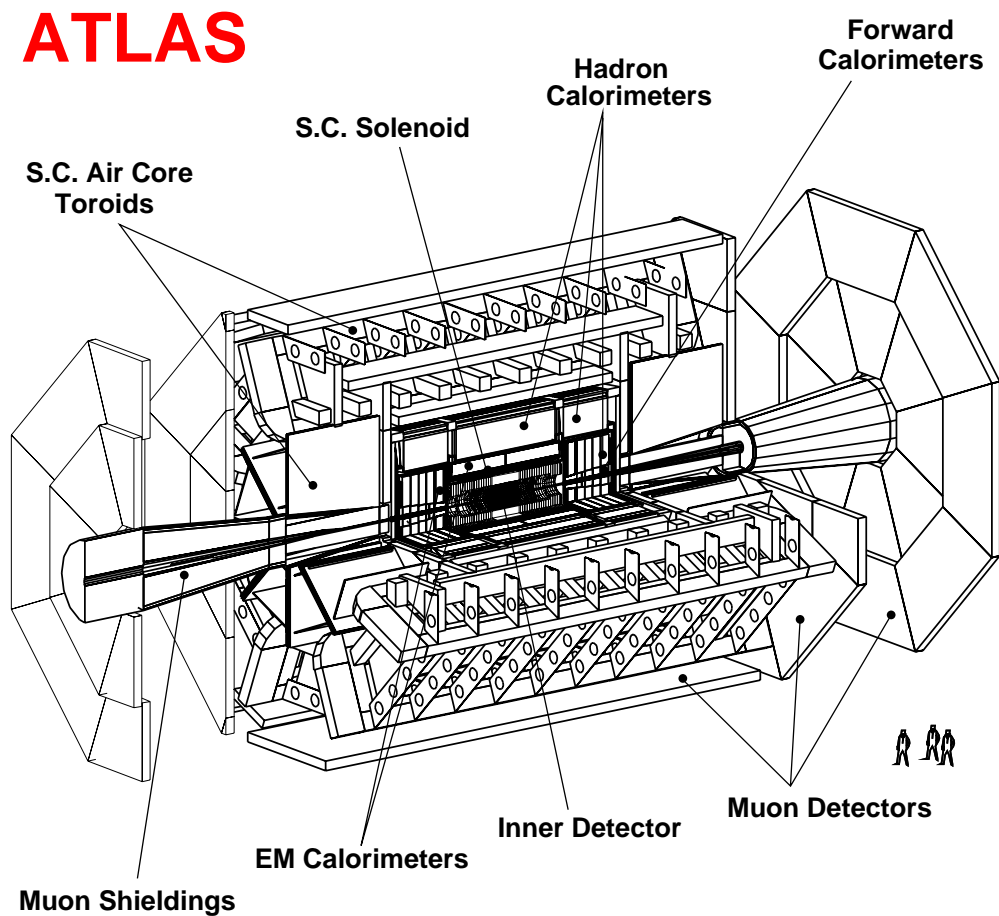


Figure 6.6: A overview of the ATLAS detector.

- ▷ **Trigger:** Efficient triggering for low p_T thresholds.

6.2.1 The ATLAS detector overview

Figure 6.6 shows the overall ATLAS detector layout and brief descriptions and coverage of sub-detector are given on the Table 6.2.

A brief overview of the ATLAS detector is presented in following Sections, concentrating on the inner tracking detector.

Detector component	Minimally required resolution, characteristics	η coverage	
		Measurement	Trigger
e.m. calorimetry	$10\%/\sqrt{E} \oplus 0.7\%$	± 3	± 2.5
Pre-shower detection	Enhanced γ - π^0 and γ -jet separation, direction measurements, and b-tagging with electrons	± 2.4	
Jet and missing E_T Calorimetry			
barrel and end-cap	$50\%/\sqrt{E} \oplus 3\%$	± 3	± 3
forward	$100\%/\sqrt{E} \oplus 10\%$	$3 < \eta < 5$	$3 < \eta < 5$
Inner detector	30% at $p_T = 500$ GeV Enhanced electron identification τ - and b-tagging Secondary vertex detection at initial luminosity	± 2.5 ± 2.5 ± 2.5 ± 2.5	
Muon detection	10% at $p_T = 1$ TeV in stand-alone mode at highest luminosity	± 3	± 2.2

Table 6.2: General detector performance goals [103].

6.2.2 Calorimetry

The Calorimetry system consisting of an inner barrel cylinder and end-caps, using intrinsically radiation resistant LAr technology surrounding the inner superconducting solenoid. It is surrounded over its full length by a hadronic scintillator tile calorimeter. A superconducting air-core toroid system surrounds the calorimetry system in order to provide muon momentum measurements. The ATLAS calorimetry must be capable of reconstructing the energy of electrons, photons, and jets in a wide energy range. It is furthermore necessary to have a full coverage in order to reconstruct the missing transverse momentum in an event. The schematic calorimeter layout is shown in Figure 6.7, and numerical characteristics are noted in Table 6.2.

6.2.3 Muon spectrometer and magnet

The magnetic field for the muon spectrometer is provided by a large superconducting air-core toroidal magnet, which has a length of 26 m and an outer radius of 19.5 m. It provides a total bending power of 3 ~ 8 Tm, depending on the pseudorapidity. The toroids form part of the three layer muon spectrometer, which has very an intrinsic muon momentum resolutions. The

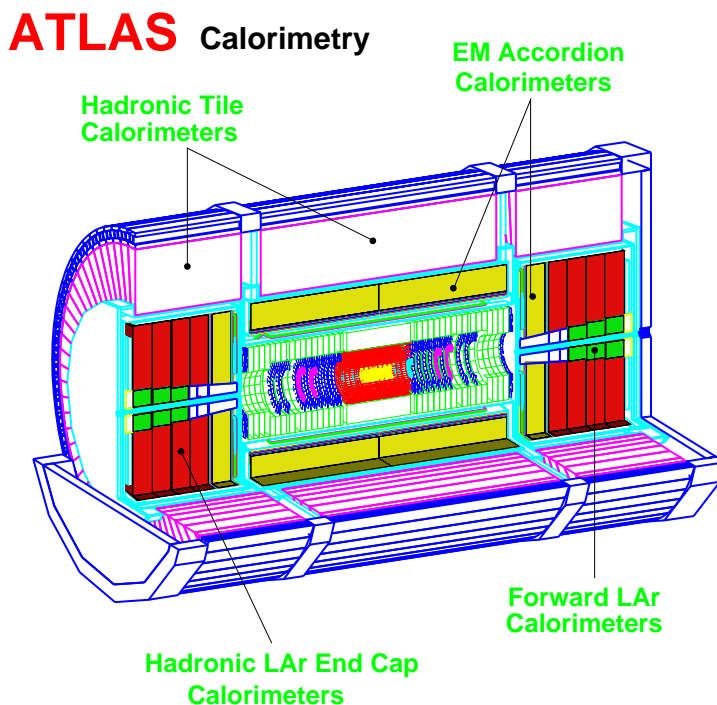


Figure 6.7: The schematic presentation of ATLAS calorimetry.

forward-backward direction is covered by the toroid cryostat, with a third layer against the cavern wall. The muon spectrometer has independent fast trigger chamber system. It covers up to $\eta = \pm 3$. A cross section of the muon spectrometer system is shown in Figure 6.8.

6.2.4 The Inner Detector

The overall layout of the inner detector system for ATLAS detector is shown in Figure 6.9. The cylindrical cavity occupies inside of the electromagnetic calorimeter cryostats and the barrel superconducting solenoid, in an envelope of 115 cm in radius and $\pm 345\text{ cm}$ along the beam axis. The design combines the high resolution detectors in the inner radii and continuous tracking elements at outer radii. The detectors will be placed in a 2 Tesla solenoidal magnetic field.

At LHC, various performance specifications [107] for the inner detector have been made. In Table 6.2, some specifications for the Inner Tracking Detector are summarised. A large tracking coverage ($|\eta| < 2.0$) is necessary for efficient particle identification and vertex finding

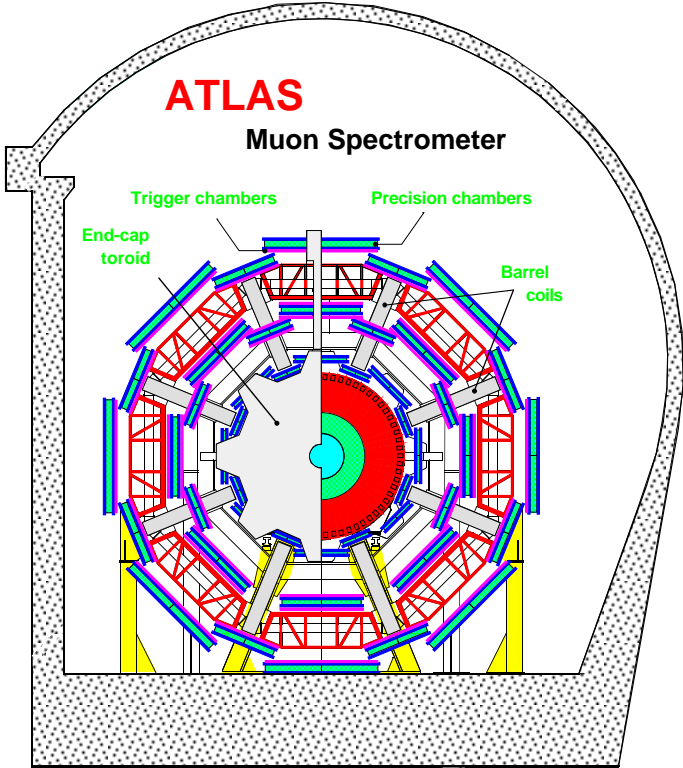


Figure 6.8: The Muon spectrometer system for ATLAS.

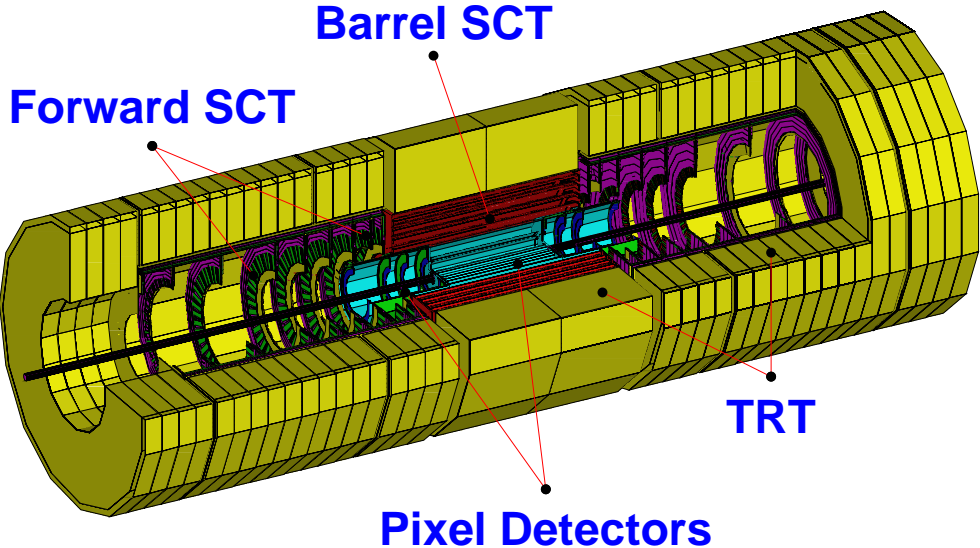


Figure 6.9: ATLAS Inner detector overview.

System	Position	Area (m ²)	Resolution σ (μ m)	Channels ($\times 10^6$)	Coverage (η)
Pixels	1 removable barrel layer	0.2	$R\phi = 12, z = 66$	16	± 2.5
	2 barrel layers	1.4	$R\phi = 12, z = 66$	81	± 1.7
	2 \times 4 end-cap disk	0.7	$R\phi = 12, z = 77$	43	1.7 – 2.5
Silicon strips	4 barrel layers	34.4	$R\phi = 16, z = 580$	3.2	± 1.4
	2 \times 9 end-cap wheels	26.7	$R\phi = 16, z = 580$	3.0	1.4 – 2.5
TRT	Axial barrel straws		170 per straw	0.1	± 0.7
	Radial end-cap straws		170 per straw	0.32	0.7 – 2.5
	36 straws per track				

Table 6.3: Sub-detector parameters of ATLAS inner detector[114]. The resolutions for the silicon detectors include charge sharing.

as well as for achieving a good momentum resolution. With $\sqrt{s} = 14$ TeV, some very high p_T charged tracks from the primary interactions will emerge. A precise momentum measurement is required for very high p_T charged tracks, up to the TeV scale. For full reconstruction of the multiple collisions in each bunch crossing (~ 23 collisions per bunch crossing) the tracking efficiency should be better than 95% over the full coverage and a wide p_T range ($>95\%$ for 5 GeV/ c , and $>90\%$ for $p_T > 1$ GeV/ c) for isolated tracks. Also to cope with multiple-interactions in a single bunch crossing, z vertex finding plays an important role. A measurement of the z coordinate of primary vertices with at least four charged tracks is expected to be better than ± 1 mm. Good electron identification ability is needed for the trigger and the subsequent reconstruction. For heavy flavour decays, tagging is made by vertex finding, and we expect a good tagging efficiency for b quark jets ($>30\%$). This implies the need for a very high granularity of the vertex detector. This is also very important for displaced τ vertex finding.

In order to satisfy these requirements, as well as criteria such as minimal material, radiation hardness, cooling, etc., the layout of the inner detector has undergone intense studies to optimise its design in a cost-effective way. The ATLAS experiment will take full advantage of the available detector technologies existing today, and on the basis of the research and development studies the associated electronics added to the detector components are thought radiation resistant enough to be used in the LHC inner cavity.

The proposed design for the layout of the inner detector is listed on Table 6.3. The large track density requires a use of tracking layers with high granularity and physics requirements

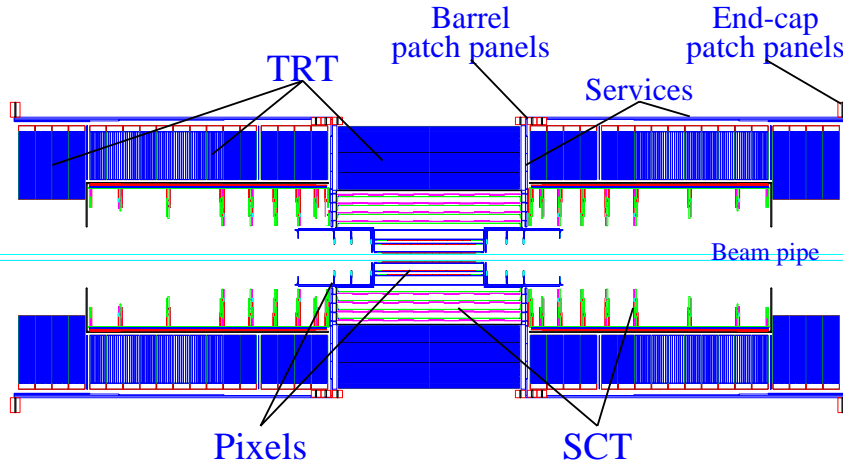


Figure 6.10: A cross section of ATLAS Inner detector for quadrant layout through the beam axis.

demand for a good momentum resolution. These criteria are satisfied with the use of semiconductor detectors. Pixel and strip silicon detector are called Semi-Conductor Tracker (SCT), and it will provide powerful stand-alone pattern-recognition performance with excellent transverse spatial resolution of $25 \mu m$ and a polar angle resolution of $< 2 \text{ mrad}$.

Figure 6.10 shows a cross-section schematic view of the detector layout. Closest to the beam pipe, pixel detectors cover the most inner radii for its high-granularity and high-precision measurement abilities without any of the ambiguities associated with projective geometries (ghost hits, which can be introduced by strip detectors). The components of the Pixel detector are three layers of barrel pixel tracker ($r = 4.0, 11.0, 14.2 \text{ cm}$ and $z = \pm 38.8, 38.4, 33.4 \text{ cm}$ for 3 barrels), covering the central regions and four end-cap disks ($r = 11 \text{ to } 20 \text{ cm}$, positioned at $z = 47.3, 63.5, 77.6, 107.2 \text{ cm}$) covering the forward/backward. Together it yields a total of 140 million readout channels. The 0-layer provides the full geometrical acceptance up to $\eta = \pm 2.5$ and all 3 layers have full acceptance to $\eta \sim \pm 1.5$.

The silicon strip detector system consists of barrel detectors and two symmetric end-cap detectors. Four barrels of silicon microstrip detectors will be installed outside of the Pixel detectors. This part of the tracking detector will provide four precision measurements per track in the intermediate radial range, allowing to measure the momentum, impact parameter, and vertex position of the charged particle emerging from the interactions. Four barrels will be placed at $r_1 = 30.0$, $r_2 = 37.3$, $r_3 = 44.7$, and $r_4 = 52.0$, each with active half-length of

74.5 *cm*. The end-cap silicon strip detector modules are arranged in wheels, similar to the Pixel End-cap detector arrangement. A total of 9 End-cap wheels on the each side (18 total) will be installed, between $z = \pm 83.5$ *cm* and $z = \pm 277.8$ *cm*. The silicon strip detectors will have a total of 6.2 million readout channels.

The Transition Radiation Tracker (TRT) is based on the use of 4 *mm* diameter straw detectors, employed with xenon gas for electron identification capability. The TRT system will be placed at most outer radii in the Inner Detector and it will provide a large number of tracking points, typically 36 points per track. It has a possibility for a good pattern recognition and high precision in the ϕ coordinate. The TRT consists of central section $|\eta| < \sim 0.7$ and two End-cap sections consisting of multi-plane wheels. The barrel section of the TRT detector will cover a radial range from 56 to 107 *cm*, extending to $|z| = 74$ *cm*. The End-cap section will cover a radial range from 48 to 103 *cm* with $|z|$ range of 83 to 335 *cm*.

Design considerations for the inner tracking, focusing on the silicon strip detector and its front-end readout electronics, is discussed in the next section.

6.3 The Semiconductor Tracking detectors (SCT)

The RD2 [108] collaboration was formed for research and development of a Silicon Tracking and Preshower detector (SITP) for the ATLAS experiment in 1990. Its aim was to evaluate the feasibility of a silicon tracking and/or preshower detector preceding the calorimeter in the ATLAS apparatus. Later in 1992, the project was changed to Silicon Tracking (SIT). Silicon was chosen as the active detector medium for its unique properties of a high intrinsic detection efficiency, a good pulse-height resolution, and a fast signal collection. The project faced the challenges of the development of a radiation hard detector, a fast and low noise signal readout electronics with the lowest possible power consumption, and a lightweight mechanical support structure with associated cooling, and a readout cable layout. The RD2 collaboration activities also included simulations and the test beam studies of the benchmark detector in a realistic LHC environment. Major aspects of this work have been incorporated into the Inner Tracker Project, and in particular the Semiconductor Tracking detector (SCT). The silicon strip detector system is divided into two parts, namely the central barrel system and forward/backward end-cap system. Details of the project can be found in reference [114].

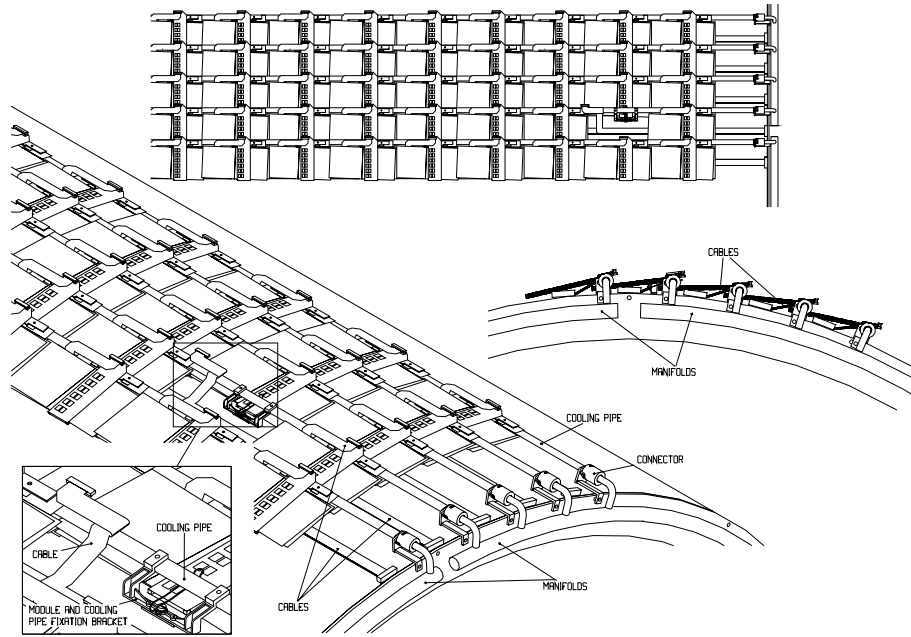


Figure 6.11: SCT layout for Silicon module and barrel overview.

6.3.1 The Barrel Silicon Tracker

The initial proposition of the barrel tracker with SIT consisted of three detector layers at radii $r = 70 \sim 100 \text{ cm}$. At SCT, the basic concept silicon detector module remains unchanged, but with four layers of silicon tracking, covering the radius of 30 cm to 52 cm and η range up to ± 2.5 (see Table 6.3). One unit of silicon detector will have an active area of $6.16 \times 6.20 \text{ cm}^2$ with 768 readout strips of $80 \mu\text{m}$ pitch and 12.32 mm long. The barrel system will contain a total of 34.4 m^2 of active area with ~ 3.2 million read out channels. Because of radiation damage to silicon detectors from the charged and neutral radiation, the detectors will be operated at -7°C . The power consumption expected from the barrel system is $\sim 13 \text{ kW}$, and an associated cooling system to maintain the low operating temperature will be required.

The modules, consisting of two single-sided silicon strip detector (768 Si strips on a detector) panel mounted together with front-end readout electronics and associated readout system, are placed on the support structure to form a barrel, as shown in Figure 6.11.

In the current design, the barrel system will contain 12×32 (barrel 1), 12×40 (barrel 2), 12×48 (barrel 3), and 12×56 (barrel 4) modules. All together 4 barrels will contain a total

of 8,448 single-sided silicon strip detectors on 2112 modules. Some of the engineering issues to build this tracking detector are:

- ▷ The spatial precision of tracking must be $\leq 22 \mu m$. The support structure must have small fraction of a radiation length. Installation of the detector should provide spatial stability at the $10 \mu m$ level in $r - \phi$.
- ▷ Provision the multiplexed readout from the detector with zero suppression. With 4 barrels of silicon tracker alone, there will be 3.2 million readout channels at interaction frequency of 40 MHz.
- ▷ Radiation hard technology is required for both detector materials and associated electronics, with full operational capability up to exposure of 100 kGy.
- ▷ Minimum material in the detector media.
- ▷ Cooling [108] to keep the detector at operational temperatures below $0^\circ C$.

Since 1992, one of the major activities has been the development and testing of the fast, dense, low power front-end readout electronic with cost-effective fabrication. The specification and development on the front-end readout electronic is detailed in references [108, 115].

- ▷ **Signal to Noise:** One of the most important issue is to obtain high signal to noise ratio (S/N) over long operational period under high LHC radiation environment. After 10 years of operation, the noise level should remain better than 12:1 on S/N, or 1500 electron equivalent noise charge (ENC). A minimum bias particle traversing the medium produces charge equivalent to $\sim 25k$ electrons in $300 \mu m$ thick silicon detector.
- ▷ **Power Consumption:** Power consumption should be minimised ($< 40 \text{ mW } cm^{-2}$), corresponding to a total power consumption of $< 13 \text{ kW}$. The generated electronics heat must be cooled by a refrigeration system. One can minimise materials introduced in the detector media by reduced cooling capacity, that is lower power consumption.
- ▷ **Speed:** Operation with 40 MHz bunch crossing frequency. This demands for an internal analogue buffer with event selection logic within. The level 1 trigger is expected to be in order of 100 kHz.

- ▷ **Radiation:** The expected radiation dose for silicon tracking detector is order of $4 \sim 10$ kGy/year [114]. The electronics must be perform reliably following intense radiation doses over an extended period.
- ▷ **Material:** Minimum material must be introduced. This implied the need for dense electronics.
- ▷ **Integration:** To perform a data processing with 40 MHz event rate, an analogue pipeline technology has been proposed. Signals coming from the silicon detector are first amplified at the pre-amplifier, then stored in an array of analogue capacities pending a first level trigger decision. The selected analogue signal is then digitised and sent out.

The RD2 collaboration developed the first fully integrated readout chip called ADAM in 1994, and intense laboratory tests and test beam study analysis were performed. This prototype design provided all of the required functionality for LHC silicon tracking applications. The only function not implemented on this chip was sparsification and one incompatibility with the LHC chip was line density at this prototype level. The chip was designed by a collaboration of CERN, Genève University, and Rutherford Laboratory to include all the functionality required for front-end silicon strip detector. In particular, the chip was aimed to have an on-chip ADC allowing digital readouts. It was successfully fabricated and test showed the full functionality.

In the next Chapter, the description of this chip with its test results are presented.

Chapter 7

The ADAM Chip

The first prototype of an integrated Front-End readout chip for the silicon tracker of the ATLAS Inner Tracking Detector for the LHC at CERN, the ADAM¹ chip, was fabricated and tested with a probe station for its direct performance and general functionality and with a full test bench laboratory set up using a data acquisition system. The chip was also tested in the realistic test beam environment.

7.1 Introduction

The ADAM chip integrates a pre-amplifier (NICON), an analogue pipeline of 32 channels by 112 cells deep memory (DHARP), an Analogue to Digital Converter (CRIAD), a digital read-out memory, and associated control logic. Sophisticated tests in laboratory have been made. We build a VME-based interface to the ADAM chip, with data acquisition system programmed with LabView [125]. The interface allows to take any desirable input signals, modify the internal functionality of the chip, and accept output signals of the chip with readout memory.

The test was made to show the functionality and feasibility of the chip's performance at the 40 MHz bunch crossing speed of the LHC. We measure a sensitivity of over 20 mV per 4 fC of injected charge ² with an r.m.s. noise of less than 1.8 mV . The resolution of two closely

¹ADAM stands for **A**tlas **D**etector **A**nalogue **M**emory. Development team was formed with F. Anghinolfi from CERN and R. Bonino, A. Leger, D. La Marra, J. P. Richeux, and H. Kambara from Université de Genève.

²The injected charge of 4 mV on 1 pF load capacitance was used as one minimum ionising particle (MIP)

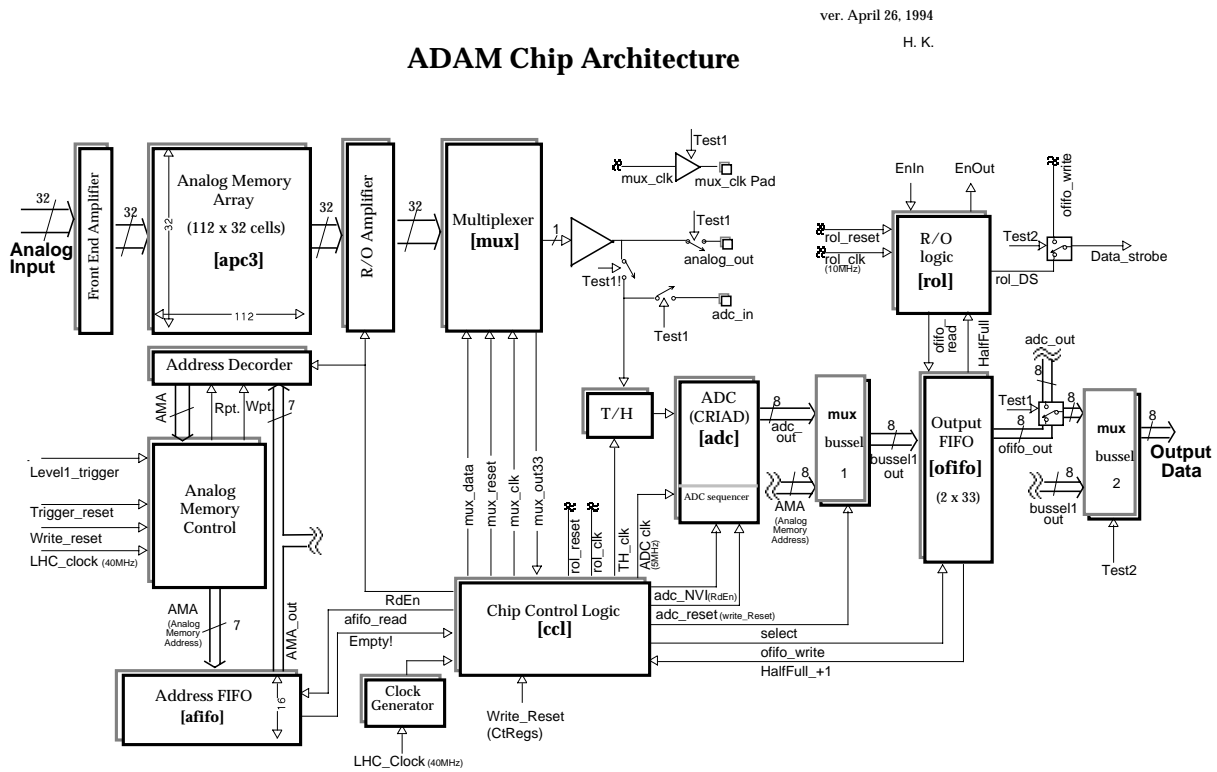


Figure 7.1: The ADAM chip architecture.

separated signals was measured to be 25 ns, which is the LHC bunch crossing clock. The chip was also tested in the realistic test beam experiment at CERN following the laboratory test and it showed satisfactory performance for the LHC operation.

7.2 The ADAM Chip

7.2.1 The Architecture of ADAM

The architecture of the ADAM is an integration of various components which were previously individually developed and tested by the RD2 Collaboration. The ADAM chip is composed of:

signal.

- Front-End Amplifier; NICON³,
- Analogue signal pipeline memory; DHARP⁴,
- Analogue pipeline control logic; APC⁵,
- Analogue to Digital Converter; CRIAD⁶,
- Digital buffer for Readout; OFIFO⁷,
- Readout Logic for the digital buffer; ROL⁸, and
- General chip control logic, CCL⁹.

The architecture schematics of the ADAM chip is shown in Figure 7.1. With the exception of sparse data readout, the architecture contains all the components required for digital readout at LHC. Of particular interest in this architecture is the integration of analogue memory, digital control, and digitisation functions.

Figure 7.2 shows a photograph of the ADAM chip. The chip was designed and simulated for digital functionality with Verilog [117] simulation software. A brief description of each component is presented in following Section¹⁰.

7.3 ADAM chip components

The fully integrated readout electronics consists of many components, and each elements had been developed individually and had gone through extensive testings before arriving the state of integration.

³New, **I**CON amplifire.

⁴Analogue pipe line used Harp technology. **D** stands for the new version

⁵**A**nalogue **P**ipeline **C**ontrol

⁶**C**harge **R**edistribution **I**nterleaved **A**nalog to **D**igital converter

⁷**O**utput **F**irst **I**n **F**irst **O**ut Buffer

⁸**R**ead **O**ut **L**ogic

⁹**C**hip **C**ontrol **L**ogic

¹⁰For complete description of the individual components, see ref. [118].

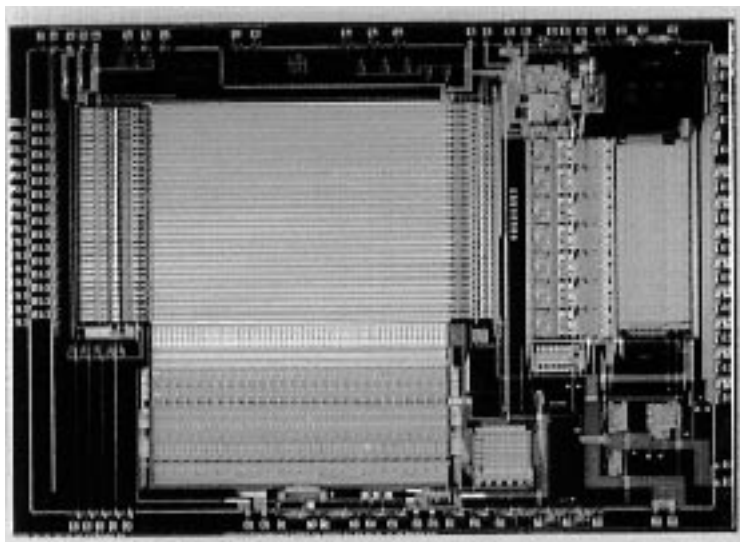


Figure 7.2: Photograph picture of the ADAM chip. Actual size is $10.9 \times 7.6 \text{ mm}$.

7.3.1 NICON front-end pre-amplifier

The previous version of the ICON [118] Front-End amplifier was improved to operate at a 3 GHz gain-bandwidth actual mode of amplifier stage, NICON for this integrated chip. Figure 7.3 shows a schematic presentation of the NICON chip.

The n-MOSFET M1 channel input is a grounded gate transistor of size $W/L = 1500\mu\text{m}/1.5\mu\text{m}$ and operates in the weak inversion region, at a drain current $I_d \leq 80\mu\text{A}$. The cascade MOSFET M2 n -channel conveys the input current on the integrating output node. The output node bias voltage is stabilised to V_{ref} by the slow amplifier A which does the stabilisation by controlling the current I_{comp} source. This technique offers the advantage of compensating the effect of the detector dark current in the case of a DC input connection. The NICON circuit has been fabricated in a $1.5\mu\text{m}$ double poly, double metal CMOS process.

A rise time (10% to 90%) of 13 nsec is measured with an 8pF input capacitance. The peak amplitude is 42 mV for 25000 electrons at the input, equivalent to a MIP signal. The power consumption of the circuit is measured as low as $400\mu\text{W}$.

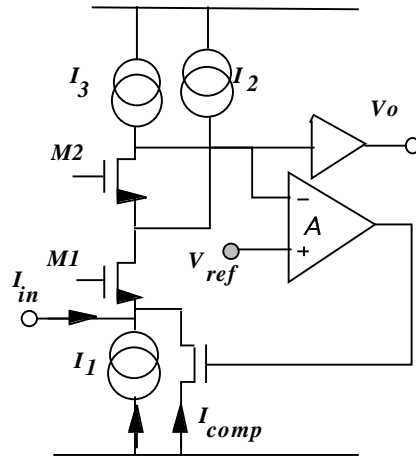


Figure 7.3: A schematic presentation of the Cascaded Grounded Gate amplifier (NICON).

7.3.2 DHARP

The analogue memory is configured to provide the necessary shaping function after the NICON Front-End amplifier. The shaping is performed during the readout process by a correlated double sampling technique (CDS).

The basic diagram of the analogue memory with CDS is shown in Figure 7.4. Two consecutive voltage samples V_1 and V_2 of the NICON output are stored in the two capacitors C_1 and C_2 of one memory cell. The first experimental DHARP chip contained 64 cells per channel. A second version of the DHARP (DHARP2) was designed with 112 cells. The LHC requirement of at least $2\mu\text{sec}$ trigger latency corresponds to 80 cells, or time columns, with 40 MHz clock. The ADAM was fabricated with 112 time columns to satisfy this $2\mu\text{sec}$ latency, plus 32 cells of memory to hold any incoming triggers with minimum dead time. The clocking scheme is such that all cells are periodically re-addressed. A particular cell can be protected against further sampling, when it is marked by the positive level 1 trigger signal. At read out the two capacitors of two different cell are connected to the inputs of a differential readout amplifier. The output of the amplifier represents the voltage difference between the two consecutive samples. The differentiation process (shaping) is thus performed with a shaping time equal to the interval between two samples (25 nsec). For differentiation being done by the simultaneous readout of two consecutive samples, a good rejection of parasitic common mode

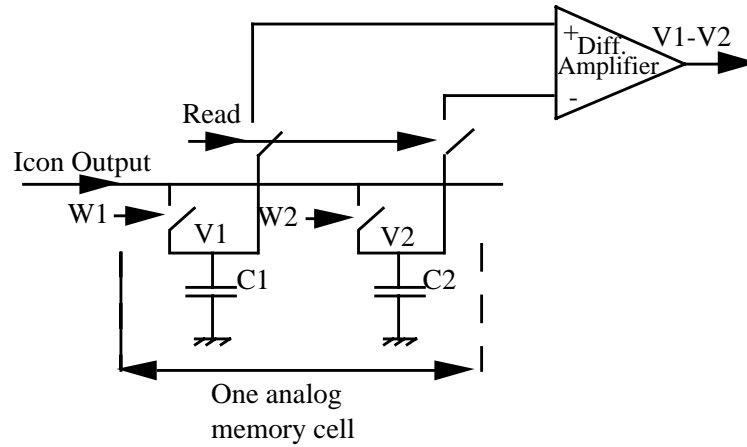


Figure 7.4: Simplified schematic of DHARP.

noise (from substrate, clock lines or power supplies) is expected. The DHARP2 circuit with 32 channels of 112 cells has been fabricated and tested. The chip is fully functional at 40 MHz sampling rate [119]. The measured signal amplitude and the noise performance did not reach the full specification values because of mismatch in DC levels and an asymmetric structure in the implementation of two capacitors at the inputs of the readout amplifier. These problems are now identified and we expect the corrected version to provide an analogue performance following the pipeline in accordance with these measured on the NICON prototype. The characterisation shows that the full signal is contained in one readout sample, with a power consumption per channel of less than 2 mW; the common mode noise at the output is 1.5 mV *r.m.s.* and the offset variation from capacitor to capacitor is 2 mV *r.m.s.*

7.3.3 CRIAD Analogue to Digital Converter

The CRIAD [120] ADC consists of a 6 bit ADC with 2 bits of segment specification.

The architecture (see Figure 7.5) consists of one track & hold (T&H) and a two-step analogue-to-digital converter. During the first step, a 2-bit flash nonlinear conversion is performed. The dynamic range is divided into four unequal parts by a resistor string: $R - R - 6R - 24R$. This allows a determination of the corresponding range (segmentation) of the input signal. The second step is performed by a 6-bit linear charge-redistribution ADC in the range previously indicated by the 2-bit flash converter, using seven 6-bit Successive Approximation ADC

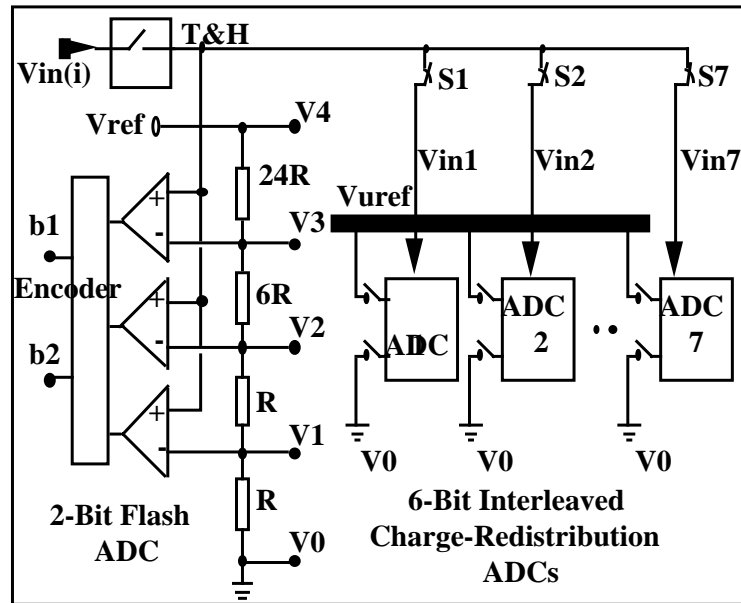


Figure 7.5: Architecture of the piece wise linear ADC, CRIAD.

(SADC) placed in the sequence.

The consequent 64 non-linear segments of ADC covering 2048 mV of range. The first segment has resolution of 1 mV , covering 64 mV of range, second with 2 mV resolution for 128 mV range, third with 8 mV resolution for 512 mV , and the last segment is with 32 mV resolution covers 2048 mV . Figure 7.6 shows the 4 ranges choices of the CRIAD.

The ADC takes the sampling first with the flash part to determine the input range of the signal and process the digitisation with appropriate segment. SADC's then digitises the input signal with the reference voltage previously specified by the flash section.

In order to reach the required data throughput of the system, seven time-interleaved charge- redistribution A/D (ADC 1 to 7 on Figure 7.5) converters are needed behind the SADC. Each ADC makes a comparison decision each clock cycle, and requires 7 clock cycles (1 clock cycle for sampling and 6 clock cycles for 6-bit digitisation). This architecture provides a full 8-bit digitised output at each clock cycle. 2 bits indicate the range value, the 6 last bits are the conversion outputs.

The CRIAD has been fabricated and fully tested [121], and Table 7.1 summaries the results. Figure 7.7 shows a 6KHz, sinusoidal signal with 800 mV amplitude, reconstructed from the

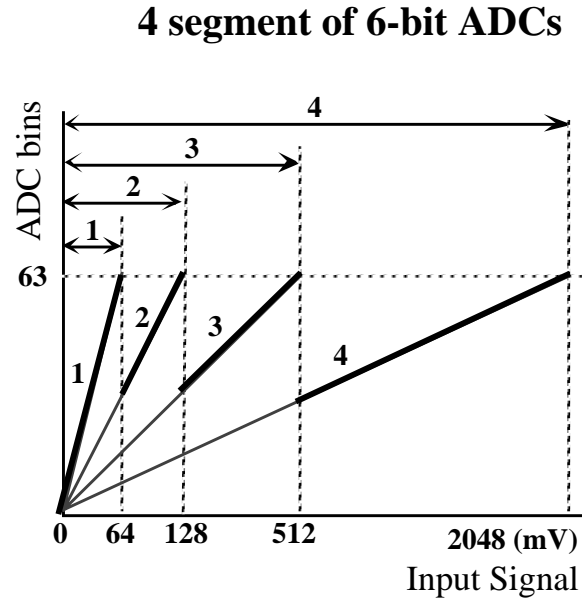


Figure 7.6: The CRIAD segment structure.

Characteristics	Value
Maximum Resolution	8 bits piecewise linear (11-bits effective)
Sampling rate	5 MHz
Differential Non-Linearity	± 0.5 LSB
Integral Non-Linearity	± 0.5 LSB
Input Range	0 to -2.048 V
Power Supply	± 2.5 V
Power consumption	25 mW
Active area	5 mm ²
Technology	1.5 μ m CMOS

Table 7.1: CRIAD experimental results.

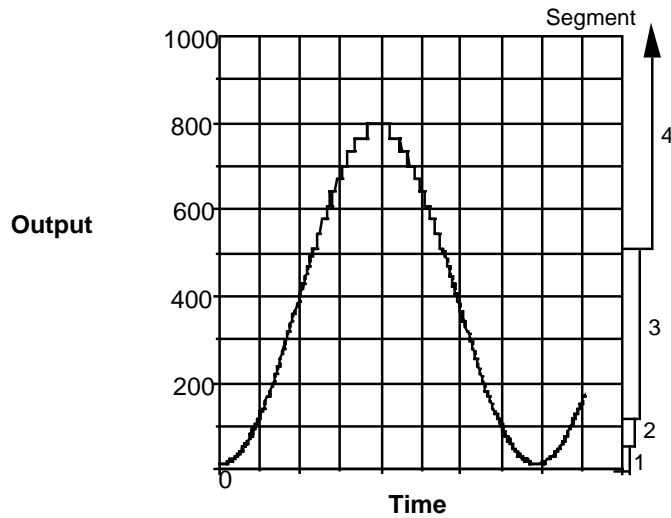


Figure 7.7: Output code for a 800 mV amplitude.

digital outputs of the ADC running at 5 $Msamples/sec$ with the flash part operating and automatic segment switching. The variation of the quantification step depends automatically on the signal amplitude that is observed, or can be manually fixed.

The CRIAD structure, implemented in the ADAM chip, allows a full characterisation of the analogue performance, including noise, pedestals and dynamic range. If a 6 bit dynamic range is sufficient in the readout of a tracker at LHC, the flash part can be removed from the final electronics implementation with a consequent reduction in power consumption.

7.3.4 APC-3 Logic and Pipeline Address

An APC3 [122] chip was designed to integrate the digital logic necessary to retrieve the data from a level 1 trigger. It was fabricated at the beginning of 1993 and tested during the remainder of that year both at RAL and at CERN. The chip consists of an analogue section containing the pre-amplifiers, an analogue memory array, and a multiplexer and a digital section with the memory management logic that is common to all channels. The major components of this logic are shown in Figure 7.8.

The functionality of the digital logic was tested at 66 MHz using a HP82000 200 MHz digital IC tester at RAL. Then extensive measurements of the chip's analogue performance

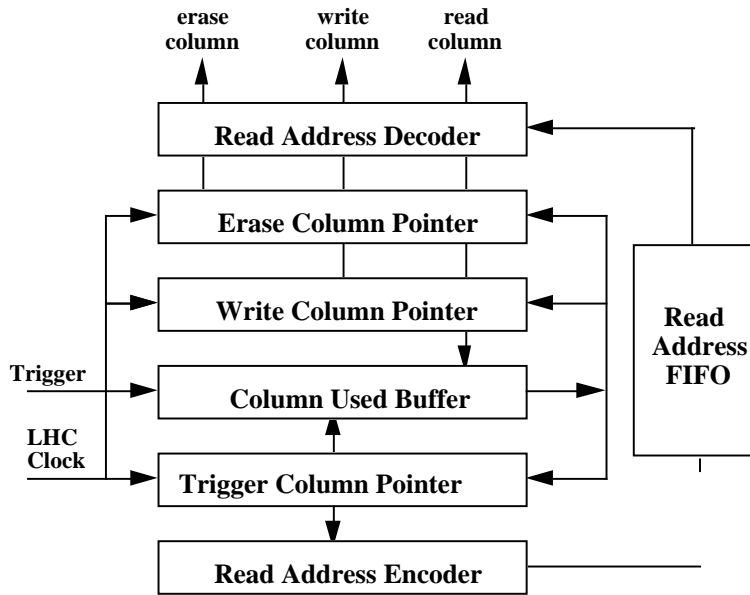


Figure 7.8: Memory management logic in PAC-3 chip.

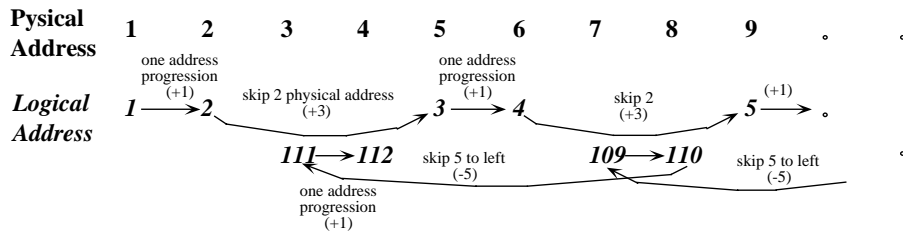


Figure 7.9: The APC3 new logic for address pointers.

were made using a VME based data acquisition system. All measurements were performed using continuous write and read operations, with a write frequency of 40 MHz and a read frequency of 5 MHz.

The address of the analogue memory is readout by APC3 logic control . In the initial prototype version of PAC logic, the write and read pointers progress along the analogue memory in the order of physical layout. At the end of the pipeline cell, the pointers will be returned to the first cell of the memory. This jumping logic at the end of the pipeline caused unstable pedestal and high noise immediately after the jump of the pointers. For integration within ADAM, a modification was developed and applied in this chip. The write and read

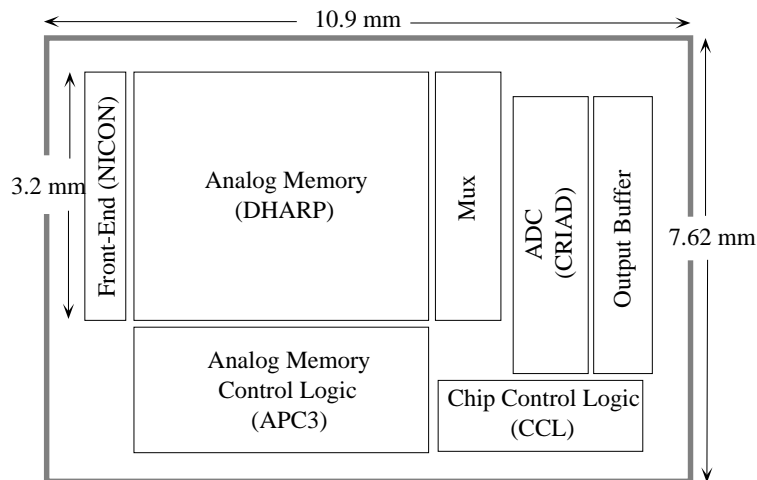


Figure 7.10: The ADAM floor plan. Components are drawn to approximately proportional size.

pointers will progress in non-linear order with groups of 4 time slots as shown in Figure 7.9.

7.3.5 ADAM Chip Specifications

Figure 7.10 shows the floor plan of the ADAM chip, and table 7.2 shows the specification of the ADAM chip.

7.4 The ADAM Test Setup

The Adam Test Setup is a stand alone system to characterise the ADAM chip with its full functionality. The setup consists of three main components; the ADAM chip on the *piggy back board*, the Adam Testing Board, and Test Board Controller. The plan over view of the test bench set up is shown in Figure 7.11.

7.4.1 The ADAM Test board

We have built an electronic circuit board providing an interface to the ADAM chip, the *TESTADAM – DPNC – 158*, developed at University of Geneva¹¹ The board allows the

¹¹Thanks to Annie Leger, University of Geneva.

Front-end Rise Time		13 ns (10 - 90%)
Coupling		AC or DC
Analogue Memory	Length	112
	Cell size	40 μ m \times 100 μ m
	Cap. Value	2 \times 0.2pF
Address FIFO		16words (7 bits)
Analogue Multiplex speed		5MHz
ADC (CRIAD)	Ref. voltage VH	3.0 V
	Ref. Voltage VL	1.0 V
	Dynamic range (total)	2.048 V
	Segment I Dynamic Range	64 mV (resolution 1 mV)
	Segment II Dynamic Range	128 mV (resolution 2 mV)
	Segment III Dynamic Range	512 mV (resolution 8 mV)
	Segment IV Dynamic Range	2048 mV (resolution 32 mV)
	Output	8 bits (of 2 of segment specification)
	Sampling Rate	5MHz (maximum)
Read Out buffer FIFO size		66words (8 bits)
	Processor speed	10 MHz
Input/Output mode	Clock, Trigger	Differential, Voltage Sensitive ;1.0 V
	Read-enable IN	Differential, Current mode 100 mA
	Read-enable OUT	Differential, Current mode 100 mA
	Data Output	Single ended Current mode 100 mA

Table 7.2: ADAM specifications.

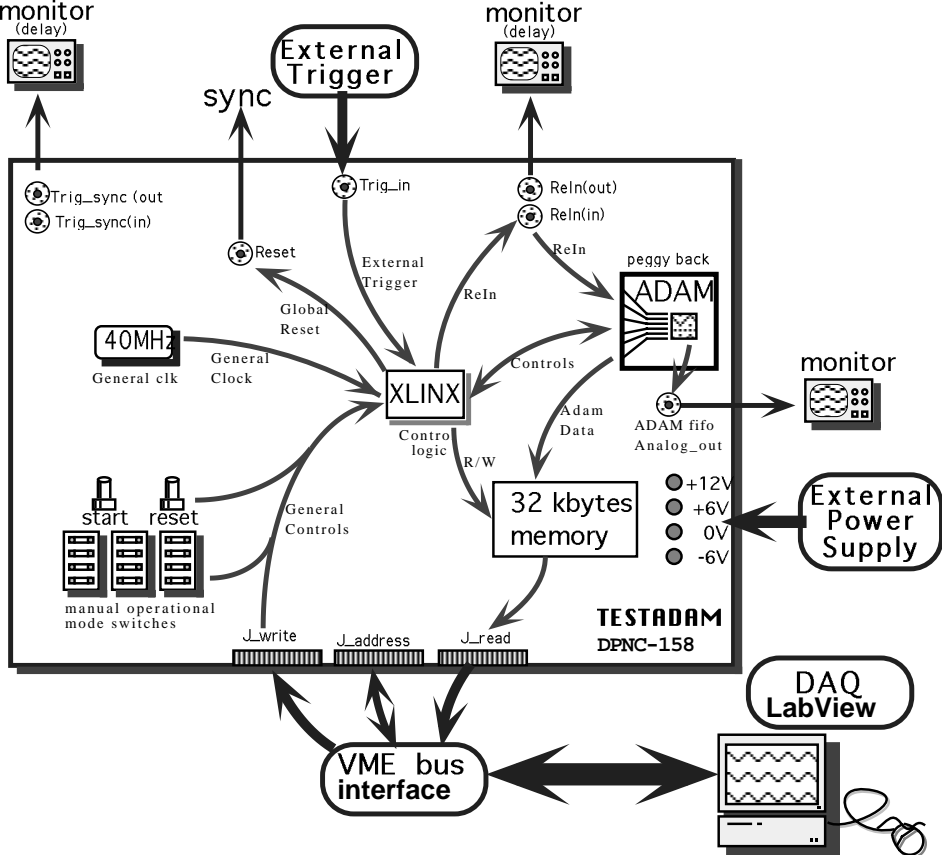


Figure 7.11: The ADAM Test bench setup.

ADAM chip to operate either manually or from DAQ system via a VME interface. The manual operation permits the board to operate without a VME interfaced DAQ system, which is useful to study the functionality of the ADAM at a probe station. An appropriate card has been developed to probe the chips under test. The ADAM test board generates a 40 MHz clock and synchronises the external signals before they are sent to the ADAM chip. The on-board generator also supplies the master 40 MHz clock of the chip. The board uses XLINX programmable logic to control its operation. The XLINX can be programmed from an external source to verify the operation of the board logic, or charged with fixed logic on board. In normal testing operation at the test bench, the XLINX logic is read from on-board memory at the time of power turn-on. However, this can be changed or monitored with on-line analysis software for studying further functionality and performance of either the board or the ADAM chip.

7.4.2 ADAM Test board Sequence

The ADAM test board with its programmable control interfaces via the VME data transfer bus and a 32k output data buffer, providing various options for the operational mode of the ADAM chip. The control logic of the XLINX reads the operation mode and sends the specification and control sequence to the ADAM chip. The logic sequence is:

- (0) Global reset.
- (1) Waits for the start signal.
- (2) Reset the memory bus and send a reset to ADAM.
- (3) Sends end-of-reset flag.
- (4) Trigger waiting, then send it to ADAM.
- (5) Store the data in the on-board memory and wait for the end-of-block from ADAM.
- (6) Go back to (1) if no data transfer is specified.
- (7) Transfer the data from the on-board memory to the VME bus.
- (8) Wait for the end-of-data flag from the memory.

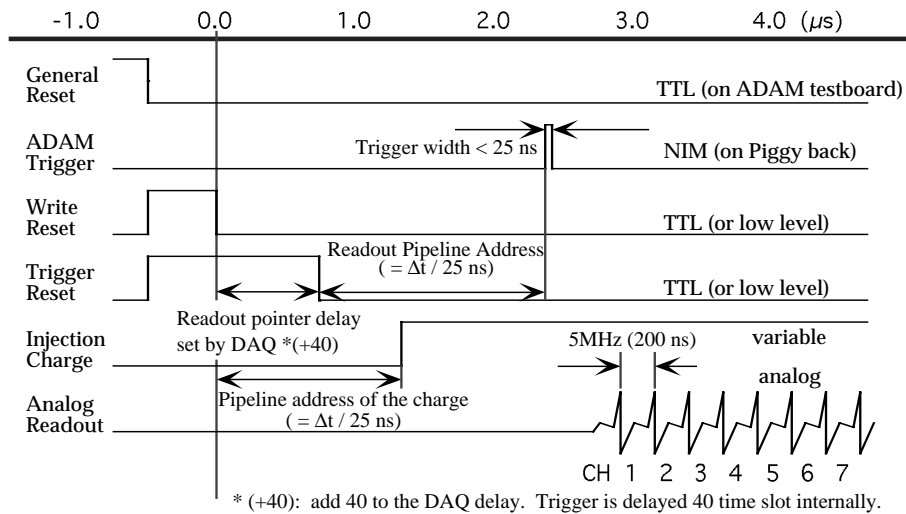


Figure 7.12: Timings of the control and output signals to the ADAM chip.

- (9) Go back to (0) for manual operation, (1) for auto operation with reset, (4) for auto operation without resetting. Analogue Memory Control Sequence.

With the DAQ system on the laboratory test bench setup, the control signals are sent via a VME bus. The LabView software was used to develop the control sequence on the Macintosh computer. Figure 7.12 shows the various timings of I/O signals to the ADAM chip. The DAQ system has the flexibility of changing the timings of various control signals to study the ADAM chip with precise timings.

The ADAM analogue memory control sequence proceeds as follows. First, the general reset signal is sent from DAQ via VME to start the cycle of the data acquisition. The ADAM test board received this signal and sends the Trigger Reset to the ADAM synchronised with general 40 MHz clock. Immediately after the Write Reset signal is sent, the write pointer (APC3) logic on the ADAM will start writing the data into the analogue pipeline (DHARP). With the delay set by DAQ, the ADAM test board will release the Trigger Reset which starts the read pointer (APC3), progressing parallel with the write pointer. The APC3 logic was designed such that the write pointer and read pointer will have 40 Time Slot of delay (25 nsec for one time slot) if the write-read delay is set to zero via DAQ. The readout sequence is triggered by sending an external trigger to the ADAM chip. The Trigger width should not be longer

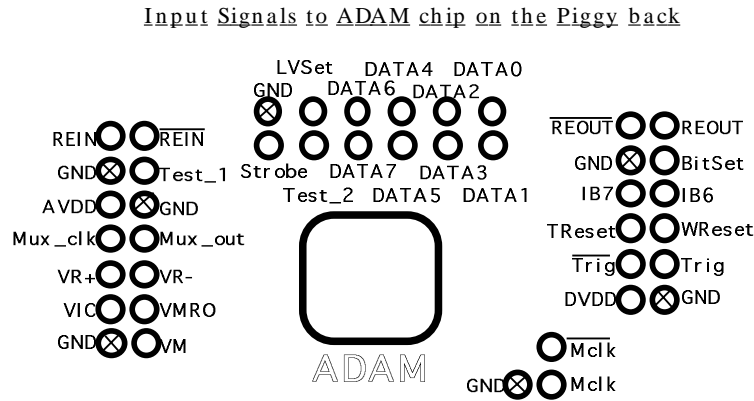


Figure 7.13: Piggy back board interface pin connection layout.

than one time slot length (25 nsec). A trigger over 25 nsec will invoke the second readout sequence. The delay between the trigger reset and the external trigger will determine the read out time column of the analogue pipeline. The delay between the write reset and injection charge will determine the address of the pipeline in which the injected charge is written to the ADAM analogue memory array. We hope to reduce the pointer location dependent noise in the ADAM chip. The result of the noise depending on the address pointer location will be presented in the following section.

7.4.3 The Piggy Back

The ADAM chip is bonded onto a separate board directly with charge injection capacitance. This board plugs directly onto the ADAM testing board. This method, the *piggy back board*, has been adapted for the ADAM testing bench to minimise any external noise and parallel capacitance which can be caused by using an extra socket to mount the chip to the system. Figure 7.13 shows the connection map of this Piggy Back interface to the ADAM testing mother board.

The direct *input/output* signals from the ADAM chip can be probed from the piggy back board.

7.4.4 DAQ Systems

A DAQ software with LabView using a Macintosh computer has been developed within the RD2 collaboration¹². It manages the control sequence to the ADAM test bench, collects the data from ADAM test board, and analyses the data on line. The module sends *I/O* control signals through the VME bus which manages the data transfer from the chip. The reset and trigger signals require a precise timing and they are generated with an external pulse generator, controlled by a GPIB bus. The user interface software sends control sequences for those signals to the generator, and the signal generation is triggered directly from the ADAM test board. The data which is collected in the on-board memory of the ADAM test board is transferred via VME bus to the on-line analysis system. The basic tasks for the on-line DAQ consists of a pedestal and noise analysis, a study of analogue memory structures, monitoring raw data, and data storage for later off-line analysis, etc. Furthermore 8 of the ADAM chips connected in parallel with readout bus is tested in the test beam environment, using Read Out Controller (ROC) module, linked with optical fiber cable to the DAQ system . The ROC can receive the master clock and trigger signals from two optical links and broadcasts them to the 8 chips on board. In this test beam setup, the detector boards are isolated from the DAC electronics. In principle the clock, trigger, and control information could be send to each ROC via a single optical, though this is not planned at this stage of the development.

7.5 Measurement Results of ADAM chip

In this section, some basic measurement results of the ADAM chip characterisation are presented. The analogue pipeline, pedestal, noise, and baseline have been studied in detail. We present the overall ADAM chip performance, and the performance of the separate components.

7.5.1 CRIAD non-linearity and measurements

The CRIAD is used as the Analogue to Digital Converter (ADC) in the ADAM chip. As noted previously, this component was designed and fabricated for individual testing in previous

¹²A flexible DAQ software, Gollum, developed by R. Bonino, is used. For further information of the ADAM test beam, refer http://atlasinfo.cern.ch/Atlas/GROUPS/INNER_DETECTOR/SCTstrips/OTP/OTP.book_1.html

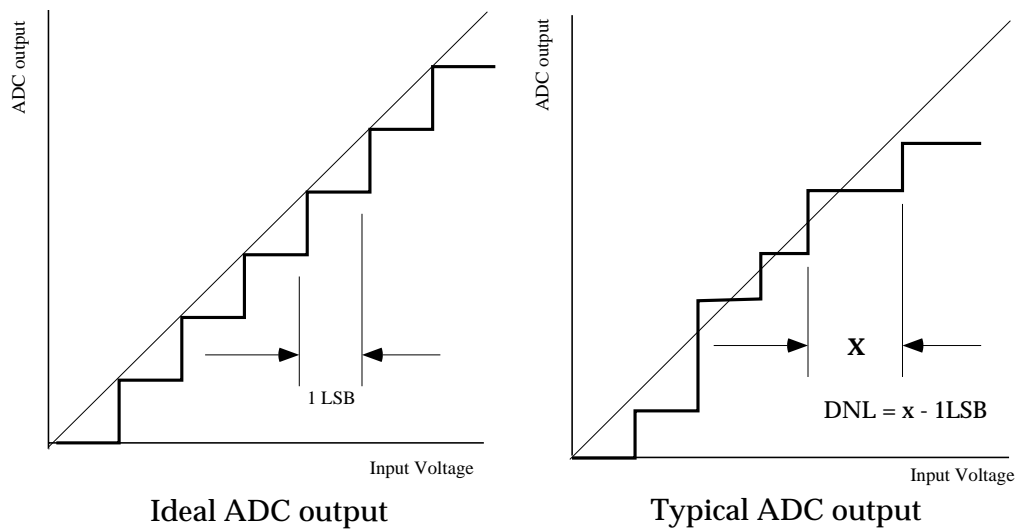


Figure 7.14: The ideal and real ADC output for linear input.

development, and the detailed functionality has been measured [121]. The ADAM can be operated in a test mode such that the CRIAD can be tested individually with its analogue input signal and direct digitised output. The CRIAD functionality was as expected from the previous measurements.

ADC Evaluation Methods– Non-Linearity

A Least Significant Bit (LSB) is defined as the range of the ADC divided by the number of ADC bins. [123]. The width of all bins are ideally equal, and also equal to one LSB. However, the read ADC dynamics is not typical perfect, generating non-linearities in the response to the linear input. Figure 7.14 shows the ideal transfer curve and a typical transfer curve of a read ADC.

The Differential Non-Linearity (DNL) is defined as the difference between the measured bin width of an ADC and the theoretical width, or one LSB. The DNL is measured for all bins. The maximum value of the DNL is used to evaluate the performance of the ADC. The Integral Non-Linearity (INL) for a given bin n is calculated by summing the DNL from the first bin to the n th bin:

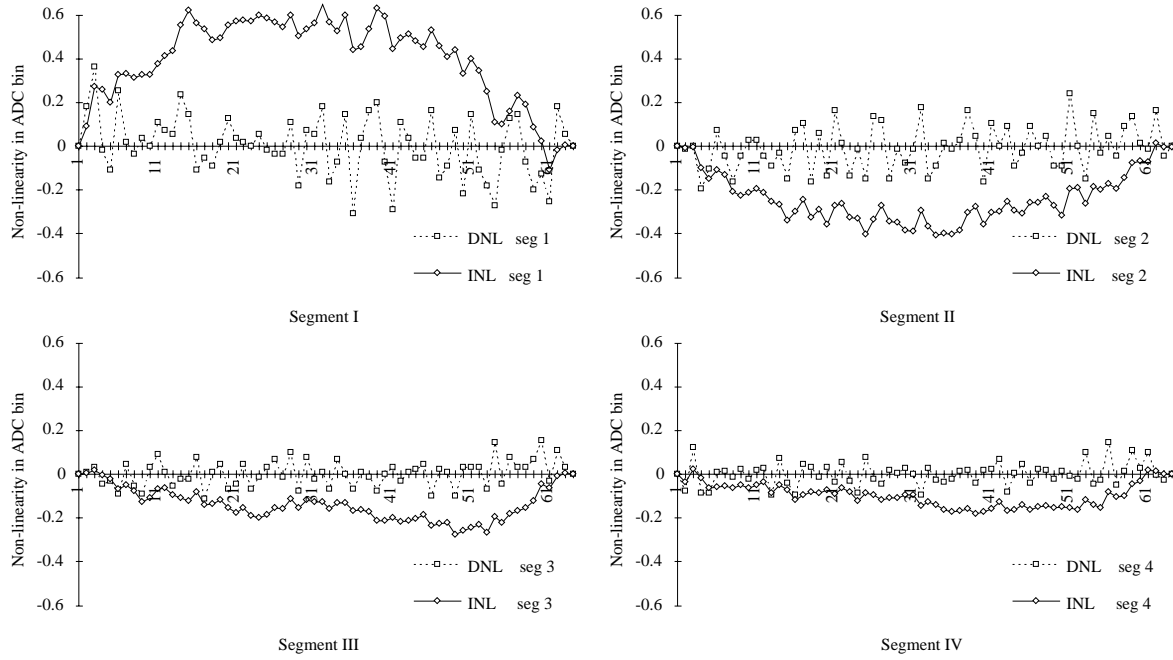


Figure 7.15: Non-linearity measurement of the CRIAD in the ADAM for all four segments.

$$INL(n) = \sum_{i=0}^n DNL(i)$$

As with DNL , INL is calculated for all bins of the ADC and the maximum value is normally taken for the evaluation of the ADC performance.

Measured Results

Figure 7.15 shows the measurement of non-linearity for the CRIAD as implanted in the ADAM chip, and running at $5MHz$ clock speed.

The Table 7.3 presents the maximum values of non-linearity of the CRIAD, extracted from Figure 7.15.

Segment	i	ii	iii	iv
LSB in mV	1.0	2.0	8.0	32.0
DNL (in LSB)	0.36	0.24	0.16	0.15
INL (in LSB)	0.65	0.41	0.27	0.18

Table 7.3: Non-linearity of the CRIAD.

7.5.2 The Baseline–Time Column Dependent Pedestal

The analogue pipeline with HARP technology has been installed in the ADAM chip and it is important to understand the pedestal fluctuation of this analogue memory array. The known problem from the last version of the pipeline, the DHARP2 [119], was the baseline fluctuation where all 32 input channels had the same pedestal structure, but with a common offset fluctuation. The major cause of this fluctuation was determined to be from internal cross-talk and/or analogue pick-up at the input amplifier. Further study is necessary to solve this problem completely. This baseline is the average value of 32 channels for each event with null signal and it is calculated by off-line software and subtracted for each event. Hence the fluctuation can be suppressed by off-line even though the direct cause is not completely determined. In the ADAM measurements we found that a major part of this baseline fluctuation is from the time column dependent pedestal shift and it comes from the Front-End amplifier (NICON) pick up. The time column dependent pedestal shift is only observed when the pedestal measurement was taken together with the Front-End amplifier.

7.5.3 Pedestal with NICON amplifier

Figure 7.16 shows the pedestal of one channel for all 112 time columns, with full functionality of the ADAM chip. The analogue pipeline is fed by the Front-End amplifier, with null signal input. No baseline subtraction is made. The plotted time column number corresponds to the logical (as read out) address of the analogue memory.

A time column dependent repeated pattern of the pedestal structure is observed. The structure consists of group of 8 logical addresses: one low cell at $\sim 30mV$, one high cell at $\sim 50mV$, and 6 consecutive cells at middle range $\sim 40mV$. The corresponding noise measurement shows higher noise on the high and low cells. The timings of the triggers and various

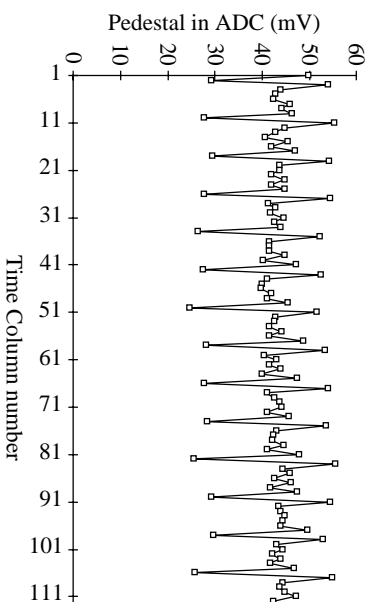


Figure 7.16: Pedestal for all 112 Time slot on Channel 8, no baseline subtraction, with NICON.

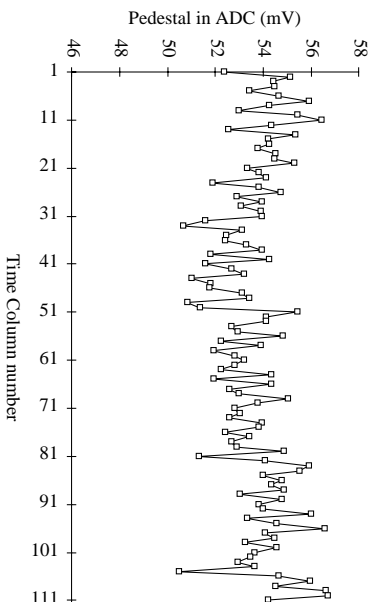


Figure 7.17: Pedestal for all 112 Time slot on Channel 8, no baseline subtraction, without NICON. $r.m.s. = 1.38$ mV.

reset signals were adjusted to study the effect on this pedestal structure, yet no correlation has been found. The jump of the pedestal every 8 cells comes from the physical location of the pipeline addresses, not perturbed by the trigger arrival time respect to write or read pointers. This repeated structure of group of 8 pedestal dependency does not correspond to the APC3 address skipping progression logic explained in the previous section. The PAC address progression logic has a group of 4 structure.

Figure 7.17 shows the pedestal measurement when the bias current supply to the last source follower of the NICON is disconnected¹³. The $r.m.s.$ pedestal fluctuation of a single channel for

¹³The NICON front-end Amplifier consist of two amplification with feed back and two source follower for the output. We have disconnected the bias current supply to the last source follower, thereby ensuring that the output from the NICON will not follow the input signal.

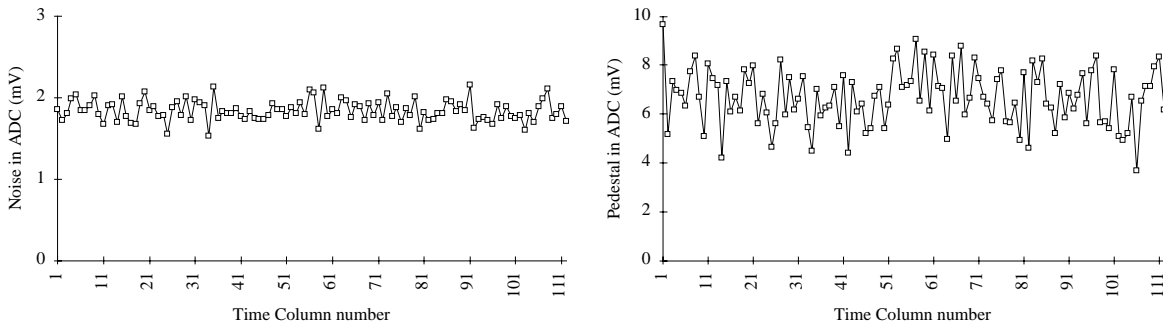


Figure 7.18: Pedestal (left) and Noise (right) for all time slot on Channel 8, with baseline subtraction.

all time column can be evaluated, and it is measured to be 1.38 mV . The repeated structure of the pedestal disappears in this setup. That is, the NICON causes an obvious baseline jump correlating to every 8 analogue memory address. This possibly results from cross-talk with the encoding of the analogue memory, the APC3 address progression logic, etc., picked up by the Front-End Amplifier. The address progression of the APC3 logic, described in the section 7.3.4, however, has grouping of 4, which does not correspond to this obvious baseline jump correlation observed. Further detail studies are in progress to understand the exact cause of this time column dependent pedestal fluctuation with the NICON. However, without the NICON pick-up on the time column dependent pedestal fluctuation, there still remains a slow structure of the pedestal. The two ends of the logical address of the pipeline have a higher pedestal value than the middle cells, by $\sim 2 \text{ mV}$. When this figure is plotted as a function of the physical address of the analogue memory (refer to Section 7.3.4 on the APC3 address progressing logic), the pedestal is higher on the beginning of the pipeline.

7.5.4 Pedestal and Noise with Baseline Subtraction

We can eliminate the above time column dependent pedestal fluctuation by performing off-line baseline subtraction. Figure 7.18 shows the pedestal and noise of the ADAM with its full functionality, after off-line baseline subtraction.

Both noise and pedestal shows a stable distribution and no obvious structure depending on the time column is observed. The baseline shift variation or time column dependent pedestal *r.m.s.*, has been measured to be 0.7 mV in this setup. This parameter has been significantly

Pedestal <i>r.m.s.</i> on a single channel	1.16 <i>mV</i>
Average Noise level for all Time Column	1.83 <i>mV</i>
RMS of the Noise level for all Time Column	0.126 <i>mV</i>
Analogue memory baseline fluctuation	0.7 <i>mV</i>

Table 7.4: Noise and pedestal with baseline subtraction.

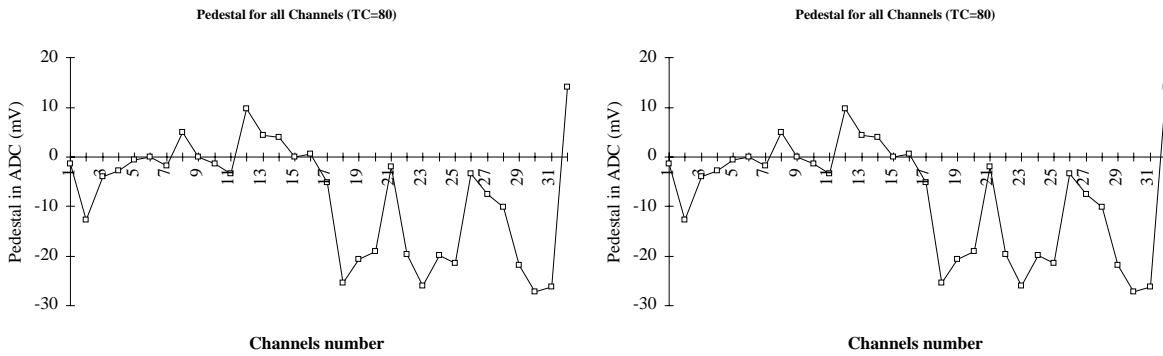


Figure 7.19: Pedestal (left) and Noise (right) on a single time column, with baseline subtraction.

improved compared to the earlier developments. It is one of the features optimised by choosing a full differential readout structure within the analogue storage array. Table 7.4 summarise the pedestal and noise.

Figure 7.19 shows the pedestal and noise on a single time column for all 32 channels. There is a clear difference between the first 16 channels and last 16 channels, due to the different Front- End amplifier layouts. Within each group, it shows a stable pedestal distribution.

When averaged over all time columns, the channel to channel pedestal variation is measured to be 4.3 *mV* on channels 1 to 16. The pedestal fluctuation and noise depends mainly on two components of the ADAM chip, the Front End preamplifier and the pipeline. We have determined that the common baseline fluctuation by event comes from the Front-End preamplifier pickup, and it is closely associated with pipeline addressing logic, the APC3. The fluctuation of the pipeline alone has been measured by disabling the Front-End, and it yields a satisfactory result. In the future development plan, a bipolar Front-End amplifier with lower noise and less external pickup than NICON amplifier is planning to be associated with DHARP pipeline to eliminate this common offset fluctuation problem.

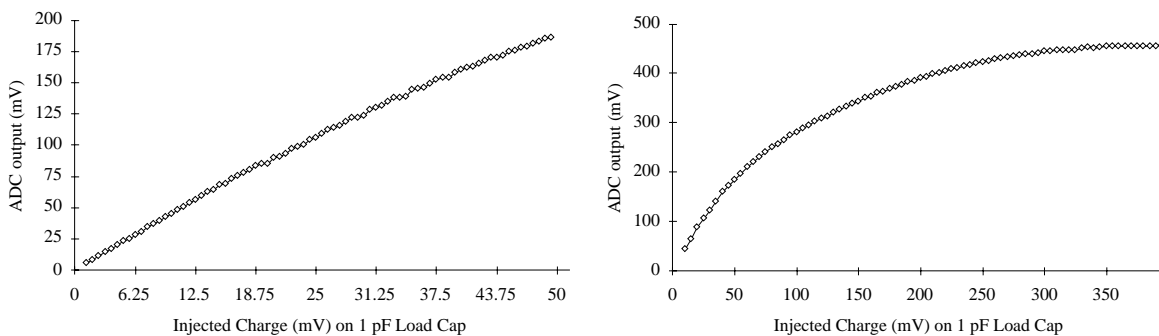


Figure 7.20: Linearity measurement. Linear region (left) and larger segment (right). Channel 3, Column 44.

7.5.5 Linearity

Linearity is measured by injecting a test pulse charge on a 1.0pF load capacitance mounted on the Piggy Back board. Figure 7.20 shows the response of the ADAM with its full functionality.

The measurement shown was taken with time column 44, channel 3. Other time columns and channels have been measured and they yields similar results. The injected charge is on a 1 pF injection capacitance, hence it yields 4 mV to 25000 electrons, or equivalent to one minimum ionising particle deposited charge from detector (MIP). Figure 7.20 shows the good linearity response of the ADAM chip over 10 MIPs of injection change. It starts to saturate above a 20 MIP equivalent charge input. In the linear region, the signal gain is measured to be $\sim 20\text{mV}$ per MIP of input, two times less than the amplitude measured at the output of the input preamplifier alone. That is, half of the charge is lost after the preamplifier output and before the pipeline output. This can be caused from several parts; on the charge transfer level between the NICON and the pipeline, the write amplifier of the pipeline capacitor, or the at the readout amplifier of the pipeline. The NICON output has been examined with a probe station, and verified that the output level of the pre-amplifier corresponds to the input signal. The strong possibility of this loss is at the write amplifier of the pipeline, though it is not possible to access to this point directly.

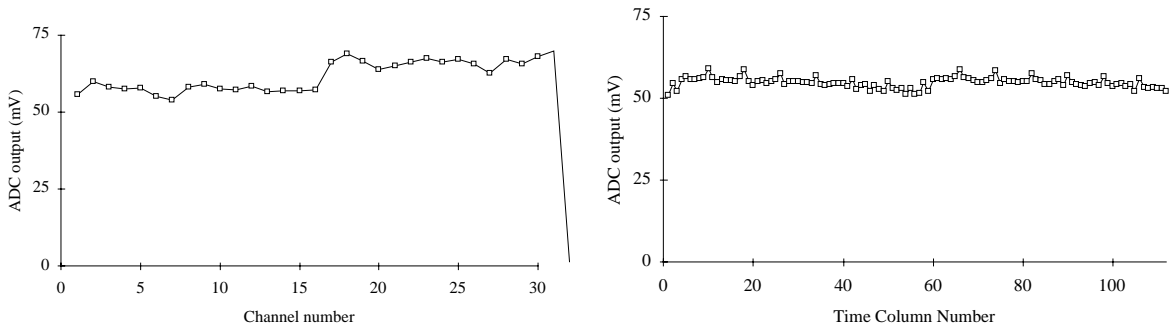


Figure 7.21: Gain. On a single time column ($t_s=44$) for all channels (right) and on a single channel (ch=7) for all Time Column (left).

7.5.6 Gain Correspondence

The gain difference on all time column and channels has been measured. A test pulse was injected to all channels and time slots to compare the gain dependency on the different capacitors of the analogue memory. Figure 7.21 shows the dependence on the channel and time column on a single time column and channel.

The channel to channel variation of the gain is plotted on the left. It shows the first 16 channels has lower gain than the last 16 channels due to the different Front-End amplifier. Within the 16 channels, it shows good gain stability. The time column dependency of the gain shows excellent over all stability, yet every 8th time column has slightly higher gain than other addresses. These time columns correspond to the ones with higher pedestal explained in earlier section. However, the difference of the gain is less than 10%. Considering that the difference of the pedestal on every 8th time column is only observed when the Front-End amplifier is connected, this time column dependent gain must also come from cross talk from the Front-End amplifier.

7.5.7 Load Capacitor and Noise Increase

We simulate the load capacitance of the detector installed with the ADAM chip and measured the noise parameter with the function of the load capacitance. Figure 7.22 shows the measured noise values of the Front-End amplifier only. The noise of the chip comes from several sources such as Front-End amplifier, the analogue memory capacitors, read-out amplifier, ADC, etc.

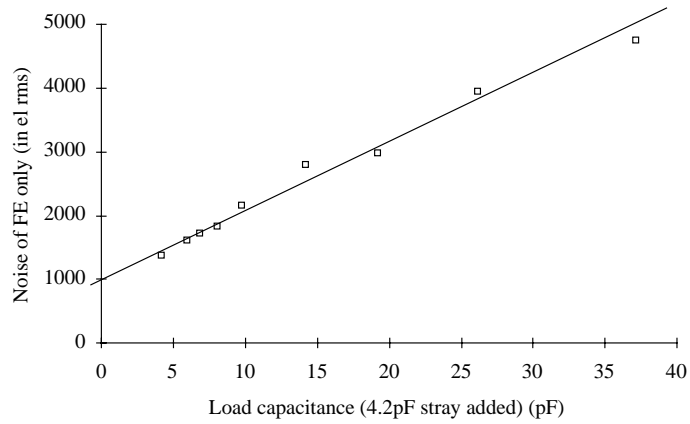


Figure 7.22: Noise *v.s.* load capacitance. Fit yields $y=103x+1056$.

However two major contributors to the noise of the chip are the Front-End amplifier and the analogue memory capacitance, and they add quadratically. We measured the internal noise of the ADAM chip without the Front-End amplifier by disabling its functionality, and subtracted quadratically from the global noise to determine the noise contribution of the Front-End amplifier only. In the figure, the 4.2 pF of the stray capacitance from the Piggy back board has been included.

The linear fit gives the slope and y-intersection. The slope is the increase of the noise per pF of added load capacitance, and y-intersection yields the bare noise value of the Front-End. The measured noise value is approximately 1000 electrons + 100 electrons/ pF . This result is somewhat higher than what was measured with DHARP¹⁴ chip. The overall signal over noise figure is > 10 for input capacitance below 10 pF , mainly because of the 6 dB gain loss observed in the channel, which makes the noise contributions of the readout stages non negligible. Figure 7.23 shows the pulse shape for various load capacitance.

With additional load capacitance, there is more delay of the Front-End amplifier, and a loss of the gain, that reaches to 30 % in the extreme case of 33 pF load capacitance.

¹⁴In the DHARP measurement, it was measured to be 800 electrons + 60 electrons/ pF .

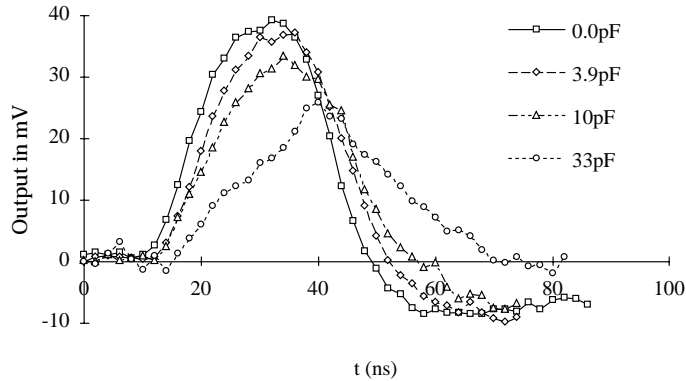


Figure 7.23: Comparison of the pulse shape of some load capacitance.

7.5.8 Multi-Trigger readout during the digitisation and readout process

The ADAM chip accepts triggers without any dead time. The analogue memory control logic has a skipping address logic which freezes the time column in which the data has been written when a trigger arrives, and continues writing the incoming analogue data into the memory array, skipping the writing to this cell till the data has been digitised and readout of the chip. However, during the process of digitisation and readout of digitised data the extra activities within the chip disturbs the analogue memory writing, effecting the pedestal and noise of the analogue memory array.

Figure 7.24 shows the timings of the multiple trigger readout. When the first trigger arrives, the ADAM chip takes some setup time for transferring the analogue memory charge to the internal ADC, which is approximately 700 nsec (**A** in the figure). The digitisation of 32 channels data follows, and in the case of 5 MHz ADC clock, it is $6.4\text{ }\mu\text{s}$ (**B**). During this period, the digital FIFO is processing the data with the first trigger. After the digitisation has been processed, there is $\sim 1\text{ }\mu\text{s}$ of set up time for read out logic control (**C**). Finally, the data is being read out to external bus from the chip at the speed of 10 MHz (**D**)¹⁵. This process takes $3.3\text{ }\mu\text{s}$ with 32 channels of data plus the address information of the analogue memory. The whole process takes approximately $11\text{ }\mu\text{s}$ to complete. The second trigger is sent

¹⁵The digital read out process will follow as described when the readout bus is ready to take the data from the ADAM, or *REIN* has been sent to the chip previous to this time. The low-level input signals are *Mclk*, *Mclk_bar*, *Trig*, and *Trig_bar*, *REIN*.

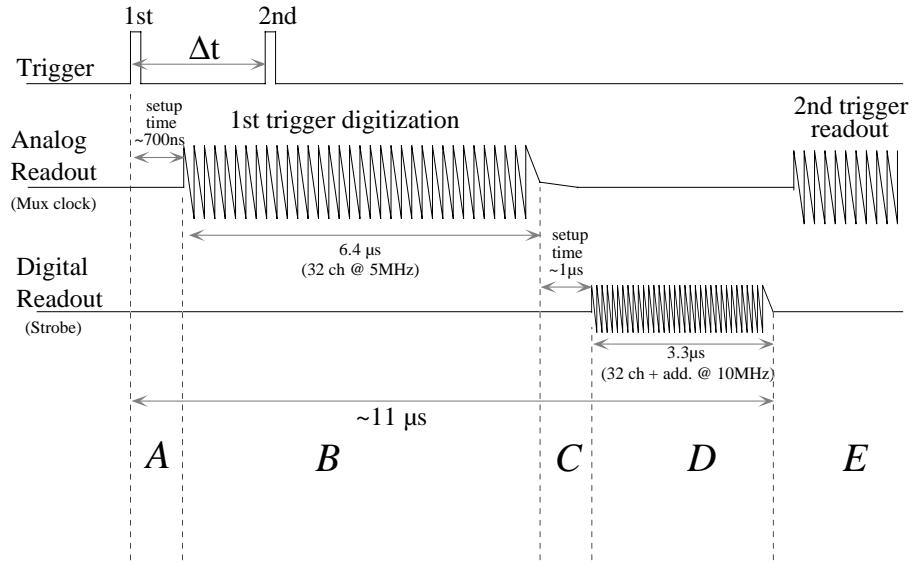


Figure 7.24: Consecutive trigger read out timing.

during this process period. The analogue memory is written while the ADAM chip process the analogue data internally, and we have observed the effect on the pedestal and noise level for this second trigger.

Figure 7.25 shows the pedestal of the first trigger by time column on a single channel and of the second trigger, taken in the time interval of (A) and (B). The ICON is activated hence the effect of the internal pick up though the FE amplifier is also included in this figure. As discussed in the previous section, the repeated pedestal pattern in every 8 time columns comes from Front-End amplifier pick-up. During the setup time (A), the pedestal is shifted by ~ 15 ADC bins uniformly through out the analogue array, keeping the same pedestal structure. Here the channel dependent pedestal structure (and noise) shows the same result. This effect is also observed when the ICON is disabled. However the corresponding noise associated with this pedestal (A) is not increased. On the right (B) the pedestal during the digitisation is plotted. Two effects on the pedestal are observed: the general increase on the pedestal bins as observed in case (A) and odd-even structure pattern along the time column. The analogue memory noise has increased by factor of 2 to 3 in corresponding measurement. This odd-even structure of the pedestal is not observed when the Front-End amplifier is disabled, thus it is another result from the parasitic pick-up with the FE amplifier. During this period

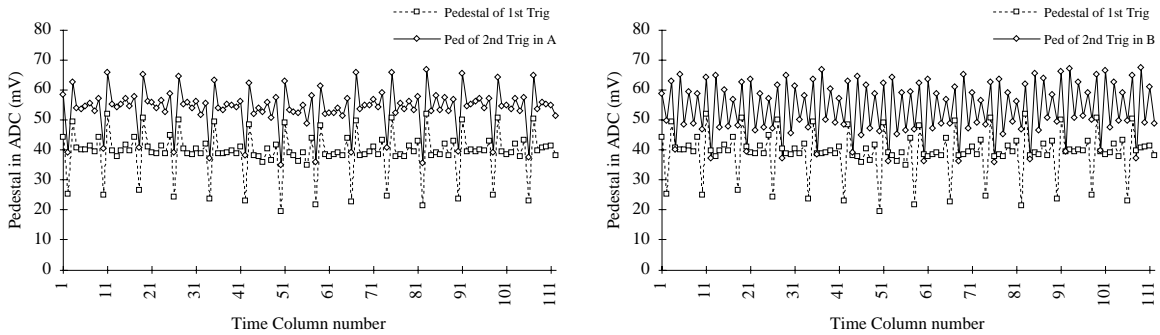


Figure 7.25: The pedestal comparison by time column during digitisation, with use of ICON pre-amplifier. **(A)** during setup time (left) and **(B)** during digitisation (right). Channel 7.

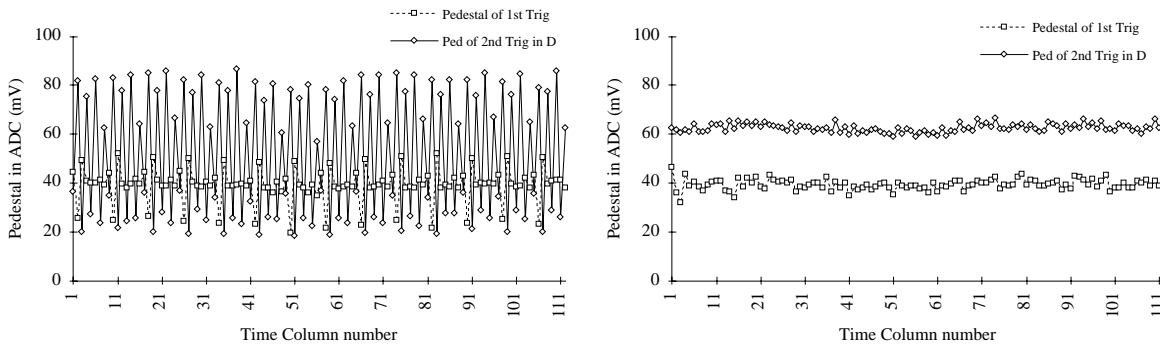


Figure 7.26: Pedestal comparison during readout, with (left) and without (right) ICON F.E. for during Readout time **(D)**. Channel 7.

(B) the noise is increased by factor of 2 to 3 compared with corresponding single-triggered measurements.

Figure 7.26 shows the pedestal during the digital readout period to the external bus from the ADAM chip **(D)**. The left figure shows with Front-End amplifier operation, and right with ICON being disconnected. The odd-even structure which has been observed during digitisation period **(B)** gets much larger during this period. The corresponding noise level increased by up to factor 4. This effect of Front-End pick-up is not observed when the ICON is disabled, plotted on the right. However the pedestal has been shifted up by ~ 20 ADC bins here. In summary, the pedestal of the second trigger is perturbed if the second trigger arrives within $11\mu sec$ or during the first trigger data processing time. The second trigger pedestal

is shifted up to 20 ADC bin (mV) from analogue memory part through out this period. It also picks up a unique time column dependent structure due to parasitic pickup from the Front-End, and the structure depends on the functionality of the chip, possibly analogue array addressing. However, the channel to channel pedestal structure stays unchanged, hence the internal activity of the ADAM chip affects the pedestal in only a time dependent way. This baseline shift of the second trigger is not observed if $\Delta t > 11\mu sec$. The corresponding noise is increased during the first trigger data processing period as well. The ADAM chip is designed to reduce possible source of noise and cross talk, as well as lowering the power consumption, by using low-level operation for which the input signals has a voltage swing of $200 mV$, and a high level corresponding to $5 V$ TTL operation. The input signals which takes this low-level operation are present at the moment of data writing/reading to the capacitor array of the chip, to eliminate any possible parasitic within the chip. With this low-level operation, however, this pedestal perturbation of the second trigger during the data processing time is also observed.

7.5.9 REIN delay

After the digitisation for the analogue memory has been performed, the digitised data is stored into the output digital buffer in the ADAM chip. The output buffer has a capacity of 2 blocks of data¹⁶. The digital readout logic (ROL) enables the digital readout when there is at least one block of data in the output digital buffer (*half full*) and a *REIN* (read enable in) signal has been received via external DAQ control. Under those two conditions, ROL sends out the digitised data with the strobe, at a $10 MHz$ clock speed provided from the general ADAM chip control. The analogue readout, however, is enabled when at least one block of the output buffer is free (*half empty*). If more than 2 blocks are requested by DAQ, at least one block of digitised data must be read out before third block can be processed. The analogue memory control waits for the half empty flag is sent from ROL. Figure 7.27 shows this readout sequence.

During the time after the completion of the second analogue readout and the end of first digital readout, the analogue signal is held in the analogue memory capacitance. We have

¹⁶One block of data consists of 33-8 bits word. 32 words for 32 channels and 1 word for analogue memory address.

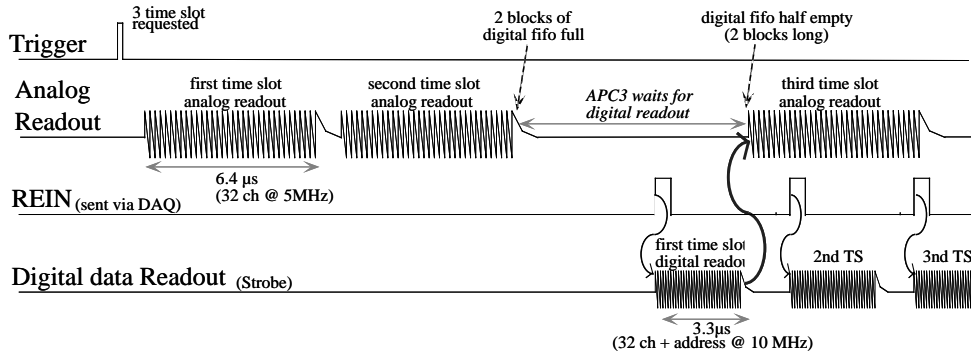


Figure 7.27: *REIN* and analog/digital readout timings.

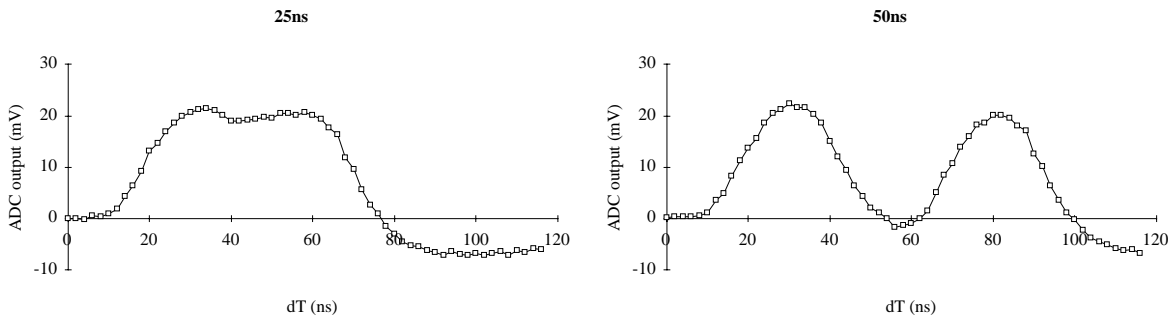


Figure 7.28: Double pulse resolution. $\Delta t = 50nsec$ (left) and $\Delta t = 25nsec$ (right).

measured the pedestal and noise effect on the third time slot readout with the delay of *REIN*, up to $100\mu sec$. No noticeable effect has been observed, proving a good stability and capability of keeping the charge in the analogue memory capacitors.

7.5.10 Double Pulse Resolution

The time resolution of the Front-End readout is another important issue in the ATLAS detector of the LHC experiments. The bunch crossing is at $25 nsec$ and it require a fast readout amplifier. The ADAM chip operates with $40 MHz$ master clock, or the LHC bunch crossing speed, and it demands the NICON Front-End amplifier to respond at equivalent speed. Figure 7.28 shows the time resolution of the ADAM chip, with double pulse injection.

It shows good resolution with a $50 nsec$ time interval (Figure 7.28 left). The pulse

Pedestal variation (time column to time column)	1.2 mV (<i>r.m.s.</i>)
Pedestal variation (channel to channel)	4.0 mV (<i>r.m.s.</i>)
Time column baseline fluctuation	0.7 mV (<i>r.m.s.</i>)
Average noise from readout amplifier	1.5 mV
Average of total noise level on a single memory cell	1.8 mV
Signal gain (for 23000 electrons = 1 MIP)	20 mV
Noise level in electron equivalent (input amplifier only in ADAM)	1000el + 100el/pF
Noise level in electron equivalent (measurement with NICON alone)	800el + 80el/pF
Signal to noise ratio (< 10pF input capacitance)	> 10
Power consumption of ADAM: DVDD (at 6V)	132mW
Power consumption of ADAM: AVDD (at 6V)	128mW
Power consumption for 128 channel ADAM	4.3mW per channel

Table 7.5: Summary of performance measurements of the ADAM chip.

shape reaches at zero before the second pulse arrives, showing the chip functionality meets the specification for the ATLAS detector. Figure 7.28 (right) shows the resolution of 25 nsec time interval double pulse. It shows that the differentiation of those two pulses is possible.

7.5.11 Power Consumption

The power consumption of the ADAM chip is measured as 132 mW for Digital processing (at 6 V) and 128 mW for Analogue part (at 6 V) which includes the ADC. From previous measurement of CRIAD, the power consumption of the ADC operating at ADAM specification is 32 mW. Expanding this figure, the expected power consumption for future 128 channels integrated chip, per channel, will be 1.28 mW for digital part and 3.01 mW for analogue part, yielding of 4.29 mW per channel.

7.6 Summary of Performance Measurements

Table 7.5 summarise the performance measurements of the ADAM chip.

7.7 The ADAM in the Test Beam

Among different configurations of electronics and semiconductor strip detectors, the functionality of the ADAM chip was tested in the H8 beam-line at the CERN SPS accelerator in 1995¹⁷, following a full laboratory test. At the test beam, the ADAM chip was equipped with *n*-type silicon strip detectors. In this Section, the result from the test beam is shown, demonstrating the adequate performance of the modules with good signal/noise ratio, spatial resolution, attained from the detector.

7.7.1 The H8 Test Beam

During 1995, several of SCT modules together with silicon strip detector equipped with associate readout electronics were tested. Micro strip silicon detectors with $300\ \mu\text{m}$ thick of $6\ \text{cm}$ (*length*) \times $200\ \mu\text{m}$ (*pitch*) were designed and fabricated by Hamamatsu cooperation according to ATLAS specifications [127]. In the testbeam environment these silicon detectors were tested with ADAM readout chip with 25 ns LHC clock speed. The ADAM chip was implemented with a full LED-based optical readout system. The data acquisition system was developed within the collaboration, using VME interface.

7.7.2 Results

Figure 7.29 shows the pedestals depending on time-slot and channel, and its deviation distributions. The pedestal deviation is the noise of the readout electronics. One ADC count is equivalent to $\sim 1\text{mV}$ in input pulse height. It shows that the pedestal dependency along the channels, yet it is stable along the time slot.

Figure 7.30 indicates the average (along Time Slots) noise level by 32 readout channels. On the channels with best performance, the noise level is approximately 2 mV.

The ADAM chip showed satisfactory result on the Signal to Noise ratio, as shown in Figure 7.31. We obtained the signal to noise ratio > 11 from our test beam experiments with 25 ns LHC clock speed operation.

¹⁷Full report can be found within ATLAS internal document [126].

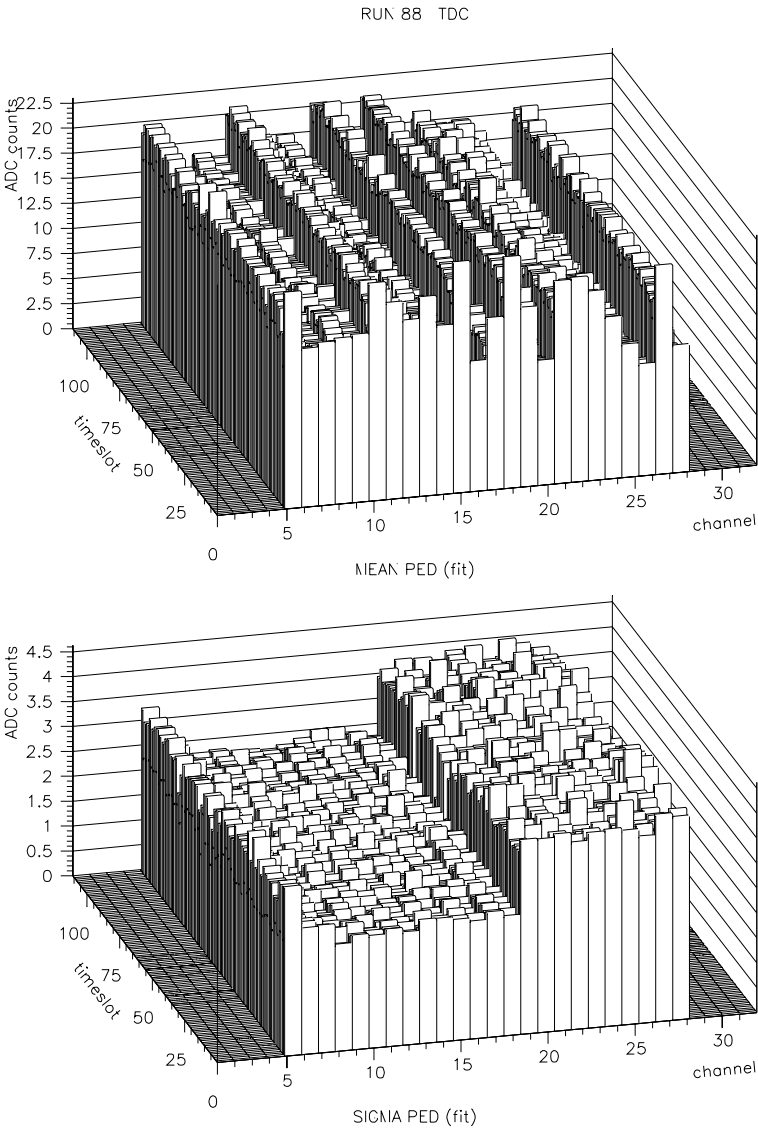


Figure 7.29: Pedestal and pedestal deviation distributions of the ADAM chip in the test beam.

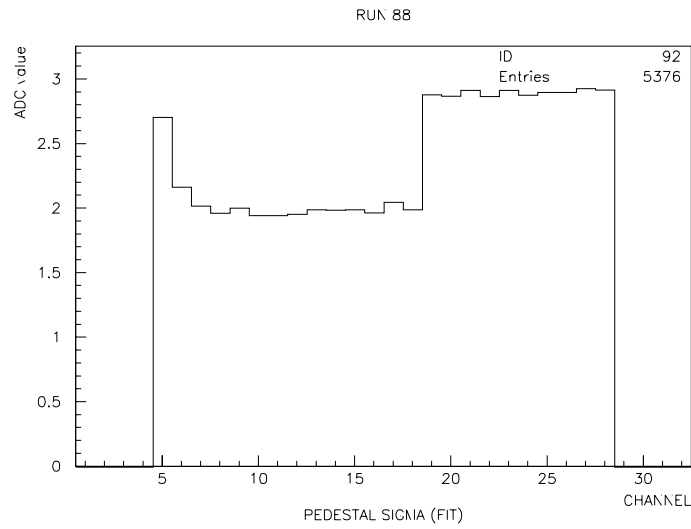


Figure 7.30: Noise level of the ADAM chip in the test beam.

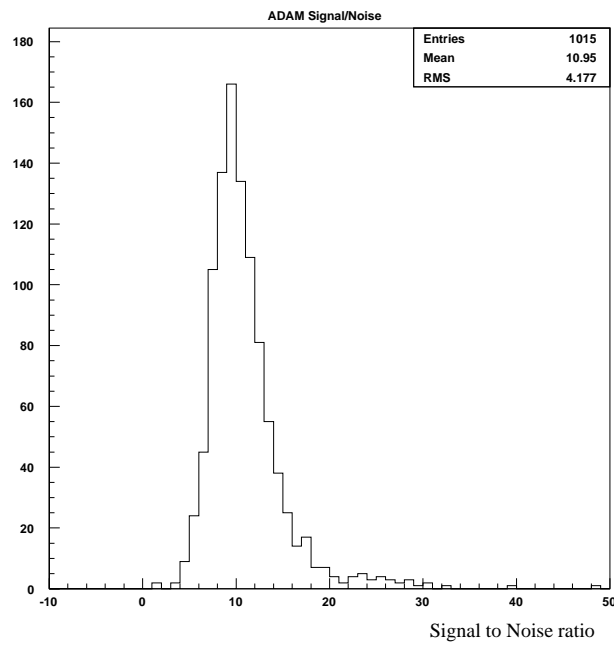


Figure 7.31: Pulse height distribution with a $200\ \mu\text{m}$ pitch, $300\ \mu\text{m}$ thick silicon detector readout with the ADAM chip. Units given in Signal/Noise.

7.8 Conclusion for ADAM Chip

The ADAM, the first prototype of an integrated Front-End digital electronic readout chip for silicon tracker, has been tested for its functionality towards the ATLAS inner detector specification. The test showed full functionality at 40 *MHz* and characteristics of individual components were obtained. The analysis of the analogue memory showed a sufficiently low noise level for a single memory cell, and stable fluctuation in the time columns. It showed a good linearity response to the injected pulse. It obtained signal to noise ratio for a MIP signal to be over 10 with 10 pF input capacitance. The double pulse resolution reaches LHC bunch crossing spacing, which is at 25 *nsec*. Power consumption for 128 channel ADAM chip, expanded from 32 channel version of ADAM, meets the ATLAS requirement. However, it was found that the NICON Front-End amplifier picks up internal cross-talk during digitisation of the analogue memory and the digital readout period. Other options such as a bipolar Front-End amplifier in place of NICON have been considered. The baseline fluctuation, or time column dependent pedestal, previously observed in DHARP analogue memory chip, has also been observed in this chip, though the amplitude of the fluctuation is less than 1 *mV*. We have configured the ADAM chip on series with optical link controlled by Read Out Control (ROC), which replace the ADAM test board and other external controllers. the control signals, received by the ROC though an optical link, will be distributed to the chip through low level signal lines. A telescope consisting of three prototype modules are installed and tested on a test beam in May, 1995, and the off-line analysis of this testbeam experiment have proved its full functionality in the realistic environment.

Chapter 8

Conclusion

A search for second generation leptoquarks with the Fermilab proton-antiproton accelerator at a center of mass collision energy of 1.8 TeV was performed using data collected at the CDF experiment from 1992 to 1995. The search was based on pair production of scalar leptoquarks which decay into a dimuon and dijet channel. The 95% confidence level limits on the cross section $\sigma(p\bar{p} \rightarrow LQ_2\bar{L}Q_2)\beta^2$, including systematic uncertainties with no background subtraction, was computed as a function of the leptoquark mass. The mass limit depends on the choice of theoretical models. Compared with a recent Next-to-Leading Order cross-section calculation a limit of $M(LQ_2) > 202 \text{ GeV}/c^2$ ($\beta = 1.0$) was derived. The publication of this result is in preparation¹. The analysis did not result in a signal for a new particle, and the analysis must go on with higher energy at the LHC, and with increased luminosity at Tevatron (Run II from 1999).

The LHC at CERN is scheduled for operation in the year 2005, and will collide pp beams with energy $\sqrt{s} = 14 \text{ TeV}$. Studies show that it will be possible to detect leptoquarks with a mass range up to $1 \text{ TeV}/c^2$, at the ATLAS experiment. An intense amount of research and development has been required to design and operate the ATLAS detector for the LHC, integrating the latest modern technologies available. Semi-conducting materials, such as silicon detectors, will play an important role in the precise measurement of charged particle tracks with good efficiency. As well as the detector, we also need to develop an associated data

¹Physical Review Letters article is in preparation.

acquisition system capable of operating at high luminosity.

The ADAM chip, the first fully integrated front-end readout micro-electronic chip for silicon strip detectors for at ATLAS experiment, has been fully tested to determine its performance and feasibility for use in the LHC environment. Such a readout chip must be fast, dense, radiation resistant, low power consuming, and cost-effective. The ADAM chip was first designed and its performance assessed through computer simulations. Subsequent laboratory tests showed the full functionality at the LHC bunch crossing speed of 40 MHz. It was also tested in a realistic test beam environment where it demonstrated a satisfactory result under LHC operating conditions. We also found room for further developments, and a new version of integrated electronic readout chips are currently under development within the ATLAS collaboration.

In recent years, research in the field of particle physics has seen great progress on both experimental and theoretical fronts. These studies seem to support the existing predictions of the Standard Model. The high precision of modern experiments and deep theoretical understanding, as well as just our simple curiosity, will lead us to search beyond this model. There is a great hope that the long-standing pressure of the mysterious success of the Standard Model will soon give us a key to the next stage of new and exciting particle physics phenomenologies. At the LHC experiments, a large amount of new and exciting phenomena are expected to emerge. We hope to take another step towards understanding the fundamental nature of physical laws that governs the universe in which we live, to see how it all works, and to satisfy our curiosities.

Appendix A

Spontaneous symmetry breaking

The SM gauge group is defined as a direct product of the three mutually commuting groups listed above. However there is no mass term included in this gauge group. The mass term will violate the symmetry of $SU(2) \otimes U(1)$ gauge invariance explained in electroweak theory. It was proved by 't Hooft and others [27] that the gauge theories are renormalisable. With vector boson mass terms this group becomes non-renormalisable. The mass term in the Proca Lagrangian (vector Lagrangian) is not locally gauge invariant, whereas the vector bosons (photon and gluon) are massless, yet W^\pm and Z^0 have rather heavy mass.

Higgs [26]¹ overcame this problem by “spontaneous symmetry breaking”, and introduced a notion of *Higg’s fields*. This lead to the renormalisable electroweak gauge theory with finite masses. The mass term originate from an expansion of a Lagrangian form. The Lagrangian of the scalar field ϕ takes a form:

$$\mathcal{L} = \frac{1}{2}(\partial_\mu\phi)(\partial^\mu\phi) + e^{-(\alpha\phi)^2} \tag{A.1}$$

where α is a real constant. In this Lagrangian, the minimum energy state (or ground state) is at $\phi = 0$. It can be expanded in a second order exponential form, and by using Klein-Gordon Lagrangian scalar field, Equation A.1 can be re-expressed as

$$\mathcal{L} = \frac{1}{2}(\partial_\mu\phi)(\partial^\mu\phi) + \frac{1}{2}\mu^2\phi^2 - \frac{1}{4}\lambda^2\phi^4 \tag{A.2}$$

¹Many literatures gives Higg’s model today along with the Standard Model introduction. See ref. [2].

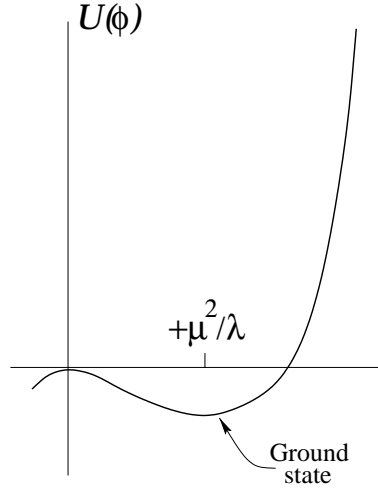


Figure A.1: The potential $U(\phi)$ for complex scalar field for the case $\mu^2 < 0$ and $\lambda > 0$, showing the ground state at $\phi^2 = -\frac{1}{2}\frac{\mu^2}{\lambda}$.

where we use the relation $\alpha^2 = \frac{1}{2}(mc/\hbar)^2$. μ and λ are real constants, the second term in Equation A.2 express the mass term, and third term is the interaction term. In general we express a new field variable η given by

$$\eta \equiv \phi \pm \frac{\mu}{\lambda} \quad (\text{A.3})$$

in which η indicates the *new* ground state, and the coefficient of η^2 term in Lagrangian gives the mass term. The ground state therefore occurs at $\phi^2 = -\frac{1}{2}\frac{\mu^2}{\lambda}$, not at $\phi^2 = 0$, as shown in Figure A.1. In the Language of quantum gauge theories, it is the non-vanishing vacuum expectation value which selects a preferred direction in weak isospin plus hypercharge space. Hence it *spontaneously breaks* the $SU(2) \times U(1)$ symmetry.

The Goldstone [128] theorem states that massless spin-0 particles appear in a theory whenever a continuous symmetry is spontaneously broken. In the Higgs mechanism, it provides the longitudinal modes for the W^\pm and Z^0 bosons.

However in the Higg's theory, known as *Weinberg-Salam model* today, the phenomenological parameters has not been observed experimentally and in future when we shall observe the Higgs particles it could well possibly replaced by more basic parameters.

The $SU(2) \otimes U(1)$ multiplets do not necessary make up physical particles, since the mass

and chirality operators do not commute. It leads to the flavour changing mixing across the different quark and lepton families, called Flavour Changing Neutral Current (FCNC). One such theory [40] explained in Section 3.2.2. However, the colour multiplets are mass eigenstates, since the right and left handed quarks can have the same colour. No sign of $SU(3)$ spontaneous symmetry breakdown has been observed experimentally.

Appendix B

Muon trigger at CDF

In the leptoquark analysis, the trigger requirement is imposed to the possible signal events. The muon trigger is categorised into 3 different types; CMU, CMP, and CMX. It is applied in the analysis presented in Section 5.5.2. In the CDF offline-analysis, there are some abbreviations used to describe the triggers. In this section, a brief description for those triggers is given.

The logic of trigger is returned with a bit: either pass or not pass. We use this information to require appropriate trigger path. The symbols for the types of triggers which concern the leptoquark analysis are listed below:

MET_35_TWO*: The total missing transverse energy is detected to be more than 35 GeV with at least two jets¹.

CMNP_CFT_12_5DEG_V*: The transverse momentum of CMP muon is larger than 12 GeV/ c . The track reconstructed with CFT must match the muon stub within 5 degrees. It is an inclusive CMU muon.

CMUP_CFT_12_5DEG_V*: The transverse momentum of CMU muon is larger than 12 GeV/ c . The track reconstructed with CFT must match the muon stub within 5 degrees. It is CMU/CMP type of muon.

¹MET_35_TEX* trigger is also used in the leptoquark analysis. MET_35_TWO* and MET_35_TEX* are indistinguishable in our analysis

CMNP_JET*: An inclusive CMU muon with one or more jets.

CMUP_JET*: A CMU/CMP muon with one or more jets.

CMU_CMP_JET*: A CMU/CMP muon with one or more jets.

CMNP_CFT_12_5DEG_M*: The energy on the wedge of the calorimeter must be less than 3 GeV in addition to CMNP_CFT_12_5DEG_V*.

CMUP_CFT_12_5DEG_M*: The energy on the wedge of the calorimeter must be less than 3 GeV in addition to CMUP_CFT_12_5DEG_V*.

CMX_CFT_12_5DEG_V*: The traverse momentum of CMX muon is larger than 12 GeV/c.

CMX_JET*: A CMX muon with one or more jets.

CMX_CFT_12_5DEG_M*: The energy on the wedge of the calorimeter is less than 3 GeV in addition to CMX_CFT_12_5DEG_V*.

CMX_CFT_12_5DEG_E*: The energy on the wedge of the calorimeter is greater than 0 GeV in addition to CMX_CFT_12_5DEG_V*.

Appendix C

SUSY and Compositeness search at ATLAS

There are numbers of search topics at LHC. Here two of models which contain leptoquark-like mediators are shown.

C.1 Search for SUSY particles

The super-symmetric particles (SUSY) theory, an extensions to the SM predicts a wide spectrum of new particles within the LHC's production energy scale and within ATLAS detector observation capability. In the SM we consider space-time symmetry forming poincaré algebra and internal symmetry. Supersymmetry is a new kind of symmetry and it permits to interrelate fermions and bosons. The SUSY algebra has a self-conjugate spin 1/2 Majorana generator, generally denoted with Q_α , which has a property of changing the total angular momentum J by a half of unit. For example, it transfer the boson fields (of spin 1) into fermion fields (of spin 1/2):

$$\begin{aligned} Q_\alpha |\text{boson} \rangle &= |\text{fermion} \rangle \\ \bar{Q}_\alpha |\text{fermion} \rangle &= |\text{boson} \rangle \end{aligned} \tag{C.1}$$

Family	Particle	symbol (Spin)	SUSY partner	symbol (Spin)
fermions/ sfermions	quark	$q_{L,R}$ (1/2)	squark	$\tilde{q}_{L,R}$ (0)
	lepton	$q_{L,R}$ (1/2)	slepton	$\tilde{q}_{L,R}$ (0)
	photon	γ (1)	photino	$\tilde{\gamma}$ (1/2)
gauge bosons/ gauginos	gluon	g (1)	gluino	\tilde{g} (1/2)
	W-boson	W (1)	wino	\tilde{W} (1/2)
	Z-boson	Z (1)	zino	\tilde{Z} (1/2)
Higgs boson/Higgsinos	Higgs	H (0)	higgsinos	\tilde{H} (1/2)

Table C.1: Spectrum of SUSY particles.

where α is a spinor index ($\alpha = 1, \dots, 4$). Two successive Q_α operations involve a space-time translation¹, which indicates that the supersymmetry involves the structure of space-time. The operator Q_α can exist in N different forms (Q_α^i , where $i = 1, \dots, N$). However SUSY theory with $N = 1$ allows only fermions in chiral representations, and we take only this case for consideration here.

With $N = 1$ SUSY operator, the model contains particles of different spin:

$$\begin{array}{ccc}
 \textit{chiral} & \textit{gauge} & \textit{graviton/gravitino} \\
 f(\frac{1}{2}) & \mathcal{G}(1) & G(2) \\
 \tilde{f}(0) & \tilde{\mathcal{G}}(\frac{1}{2}) & \tilde{G}(\frac{3}{2})
 \end{array}$$

where in the brackets the spin is indicated. The local gauge symmetry based with Poincaré group involves spin-1 gauge fields and the general relativity theory predicts spin-2 gravitons. In supersymmetry model the supersymmetric partners of the gauge bosons and gravitons are the spin $\frac{1}{2}$ gauginos and the spin $\frac{3}{2}$ gravitinos. Two Higgs doublets are predicted to give fermion masses, and they correspond to spin $\frac{1}{2}$ Higgsinos. Table C.1 shows a list of SUSY particles.

The masses of the supersymmetry partner particles are unknown. In the frame work

¹The anti-commutation rules of SUSY operators gives

$$\{Q_\alpha, \bar{Q}_\beta\} = -2(\gamma_\mu)_{\alpha\beta} P^\mu \quad (\text{C.2})$$

where P^μ is space-time translation generators.

of the minimal super-symmetric extension to the Standard Model (MSSM), Monte Carlo simulations [129] have shown the discovery potentials of squarks \tilde{q} , gluinos \tilde{g} , charginos and neutralinos X , for accessible mass range at the LHC.

Possible signatures of SUSY particles include:

- ▷ **Multi-jet + \cancel{E}_T channel:** For \tilde{q} and \tilde{g} signatures, we look for high jet multiplicity and a large missing transverse momentum (\cancel{E}_T). This is one of the most common decay signatures. The background signals can be suppressed by cutting on the $\cancel{E}_T > 300$ GeV with high energy jets ($E_{jet} > 200$ GeV) [130]. With integrated luminosity of 10^5pb^{-1} , we expect to see signals for $M_{\tilde{g}} < 2300 \text{ GeV}/c^2$ for $M_{\tilde{q}} = M_{\tilde{g}}$.
- ▷ **Same-sign dilepton channel:** Another channel is the cascade decay from \tilde{q} and \tilde{g} by producing isolated leptons, into charginos and neutralinos. The final states in this channel is:

$$\tilde{g}\tilde{g}, \tilde{g}\tilde{q}, \tilde{q}\tilde{q} \rightarrow 2\ell^\pm + n\text{jets} + \cancel{E}_T$$

in which two leptons have the same sign. Additional n jets and substantial \cancel{E}_T will display a very distinctive topology. Backgrounds can come from $t\bar{t}$ events in dilepton decay channel, where the charge of one of the high p_T leptons is misidentified. Bremsstrahlung in the inner detector material may create confusion in the pattern recognition contributing a charge-sign misidentifications. Muons are both measured by the inner tracker and the outer muon system therefore the charge-sign identification is more precise than the electron case. Many possible reconstructions and signal selection criteria are tested in the Monte Carlo simulation, and the mass limit for the discovery with an integrated luminosity of 10^5pb^{-1} is at $M_{\tilde{g}} < 1800 \text{ GeV}/c^2$ for $M_{\tilde{q}} = M_{\tilde{g}}$.

- ▷ **Chargino and neutralino pairs:** they can be produced through the Drell-Yan mechanism or squark exchange, may be detected through their leptonic decays where the final state signature is three isolated leptons plus \cancel{E}_T . The main backgrounds from WZ/ZZ and $t\bar{t}$ production can be suppressed by the Z mass window cut and veto on low E_T jets, thus this channel is more appropriate for low luminosity runs. In this case, for an integrated luminosity of 10^4pb^{-1} , a SUSY signal can be extracted for $M_{\tilde{g}} < 600 \text{ GeV}/c^2$

for $\tan(\beta) = 2$, or for $M_{\tilde{g}} < 400 \text{ GeV}/c^2$ for $\tan(\beta) = 20$.

C.2 Search for Compositeness

If quarks and/or leptons contain more fundamental constituents called *preons*, characterised by a compositeness scale Λ , one would expect to observe deviations from the SM predictions which would result in different coupling factors above certain energy scale. The gauge boson-fermion coupling would be modified by factors:

$$F(Q^2) = \left(1 + \frac{Q^2}{\Lambda^2}\right)^{-1} \quad (\text{C.3})$$

where Λ characterises the compositeness scale. Λ_{qq} and Λ_{lq} denote the coupling strength for quark-quark or quark-lepton scattering. The effective Lagrangian is given by assuming the colour-singlet isoscalar exchanges between left-handed u quark and d quarks [131], in which the coupling strength factor will be introduced. Furthermore if the subprocess energy at the LHC is much greater than the compositeness scaling factor Λ , multi-fermion production will dominate which will introduce many new phenomena.

In ATLAS, searches for quark substructure can be carried out using the inclusive differential jet cross-section which is sensitive to the Λ_{qq} factor. The statistical sensitivity with an integrated luminosity of 10^5 pb^{-1} can reach up to $\Lambda_{qq} < 20 \text{ TeV}$. However the systematics of energy measurement at very high p_T affect strongly to the final sensitivity. For example an uncorrected non-linearity of 4% between 500 GeV and 4 TeV will fake a compositeness signal with $\Lambda_{qq} \sim 15 \text{ TeV}$, thus reducing the final sensitivity to below this value. Theoretical uncertainties due to the structure function, jet fragmentation, and/or higher order contributions to the cross-section will further limit the final sensitivity.

If both quarks and leptons are made of more fundamental constituents, a study of lepton-pair production at large dilepton invariant masses will provide good sensitivity to Λ_{lq} . Above a dilepton mass of $1 \text{ TeV}/c^2$ for leptons with $p_T > 400 \text{ GeV}/c^2$, the SM rate is dominated by Drell-Yan pairs with a small contribution from $t\bar{t}$. In contrast to the search for quark substructure, the experimental systematic uncertainties are small and the dominant uncertainty rises from the structure function parametrisation, which is estimated to be $\sim 25\%$. For an

integrated luminosity of 10^4 pb^{-1} , the expected rate is 70 reconstructed electron and muon pairs from the SM, with an expected excess of 60 pairs for $\Lambda_{\ell q} = 16 \text{ TeV}$. For 10^5 pb^{-1} , the search limit of the ATLAS detector can reach up to $\sim 30 \text{ TeV}$.

References

- [1] M. Krämer, T. Plehn, M. Spira, and P. Zerwas, “Pair production of scalar leptoquarks at the Tevatron”, *Phys. Rev. Lett.* **79** 341 (1997)
- [2] *For example, see:*
 - D. Griffiths, “Introduction to Elementary Particle Physics”, *Wiley* (1987),
 - F. Halzen and A. Martin, “Quarks and Leptons”, *Wiley* (1984),
 - D. Perkins, “Introduction to High Energy Physics”, *Addison Wesley* (1987),
 - J. Aichison and A. Hey, “Gauge Theories in Pariticle Physics (2nd ed.)”, *Adam Hilger* (1989)
- [3] “Partial-symmetries of weak interactions” S. L. Glashow, *Nucl.Phys.* **22** 579 (1961)
- [4] S. Weinberg, *Phys.Rev.Lett.* **19** 1264 (1967)
- [5] A. Salam, “Elementary Particle Theory”, *ed. N. Svarthholm*, Stockholm (1968)
- [6] *For example, see:* CDF collaboration, “The Collider Detector at Fermilab”, *Nucl. Inst. Meth. Phys. Res.*, **A 271** 387 (1988)
- [7] J. L. Hewett, S. Pakvasa, “Scalar-leptoquark production at hadron colliders”, *Phys. Rev. D* **37** 3165 (1988)
- [8] (*CDF collaboration*) F. Abe *et al.*, *Phys. Rev. Lett.* **75** 1012 (1995)
- [9] (*D0 collaboration*) S. Abachi *et al.*, *Phys. Rev. Lett.* **75** 3618 (1995)
- [10] Torbjörn Sjöstrand, “Pythia 5.7 and Jetset 7.4, Physics and Manual”, *CERN-TH.7112/93* (1994)
- [11] J. Benloch *et al.*, “A user’s guide to QFL”,
CDF/ANAL/MONTECARLO/PUBLIC/1810 (1992)
- [12] H. Kambara, “Second Generation Leptoquark Search at CDF”, *presented at American Physics Society Conference, Washington D.C. Apr.7-12, 1997*

- [13] H. Kambara, “Leptoquark Searches at CDF”, *presented at XIIth Hadron Collider Physics Symposium, Stony Brook, NY*, Jun. 5-11, 1997
- [14] H. Kambara, “Leptoquark Searches at CDF”, *hep-ex/9706026 Proceedings for XIIth Hadron Collider Physics Symposium, Stony Brook, NY*(1997)
- [15] G. D. Rochester and C. C. Bulter, “Nature” **160**, 855 (1947)
- [16] M. Gell-Mann, *Phys.Rev.* **92**, 883 (1953)
- [17] T. Nakano and K. Nishijima, *Prog.Thor.Phys.* **10**, 581 (1953)
- [18] M. Gell-Mann and Y. Ne’eman, “The Eightfold Way” *New York: Benjamin* (1964)
- [19] V. E. Barnes *et al.*, “Observation of a Hyperon with Strangeness”, *Phys.Rev.Lett.* **12**, 204 (1964)
- [20] M. Gell-Mann, *Phys. Lett.* **8**, 214 (1964)
- [21] G. Zweig, *CERN preprint TH401*, 412 (unpublished) (1964)
- [22] M. Y. Han and Y. Nambu, *Phys. Rev.* **139**, B1006 (1965)
- [23] O. W. Greenberg, *Phys. Rev. Lett.* **13**, 598 (1964)
- [24] Mark-J Collaboration, “The first Year of Mark-K”, *MIT Lab for Nucl. Sci. Rep.* 107 (1979)
- [25] S. A. Bludman, *Nuovo Cimento* **9**, 443 (1958)
- [26] P. W. Higgs, *Phys. Rev. Lett.* **12**, 132 (1964); **13**, 321 (1964); **13**, 585 (1964)
- [27] G. ’t Hooft, *Nucl. Phys.* **B 33**, 173 (1971); **B 35**, 167 (1971)
- [28] (*UA1 Collaboration*) G. Arnison *et al.*, *Phys.Lett.* **122 B**, 103 (1983)
- [29] (*UA2 Collaboration*) G. Banner *et al.*, *Phys.Lett.* **122 B**, 476 (1983)
- [30] (*UA1 Collaboration*) G. Arnison *et al.*, *Phys.Lett.* **126 B**, 398 (1983)
- [31] (*UA2 Collaboration*) G. Bagnaia *et al.*, *Phys.Lett.* **129 B**, 130 (1983)

- [32] CDF collaboration, F. Abe, *et al.*, “Observation of Top Quark Production in $p\bar{p}$ Collisions with CDF Detector at Fermilab”, *Phys. Rev. Lett.* **74** 2626 (1995)
- [33] UA1 Collaboration, T. Akesson *et al.*, “Search for new heavy quarks in proton-antiproton collisions at $\sqrt{s} = 0.63$ TeV” *Z. Phys.* **C 4**, 1 (1990),
UA2 Collaboration, C. Albajar *et al.*, “Search for top quark production at the CERN $\bar{p}p$ collider” *Z. Phys.* **C 46**, 179 (1990),
- [34] CDF collaboration, F. Abe, *et al.*, “Lower limit on the top quark mass from events with two leptons in $p\bar{p}$ collisions at $\sqrt{s} = 1.8$ TeV” *Phys. Rev. Lett.* **68**, 447 (1992), and references therein.
- [35] W. Heisenberg, *Z. Phys.* **77**, 1 (1932) *A translation for English can be found in* :
D. M. Brink, “Nuclear Forces”, *Elmsford, NY*, Pergamon (1965)
- [36] G. Ross, “Grand Unified Theories”, 195 The Benjamin/Cumminigs Publishing Co. Inc. (1984)
- [37] W. Büchmüller, D. Wyler, *Phys. Lett.* **B 177** 337 (1986)
- [38] H. Georgi and S. L. Glashow, “Unified theory of elementary-particle forces”, *Physics Today* Sep. 1980, 30 (1980);
“Unity of all elementary-particle forces”, *Phys. Rev. Lett.* **32** 438 (1974)
- [39] *Phys. Rev.* **D 50** 1673 (1994)
- [40] J. Pati and A. Salam, “Lepton number as the fourth color”, *Phys. Rev.* **D 10** Nr.1, 275(1974)
- [41] G. Valencia, S. Willenbrock, *phys. rev.*, **d50** 6843 (1994)
- [42] H. Wenzel, K. Maeshima, *CDF internal note 4224* (1997)
- [43] E. Farhi, “Technicolour”, *Phys. Rep.* **74** No.3, 277 (1981)
- [44] B.Schremp and F.Schremp, “Light leptoquarks”, *Nucl. Phys.* **B 231** 109 (1984);
“A confining SU(2) X SU(2) gauge model of the weak interactions”, *Phys. Lett.* **153 B** 101 (1985)

- [45] W. Buchmüller, S. Love, R. Peccei, and T. Yanagida, *Phys. Lett.* **115 B** 233 (1982)
- [46] W. Buchmüller, R. Peccei, and T. Anagida, “The structure of weak interactions for composite quarks and leptons”, *Nucl. Phys.* **B 244** 186 (1984);
J. Wudka, “Composit leptoquarks”, *Phys. Lett.* **167 B** 337 (1986)
- [47] J. Schwarz, “Superstring theory”, *Phys. Rep.* **89** No.3, 223 (1982);
E. Witten, “Symmetry breaking patterns in superstring models”, *Nucl. Phys.* **B 258** 75 (1985);
M. Dine, *et al.*, *Nucl.Phys.* **B 259** 519 (1985);
J. Breit, B. A. Ovrut, and G. Segre, *Phys.Lett.* **158 B** 33 (1985)
- [48] S. Pakvasa, “Signatures for horizontal symmetries and some other exotica at hadron colliders”, *Int. Journ. Mod. Phys.* **A 2**, 1317 (1987)
- [49] L. F. Abbott and E. Farhi, “Are the weak interactions strong?”, *Phys.Lett.* **101B** 69 (1981)
- [50] W. Buchmüller and D. Wyler, “Leptoquarks in Lepton-Quark Collisions”, *Phys. Lett.* **B 191**, 442 (1987)
- [51] J. Blümlein, *et al.*, “Lqptoquark Pair Production in Hadronic Interactions”, *DESY96-174* (1996)
- [52] P.Aurenche, “Chromodynamique quantique perturbative et applications”, Classes given in *Troisieme cycle de la physique en swiss romande, semestre d’hiver 1994*
- [53] M. Krämer, “Leptoquark production at Tevatron”, *RAL-TR-97-033, hep-ph/9707422*
- [54] P. Arnold and C. Wendt, *Phys. Rev.* **D 33**, 1873 (1986); G. Borisov, *et al.*, *Z. Phys.* **C 36**, 217 (1987)
- [55] W. Beenakker, H. Kuijf, and W. L. van Neerven, “QCD corrections to heavy-production in $p\bar{p}$ collisions”, *Phy. Rev.* **D 40** 54 (1989)
- [56] H. L. Lai, *et al.*, *Phys.Rev.* **D51** 4763 (1995)
- [57] Particle Data Group, “Particles and Fields”, *Phys. Rev.* **D 54** (1996)

- [58] (*ALEPH collaboration*) DeComp *et al.*, *Phys. Rept.* **216** 253 (1992),
(*DELPHI collaboration*) P. Abreu *et al.*, *Phys. Lett. B* **316** 620 (1993),
(*L3 collaboration*) Adriani *et al.*, *Phys. Rept.* **236** 1 (1993),
(*OPAL collaboration*) G. Alexiander *et al.*, *Phys. Lett. B* **268** 122 (1993),
(*H1 collaboration*) I. Ahmed *et al.*, *Z.Phys. C* **64** 545 (1993),
(*ZEUS collaboration*) M. Derrick *et al.*, *Phys. Lett. B* **306** 173 (1993)
- [59] S. Park, “Second Generation Leptoquark Search in Dimuon + Dijet Channel from Run IA and Run IB”,
CDF/ANAL/EXOTIC/CDFR/3063 (1995),
“Second Generation Leptoquark Search in Dimuon + Dijet Channel”,
CDF/ANAL/EXOTIC/CDFR/2468 (1995)
- [60] F. Abe *et al.*, *Phys. Rev. D* **48**, 3939 (1993)
- [61] S. Abachi *et al.*, *Phys. Rev. Lett.* **72**, 965 (1994)
- [62] S. Aid *et al.*, *Phys. Lett. B* **369**, 173 (1995)
- [63] F. Abe *et al.*, *Phys. Rev. D* **78**, 2906 (1997)
- [64] Results from proceedings of *The 32nd Recontres de Moriond, Les Arcs, France. March 1997*
- [65] F. Abe *et al.*, “Search for First Generation Leptoquark Pair Production in $p\bar{p}$ Collisions at $\sqrt{s} = 1.8$ TeV”, *hep-ex/9708017*, submitted to *Phys. Rev. Lett.* (1997)
- [66] (*CDF collaboration*) F.Abe *et.al.*, *Nucl. Instrum. Methods A* **271** 387 (1988), and the references therein.
- [67] D. Amidei *et al.*, “The CDF SVX: a Silicon Vertex Detector for a Hadron Collider”, *Nucl. Instr. Meth. A* **289** 388 (1990)
- [68] D. Amidei *et al.*, “The Silicon Vertex Detector for the Collider Detectot at Fermilab”, *Nucl. Instr. Meth. A* **350** 73 (1994)
- [69] (*CDF collaboration*) F.Abe *et.al.*, “Proposal for an Upgraded CDF detector”, *CDF internal note 1172* (1990)

- [70] D. Amidei, *et al.*, “Design and Construction of the CDF Central Tracking Chamber”, *Nucl. Instr. Meth. A* **268** 50 (1988)
- [71] L.Balka, *et al.*, “The CDF Central Electromagnetic Calorimeter”, *Nucl. Instr. Meth. A* **267** 272 (1988)
- [72] S.Bertolucci, *et al.*, “The CDF Central and Endwall Hadron Calorimeter”, *Nucl. Instr. Meth. A* **267** 301 (1988)
- [73] Y.Fukui, *et al.*, “CDF End Plug Electromagnetic Calorimeter using Conductive Plastic Proportional Tubes”, *Nucl. Instr. Meth. A* **267** 280 (1988)
- [74] G. Ascoli *et al.*, “CDF Central Muon Detector”, *Nucl. Instr. Meth. A* **268** 33 (1988)
- [75] N. Eddy, S. B. Kim, and S. Vejcik, *CDF internal note, CDF/ANAL/TOP/CDFR/3506* (1996)
- [76] G. Ascoli, *et al.*, “CDF Central Muon Detector”, *Nucl. Instr. Meth.*, **A 268** 33 (1988)
- [77] K. Byrum *et al.*, “The CDF Forward Muon System”, *Nucl. Instr. Meth. A* **268** 46 (1988)
- [78] A. Gaultier *et al.*, “Design and Performance of Drift Chambers for the Central Muon Upgrade”, *CDF internal note # 1500* (1991)
- [79] A. Daw *et al.*, “Study of the performance of CMEX Drift tubes”, *CDF internal note # 1614* (1991)
- [80] G. Ascoli *et al.*, “CDF Central Muon Level-1 Trigger Electronics” *Nucl. Instr. Meth. A* **269** 63 (1988)
- [81] D. Amidei *et al.*, “A Two Level Fastbus Based Trigger System for CDF” *Nucl. Instr. Meth. A* **269** 51 (1988)
- [82] J.T. Carroll *et al.*, “The CDF Level 3 Trigger”, *Nucl. Instr. Meth. A* **300** 552 (1992)
- [83] G.W. Foster *et al.*, “A Fast Hardware Track-Finder for the CDF Central Tracking Chamber” *Nucl. Instr. Meth. A* **269** 93 (1988)

- [84] H.Kambara *et al.*, “Search for second generation leptoquark with 110 pb^{-1} Run IA+B data and the preliminary results”
CDF/ANAL/EXOTIC/CDFR/4108 (1997)
- [85] M. Pillai *et al.*, “A search for Z' decaying to $\mu\mu$ using Run IA data and a first look at Run IB data”,
CDF/ANAL/EXOTIC/CDFR/2910 (1995)
- [86] M. Pillai *et al.*, “A search for Z' decaying to $\mu\mu$ from Run IA and Run IB”,
CDF/ANAL/EXOTIC/CDFR/3598 (1996)
- [87] P. de Barbaro *et al.*, “Z and drell-yan cross section measurement in dimuon channel”,
CDF/ANAL/ELECTROWEAK/CDFR/3510 (1996)
- [88] M. Krasberg, “Hight- p_T central muon data sets”,
CDF/ANAL/EXOTIC/CDFR/2326 (1993)
- [89] J. Wudka, *Phys. Lett.* **167 B** 337 (1986)
- [90] F.Abe *et al.*, *Phys. Rev.* **D 52** 2651, (1995)
- [91] Tony Liss, “A fast muon trigger simulation”,
CDF/DOC/TOP/GROUP/2998 (1995)
- [92] Phil Schlabach, “Efficiency of the cmx single muon triggers in run Ib”,
CDF/MEMO/MUON/CDFR/2718 (1994)
- [93] S. Catani *et al.*, “The Top Cross Section in Hadronic Collisions”, *CERN-TH/96-21, hep-ph/9602208* (1996)
- [94] T. Chikamatsu *et al.*, “Top dilepton analysis”,
CDF/ANAL/TOP/CDFR/1975 (1993)
- [95] L. Song *et al.*, “Study of Top Dilepton Background from $b\bar{b}$ Sources”,
CDF/ANAL/TOP/CDFR/2106 (1993)
- [96] J. Ohnemus, *Phys. Rev.* **D 44** 1403 (1993)

- [97] J. Wang *et al.*, “Estimate of $Z \rightarrow \tau^+ \tau^-$ background in the Top Dilepton Analysis”, *CDF/ANAL/TOP/CDFR/2108* (1993)
- [98] I. Yu and M. Schmidt “Studies of Muon Backgrounds in Low p_T Dimuon Events”, *CDF/ANAL/BOTTOM/CDFR/2674* (1994)
- [99] A. Amadon, C. Grosso-Pilcher, and F. Strumia, “Search for first generation leptoquark pair production”, *CDF/ANAL/EXOTIC/CDFR/4126* (1997)
- [100] *See, e.g.:* J. Blümlein, E. Boos, and A. Kryukov, *hep-ph/9610408*
- [101] LHC study group, “The Large Hadron Collider, Conceptual Design Report”, *CERN/AC/95-05* (1995)
- [102] ATLAS collaboration, “Letter of Intent”, *CERN/LHCC/92-4* (1992),
- [103] ATLAS collaboration, “Technical Proposal”, *CERN/LHCC/94-43* (1994)
- [104] CMS collaboration, “The compact muon solenoid– Technical proposal”, *CERN/LHCC/92-38* (1995)
- [105] LHC-B collaboration, “Letter of Intent for a dedicated LHC collider beauty experiment for precision measurements of CP-violation”, *CERN/LHCC/95-5* (1995)
- [106] ALICE collaboration, “Technical proposal for a large ion collider experiemnt at the CERN LHC”, *CERN/LHC/95-71* (1995)
- [107] D. Froidevaux and M. A. Parker, *ATLAS Internal Note INDET-NO0-046* (1994)
- [108] RD2 collaboration, “RD2 status report”, *CERN/DRDC/92-4*, (1992)
- [109] J. Blümlein, “Leptoquark pair production in hadronic interactions”, *DESY 96-174* (1996)
- [110] O. Éboli, R. Funchal, and T. Lungov, “Signal and backgrounds for leptoquarks at the LHC”, *hep-ph/9709319* (1997)

- [111] J. Botts *et al.*, *Phys. Rev.* **D 51**, 4763 (1995)
- [112] B. Dion, M. de Montigny, L. Marleau, and G. Simon, “Scalar leptoquark pair production at CERN LHC: Signal and Backgrounds”, *LAVAL-PHY-96-17*, *ALBERTA-THY-39-96* (1996)
- [113] G. Jarlskog, D. Rein, “Proceedings at Aachen, Germany”, *cern 90-10 V.3* (Oct. 1990)
- [114] ATLAS collaboration, “Inner Detector Technical Design Report”, *CERN/LHCC/97-16* (1997)
- [115] SCT group, *ATLAS Internal Note INDET-NO-085* (1994)
- [116] ATLAS collaboration, “ATLAS Technical Proposal”, *CERN/LHCC/94-43*, *LHCC/P2*, CERN (Dec. 1994)
- [117] Gateway software, “Verilog”, Instruction booklet (1991)
- [118] RD2/ATLAS, “1994 RD2 status report: Electronics”, CERN, (1994)
- [119] S. Siem, “Measurement of a new version of DHARP”, *SITP-No-110*, CERN (1994)
- [120] F. Anghinolfi *et al.*, “A Low Power Piecewise Linear Analog To Digital Converter for Use in Particle Tracking”, *Presented at the 1994 Nuclear Science Symposium, Norfolk Virginia* (1994)
- [121] H. Kambara, “The ADC chip (CRIAD) test result for RD2 detector application”, *SITP NOTE TR-101* (1994)
- [122] RD2 collaboration, “APC3 a 32 Channel CMOS Analog Pipeline Chip”, *RAL internal report* (1992)
- [123] M. Hansen, “An evaluation system for A/D converters”, *FERMI Note #9*, CERN (1992)
- [124] V. Valencic, P. Deval, “Non-Linear A/D converter For RD-2 detector application”, *MEAD Microelectronics, S.A.*, Nov. 10, 1992
- [125] National Instrument Cooperation, “LabVIEW software manual”

- [126] P. Allport, "ATLAS beam test result", *2nd international symposium on development and applications of semiconductor tracking detectors*, Hiroshima, Japan (Oct 10-13, 1995)
- [127] Atlas Collaboration, "Progress Report on the RD2 project", *CERN/DRDC-94-39* (1994)
- [128] J. Goldstone, *N. Cim.* **19**, 154 (1961); J. Goldstone, A. Salam, and S. Weinberg, *Phys. Rev.* **127**, 965 (1962)
- [129] F. Paige and S. Protopopescu, *Supercollider Physics*, p. 41, ed. D. Soper (World Scientific, Singapore, 1986),
H. Baer *et al.*, *FSU-HEP-930329* (1993), to appear in *Proceedings of the Workshop on Physics at Current Accelerators and the Supercollider*, ed. J. Hewett, A. White and D. Zeppenfeld, (World Scientific, Singapore, 1993).
- [130] G. Polesello, *ATLAS Internal Note PHYS-NO-059* (1994)
- [131] E. J. Eichten *et al.*, "Test for Quark and Lepton Substructure", *Phys. Rev. Lett.* **50** 811 (1983)

